Spring 2020

Investigating the Feasibility and Stability for Modeling Acoustic Wave Scattering Using a Time-Domain Boundary Integral Equation with Impedance Boundary Condition

Michelle E. Rodio
Old Dominion University, michelle.e.rodio@gmail.com

INVESTIGATING THE FEASIBILITY AND STABILITY FOR MODELING ACOUSTIC WAVE SCATTERING USING A TIME-DOMAIN BOUNDARY INTEGRAL EQUATION WITH IMPEDANCE BOUNDARY CONDITION

by

Michelle E. Rodio
B.S. May 2010, Embry-Riddle Aeronautical University
M.S. May 2012, Embry-Riddle Aeronautical University
M.S. December 2015, Old Dominion University

A Dissertation Submitted to the Faculty of
Old Dominion University in Partial Fulfillment of the
Requirements for the Degree of

DOCTOR OF PHILOSOPHY

COMPUTATIONAL AND APPLIED MATHEMATICS

OLD DOMINION UNIVERSITY
May 2020

Approved by:

Fang Q. Hu (Director)

Douglas M. Nark (Member)

Yan Peng (Member)

John Tweed (Member)

Ruhai Zhou (Member)

ABSTRACT

INVESTIGATING THE FEASIBILITY AND STABILITY FOR MODELING ACOUSTIC WAVE SCATTERING USING A TIME-DOMAIN BOUNDARY INTEGRAL EQUATION WITH IMPEDANCE BOUNDARY CONDITION

Michelle E. Rodio
Old Dominion University, 2020
Director: Dr. Fang Q. Hu

Reducing aircraft noise is a major objective in the field of computational aeroacoustics. When designing next generation quiet and environmentally friendly aircraft, it is important to be able to accurately and efficiently predict the acoustic scattering by an aircraft body from a given noise source. Acoustic liners are an effective tool for aircraft noise reduction and are characterized by a frequency-dependent impedance. Converted into the time-domain using Fourier transforms, an impedance boundary condition can be used to simulate the acoustic wave scattering by geometric bodies treated with acoustic liners.

This work considers using either an impedance or an admittance (inverse of impedance) boundary condition to allow for acoustic scattering problems to be modeled with geometries consisting of both un-lined and lined surfaces. Three acoustic liner models are discussed: the *Extended Helmholtz Resonator Model*, the *Three-Parameter Impedance Model*, and the *Broadband Impedance Model*. In both the *Helmholtz* and *Three-Parameter* models, liner impedance is specified at a given frequency, whereas the *Broadband* model allows for the investigation of multiple frequencies simultaneously. The impedance and admittance boundary conditions for acoustic liners are derived for each model and coupled with a time-domain boundary integral equation. The scattering solution is obtained iteratively using a boundary element method with constant spatial and third-order temporal basis functions.

Time-domain boundary integral equations are unfortunately prone to numerical instabilities due to resonant frequencies resulting from non-trivial solutions in the interior domain. When reformulated with the Burton-Miller method, the instabilities are eliminated. Using a Burton-Miller reformulation, the stability of the boundary element method assuming a liner boundary condition is assessed using eigenvalue analysis. The stability of each liner model is discussed, and it is shown that the *Three-Parameter* and *Broadband* models are sufficient for modeling an acoustic liner on the surface of scattering bodies. The *Helmholtz* model demonstrates strict limitations for stability, whereas the *Three-Parameter* and *Broadband*

models are stable for most cases.

Also included in this work is an assessment of the spatial accuracy of the time-domain boundary element method with respect to the surface element basis functions, as well as a performance study of the numerical algorithm.

This dissertation is dedicated to Dr. Shahrdad Sajjadi, may he rest in peace, for reinvigorating my love of mathematics and supporting my decision to pursue a doctoral degree. And to Philly, my one and only, for always being there when I needed it most.

ACKNOWLEDGEMENTS

There are many people who have contributed to the successful completion of this dissertation and to which I owe my deepest gratitude. I extend many thanks to ...

Dr. Fang Hu

Dr. Hu been a constant source of knowledge and guidance since my first semester as a graduate student at Old Dominion University. He taught my favorite mathematics course, the one that drove my desire to pursue a doctoral degree in mathematics: partial differential equations. I could not have asked for a better advisor than him. His patience, understanding, and kindness were paramount to my success as a graduate student.

Dr. Kim Bey

There are not enough words in the English language that can accurately express my gratitude for this woman. Kim has been my mentor and friend since my first week at NASA Langley Research Center in January 2014. Since then, she has pushed me to become a better mathematician, scientist, engineer, and researcher. Always on hand to share advice, Kim has shaped my life in insurmountable ways.

The Chandler Family

Charlotte, John, and their children scooped me up under their wing faster than I could say hello, offering their guidance, love, and support during some of the hardest years of my life. Though starting out as simply a tutor for their children, I quickly found myself immersed in the most loving of environments full of home-cooked meals, belly-clenching laughter, and timeless memories. After many long nights of studying, the Chandler family was always there to cheer me on and fill me coffee so I could keep on pushing through. Meeting them in August 2015 has changed my life and I truly would not have been successful in this program without them. It is because of them that I have a family in Virginia and a place to call home.

Dr. Douglas Nark

Doug was an excellent mentor for me throughout my doctoral education. He was always there to offer guidance and support which has made me a much better student and civil servant. I am incredibly grateful and honored to call him a colleague.

Drs. John Adam and Gordon Melrose

Drs. Adam and Melrose have not only been great educators for me, but also great friends. I have leaned on them for support more times than I can count throughout my time at Old Dominion University. I enjoyed our many, many talks and the excellent guidance I received from them both. Dr. Adam: thank you for our neighborhood walks, always checking in on me, and for the countless hugs you offered when I needed it most. Dr. Melrose: thank you for all our heart to hearts and for keeping me sane these many years. I am very grateful to you both.

Anthony Williams

Anthony was, and always will be, a great classmate, office-mate, co-worker, and friend. Thank you for the countless memories and for always pushing me to be a better student. I have looked up to you for many years and continue to do so each and every day at work. Now get your butt in gear ... it is your turn.

Christopher Volle and Gabriela Sanz-Douglass

Chris and Gabi have been godsends to me these past several years. They were always there cheering me on and lifting me up when I was down. They are not only the best of friends but also two of the most amazing humans I know. Building 1148 would not have been the same without the two of you. Thank you for all that you do for me on a daily basis and for keeping things interesting. Life would not be the same without you both.

Amy Rodio, Kaitlin Rodio, and Allen Campione

I would not have survived these past seven years without the love and support of Amy, Katie, and Allen. I truly do not know how to thank you all for all that you have done for me. I love you all to pieces. I hope to have made you PROWD.

Drs. Yan Peng, John Tweed, and Ruhai Zhou

To my committee, Drs. Peng, Tweed, and Zhou: thank you for your years of support. I treasure having learned so much from you while studying at Old Dominion University. My education would not have been the same without you. I am honored to have had you all on my committee. Thank you for everything.

My "Kids" and Their Parents

My doctoral education would not have been nearly as interesting nor fun if not for being able to spend my weeknights and weekends working with so many wonderful families around Norfolk. To my kids: you have been a blessing to teach these many years and I hope to have instilled a love of mathematics in your hearts. Being able to spend my nights with you teaching you how to graph and rationalize fractions, though you may have hated it from time to time, really kept me going during some hard times. To the parents: thank you for opening your homes to me and allowing me the privilege to get to know your children and help them each night with their own schoolwork. You may have brought me on to teach them mathematics, but they have taught me much more than I have ever taught them. Thank you for the many laughs, dinners, and countless times you have all cheered me on.

My Family and Friends

Last but not least, I want to extend gratitude to all my friends and family. In New Jersey and Virginia. From NASA and home. From college and high school. From near and far. Parents, aunts, uncles, cousins, and pets. THANK YOU ALL. I owe each and every one of you a little piece of this work. This has been a long seven years and your love and support have been a guiding light each and every day. Thank you for believing in me. For pushing me. And for never letting me give up.

NOMENCLATURE

Abbreviations and Symbols

CHIEFS	Combined Helmholtz Integral Equation Formulation
CPU	Central Processing Unit
GPU	Graphics Processing Unit
PPW	Points-Per-Wavelength
PPW2	Points-Per-Wavelength-Squared
TF-FAST	Time-Domain Fast Acoustics Scattering Toolkit
$\star\star\star$	Denotes Eigenvalues Greater than Two
dnc	Denotes Solutions that Do Not Converge by 5,000 Iterations
dnc †	Denotes Solutions that Do Not Converge by 10^6 Iterations
emb	Denotes Matrices that Exceed MATLAB Memory Bounds

Greek Letters

α	Variable Used in the Green's Function Solution where $\alpha = \sqrt{1 - M^2}$
α_ℓ	Parameter of *Broadband Impedance Model*
$\boldsymbol{\beta}$	Variable Used in the Green's Function Solution where $\boldsymbol{\beta} = \boldsymbol{M}/(c\alpha^2)$
β_ℓ	Parameter of *Broadband Impedance Model*
γ	Analytical Solution Parameter
γ_ℓ	Parameter of *Broadband Impedance Model*
∇	Divergence Operator
Δt	Numerical Time Step
δ	Dirac Delta Function; Tolerance of Matrix Power Iteration Method
δ_{ij}	Kronecker Delta Function
$\partial/\partial\overline{n}$	Modified Normal Derivative for Scattering Body
$\partial/\partial\overline{n'}$	Modified Normal Derivative for Observer Body
ϵ	Characteristic Dimension; Damping; Spherical Coordinate of (ϵ, ϕ, θ)
η	Local Coordinate of (ξ, η)
θ	Polar Coordinate of (r, θ); Spherical Coordinate of (ϵ, ϕ, θ)
λ	Eigenvalue
$\lambda_{\max}$	Largest Eigenvalue

ν	Multiple of the Time Step
ξ	Analytical Solution Parameter; Local Coordinate of (ξ, η)
ρ_0	Average Fluid Density
σ	Parameter of Source Term
τ	Integration Variable for Time
ϕ	Spherical Coordinate of (ϵ, ϕ, θ); Velocity Potential
$\hat{\phi}$	Total Field Solution
ϕ_{inc}	Plane Wave Solution for Incident Wave
$\hat{\phi}_{\text{inc}}$	Modified Plane Wave Solution for Incident Wave
ϕ_j	Surface Element Basis Function at Node j
ϕ_{ref}	Plane Wave Solution for Reflected Wave
$\hat{\phi}_{\text{ref}}$	Modified Plane Wave Solution for Reflected Wave
ψ_k	Temporal Basis Functions at Time Step Increment k
Ψ	Lagrange Function
ω	Frequency, Non-Dimensionalized by $\omega = 2\pi c/L$
ωm	Face-Sheet Mass Reactance

Roman Letters

$\boldsymbol{A}$	Matrix Used for the March-On-in-Time Scheme
$\hat{A}$	Analytical Solution Parameter
A_0	Impedance Parameter of *Three-Parameter Model*
$\overline{A_0}$	Admittance Parameter of *Three-Parameter Model*
A_ℓ	Parameter of *Broadband Impedance Model*
A_{INT}	Simplification Used for Burton-Miller Analysis
A_{inc}	Analytical Solution Parameter for Incident Wave
A_{ref}	Analytical Solution Parameter for Reflected Wave
a	Stability Condition Parameter Used for Burton-Miller
$\boldsymbol{B}$	Matrix Used for Burton-Miller Reformulation
B_ℓ	Parameter of *Broadband Impedance Model*
B_{INT}	Simplification Used for Burton-Miller Analysis
B'_{INT}	Simplification Used for Burton-Miller Analysis after Regularization
b	Stability Condition Parameter Used for Burton-Miller
C	CPU Core Count

$\boldsymbol{C}$	Matrix Used for Burton-Miller Reformulation
C_ℓ	Parameter of *Broadband Impedance Model*
C_s	Cauchy Principal Value
C_{INT}	Simplification Used for Burton-Miller Analysis
c	Speed of Sound
c_o	Arbitrary Positive Constant
$\boldsymbol{D}$	Time Step Increment k
d_k	Coefficient of $\boldsymbol{D}$ Diagonal Matrix
$\boldsymbol{E}$	Matrix Used for Impedance Boundary Condition
E_j	Element on Scattering Body
$\boldsymbol{e}$	Eigenvector
e_k	Coefficient of $\boldsymbol{E}$ Diagonal Matrix
$\boldsymbol{e}_\eta$	Unit Vector in Local Coordinate System (ξ, η)
$\boldsymbol{e}_\xi$	Unit Vector in Local Coordinate System (ξ, η)
$\boldsymbol{F}$	Arbitrary Vector; Matrix Used for Impedance Boundary Condition
$F(r, \theta)$	Arbitrary Function Used in Burton-Miller Formulation
$F(\omega)$	Fourier Transform
F_R	Face-Sheet Resistance Impedance Constant
$\overline{F_R}$	Face-Sheet Resistance Admittance Constant
F_β	Impedance Parameter Used for Varying the Cavity Reactance
$\overline{F_\beta}$	Admittance Parameter Used for Varying the Cavity Reactance
f	Arbitrary Function Used to Illustrate Operator Identities
$f(t)$	Inverse Fourier Transform
$\boldsymbol{G}$	Matrix Used for Impedance Boundary Condition
G_0	Variable Used in the Green's Function Solution where $G_0 = 1/\overline{R}$
$\tilde{G}$	Free-Space Adjoint Green's Function
g	Arbitrary Function Used to Illustrate Operator Identities
h_0	Impedance Parameter of *Broadband*, *Three-Parameter* Models
$\overline{h_0}$	Admittance Parameter of *Three-Parameter Model*
$\boldsymbol{I}$	Identity Matrix
i	Imaginary Unit where $i^2 = -1$; Loop Increment Counter
J	Variable Used to Denote Finite Number of Time Steps
$\boldsymbol{\mathcal{J}}$	Matrix Used for Impedance Boundary Condition
J_1	Parameter of *Broadband Impedance Model*

J_2	Parameter of *Broadband Impedance Model*
j	Loop Increment Counter
K	Variable Used to Denote Finite Number of Time Steps
$\boldsymbol{\mathcal{K}}$	Matrix Used for Impedance Boundary Condition
k	Time Step Counter; Loop Increment Counter; Wave Number
k_x	Analytical Solution Parameter Along the x-Direction
k_y	Analytical Solution Parameter Along the y-Direction
L	Arbitrary Length, or Resonator Cavity Depth
$\boldsymbol{\mathcal{L}}$	Matrix Used for Impedance Boundary Condition
L_x	Plate Length Along the x-Direction
L_y	Plate Length Along the y-Direction
L_z	Plate Length Along the z-Direction
ℓ	Loop Increment Counter
$\boldsymbol{M}$	Mach Number where $\boldsymbol{M} = \boldsymbol{U}/c$
M	Magnitude of Mach Number where $M = \lvert\boldsymbol{M}\rvert$
$\boldsymbol{\mathcal{M}}$	Matrix Used for Impedance Boundary Condition
M_n	Mach Number of Mean Flow Normal to the Scatterer where $M_n = \boldsymbol{M} \cdot \boldsymbol{n}$
M_n'	Mach Number of Mean Flow Normal to the Observer where $M_n' = \boldsymbol{M} \cdot \boldsymbol{n}'$
$\boldsymbol{M_T}$	Tangential Component of the Mach Number
N	Loop Increment Counter; Number of Surface Elements
$\boldsymbol{\mathcal{N}}$	Matrix Used for Impedance Boundary Condition
N_e	Total Number of Surface Nodes
N_t	Total Number of Time Steps
N_x	Surface Discretization Along the x-Direction
N_y	Surface Discretization Along the y-Direction
N_z	Surface Discretization Along the z-Direction
$\boldsymbol{n}$	Unit Normal Vector Pointing Inward to the Scattering Body
$\boldsymbol{n}'$	Unit Normal Vector Pointing Inward to the Observer Body
$\overline{\boldsymbol{n}}$	Modified Unit Normal Vector Pointing Inward to the Scattering Body
$\overline{\boldsymbol{n}}'$	Modified Unit Normal Vector Pointing Inward to the Observer Body
$\boldsymbol{\mathcal{P}}$	Matrix Used for Impedance Boundary Condition
P_n	Normal Derivative of Acoustic Pressure on Soft Body (Lined Surfaces)
P_{eff}	Parallel Efficiency Due to Increasing Core Counts
p	Order of the Spatial Basis Function

$p(\boldsymbol{r}, \omega)$	Acoustic Pressure in the Frequency-Domain
$p(\boldsymbol{r}, t)$	Acoustic Pressure in the Time-Domain
$\boldsymbol{p}_j^{(0,1,2)}$	Solution for the Discretized System of Partial Differential Equations
$\boldsymbol{\mathcal{Q}}$	Matrix Used for Impedance Boundary Condition
$q(\boldsymbol{r}, t)$	Known Acoustic Source in the Time-Domain
$\overline{R}$	Variable Used in the Green's Function Solution where $\overline{R} = 1/G_0$
R_0	Impedance Parameter of *Broadband*, *Three-Parameter* Models
$\overline{R_0}$	Admittance Parameter of *Three-Parameter Model*
r	Polar Coordinate of (r, θ)
$\boldsymbol{r}$	Arbitrary Point in Three-Dimensional Space where $\boldsymbol{r} = \boldsymbol{r}(x, y, z)$
$\boldsymbol{r'}$	Observer Point in Three-Dimensional Space where $\boldsymbol{r'} = \boldsymbol{r'}(x', y', z')$
$\boldsymbol{r}_s$	Arbitrary Point on the Scattering Body Surface where $\boldsymbol{r}_s = \boldsymbol{r}_s(x_s, y_s, z_s)$
$\boldsymbol{r}'_s$	Observer Point on the Scattering Body Surface where $\boldsymbol{r}'_s = \boldsymbol{r}'_s(x'_s, y'_s, z'_s)$
r_i	Collocation Point
S	Acoustic Scattering Surface
S_0	Rigid Body (Un-lined Surfaces)
S_l	Soft Body (Lined Surfaces)
S_{CPU}	Speedup Due to Increasing Core Counts
S_ϵ	Hemispherical Surface of Characteristic Dimension ϵ
S'_ϵ	Complement of S_ϵ where $S'_\epsilon = V \cap S_\epsilon$
s	Serial Portion of Code
T	Total Simulation Time
t	Time
t'	Instantaneous Time
t_k	Time at Time Step Increment k
t'_R	Retarded Time
$\boldsymbol{U}$	Mean Flow Velocity Vector
U	Mean Flow Magnitude where $U = \lvert\boldsymbol{U}\rvert$
U_n	Normal Component of the Mean Flow where $U_n = \boldsymbol{U} \cdot \boldsymbol{n}$
$\boldsymbol{U_T}$	Tangential Component of the Mean Flow
u_j^k	Numerical Solution of p on the j-th Node at Time t_k
$\boldsymbol{u^n}$	Rigid Body Solution for the Discretized System of Equations
V	Volume Exterior of the Scattering Surface
$v(\boldsymbol{r}, \omega)$	Acoustic Velocity Vector in the Frequency-Domain

v_j^k	Numerical Solution of P_n on the j-th Node at Time t_k
$\boldsymbol{v^n}$	Soft Body Solution for the Discretized System of Equations
$\boldsymbol{w^n}$	Solution for the Simplified Discretized System of Equations
X	Speedup Multiplier
x	x-Component of Arbitrary Point in Three-Dimensional Space (x, y, z)
x'	x-Component of Observer Point in Three-Dimensional Space (x', y', z')
x_s	x-Component of Surface Point in Three-Dimensional Space (x_s, y_s, z_s)
$Y(\omega)$	Surface Admittance in Frequency-Domain
Y_I	Imaginary Component of Admittance
Y_R	Real Component of Admittance
$y(t)$	Surface Admittance in Time-Domain
y	y-Component of Arbitrary Point in Three-Dimensional Space (x, y, z)
y'	y-Component of Observer Point in Three-Dimensional Space (x', y', z')
y_s	y-Component of Surface Point in Three-Dimensional Space (x_s, y_s, z_s)
$Z(\omega)$	Surface Impedance in Frequency-Domain
Z_I	Imaginary Component of Impedance
Z_R	Real Component of Impedance
$z(t)$	Surface Impedance in Time-Domain
z	z-Component of Arbitrary Point in Three-Dimensional Space (x, y, z)
z'	z-Component of Observer Point in Three-Dimensional Space (x', y', z')
z_s	z-Component of Surface Point in Three-Dimensional Space (x_s, y_s, z_s)
$\mathbf{0}$	Zero Matrix

TABLE OF CONTENTS

LIST OF TABLES

LIST OF FIGURES

CHAPTER 1

INTRODUCTION AND RELATED WORK

Reducing aircraft noise is a major objective in the field of computational aeroacoustics. When designing next generation quiet and environmentally friendly aircraft, it is important to be able to accurately and efficiently predict the acoustic scattering by an aircraft body from a given noise source [1, 2]. Acoustic scattering problems can be modeled by reformulating the convective wave equation as an integral equation. As stated by Meyer *et. al.*, integral equations "appear very attractive because they eliminate the need to consider the infinite domains normally associated with radiation problems, reduce the dimensionality of the problem by one (*e.g.*, from a three-dimensional partial differential equation to a two-dimensional surface integral equation), and can readily handle arbitrary geometries and boundary conditions" [3].

One method of deriving an integral equation for acoustic scattering is through coordinate transformation. Blokhintzev [4] derived an integral equation for an inhomogeneous moving media using coordinate transformation and reduced volume integrals to surface integrals in the time-domain using Green's Theorem. Another such way to derive an integral equation is through generalized function theory. The derivation, first introduced by Ffowcs-Williams and Hawking [5] in 1969, demonstrates the basis of generalized function theory to be that "generalized forms of the field variables are established to hold over a continuous infinite space." Ffowcs-Williams and Hawking's work was an extension of Lighthill's 1952 acoustic analogy theory [6] and handles surface discontinuities as concentrated surface source distributions. Farassat [7] and Meyers [8] continued work with generalized function theory through the 1970s and 1980s. They extended the analysis to scattering by moving surfaces by providing the derivation of Kirchhoff's formula which uses boundary integral equations to solve for the acoustic scattering problem on moving surfaces [9].

Numerical solutions of boundary integral equations can be obtained through a variety of methods. One such way is to discretize the surface and solve iteratively using boundary element methods [10–18]. As stated by Wu and Yu [18], "to reconstruct the acoustic pressures over the entire surface of a vibrating object, one can utilize Kirchhoff integral theory [which] correlates the radiated acoustic pressures to the surface acoustic quantities which can be determined by solving an integral equation numerically using [boundary element methods]."

Numerical solutions can also be obtained by using the method of least squares [18,19]. This method reconstructs "the radiated acoustic pressures from a vibrating object [by employing] an expansion of acoustic modes that satisfy the Helmholtz equation" [18]. The method of least squares is uniformly convergent, minimizes errors, and yields a unique solution. Boundary element methods, on the other hand, may produce non-unique solutions yet offer a unique advantage over least squares: they effectively handle singular and infinite fields due to using only surface element discretization which ultimately saves computing memory and maintains high computational efficiency [1,10,20,21].

The Ffowcs-Williams-Hawking [5] and Farassat-Meyers [7,8] methods for deriving Kirchhoff's formula to solve acoustic scattering problems using integral equations have been studied extensively in both the frequency- and time-domains [9,22–26]. Frequency-domain solvers are the most used and researched within literature; they have a reduced computational cost [27] and allow for modeling time-harmonic fields at a single frequency [15,27,28]. Moreover, frequency-domain solvers eliminate the growth of Kelvin-Helmholtz instabilities caused by velocity shear of two interacting fluids and allow for an impedance boundary condition to be imposed more naturally [28].

Despite the benefits of frequency-domain solvers, there are several distinct advantages to using a time-domain solver [1,29]. Time-domain solvers allow for the simulation and study of broadband sources and time-dependent transient signals, whereas studying broadband sources in the frequency-domain carry a high computational cost. Time-domain solvers also allow for the scattering solution at all frequencies to be obtained within a single computation and avoid needing to invert a large dense linear system as is required in the frequency-domain. Moreover, a time-domain solution is more naturally coupled with a nonlinear computational fluid dynamics simulation of noise sources. As Reymen *et. al.* stated in 2008, "time-domain computational methods have a clear advantage over frequency-domain methods not only for broadband problems, nonlinear interaction investigations, and transient wave problems, but also for large problems (*e.g.*, three-dimensional high frequencies)" [30].

Time-domain boundary integral equations have been used since the 1960s to study wave propagation problems [31–35]. In 1962, Friedman and Shaw [31] studied the scattering of a plane acoustic wave by cylindrical bodies of arbitrary cross-section with rigid surfaces. In [31], time-domain boundary integral equations were used to solve for the acoustic pressure at an arbitrary field point using initial conditions and time-retarded values of pressure and its normal derivative on the surface. Friedman and Shaw continued their work by studying cylindrical bodies of arbitrary cross-section with soft surfaces when, in 1966, Shaw [32]

published a study using mixed, or Robin-type, boundary conditions on the surface of the scattering body. In 1963, Banaugh and Goldsmith [33] also used boundary integral equations to study wave diffraction in both the near- and far-field by rigid bodies of arbitrary cross-section. In 1966, Mitzner [34] used time-domain boundary integral equations to study acoustic scattering by both soft and rigid bodies using the normal velocity and velocity potential on the surface. He furthered his work in 1967 by introducing a numerical method for solving these model equations explicitly using retarded time values. This method better handled resonance regions when "the length of the incident pulse is of the order of the characteristic dimensions of the scatterer" [35].

As computers advanced and processing power improved, researchers discovered numerical instabilities when solving time-domain boundary integral equations. Over longer run times, instabilities appeared as exponentially growing oscillations [10, 36–43]. This numerical instability has been observed across multiple disciplines including acoustics, electromagnetics, and elastodynamics [42]. Rynne and Smith noted that when integral equations are solved via explicit time marching, *i.e.*, obtaining a solution at the k-th time step $t_k = k\Delta t$ using solutions from retarded time steps $\Delta t, 2\Delta t, \ldots, (k-1)\Delta t$, numerical instability tends to occur at large time steps as a result of "the existence of internal modes of resonance of the body which correspond to time harmonic solutions of the integral equation" [42], *i.e.*, at the internal eigenfrequencies [3]. In the frequency-domain, resonant modes near the frequency of interest yield an ill-conditioned matrix due to the existence of non-unique solutions at the resonant frequencies [11, 43]. These resonant modes result in numerical instabilities in the time-domain solution.

Time-domain numerical instability has been studied extensively by many authors [9]. In [37, 38, 40–44], instability was reduced using time-averaging schemes, but this method was found to increase computational cost. For example, Rynne and Smith [42] noted that, if the scattering body has internal resonances or a pole close to the imaginary axis, time-averaging eliminates numerical instabilities at the risk of the computational cost increasing by 10% [43]. Time-averaging may also affect solution accuracy [45]. Instability can also be reduced using higher order approximation in both space and time [10, 40, 41, 46] but this method was found to cause instability in the exterior problem [44]. Implicit time marching schemes that "employ accurate surface representations and sophisticated numerical integration and differentiation rules" [11] have also be shown to eliminate instability. In [9], *e.g.*, Lee and Lee use implicit time marching to solve time-domain boundary integral equations and successfully avoid longer run time instability but as Ergin and Shankar [11] noted, this

too increased computational cost. Geranmayeh *et. al.* [47] further demonstrated that "the conformity of the order of time integration and the time interpolation is essential for the establishment of a stable time-domain boundary integral equation solver."

Dodson *et. al.* [39] and Bluck and Walker [46] use implicit time marching with high-order Gauss-quadrature to remove numerical instabilities apparent in explicit schemes. In [46], *e.g.*, quadratic spatial and temporal elements are utilized, and a time marching algorithm is used to solve matrices with a conjugate gradient method. Galerkin methods have also been employed by many authors [48–50] but these methods are not only very difficult to implement but also very costly to use [10]. Another method used to suppress fictitious internal modes in the time-domain is the Combined Helmholtz Integral Equation Formulation, or CHIEFS [51]. Jang and Ih studied CHIEFS, a method which "constrains the surface Kirchhoff integral by forcing the pressures at the additional interior points to be zero when the shortest retarded time between boundary nodes and an interior point elapses," but found that the method was unable to eliminate fictitious modes at frequencies higher than the frequency limit of the boundary element method. In [11], Ergin, Shankar, and Michielssen recommend using a Burton-Miller-type reformulation of the time-domain boundary integral equation to eliminate the numerical instability. This method, first introduced in 1971 [52], derives a supplementary integral equation resulting in a unique solution for the exterior problem. The Burton-Miller approach has been studied extensively for eliminating numerical instability in the time-domain [1, 3, 10, 53–56].

Though Burton-Miller eliminates time-domain numerical instability, this method results in the formation of hypersingular integrals. To mitigate the hypersingularities, the integrals can be reformulated into weak singularities using Taylor expansion and a limiting process [1, 10, 57] by applying a regularization method [52]. Time-domain boundary integral equation solvers also carry a high computational cost, especially when reformulated with the Burton-Miller method. In recent years, numerical techniques for modeling acoustic wave scattering using Burton-Miller-type time-domain boundary integral equations have been under development [1, 53–55]. It has been shown that both computational cost and computational time can be reduced using fast algorithms and high performance computing.

The objective of this study is to investigate the feasibility and stability for modeling acoustic wave scattering using a Burton-Miller-type time-domain boundary integral equation with an impedance boundary condition applied on the scattering surface. The numerical solution is obtained using boundary element methods. Outlines of subsequent chapters are as follows. In Chapter 2, the derivation of a time-domain boundary integral equation

reformulated from the convective wave equation is presented. The formulation shown uses an adjoint free space Green's function and is equivalent to results obtained by generalized function theory [1]. The Burton-Miller reformulation and reduction of hypersingularities via method of regularization is also derived and presented. All derivations follow the cited references as they evolved over time, for completeness.

In Chapter 3, boundary element methods are introduced for solving the Burton-Miller-type time-domain boundary integral equation derived in Chapter 2. The scattering solution is obtained using temporal and spatial basis functions and a March-On-in-Time scheme in which a sparse matrix is solved iteratively using retarded time values. The time marching scheme is introduced and, as with Chapter 2, all derivations follow the cited references as they evolved over time, for completeness.

In [53], Hu performed a Fourier analysis of various well-known shifted Lagrange basis functions to assess the temporal resolution of the boundary element method. He demonstrated that "the accuracy limits of the conventional third-, fourth- and fifth-order shifted Lagrange basis functions are increased from 25, 18 and 14 points per wave period to 22, 12 and 10 points per wave period by using the optimized temporal basis functions respectively." For the work presented herein, third-order shifted Lagrange temporal basis functions and constant spatial basis functions are used and, following the assessment in [53], the spatial resolution of the constant basis functions is studied. This assessment represents a new contribution of the present work. All results are discussed in Chapter 3.

Further, given that time-domain boundary integral equation solvers carry a high computational cost, a performance study is conducted for the time-domain solver used, aptly named TD-FAST, the Time-Domain Fast Acoustic Scattering Toolkit. Though a performance study is not groundbreaking research, it is an important facet for understanding the computational complexity of time-domain acoustic solvers and for developing skills required in the field of high performance computing. In Chapter 4, key terminology is introduced and the performance of TD-FAST is studied using a combination of different problem sizes and compute resources. This assessment represents another contribution of the present work though not unique in the field of research. All results are discussed in Chapter 4.

When studying the diffraction of acoustic waves around a scattering body, the boundary condition on the surface must be properly defined. As previously mentioned, time-domain boundary integral equations are used to solve for the acoustic pressure at an arbitrary field point using initial conditions and time-retarded values of pressure and its normal derivative on the surface. Boundary conditions are defined through the terms involving the normal

derivative of pressure. When considering the scattering effects of rigid bodies, the normal derivative of pressure is equal to zero. For soft bodies, the terms involving the normal derivative of pressure are non-zero and are defined by an impedance boundary condition, herein denoted by $Z(\omega)$. Impedance is a "means to characterize the absorption and reflection of waves at a surface" [58] and is a complex-valued quantity such that $\mathrm{Re}(Z)$ is given to be the acoustic resistance and $\mathrm{Im}(Z)$ is given to be the acoustic reactance [29, 59, 60]. Transformed into the time-domain using Fourier transforms, an impedance boundary condition may be coupled with a time-domain boundary integral equation to model acoustic wave scattering by soft surfaces. Alternatively, an admittance boundary condition may also be used. Admittance, herein denoted by $Y(\omega)$, is defined to be the inverse of impedance: $Y(\omega) = 1/Z(\omega)$.

Soft surfaces of scattering bodies are surfaces in which an acoustic liner is applied. Typically composed of an array of Helmholtz resonators arranged in a honeycomb structure for support and covered with a perforate face-sheet, acoustic liners are used for dissipating the incident acoustic wave and are very effective at absorbing sound near the design frequency [29, 30, 59–63]. Liners can used for suppressing jet engine noise by inlet and exhaust ducts, *e.g.*, [64] and work by "inducing vortex shedding at the mouths of resonators" [65]. Acoustic liners are characterized by a frequency-dependent impedance value and, when converted into the time-domain, yield a suitable impedance boundary condition for acoustically treated surfaces.

Time-domain impedance boundary conditions are widely researched in literature [29, 30, 59, 66–68]. When converted into the time-domain using inverse Fourier transforms, a convolution integral is introduced which is very time-consuming to solve. But, when the impedance boundary condition is "represented by a sum of certain special functions, the evaluation of the convolution may be carried out in a simple systematic manner" [62]. For the time-domain boundary condition to be physical, the representative impedance model is required to be causal, real, and passive [59]. Causality expresses the notion that if a source is turned on at any time in the past, then the pressure should be zero for all times prior [58, 69].

In [59], Rienstra introduced an *Extended Helmholtz Resonator Model* and in [29, 65] Tam and Auriault introduced a *Three-Parameter Impedance Model*. Both models represent acoustic liner impedance at a single frequency. In the *Helmholtz* model, the free parameters are determined by the Helmholtz resonator geometry noting that the length, shape, and perforation face-sheet porosity affect the resonance frequency [70], *i.e.*, the frequency at

which the liner approaches its maximum frequency. In the *Three-Parameter* model, the free parameters are determined from measured data. For both models, the parameters must satisfy the casual, real, and passive properties required for the boundary condition to represent a physical quantity.

One of the key advantages of using time-domain solvers over frequency-domain solvers is the ability to study and simulate broadband sources. Though the *Helmholtz* and *Three-Parameter* models are both effective at modeling an impedance boundary condition in the frequency-domain, they are ineffective over a wide range of frequencies. Both were studied by Richter *et. al.* [66], and it was found that while the models yield similar numerical results for predicting noise scattering, instability is observed in the *Helmholtz* model. The instability can be reduced by filtering retarded time values.

In [62], Li, Li, and Tam developed a *Broadband Impedance Model* to represent liner impedance at a wide range of frequencies. The model was derived from the multipole impedance model in [30] and was further studied in the works of Dragna *et. al.* [67] and Troian *et. al.* [68]. The *Broadband* model satisfies causality and reality, however "the parameters of the model must be properly adjusted or else the passivity condition may not be satisfied" [62]. The model is derived using recursive combination methods combined with first-order partial differential equations and is effective when used with high-order numerical schemes.

Since simulation of time-domain boundary integral equations without Burton-Miller reformulation is prone to numerical instabilities [55], it is necessary to study the integral equation reformulation to ensure stability of the system once coupled with a liner boundary condition. In literature, stability analysis has proven convolution quadrature methods second-order convergent for basis functions constant in space and linear in time [71], but no theoretical proof has yet been provided for other methods. Eigenvalue analysis is the current standard for studying the stability of time-domain boundary integral equations [39, 44, 51]. Though eigenvalue analysis alone is not sufficient for proving stability, it is necessary that the numerical scheme has maximum eigenvalues no greater than unity. In [44], *e.g.*, Wang *et. al.* studied the link between solving the exterior acoustic problem in the frequency-domain to the corresponding time marching instabilities in the time-domain by assessing the eigenvalues of the iterating matrix. Moreover, in [51], Jang and Ih express that "the stability of a [time-domain boundary element method] depends on the eigensystem of the single iterative matrix" because in "[time-domain boundary element method] calculations employing a discrete model, of which the involved single iterative matrix is nonsymmetric and non-normal,

one cannot always assure the completeness of the eigenspace mathematically."

In previous work [2,72], the numerical stability of coupling either an impedance or admittance boundary condition with a Burton-Miller-type time-domain boundary integral equation was studied. Both the *Extended Helmholtz Resonator Model* and the *Three-Parameter Impedance Model* were considered in the analyses. A numerical eigenvalue study was conducted, and it was demonstrated that each model yields numerical stability following observable conditions.

To fully assess the stability of an acoustic liner impedance boundary condition, it is now proposed to include and study the *Broadband Impedance Model* to allow for the investigation of multiple frequencies simultaneously. This assessment represents a major contribution of the present work. In Chapter 5, the numerical scheme for an impedance boundary condition is derived and all three acoustic liners discussed in this work are introduced: the *Extended Helmholtz Resonator Model*, the *Three-Parameter Impedance Model*, and the *Broadband Impedance Model*. All derivations follow the cited references as they evolved over time, for completeness. In Chapter 6, the methodology for conducting the eigenvalue study is presented and stability results are discussed for all three acoustic liner models. Concluding remarks are provided in Chapter 7 and all applicable figures, graphs, and tables not included in the main body are listed in the appendices.

CHAPTER 2

STABLE TIME-DOMAIN BOUNDARY INTEGRAL EQUATION

The acoustic signature of an aircraft is best predicted when accounting for both the direct noise source and the scattering of a sound field by objects such as the fuselage, landing gear, engine duct, propellers, *etc.* [26]. Time-domain boundary integral equations allow for the accurate and efficient prediction of the acoustic signature from a given noise source in the presence of a constant mean flow. However, the time-domain boundary integral equation with solid wall boundary conditions has an intrinsic numerical instability due to resonant frequencies resulting from non-trivial solutions in the interior domain [9, 11, 43]. Using a Burton-Miller-type reformulation of the time-domain boundary integral equation resonant frequencies can be eliminated. This chapter presents the derivation of a time-domain boundary integral equation with Burton-Miller-type reformulation.

2.1 TIME-DOMAIN BOUNDARY INTEGRAL EQUATION

Acoustic waves are assumed to be disturbances of small amplitudes. With a uniform mean flow, acoustic disturbances are governed by the linear convective wave equation [1, 9, 24–26]. Consider the linear convective wave equation given a constant mean flow $\boldsymbol{U}$:

$$\left(\frac{\partial}{\partial t}+\boldsymbol{U}\cdot\nabla\right)^2 p\left(\boldsymbol{r},t\right)-c^2\nabla^2 p\left(\boldsymbol{r},t\right)=q\left(\boldsymbol{r},t\right) \tag{1}$$

with homogeneous initial conditions:

$$p(\boldsymbol{r},0)=\frac{\partial p}{\partial t}(\boldsymbol{r},0)=0,\ t=0 \tag{2}$$

where $\boldsymbol{r}$ is an arbitrary point in three-dimensional space, $p(\boldsymbol{r},t)$ is the acoustic pressure, $q(\boldsymbol{r},t)$ is the known acoustic source, and c is the speed of sound. The acoustic pressure is assumed to be small perturbations at any point $(\boldsymbol{r},t)$ in three-dimensional acoustic field. The solution of (1) with initial conditions (2) is dependent on the applied boundary conditions on the surface or collection of surfaces, S, for the scattering problem as illustrated in Figure 1. The applied boundary condition on surface(s) S will be discussed in Chapter 5. By assuming

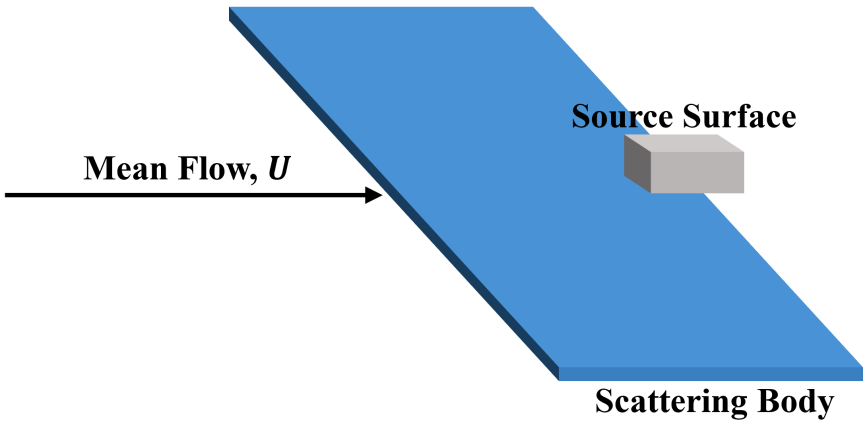

Fig. 1: Schematic diagram illustrating the relationship between the mean flow, the surface of the scattering body, and the surface of the acoustic source.

uniform mean flow, the governing equation is the linear convective wave equation (1). If $\boldsymbol{U}$ were assumed non-uniform, the Euler equation would be used in place of (1).

The convective wave equation (1) and initial conditions (2), along with suitable boundary conditions, is reformulated into an integral equation by introducing a free-space adjoint Green's function $\tilde{G}(\boldsymbol{r}, t; \boldsymbol{r'}, t')$, that for convenience of discussion, is defined as follows:

$$\left(\frac{\partial}{\partial t} + \boldsymbol{U} \cdot \nabla\right)^2 \tilde{G}(\boldsymbol{r}, t; \boldsymbol{r'}, t') - c^2 \nabla^2 \tilde{G}(\boldsymbol{r}, t; \boldsymbol{r'}, t') = \delta\left(\boldsymbol{r} - \boldsymbol{r'}\right) \delta\left(t - t'\right) \tag{3}$$

with homogeneous initial conditions:

$$\tilde{G}(\boldsymbol{r}, t; \boldsymbol{r'}, t') = \frac{\partial \tilde{G}}{\partial t}(\boldsymbol{r}, t; \boldsymbol{r'}, t') = 0, \ t > t' \tag{4}$$

where δ is the Dirac delta function. The Green's function $\tilde{G}(\boldsymbol{r}, t; \boldsymbol{r'}, t')$ is a distribution of singularities [57]. It is the acoustic pressure response at position $\boldsymbol{r}$ and time t due to a source located at arbitrary position $\boldsymbol{r'}$. It acts instantaneously at time t' and is therefore zero for all $t < t'$, *i.e.*, for $t \in (-\infty, t']$ [73]. The fundamental solution to (3) and (4) is well-known and is given by [1, 7–9, 24, 74]:

$$\tilde{G}(\boldsymbol{r}, t; \boldsymbol{r'}, t') = \frac{G_0}{4\pi c^2} \delta\left(t' - t + \boldsymbol{\beta} \cdot (\boldsymbol{r'} - \boldsymbol{r}) - \frac{\overline{R}}{c\alpha^2}\right) \tag{5}$$

where

$$\overline{R}(\boldsymbol{r}, \boldsymbol{r'}) = \sqrt{\left|\boldsymbol{M} \cdot (\boldsymbol{r} - \boldsymbol{r'})\right|^2 + \alpha^2 \left|\boldsymbol{r} - \boldsymbol{r'}\right|^2}, \ G_0 = \frac{1}{\overline{R}(\boldsymbol{r}, \boldsymbol{r'})} \tag{6}$$

in which

$$\boldsymbol{M} = \frac{\boldsymbol{U}}{c},\ \alpha = \sqrt{1 - M^2},\ \boldsymbol{\beta} = \frac{\boldsymbol{U}}{c^2 - U^2} = \frac{\boldsymbol{M}}{c\alpha^2}. \tag{7}$$

In (5) through (7), $M = |\boldsymbol{M}|$ is the magnitude of Mach number $\boldsymbol{M}$, $U = |\boldsymbol{U}|$ is the magnitude of mean flow $\boldsymbol{U}$, and $\boldsymbol{r'}$ is an arbitrary point on the scattering body surface.

Consider the following differential operator properties [73] for arbitrary functions f, g and vector $\boldsymbol{F}$:

$$f\nabla^2 g - g\nabla^2 f = \nabla \cdot (f\nabla g - g\nabla f) \tag{8}$$

and

$$\begin{aligned} f\left(\frac{\partial}{\partial t} + \boldsymbol{F}\cdot\nabla\right)^2 g - g\left(\frac{\partial}{\partial t} + \boldsymbol{F}\cdot\nabla\right)^2 f &= \frac{\partial}{\partial t}\left[f\left(\frac{\partial}{\partial t} + \boldsymbol{F}\cdot\nabla\right)g - g\left(\frac{\partial}{\partial t} + \boldsymbol{F}\cdot\nabla\right)f\right] \\ &+ \nabla\cdot\left\{\left[f\left(\frac{\partial}{\partial t} + \boldsymbol{F}\cdot\nabla\right)g - g\left(\frac{\partial}{\partial t} + \boldsymbol{F}\cdot\nabla\right)f\right]\boldsymbol{F}\right\}. \end{aligned} \tag{9}$$

The wave propagation problem is reformulated into a time-domain boundary integral equation by considering the following operation with Green's Function $\tilde{G}$ and mean flow $\boldsymbol{U}$:

$$\tilde{G}\left(\frac{\partial}{\partial t} + \boldsymbol{U}\cdot\nabla\right)^2 p - p\left(\frac{\partial}{\partial t} + \boldsymbol{U}\cdot\nabla\right)^2 \tilde{G}.$$

Using (1) for the first term, (3) for the second term, and simplifying yields:

$$\begin{aligned} &\tilde{G}\left(\frac{\partial}{\partial t} + \boldsymbol{U}\cdot\nabla\right)^2 p - p\left(\frac{\partial}{\partial t} + \boldsymbol{U}\cdot\nabla\right)^2 \tilde{G} \\ &\qquad = \tilde{G}c^2\nabla^2 p + \tilde{G}q - pc^2\nabla^2\tilde{G} - p\delta\left(\boldsymbol{r} - \boldsymbol{r'}\right)\delta\left(t - t'\right) \\ &\qquad = c^2\left(\tilde{G}\nabla^2 p - p\nabla^2\tilde{G}\right) + \tilde{G}q - p\delta\left(\boldsymbol{r} - \boldsymbol{r'}\right)\delta\left(t - t'\right) \\ &\qquad = c^2\nabla\cdot\left(\tilde{G}\nabla p - p\nabla\tilde{G}\right) + \tilde{G}q - p\delta\left(\boldsymbol{r} - \boldsymbol{r'}\right)\delta\left(t - t'\right). \end{aligned} \tag{10}$$

Note that property (8) was used in the last step of (10). Setting $f = \tilde{G}$, $g = p$, and $\boldsymbol{F} = \boldsymbol{U}$ in property (9) gives:

$$\begin{aligned} &\tilde{G}\left(\frac{\partial}{\partial t} + \boldsymbol{U}\cdot\nabla\right)^2 p - p\left(\frac{\partial}{\partial t} + \boldsymbol{U}\cdot\nabla\right)^2 \tilde{G} \\ &\qquad = \frac{\partial}{\partial t}\left[\tilde{G}\left(\frac{\partial}{\partial t} + \boldsymbol{U}\cdot\nabla\right)p - p\left(\frac{\partial}{\partial t} + \boldsymbol{U}\cdot\nabla\right)\tilde{G}\right] \\ &\qquad + \nabla\cdot\left\{\left[\tilde{G}\left(\frac{\partial}{\partial t} + \boldsymbol{U}\cdot\nabla\right)p - p\left(\frac{\partial}{\partial t} + \boldsymbol{U}\cdot\nabla\right)\tilde{G}\right]\boldsymbol{U}\right\}. \end{aligned} \tag{11}$$

Combining (10) and (11) and solving for $\tilde{G}q - p\delta\left(\boldsymbol{r}-\boldsymbol{r}'\right)\delta\left(t-t'\right)$ yields:

$$\begin{aligned}
&\tilde{G}q - p\delta\left(\boldsymbol{r}-\boldsymbol{r}'\right)\delta\left(t-t'\right) \\
&\quad = \frac{\partial}{\partial t}\left[\tilde{G}\left(\frac{\partial}{\partial t}+\boldsymbol{U}\cdot\nabla\right)p - p\left(\frac{\partial}{\partial t}+\boldsymbol{U}\cdot\nabla\right)\tilde{G}\right] \\
&\quad + \nabla\cdot\left\{\left[\tilde{G}\left(\frac{\partial}{\partial t}+\boldsymbol{U}\cdot\nabla\right)p - p\left(\frac{\partial}{\partial t}+\boldsymbol{U}\cdot\nabla\right)\tilde{G}\right]\boldsymbol{U}\right\} - c^2\nabla\cdot\left(\tilde{G}\nabla p - p\nabla\tilde{G}\right)
\end{aligned} \tag{12}$$

where $p = p(\boldsymbol{r},t)$, $q = q(\boldsymbol{r},t)$, and $\tilde{G} = \tilde{G}(\boldsymbol{r},t;\boldsymbol{r'},t')$. Integrating (12) over the volume V exterior to the scattering surface S for space, *i.e.* a volume that encompasses the surface of the scattering body but does not include the interior region, and over an interval $[0^-, t'^+]$ for time t yields:

$$\begin{aligned}
&\int_{0^-}^{t'^+}\int_V \tilde{G}(\boldsymbol{r},t;\boldsymbol{r'},t')q(\boldsymbol{r},t)d\boldsymbol{r}dt - \int_{0^-}^{t'^+}\int_V p(\boldsymbol{r},t)\delta\left(\boldsymbol{r}-\boldsymbol{r}'\right)\delta\left(t-t'\right)d\boldsymbol{r}dt \\
&\qquad = \int_{0^-}^{t'^+}\int_V \frac{\partial}{\partial t}\left[\tilde{G}\left(\frac{\partial}{\partial t}+\boldsymbol{U}\cdot\nabla\right)p - p\left(\frac{\partial}{\partial t}+\boldsymbol{U}\cdot\nabla\right)\tilde{G}\right]d\boldsymbol{r}dt \\
&\qquad + \int_{0^-}^{t'^+}\int_V \nabla\cdot\left\{\left[\tilde{G}\left(\frac{\partial}{\partial t}+\boldsymbol{U}\cdot\nabla\right)p - p\left(\frac{\partial}{\partial t}+\boldsymbol{U}\cdot\nabla\right)\tilde{G}\right]\boldsymbol{U}\right\}d\boldsymbol{r}dt \\
&\qquad - \int_{0^-}^{t'^+}\int_V c^2\nabla\cdot\left(\tilde{G}\nabla p - p\nabla\tilde{G}\right)d\boldsymbol{r}dt
\end{aligned} \tag{13}$$

where

$$\int_{0^-}^{t'^+}\int_V \frac{\partial}{\partial t}\left[\tilde{G}\left(\frac{\partial}{\partial t}+\boldsymbol{U}\cdot\nabla\right)p - p\left(\frac{\partial}{\partial t}+\boldsymbol{U}\cdot\nabla\right)\tilde{G}\right]d\boldsymbol{r}dt = 0 \tag{14}$$

by the initial conditions and

$$\int_{0^-}^{t'^+}\int_V p(\boldsymbol{r},t)\delta\left(\boldsymbol{r}-\boldsymbol{r}'\right)\delta\left(t-t'\right)d\boldsymbol{r}dt = p(\boldsymbol{r'},t') \tag{15}$$

by definition [73].

Consider the Divergence Theorem for arbitrary vector $\boldsymbol{F}$: $\int_V \nabla\cdot\boldsymbol{F}dV = \int_S \boldsymbol{F}\cdot d\boldsymbol{a}$. The application of this theorem transforms an integration over a volume to an integration over a surface. Applying the Divergence Theorem to the second and third integrals of (13) yields:

$$\begin{aligned}
&\int_{0^-}^{t'^+}\int_V \nabla\cdot\left\{\left[\tilde{G}\left(\frac{\partial}{\partial t}+\boldsymbol{U}\cdot\nabla\right)p - p\left(\frac{\partial}{\partial t}+\boldsymbol{U}\cdot\nabla\right)\tilde{G}\right]\boldsymbol{U}\right\}d\boldsymbol{r}dt \\
&\qquad = \int_{0^-}^{t'^+}\int_S \left[\tilde{G}\left(\frac{\partial p}{\partial t}+\boldsymbol{U}\cdot\nabla p\right) - p\left(\frac{\partial\tilde{G}}{\partial t}+\boldsymbol{U}\cdot\nabla\tilde{G}\right)\right]U_n d\boldsymbol{r}_s dt
\end{aligned} \tag{16}$$

and

$$\int_{0^-}^{t'^+}\int_V c^2\nabla\cdot\left(\tilde{G}\nabla p - p\nabla\tilde{G}\right)d\boldsymbol{r}dt = c^2\int_{0^-}^{t'^+}\int_S\left(\tilde{G}\frac{\partial p}{\partial n} - p\frac{\partial\tilde{G}}{\partial n}\right)d\boldsymbol{r}_s dt \tag{17}$$

where $\boldsymbol{r}_s$ denotes points on the surface S, $U_n = \boldsymbol{U}\cdot\boldsymbol{n}$ denotes the normal component of the mean velocity on surface point $\boldsymbol{r}_s$, and $\boldsymbol{n}$ is the unit normal vector. The assumption is made such that $\boldsymbol{n}$ points inward to the body, *i.e.*, outward from the solution domain for exterior scattering problems [1]. Substituting (14) through (17) into (13) and solving for $p(\boldsymbol{r'},t')$ yields the Kirchhoff integral representation of the acoustic field in the presence of a uniform mean flow [1]:

$$\begin{aligned}p(\boldsymbol{r'},t') = &\int_{0^-}^{t'^+}\int_V \tilde{G}(\boldsymbol{r}_s,t;\boldsymbol{r'},t')q(\boldsymbol{r}_s,t)d\boldsymbol{r}dt + c^2\int_{0^-}^{t'^+}\int_S\left(\tilde{G}\frac{\partial p}{\partial n} - p\frac{\partial\tilde{G}}{\partial n}\right)d\boldsymbol{r}_s dt\\ &-\int_{0^-}^{t'^+}\int_S\left[\tilde{G}\left(\frac{\partial p}{\partial t}+\boldsymbol{U}\cdot\nabla p\right) - p\left(\frac{\partial\tilde{G}}{\partial t}+\boldsymbol{U}\cdot\nabla\tilde{G}\right)\right]U_n d\boldsymbol{r}_s dt.\end{aligned} \tag{18}$$

Using the Green's function solution (5) at surface point $\boldsymbol{r} = \boldsymbol{r}_s$:

$$\begin{aligned}\frac{\partial\tilde{G}}{\partial n} &= \frac{\partial}{\partial n}\left[\frac{G_0}{4\pi c^2}\delta\left(t'-t+\boldsymbol{\beta}\cdot(\boldsymbol{r'}-\boldsymbol{r}_s)-\frac{\overline{R}}{c\alpha^2}\right)\right]\\ &= \frac{1}{4\pi c^2}G_0\delta'\left(t'-t+\boldsymbol{\beta}\cdot(\boldsymbol{r'}-\boldsymbol{r}_s)-\frac{\overline{R}}{c\alpha^2}\right)\left(-\boldsymbol{\beta}\cdot n-\frac{1}{c\alpha^2}\frac{\partial\overline{R}}{\partial n}\right)\\ &+\frac{1}{4\pi c^2}\frac{\partial G_0}{\partial n}\delta\left(t'-t+\boldsymbol{\beta}\cdot(\boldsymbol{r'}-\boldsymbol{r}_s)-\frac{\overline{R}}{c\alpha^2}\right)\text{ and}\end{aligned} \tag{19}$$

$$\begin{aligned}\nabla\tilde{G} &= \nabla\left[\frac{G_0}{4\pi c^2}\delta\left(t'-t+\boldsymbol{\beta}\cdot(\boldsymbol{r'}-\boldsymbol{r}_s)-\frac{\overline{R}}{c\alpha^2}\right)\right]\\ &= \frac{1}{4\pi c^2}G_0\delta'\left(t'-t+\boldsymbol{\beta}\cdot(\boldsymbol{r'}-\boldsymbol{r}_s)-\frac{\overline{R}}{c\alpha^2}\right)\left(-\boldsymbol{\beta}-\frac{1}{c\alpha^2}\nabla\overline{R}\right)\\ &+\frac{1}{4\pi c^2}\left(\nabla G_0\right)\delta\left(t'-t+\boldsymbol{\beta}\cdot(\boldsymbol{r'}-\boldsymbol{r}_s)-\frac{\overline{R}}{c\alpha^2}\right).\end{aligned} \tag{20}$$

The Dirac delta functions in (19) and (20) restrict the spatial integration to the scattering surface, effectively equaling zero outside the surface boundary, and the temporal integration to a retarded time, t'_R [8,9]. When integrating over a surface, points on the surface experience acoustic signals at different times based on the motion of the body and location of the observer. Evaluating the integral at a retarded time accounts for the effects of the acoustic signal reaching different points on the body surface at different times [57]. Substituting (5), (19), and (20) into (18) and further expressing as an integration of retarded time values $t_R{}'$ such that

$$t'_R = t'+\boldsymbol{\beta}\cdot(\boldsymbol{r'}-\boldsymbol{r})-\frac{\overline{R}}{c\alpha^2} = t'+\frac{\boldsymbol{M}\cdot(\boldsymbol{r'}-\boldsymbol{r})-\overline{R}}{c\alpha^2}$$

yields:

$$
\begin{aligned}
p(\boldsymbol{r}', t') = & \frac{1}{4\pi c^2}\int_{0^-}^{t'^+}\int_V G_0 q(\boldsymbol{r}_s, t)\delta\left(t'_R - t\right) d\boldsymbol{r}_s dt + \frac{1}{4\pi}\int_{0^-}^{t'^+}\int_S G_0 \frac{\partial p}{\partial n}\left(\boldsymbol{r}_s, t\right)\delta\left(t'_R - t\right) d\boldsymbol{r}_s dt \\
& - \frac{1}{4\pi}\int_{0^-}^{t'^+}\int_S G_0 p\left(\boldsymbol{r}_s, t\right)\delta'\left(t'_R - t\right)\left(-\boldsymbol{\beta}\cdot n - \frac{1}{c\alpha^2}\frac{\partial \overline{R}}{\partial n}\right) d\boldsymbol{r}_s dt \\
& - \frac{1}{4\pi}\int_{0^-}^{t'^+}\int_S \frac{\partial G_0}{\partial n} p\left(\boldsymbol{r}_s, t\right)\delta\left(t'_R - t\right) d\boldsymbol{r}_s dt + \int_{0^-}^{t'^+}\int_S \frac{\partial \tilde{G}}{\partial t} p\left(\boldsymbol{r}_s, t\right) U_n d\boldsymbol{r}_s dt \\
& - \frac{1}{4\pi c^2}\int_{0^-}^{t'^+}\int_S G_0\left(\frac{\partial p}{\partial t}\left(\boldsymbol{r}_s, t\right) + \boldsymbol{U}\cdot\nabla p\left(\boldsymbol{r}_s, t\right)\right)\delta\left(t'_R - t\right) U_n d\boldsymbol{r}_s dt \\
& + \frac{1}{4\pi c^2}\int_{0^-}^{t'^+}\int_S G_0 \boldsymbol{U}\cdot\left(-\boldsymbol{\beta} - \frac{1}{c\alpha^2}\nabla\overline{R}\right) p\left(\boldsymbol{r}_s, t\right)\delta'\left(t'_R - t\right) U_n d\boldsymbol{r}_s dt \\
& + \frac{1}{4\pi c^2}\int_{0^-}^{t'^+}\int_S \left(\boldsymbol{U}\cdot\nabla G_0\right) p\left(\boldsymbol{r}_s, t\right)\delta\left(t'_R - t\right) U_n d\boldsymbol{r}_s dt. \qquad (21)
\end{aligned}
$$

Consider the identities of the Dirac delta function:

$$
\begin{aligned}
&\int_{-\infty}^{\infty} f(x)\delta[\pm(x-a)]dx = f(a) \\
&\int_{-\infty}^{\infty} f(x)\delta'[\pm(x-a)]dx = \mp f'(a) \\
&\int_{-\infty}^{\infty} f(x)\delta''[\pm(x-a)]dx = f''(a) \text{ for all } a \in \mathbb{R}
\end{aligned}
$$

With these identities, terms with δ in (21) are reduced to:

$$
\int_{0^-}^{t'^+} p\left(\boldsymbol{r}_s, t\right)\delta(t'_R - t)dt = \int_{0^-}^{t'^+} p\left(\boldsymbol{r}_s, t\right)\delta[-(t - t'_R)]dt = p\left(\boldsymbol{r}_s, t'_R\right)
$$

and

$$
\int_{0^-}^{t'^+} p\left(\boldsymbol{r}_s, t\right)\delta'(t'_R - t)dt = \int_{0^-}^{t'^+} p\left(\boldsymbol{r}_s, t\right)\delta'[-(t - t'_R)]dt = +\frac{\partial p}{\partial t}\left(\boldsymbol{r}_s, t'_R\right).
$$

Noting that

$$
\frac{\partial \tilde{G}}{\partial t} = \frac{\partial}{\partial t}\left[\frac{G_0}{4\pi c^2}\delta\left(t'_R - t\right)\right] = \frac{G_0}{4\pi c^2}\frac{\partial}{\partial t}\left[\delta\left(t'_R - t\right)\right] = -\frac{1}{4\pi c^2} G_0 \delta'\left(t'_R - t\right)
$$

and integrating with respect to time, (21) becomes:

$$\begin{aligned}4\pi c^2 p(\boldsymbol{r'},t') = &\int_V G_0 q(\boldsymbol{r}_s,t'_R)d\boldsymbol{r}_s + c^2\int_S G_0\frac{\partial p}{\partial n}\left(\boldsymbol{r}_s,t'_R\right)d\boldsymbol{r}_s \\ &- c^2\int_S \frac{\partial G_0}{\partial n}p\left(\boldsymbol{r}_s,t'_R\right)d\boldsymbol{r}_s + c^2\int_S G_0\left(\boldsymbol{\beta}\cdot n + \frac{1}{c\alpha^2}\frac{\partial \overline{R}}{\partial n}\right)\frac{\partial p}{\partial t}\left(\boldsymbol{r}_s,t'_R\right)d\boldsymbol{r}_s \\ &- \int_S U_n G_0\left[\boldsymbol{U}\cdot\nabla p\left(\boldsymbol{r}_s,t'_R\right)\right]d\boldsymbol{r}_s + \int_S U_n\left(\boldsymbol{U}\cdot\nabla G_0\right)p\left(\boldsymbol{r}_s,t'_R\right)d\boldsymbol{r}_s \\ &+ \int_S U_n G_0\left[-2-\boldsymbol{U}\cdot\boldsymbol{\beta}+\left(-\frac{1}{c\alpha^2}\right)\left(\boldsymbol{U}\cdot\nabla\overline{R}\right)\right]\frac{\partial p}{\partial t}\left(\boldsymbol{r}_s,t'_R\right)d\boldsymbol{r}_s dt. \end{aligned} \tag{22}$$

Terms multiplied by the Dirac delta functions are considered source terms for the convective wave equation [7, 8]. Noting that $c^2\boldsymbol{\beta}\cdot\boldsymbol{n} + U_n(-2-\boldsymbol{U}\cdot\boldsymbol{\beta}) = -U_n$ from (7), the integrals with $\partial p/\partial t$ in (22) simplify, reducing the equation to:

$$\begin{aligned}4\pi c^2 p(\boldsymbol{r'},t') = &\int_V G_0 q(\boldsymbol{r}_s,t'_R)d\boldsymbol{r}_s + c^2\int_S G_0\frac{\partial p}{\partial n}\left(\boldsymbol{r}_s,t'_R\right)d\boldsymbol{r}_s - \int_S U_n G_0\left[\boldsymbol{U}\cdot\nabla p\left(\boldsymbol{r}_s,t'_R\right)\right]d\boldsymbol{r}_s \\ &+ \int_S \frac{G_0}{c\alpha^2}\left[c^2\frac{\partial\overline{R}}{\partial n} - U_n c\alpha^2 - U_n\left(\boldsymbol{U}\cdot\nabla\overline{R}\right)\right]\frac{\partial p}{\partial t}\left(\boldsymbol{r}_s,t'_R\right)d\boldsymbol{r}_s dt \\ &+ \int_S\left[U_n\left(\boldsymbol{U}\cdot\nabla G_0\right) - c^2\frac{\partial G_0}{\partial n}\right]p\left(\boldsymbol{r}_s,t'_R\right)d\boldsymbol{r}_s. \end{aligned} \tag{23}$$

Equation (23) is further reduced by decomposing the mean flow $\boldsymbol{U}$ into normal and tangential components, *i.e*, $\boldsymbol{U} = U_n\boldsymbol{n} + \boldsymbol{U_T}$ noting that

$$\begin{aligned}\boldsymbol{U}\cdot\nabla p\left(\boldsymbol{r}_s,t'_R\right) &= \left(U_n\boldsymbol{n}+\boldsymbol{U_T}\right)\cdot\nabla p\left(\boldsymbol{r}_s,t'_R\right) = U_n\boldsymbol{n}\cdot\nabla p\left(\boldsymbol{r}_s,t'_R\right) + \boldsymbol{U_T}\cdot\nabla p\left(\boldsymbol{r}_s,t'_R\right) \\ &= U_n\frac{\partial p}{\partial n}\left(\boldsymbol{r}_s,t'_R\right) + \boldsymbol{U_T}\cdot\nabla p\left(\boldsymbol{r}_s,t'_R\right),\end{aligned}$$

and introducing the following modified normal derivatives:

$$\frac{\partial\overline{R}}{\partial\overline{n}} = \frac{\partial\overline{R}}{\partial n} - M_n(\boldsymbol{M}\cdot\nabla\overline{R}) = \frac{\partial\overline{R}}{\partial n} - \frac{U_n(\boldsymbol{U}\cdot\nabla\overline{R})}{c^2} = \frac{\alpha^2\boldsymbol{n}\cdot\boldsymbol{(r-r')}}{\overline{R}} \text{ and} \tag{24}$$

$$\frac{\partial G_0}{\partial\overline{n}} = \frac{\partial G_0}{\partial n} - M_n(\boldsymbol{M}\cdot\nabla G_0) = \frac{\partial G_0}{\partial n} - \frac{U_n(\boldsymbol{U}\cdot\nabla G_0)}{c^2} = \frac{-\alpha^2\boldsymbol{n}\cdot\boldsymbol{(r-r')}}{\overline{R}^3} \tag{25}$$

where $M_n = \boldsymbol{M}\cdot\boldsymbol{n}$ is the Mach number of mean flow normal to the body surface and $\overline{\boldsymbol{n}} = \boldsymbol{n} - M_n\boldsymbol{M}$. Substituting equations (24) and (25) into (23) and further modifying terms with mean flow yields the following result in terms of $\boldsymbol{U}$:

$$\begin{aligned}4\pi c^2 p(\boldsymbol{r'},t') = &\int_V G_0 q(\boldsymbol{r}_s,t'_R)d\boldsymbol{r}_s + \int_S G_0\left(c^2-U_n^2\right)\frac{\partial p}{\partial n}\left(\boldsymbol{r}_s,t'_R\right)d\boldsymbol{r}_s - c^2\int_S\frac{\partial G_0}{\partial\overline{n}}p\left(\boldsymbol{r}_s,t'_R\right)d\boldsymbol{r}_s \\ &- \int_S U_n G_0\boldsymbol{U_T}\cdot\nabla p\left(\boldsymbol{r}_s,t'_R\right)d\boldsymbol{r}_s + \int_S\frac{G_0}{c\alpha^2}\left(c^2\frac{\partial\overline{R}}{\partial\overline{n}} - U_n c\alpha^2\right)\frac{\partial p}{\partial t}\left(\boldsymbol{r}_s,t'_R\right)d\boldsymbol{r}_s\end{aligned}$$

and in terms of $\boldsymbol{M}$:

$$4\pi p(\boldsymbol{r'},t') = \frac{1}{c^2}\int_V G_0 q(\boldsymbol{r}_s,t'_R)d\boldsymbol{r}_s + \int_S G_0\left(1-M_n^2\right)\frac{\partial p}{\partial n}\left(\boldsymbol{r}_s,t'_R\right)d\boldsymbol{r}_s - \int_S \frac{\partial G_0}{\partial \overline{n}} p\left(\boldsymbol{r}_s,t'_R\right)d\boldsymbol{r}_s$$
$$- \int_S M_n G_0 \boldsymbol{M_T}\cdot\nabla p\left(\boldsymbol{r}_s,t'_R\right)d\boldsymbol{r}_s + \int_S \frac{G_0}{c\alpha^2}\left(\frac{\partial \overline{R}}{\partial \overline{n}} - M_n\alpha^2\right)\frac{\partial p}{\partial t}\left(\boldsymbol{r}_s,t'_R\right)d\boldsymbol{r}_s \qquad (26)$$

recalling that $G_0 = G_0(\boldsymbol{r}_s,\boldsymbol{r}')$. Equation (26) is a modification to the general Kirchhoff integral equation (21) for a source in a general mean flow. The solution of (26), $p(\boldsymbol{r}',t')$, is related to the direct contribution of the source noise q as well as the surface contribution involving the retarded time values of p and their normal derivatives [1]. When the pressure p and its derivatives are calculated on the surface S, (26) predicts the pressure at an arbitrary observer point r' exterior to the surface [25].

When both $p\left(\boldsymbol{r}_s,t'_R\right)$ and $\partial p/\partial n\left(\boldsymbol{r}_s,t'_R\right)$ on the surface S are known, acoustic pressure at any observer field point $\boldsymbol{r'}$ can be computed. However, $p\left(\boldsymbol{r}_s,t'_R\right)$ and $\partial p/\partial n\left(\boldsymbol{r}_s,t'_R\right)$ are not independent. They must satisfy the boundary integral equation when the observer $\boldsymbol{r}'$ is taken as a boundary point $\boldsymbol{r}'_s$. Mathematically speaking, singularities arise when using Green's functions to obtain information on the surface due to the location of the observer. To evaluate a singular integral, a limiting process is used whereby the observer approaches the boundary of the surface, *i.e.*, as $\boldsymbol{r'}$ approaches $\boldsymbol{r}'_s$ [57]. The time-domain boundary integral equation therefore results by taking the limit of (26) as $\boldsymbol{r'}\to\boldsymbol{r}'_s$. With the exception of the $\partial G_0/\partial\overline{n} = \partial G_0/\partial\overline{n}(\boldsymbol{r}_s,\boldsymbol{r}')$ integral in (26), all integrals are evaluated numerically by interchanging this limit with the integration. This cannot be done with the $\partial G_0/\partial\overline{n}(\boldsymbol{r}_s,\boldsymbol{r}')$ integral as it contains a surface singularity. Instead, the limit is found by enclosing the surface S with a hemispherical surface S_ϵ centered at $\boldsymbol{r}'_s$ letting $\epsilon\to 0$ as illustrated in Figure 2. This modification to the surface S eliminates the $\partial G_0/\partial\overline{n}(\boldsymbol{r}_s,\boldsymbol{r}')$ integral singularity in equation 26 [1, 7, 25]:

$$\lim_{\boldsymbol{r'}\to\boldsymbol{r}'_s}\int_S \frac{\partial G_0}{\partial\overline{n}}(\boldsymbol{r}_s,\boldsymbol{r}')p\left(\boldsymbol{r}_s,t'_R\right)d\boldsymbol{r}_s$$
$$= \lim_{\boldsymbol{r'}\to\boldsymbol{r}'_s}\int_{S-S_\epsilon}\frac{\partial G_0}{\partial\overline{n}}(\boldsymbol{r}_s,\boldsymbol{r}')p\left(\boldsymbol{r}_s,t'_R\right)d\boldsymbol{r}_s + \lim_{\boldsymbol{r'}\to\boldsymbol{r}'_s}\int_{S_\epsilon}\frac{\partial G_0}{\partial\overline{n}}(\boldsymbol{r}_s,\boldsymbol{r}')p\left(\boldsymbol{r}_s,t'_R\right)d\boldsymbol{r}_s$$
$$= \lim_{\boldsymbol{r'}\to\boldsymbol{r}'_s}\int_{S-S_\epsilon}\frac{\partial G_0}{\partial\overline{n}}(\boldsymbol{r}_s,\boldsymbol{r}')p\left(\boldsymbol{r}_s,t'_R\right)d\boldsymbol{r}_s + p\left(\boldsymbol{r}'_s,t'\right)\lim_{\boldsymbol{r'}\to\boldsymbol{r}'_s}\int_{S_\epsilon}\frac{\partial G_0}{\partial\overline{n}}(\boldsymbol{r}_s,\boldsymbol{r}')d\boldsymbol{r}_s$$
$$+ \lim_{\boldsymbol{r'}\to\boldsymbol{r}'_s}\int_{S_\epsilon}\frac{\partial G_0}{\partial\overline{n}}(\boldsymbol{r}_s,\boldsymbol{r}')\left[p\left(\boldsymbol{r}_s,t'_R\right)-p\left(\boldsymbol{r}_s,t'\right)\right]d\boldsymbol{r}_s. \qquad (27)$$

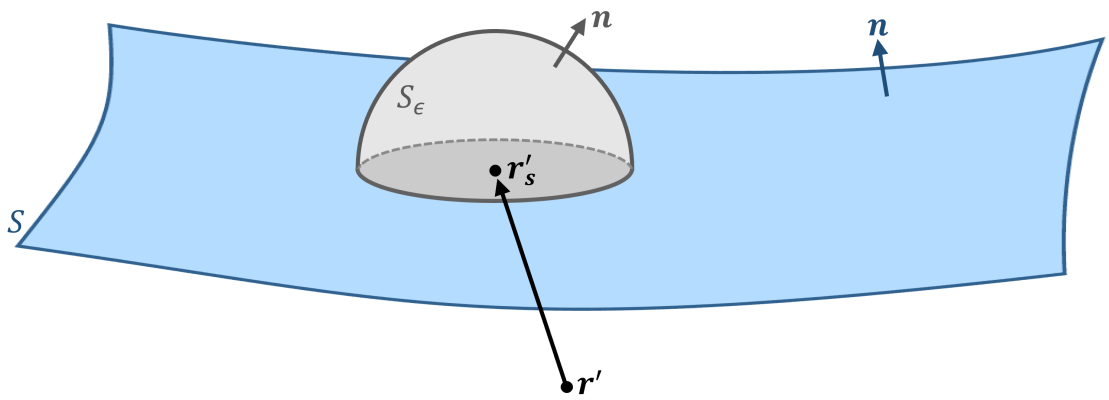

Fig. 2: Schematic diagram illustrating the modification of surface S to include a hemisphere of characteristic dimension ϵ centered at boundary point $\boldsymbol{r}'_s$.

There is no singularity on the sphere S_ϵ. Thus,

$$\lim_{\boldsymbol{r}'\to\boldsymbol{r}'_s}\int_{S_\epsilon}\frac{\partial G_0}{\partial \overline{n}}(\boldsymbol{r}_s,\boldsymbol{r}')d\boldsymbol{r}_s=\int_{S_\epsilon}\left(\lim_{\boldsymbol{r}'\to\boldsymbol{r}'_s}\frac{\partial G_0}{\partial \overline{n}}(\boldsymbol{r}_s,\boldsymbol{r}')\right)d\boldsymbol{r}_s=\int_{S_\epsilon}\frac{\partial G_0}{\partial \overline{n}}(\boldsymbol{r}_s,\boldsymbol{r}'_s)d\boldsymbol{r}_s.$$

Moreover,

$$\frac{\partial G_0}{\partial \overline{n}}=\frac{\partial G_0}{\partial \overline{n}}(\boldsymbol{r}_s,\boldsymbol{r}'_s)=-\frac{\alpha^2}{\overline{R}^3}\left[\boldsymbol{n}\cdot(\boldsymbol{r}-\boldsymbol{r}')\right]=-\frac{\alpha^2}{\overline{R}^3}\epsilon$$

which gives:

$$\lim_{\boldsymbol{r}'\to\boldsymbol{r}'_s}\int_{S_\epsilon}\frac{\partial G_0}{\partial \overline{n}}(\boldsymbol{r}_s,\boldsymbol{r}')d\boldsymbol{r}_s=-\alpha^2\int_{S_\epsilon}\frac{\epsilon}{\overline{R}^3}d\boldsymbol{r}_s$$

where $\overline{R}=\left((x_s-x'_s)^2+\alpha^2(y_s-y'_s)^2+\alpha^2(z_s-z'_s)^2\right)^{1/2}$. By introducing spherical coordinates centered at $\boldsymbol{r}'_s$, *i.e.*,

$$\begin{aligned}x_s-x'_s&=\epsilon\cos\phi\\ y_s-y'_s&=\epsilon\sin\phi\cos\theta\\ z_s-z'_s&=\epsilon\sin\phi\sin\theta\end{aligned}$$

for $0\le\phi\le\pi$, $0\le\theta\le2\pi$, and $d\boldsymbol{r}_s=\epsilon^2\sin\phi d\phi d\theta$, and by the symmetry of $\overline{R}$ with respect to S_ϵ and its complement $S'_\epsilon=V\cap S_\epsilon$, the following integral can be reduced to -2π:

$$-\alpha^2\int_{S_\epsilon}\frac{\epsilon}{\overline{R}^3}d\boldsymbol{r}_s=-\frac{\alpha^2}{2}\int_{S_\epsilon+S'_\epsilon}\frac{\epsilon}{\overline{R}^3}d\boldsymbol{r}_s=-\frac{\alpha^2}{2}\int_0^{2\pi}\int_0^{\pi}\frac{\sin\phi}{\left(\cos^2\phi+\alpha^2\sin^2\phi\right)^{3/2}}d\phi d\theta=-2\pi.$$

Hence, as $\epsilon\to0$, the $\partial G_0/\partial\overline{n}$ integral in (27) is a convergent surface integral over S and yields a unique finite result as follows:

$$\lim_{\boldsymbol{r}'\to\boldsymbol{r}'_s}\int_S\frac{\partial G_0}{\partial \overline{n}}(\boldsymbol{r}_s,\boldsymbol{r}')p\left(\boldsymbol{r}_s,t'_R\right)d\boldsymbol{r}_s=\int_S\frac{\partial G_0}{\partial \overline{n}}(\boldsymbol{r}_s,\boldsymbol{r}'_s)p\left(\boldsymbol{r}_s,t'_R\right)d\boldsymbol{r}_s-2\pi p\left(\boldsymbol{r}'_s,t'\right). \tag{28}$$

Taking the limit of (26) as $\boldsymbol{r'} \to \boldsymbol{r}'_s$ assuming that $\boldsymbol{r}'_s$ is a smooth boundary collocation point and substituting in (28) yields:

$$2\pi p(\boldsymbol{r}'_s, t') = \frac{1}{c^2}\int_V G_0 q(\boldsymbol{r}_s, t'_R) d\boldsymbol{r}_s + \int_S G_0 \left(1 - M_n^2\right) \frac{\partial p}{\partial n}\left(\boldsymbol{r}_s, t'_R\right) d\boldsymbol{r}_s - \int_S \frac{\partial G_0}{\partial \overline{n}} p\left(\boldsymbol{r}_s, t'_R\right) d\boldsymbol{r}_s$$
$$- \int_S M_n G_0 \boldsymbol{M_T} \cdot \nabla p\left(\boldsymbol{r}_s, t'_R\right) d\boldsymbol{r}_s + \int_S \frac{G_0}{c\alpha^2}\left(\frac{\partial \overline{R}}{\partial \overline{n}} - M_n\alpha^2\right) \frac{\partial p}{\partial t}\left(\boldsymbol{r}_s, t'_R\right) d\boldsymbol{r}_s, \qquad (29)$$

where G_0 is now defined such that $G_0 = G_0(\boldsymbol{r}_s, \boldsymbol{r}'_s)$. Combining equations (26) and (29) and simplifying with

$$G_0 \frac{\partial \overline{R}}{\partial \overline{n}} = G_0\left(-\overline{R}^2 \frac{\partial G_0}{\partial \overline{n}}\right) = -\overline{R}\frac{\partial G_0}{\partial \overline{n}}$$

gives the following expression:

$$4\pi C_s p(\boldsymbol{r}'_s, t') = Q(\boldsymbol{r}'_s, t') + \int_S G_0 \left(1 - M_n^2\right) \frac{\partial p}{\partial n}\left(\boldsymbol{r}_s, t'_R\right) d\boldsymbol{r}_s$$
$$- \int_S \frac{\partial G_0}{\partial \overline{n}}\left[p\left(\boldsymbol{r}_s, t'_R\right) + \frac{\overline{R}}{c\alpha^2}\frac{\partial p}{\partial t}\left(\boldsymbol{r}_s, t'_R\right)\right] d\boldsymbol{r}_s$$
$$- \int_S M_n G_0 \left[\boldsymbol{M_T} \cdot \nabla p\left(\boldsymbol{r}_s, t'_R\right) + \frac{1}{c}\frac{\partial p}{\partial t}\left(\boldsymbol{r}_s, t'_R\right)\right] d\boldsymbol{r}_s \qquad (30)$$

where

$$C_s = \left\{ \begin{array}{ll} 0, & \text{when } \boldsymbol{r}'_s \text{ is on the interior of } S \\ 1, & \text{when } \boldsymbol{r}'_s \text{ is on the exterior of } S \\ 1/2, & \text{when } \boldsymbol{r}'_s \text{ is a smooth point on the boundary of } S \end{array} \right\}$$

and

$$Q(\boldsymbol{r}'_s, t') = \frac{1}{c^2}\int_V G_0 q(\boldsymbol{r}_s, t'_R) d\boldsymbol{r}_s$$

for $G_0 = G_0(\boldsymbol{r}_s, \boldsymbol{r}'_s)$.

Equation (30) is the resulting time-domain boundary integral equation derived from the linear convective wave (1) with initial conditions (2) using Green's function (3) with initial conditions (4). The volume integral denotes the contribution from the external sources to the boundary observer point $\boldsymbol{r}'_s$. The surface integrals denote the contribution from the source surface and scattering surface. For sound scattering problems, $p(\boldsymbol{r}'_s, t')$ on the scattering surface S is determined by (30) when the boundary condition $\partial p/\partial n$ on S is known. Suitable boundary conditions will be introduced and derived further in Chapter 5. Note that for rigid body scattering only, $\partial p/\partial n = 0$.

2.2 BURTON-MILLER REFORMULATION

As previously mentioned, the time-domain boundary integral equation has intrinsic numerical instabilities due to resonant frequencies resulting from non-trivial solutions in the interior domain. Using a Burton-Miller-type reformulation of (30), resonant frequencies can be eliminated, and stability achieved. The reformulation results from taking the derivative of (30) in the form of:

$$a\frac{\partial}{\partial t'} + bc\frac{\partial}{\partial \overline{n}'} \tag{31}$$

where a and b are arbitrary parameters that must satisfy the stability condition: $a/b < 0$. Applying operation (31) to (30) and taking the limit as $\boldsymbol{r}' \to \boldsymbol{r}'_s$, the following result is obtained [1, 53–55, 75]:

$$\begin{aligned} &4\pi a C_s \frac{\partial p}{\partial t'}(\boldsymbol{r}'_s, t') + 4\pi bc C_s \frac{\partial p}{\partial \overline{n}'}(\boldsymbol{r}'_s, t') + 4\pi bc \frac{\partial C_s}{\partial \overline{n}'} p(\boldsymbol{r}'_s, t') \\ &\qquad = a\frac{\partial Q}{\partial t'}(\boldsymbol{r}'_s, t') + bc\frac{\partial Q}{\partial \overline{n}'}(\boldsymbol{r}'_s, t') + a\left(A_{\mathrm{INT}}\right) + bc\left(B_{\mathrm{INT}}\right) + \frac{b}{\alpha^2}\left(C_{\mathrm{INT}}\right) \end{aligned} \tag{32}$$

where

$$\begin{aligned} A_{\mathrm{INT}} = &\int_S G_0\left(1 - M_n^2\right)\frac{\partial}{\partial t}\left(\frac{\partial p}{\partial n}\left(\boldsymbol{r}_s, t'_R\right)\right) d\boldsymbol{r}_s - \int_S \frac{\partial G_0}{\partial \overline{n}}\left[\frac{\partial p}{\partial t}\left(\boldsymbol{r}_s, t'_R\right) + \frac{\overline{R}}{c\alpha^2}\frac{\partial^2 p}{\partial t^2}\left(\boldsymbol{r}_s, t'_R\right)\right] d\boldsymbol{r}_s \\ &- \int_S M_n G_0\left[\boldsymbol{M_T}\cdot\nabla\frac{\partial p}{\partial t}\left(\boldsymbol{r}_s, t'_R\right) + \frac{1}{c}\frac{\partial^2 p}{\partial t^2}\left(\boldsymbol{r}_s, t'_R\right)\right] d\boldsymbol{r}_s, \end{aligned} \tag{33}$$

$$\begin{aligned} B_{\mathrm{INT}} = &\int_S \left(1 - M_n^2\right)\left[\frac{\partial G_0}{\partial \overline{n}'}\frac{\partial p}{\partial n}\left(\boldsymbol{r}_s, t'_R\right) + G_0\frac{\partial}{\partial \overline{n}'}\left(\frac{\partial p}{\partial n}\right)\right]\left(\boldsymbol{r}_s, t'_R\right) d\boldsymbol{r}_s \\ &- \int_S \frac{\partial^2 G_0}{\partial \overline{n}\partial \overline{n}'}\left[p\left(\boldsymbol{r}_s, t'_R\right) + \frac{\overline{R}}{c\alpha^2}\frac{\partial p}{\partial t}\left(\boldsymbol{r}_s, t'_R\right)\right] d\boldsymbol{r}_s \\ &- \int_S M_n\frac{\partial G_0}{\partial \overline{n}'}\left[\boldsymbol{M_T}\cdot\nabla p\left(\boldsymbol{r}_s, t'_R\right) + \frac{1}{c}\frac{\partial p}{\partial t}\left(\boldsymbol{r}_s, t'_R\right)\right] d\boldsymbol{r}_s, \text{ and} \end{aligned} \tag{34}$$

$$\begin{aligned} C_{\mathrm{INT}} = &-\int_S \frac{\partial G_0}{\partial \overline{n}}\left[\left(\boldsymbol{M}\cdot\overline{\boldsymbol{n}}'\right)\frac{\partial p}{\partial t}\left(\boldsymbol{r}_s, t'_R\right) + \frac{\overline{R}}{c\alpha^2}\left(\boldsymbol{M}\cdot\overline{\boldsymbol{n}}' - \frac{\partial \overline{R}}{\partial \overline{n}'}\right)\frac{\partial^2 p}{\partial t^2}\left(\boldsymbol{r}_s, t'_R\right)\right] d\boldsymbol{r}_s \\ &- \int_S M_n G_0\left(\boldsymbol{M}\cdot\overline{\boldsymbol{n}}' - \frac{\partial \overline{R}}{\partial \overline{n}'}\right)\left[\boldsymbol{M_T}\cdot\nabla\frac{\partial p}{\partial t}\left(\boldsymbol{r}_s, t'_R\right) + \frac{1}{c}\frac{\partial^2 p}{\partial t^2}\left(\boldsymbol{r}_s, t'_R\right)\right] d\boldsymbol{r}_s. \end{aligned} \tag{35}$$

Note that expression (32) is simplified using the identities

$$\begin{aligned}
&\frac{\partial}{\partial \overline{n}'}\left[p\left(\boldsymbol{r}_s, t'_R\right)+\frac{\overline{R}}{c\alpha^2}\frac{\partial p}{\partial t}\left(\boldsymbol{r}_s, t'_R\right)\right] \\
&\quad=\frac{\partial p}{\partial t}\left(\boldsymbol{r}_s, t'_R\right)\frac{\partial t'_R}{\partial \overline{n}'}+\frac{\overline{R}}{c\alpha^2}\frac{\partial^2 p}{\partial t^2}\left(\boldsymbol{r}_s, t'_R\right)\frac{\partial t'_R}{\partial \overline{n}'}+\frac{1}{c\alpha^2}\frac{\partial p}{\partial t}\left(\boldsymbol{r}_s, t'_R\right)\frac{\partial \overline{R}}{\partial \overline{n}'} \\
&\quad=\frac{1}{c\alpha^2}\left(\boldsymbol{M}\cdot\overline{\boldsymbol{n}}'-\frac{\partial \overline{R}}{\partial \overline{n}'}\right)\left[\frac{\partial p}{\partial t}\left(\boldsymbol{r}_s, t'_R\right)+\frac{\overline{R}}{c\alpha^2}\frac{\partial^2 p}{\partial t^2}\left(\boldsymbol{r}_s, t'_R\right)\right]+\frac{1}{c\alpha^2}\frac{\partial p}{\partial t}\left(\boldsymbol{r}_s, t'_R\right)\frac{\partial \overline{R}}{\partial \overline{n}'} \\
&\quad=\frac{1}{c\alpha^2}\left[\left(\boldsymbol{M}\cdot\overline{\boldsymbol{n}}'\right)\frac{\partial p}{\partial t}\left(\boldsymbol{r}_s, t'_R\right)+\frac{\overline{R}}{c\alpha^2}\left(\boldsymbol{M}\cdot\overline{\boldsymbol{n}}'-\frac{\partial \overline{R}}{\partial \overline{n}'}\right)\frac{\partial^2 p}{\partial t^2}\left(\boldsymbol{r}_s, t'_R\right)\right]
\end{aligned}$$

and

$$\begin{aligned}
&\frac{\partial}{\partial \overline{n}'}\left[\boldsymbol{M_T}\cdot\nabla p\left(\boldsymbol{r}_s, t'_R\right)+\frac{1}{c}\frac{\partial p}{\partial t}\left(\boldsymbol{r}_s, t'_R\right)\right] \\
&\quad=\left(\boldsymbol{M_T}\cdot\nabla\frac{\partial p}{\partial t}\left(\boldsymbol{r}_s, t'_R\right)\right)\frac{\partial t'_R}{\partial \overline{n}'}+\frac{1}{c}\frac{\partial^2 p}{\partial t^2}\left(\boldsymbol{r}_s, t'_R\right)\frac{\partial t'_R}{\partial \overline{n}'} \\
&\quad=\frac{1}{c\alpha^2}\left(\boldsymbol{M}\cdot\overline{\boldsymbol{n}}'-\frac{\partial \overline{R}}{\partial \overline{n}'}\right)\left[\boldsymbol{M_T}\cdot\nabla\frac{\partial p}{\partial t}\left(\boldsymbol{r}_s, t'_R\right)+\frac{1}{c}\frac{\partial^2 p}{\partial t^2}\left(\boldsymbol{r}_s, t'_R\right)\right].
\end{aligned}$$

such that

$$\frac{\partial t'_R}{\partial \overline{n}'}=\frac{\partial}{\partial \overline{n}'}\left[t'+\frac{\boldsymbol{M}\cdot(\boldsymbol{r'}-\boldsymbol{r})-\overline{R}}{c\alpha^2}\right]=\frac{1}{c\alpha^2}\frac{\partial}{\partial \overline{n}'}\left[\boldsymbol{M}\cdot(\boldsymbol{r'}-\boldsymbol{r})-\overline{R}\right]=\frac{1}{c\alpha^2}\left(\boldsymbol{M}\cdot\overline{\boldsymbol{n}}'-\frac{\partial \overline{R}}{\partial \overline{n}}\right).$$

In (32), the normal derivative of pressure, $\partial p/\partial n$, contains information regarding the boundary condition of the source surface. This term will be discussed in Chapter 5. Moreover, the B_{INT} integral (34) containing the single and double normal derivatives of G_0, $\partial G_0/\partial \overline{n}'$ and $\partial^2 G_0/\partial \overline{n}\partial \overline{n}'$ respectively, is both weakly singular and hypersingular. For a mean flow in a general direction, the second derivative is computed using (25) giving [1, 54, 55, 75]:

$$\frac{\partial^2 G_0}{\partial \overline{n}\partial \overline{n}'}=\frac{\partial}{\partial \overline{n}'}\left[\frac{-\alpha^2\boldsymbol{n}\cdot(\boldsymbol{r}-\boldsymbol{r'})}{\overline{R}^3}\right]=\frac{\alpha^2\left(\boldsymbol{n}\cdot\boldsymbol{n}'-M_{n'}M_n\right)}{\overline{R}^3}+\frac{3\alpha^4\left[\boldsymbol{n}\cdot(\boldsymbol{r}-\boldsymbol{r}')\right]\left[\boldsymbol{n}'\cdot(\boldsymbol{r}-\boldsymbol{r}')\right]}{\overline{R}^5}.$$

Note that $\partial^2 G_0/\partial \overline{n}\partial \overline{n}'=O(1/|\boldsymbol{r}-\boldsymbol{r}'|^3)$ is hypersingular at the collocation point $\boldsymbol{r}'_s$. The single normal derivative of G_0 in the B_{INT} integral (34),

$$\frac{\partial G_0}{\partial \overline{n}'}=-\frac{\alpha^2\left[\boldsymbol{n}'\cdot(\boldsymbol{r}-\boldsymbol{r}')\right]}{\overline{R}^3}$$

is weakly singular. Using the Cauchy Principal Value introduced by [1]

$$4\pi(1-C_s)=\int_S\frac{\partial G_0}{\partial \overline{n}}d\boldsymbol{r}_s, \tag{36}$$

the singularities can be reduced in (32) via regularization noting that

$$4\pi\frac{\partial C_s}{\partial\overline{n}'}=-\frac{\partial}{\partial\overline{n}'}\left(\int_S\frac{\partial G_0}{\partial\overline{n}}d\boldsymbol{r}_s\right)=-\int_S\frac{\partial^2 G_0}{\partial\overline{n}\partial\overline{n}'}d\boldsymbol{r}_s.$$

By applying a regularization technique, the singularities involving G_0 can be reduced prior to performing discretization [3, 10, 21]. Equation (32) is reduced to:

$$\begin{aligned}4\pi aC_s\frac{\partial p}{\partial t'}(\boldsymbol{r}'_s,t')+4\pi bcC_s\frac{\partial p}{\partial\overline{n}'}(\boldsymbol{r}'_s,t')\\ =a\frac{\partial Q}{\partial t'}(\boldsymbol{r}'_s,t')+bc\frac{\partial Q}{\partial\overline{n}'}(\boldsymbol{r}'_s,t')+a\left(A_{\rm INT}\right)+bc\left(B'_{\rm INT}\right)+\frac{b}{\alpha^2}\left(C_{\rm INT}\right)\end{aligned}\tag{37}$$

where $A_{\rm INT}$ and $C_{\rm INT}$ are as defined in (33) and (35) and

$$\begin{aligned}B'_{\rm INT}=&\int_S\left(1-M_n^2\right)\left[\frac{\partial G_0}{\partial\overline{n}'}\frac{\partial p}{\partial n}\left(\boldsymbol{r}_s,t'_R\right)+\frac{G_0}{c\alpha^2}\left(\boldsymbol{M}\cdot\overline{\boldsymbol{n}}'-\frac{\partial\overline{R}}{\partial\overline{n}}\right)\frac{\partial}{\partial t}\left(\frac{\partial p}{\partial n}(\boldsymbol{r}_s,t'_R)\right)\right]d\boldsymbol{r}_s\\ &-\int_S\frac{\partial^2 G_0}{\partial\overline{n}\partial\overline{n}'}\left[p\left(\boldsymbol{r}_s,t'_R\right)-p(\boldsymbol{r}'_s,t')+\frac{\overline{R}}{c\alpha^2}\frac{\partial p}{\partial t}\left(\boldsymbol{r}_s,t'_R\right)\right]d\boldsymbol{r}_s\\ &-\int_S M_n\frac{\partial G_0}{\partial\overline{n}'}\left[\boldsymbol{M_T}\cdot\nabla p\left(\boldsymbol{r}_s,t'_R\right)+\frac{1}{c}\frac{\partial p}{\partial t}\left(\boldsymbol{r}_s,t'_R\right)\right]d\boldsymbol{r}_s\end{aligned}\tag{38}$$

noting that

$$\frac{\partial}{\partial\overline{n}'}\left(\frac{\partial p}{\partial n}(\boldsymbol{r}_s,t'_R)\right)=\frac{\partial}{\partial t}\left(\frac{\partial p}{\partial n}(\boldsymbol{r}_s,t'_R)\right)\frac{\partial t'_R}{\partial\overline{n}'}.$$

Following [1, 54, 55, 75], the hypersingular integral in (37) with term $\partial^2 G_0/\partial\overline{n}\partial\overline{n}'$ can be evaluated numerically by discretizing S into surface elements E_j, mapping each element E_j to a local coordinate $(\xi,\eta)\in[-1,1]\times[-1,1]$, and then mapping to a local polar coordinate (r,θ) centered at $\boldsymbol{r}'_s$. Let

$$F(r,\theta)=\frac{\partial^2 G_0}{\partial\overline{n}\partial\overline{n}'}\left[p\left(\boldsymbol{r}_s,t'_R\right)-p(\boldsymbol{r}'_s,t')+\frac{\overline{R}}{c\alpha^2}\frac{\partial p}{\partial t}\left(\boldsymbol{r}_s,t'_R\right)\right]\times|\boldsymbol{r}_\xi\times\boldsymbol{r}_\eta|.$$

Then, $F(r,\theta)=O(1/r^2)$ as $r\to 0$ because

$$p\left(\boldsymbol{r}_s,t'_R\right)-p(\boldsymbol{r}'_s,t')+\frac{\overline{R}}{c\alpha^2}\frac{\partial p}{\partial t}\left(\boldsymbol{r}_s,t'_R\right)=\nabla p(\boldsymbol{r}'_s,t')\cdot(\boldsymbol{r}_s-\boldsymbol{r}'_s)+\boldsymbol{\beta}\cdot(\boldsymbol{r}_s-\boldsymbol{r}'_s)\times\frac{\partial p}{\partial t}(\boldsymbol{r}'_s,t')+O(|\boldsymbol{r}_s-\boldsymbol{r}'_s|^2).$$

Moreover, letting

$$\lim_{r\to0}r^2F(r,\theta)=G(\theta),$$

the following limit is obtained:

$$\begin{aligned}\lim_{\epsilon\to0}\int_0^{2\pi}\int_\epsilon^{r(\theta)}F(r,\theta)rdrd\theta&=\lim_{\epsilon\to0}\int_0^{2\pi}\int_\epsilon^{r(\theta)}\left[\frac{r^2F(r,\theta)-G(\theta)}{r}+\frac{G(\theta)}{r}\right]drd\theta\\ &=\int_0^{2\pi}\int_0^{r(\theta)}\frac{r^2F(r,\theta)-G(\theta)}{r}drd\theta+\lim_{\epsilon\to0}\int_0^{2\pi}G(\theta)[\ln r(\theta)-\ln\epsilon]d\theta\\ &=\int_0^{2\pi}\int_0^{r(\theta)}\frac{r^2F(r,\theta)-G(\theta)}{r}drd\theta+\int_0^{2\pi}G(\theta)\ln r(\theta)d\theta.\end{aligned}\tag{39}$$

The integrals in (39) can be evaluated with high-order numerical quadrature techniques [10, 75, 76]. Moreover, the weakly singular integral in (37) with term $\partial G_0/\partial \overline{n}'$ can be evaluated numerically [44] using the Cauchy Principal Value (36):

$$\begin{aligned}\frac{1}{4\pi}\int_S \frac{\partial G_0}{\partial \overline{n}} d\boldsymbol{r}_s &= 1 - C_s \\ &= 1 - \left\{ \begin{array}{ll} 0, & \text{when } \boldsymbol{r}' \text{ is on the interior of } S \\ 1, & \text{when } \boldsymbol{r}' \text{ is on the exterior of } S \\ 1/2, & \text{when } \boldsymbol{r}' \text{ is a smooth point on the boundary of } S \end{array} \right\} \\ &= \left\{ \begin{array}{ll} 1, & \text{when } \boldsymbol{r}' \text{ is on the interior of } S \\ 0, & \text{when } \boldsymbol{r}' \text{ is on the exterior of } S \\ 1/2, & \text{when } \boldsymbol{r}' \text{ is a smooth point on the boundary of } S \end{array} \right\}\end{aligned}$$

By reducing the singularities in (34), the Burton-Miller reformulation of the time-domain boundary integral (37) with integrals (33), (38), and (35) can be evaluated using boundary element methods and high-order quadrature techniques [21, 54, 75]. This is done using the identities given by

$$\frac{\partial p}{\partial \overline{n}'}(\boldsymbol{r}'_s, t') = \frac{\partial p}{\partial n'}(\boldsymbol{r}'_s, t') - M_{n'}\boldsymbol{M}\cdot\nabla p(\boldsymbol{r}'_s, t') = (1 - M_n^2)\frac{\partial p}{\partial n}(\boldsymbol{r}'_s, t') - M_{n'}\boldsymbol{M_{T'}}\cdot\nabla p(\boldsymbol{r}'_s, t')$$

and

$$\boldsymbol{M}\cdot\overline{\boldsymbol{n}} = \boldsymbol{M}\cdot(\boldsymbol{n} - M_n\boldsymbol{M}) = M_n - M_n M^2 = \alpha^2 M_n.$$

Further, the tangential derivative terms involving $\boldsymbol{M_T}$ can be numerically evaluated using spatial derivatives of the surface basis functions as detailed in Chapter 3. This is done by decomposing $\boldsymbol{M}$ to be $\boldsymbol{M} = M_n\boldsymbol{n} + M_{T_1}\boldsymbol{e}_\xi + M_{T_2}\boldsymbol{e}_\eta$ where $\boldsymbol{e}_\xi$ and $\boldsymbol{e}_\eta$ are unit vectors in the local coordinate $(\xi, \eta) \in [-1, 1] \times [-1, 1]$ such that

$$\boldsymbol{M}\cdot\boldsymbol{e}_\xi = M_{T_1} + M_{T_2}(\boldsymbol{e}_\xi\cdot\boldsymbol{e}_\eta) \text{ and } \boldsymbol{M}\cdot\boldsymbol{e}_\eta = M_{T_1}(\boldsymbol{e}_\xi\cdot\boldsymbol{e}_\eta) + M_{T_2}.$$

Thus,

$$M_{T_1} = \frac{\boldsymbol{M}\cdot\boldsymbol{e}_\xi - (\boldsymbol{e}_\xi\cdot\boldsymbol{e}_\eta)\boldsymbol{M}\cdot\boldsymbol{e}_\eta}{1 - (\boldsymbol{e}_\xi\cdot\boldsymbol{e}_\eta)^2} \text{ and } M_{T_2} = \frac{\boldsymbol{M}\cdot\boldsymbol{e}_\eta - (\boldsymbol{e}_\xi\cdot\boldsymbol{e}_\eta)\boldsymbol{M}\cdot\boldsymbol{e}_\xi}{1 - (\boldsymbol{e}_\xi\cdot\boldsymbol{e}_\eta)^2}$$

which gives:

$$\boldsymbol{M_T}\cdot\nabla p\left(\boldsymbol{r}_s, t'_R\right) = M_{T_1}\frac{\partial}{\partial\xi}\frac{\partial p}{\partial t}\left(\boldsymbol{r}_s, t'_R\right) + M_{T_2}\frac{\partial}{\partial\eta}\frac{\partial p}{\partial t}\left(\boldsymbol{r}_s, t'_R\right)$$

for the $\boldsymbol{M_T}\cdot\nabla p\left(\boldsymbol{r}_s, t'_R\right)$ terms in integrals (33), (38), and (35).

The Burton-Miller reformulation (37) of the time-domain boundary integral (30) eliminates the intrinsic numerical instability due to resonant frequencies resulting from non-trivial solutions in the interior domain provided it satisfies the stability condition $a/b < 0$

for a and b in (31). It is verified in [75] that no non-trivial solutions exist provided that $a/b < -\max M_n$ for all M_n over the entire scattering surface. A simple choice for a and b is $a = -b = 1$. The stability of (37) is further discussed in Chapter 6.

CHAPTER 3

BASIS FUNCTIONS AND SPATIAL RESOLUTION

3.1 BASIS FUNCTIONS

The stable Burton-Miller reformulation (37) of the time-domain boundary integral equation (30) derived in Chapter 2 is discretized using collocation methods as detailed in [53–55, 75]. The surface S is divided into a set of N_e boundary elements $\{E_j, j = 1, \ldots, N_e\}$ where the collocation point $\boldsymbol{r}_j$ is located at the centroid of E_j. The time-domain is divided into N_t uniform time steps where $t_k = k\Delta t$. It is further assumed that the scattering surface S is comprised of both rigid and soft surfaces, denoted herein by S_0 and S_l, respectively, such that $S = S_0 \cup S_l$. Rigid surfaces are regions of the scattering body where no acoustic liner is applied, and soft surfaces are regions where there is an acoustic liner applied.

The solution to (37), $p(\boldsymbol{r}'_s, t')$, is obtained by approximating terms involving $p(\boldsymbol{r}_s, t)$ and $\partial p/\partial n(\boldsymbol{r}_s, t)$ using surface element basis functions $\phi_j(\boldsymbol{r}_s)$ and temporal basis functions $\psi_k(t)$ as follows:

$$p(\boldsymbol{r}_s, t) = \sum_{k=0}^{N_t} \sum_{j=1}^{N_e} u_j^k \phi_j(\boldsymbol{r}_s) \psi_k(t) \tag{40}$$

and

$$\frac{\partial p}{\partial n}(\boldsymbol{r}_s, t) = \sum_{k=0}^{N_t} \sum_{j=1}^{N_e} v_j^k \phi_j(\boldsymbol{r}_s) \psi_k(t). \tag{41}$$

In (40) and (41), u_j^k and v_j^k denote the value of the solution of $p(\boldsymbol{r}_s, t)$ and $\partial p/\partial n(\boldsymbol{r}_s, t)$, respectively, of the j-th node at time t_k. For soft body scattering, the Burton-Miller reformulation includes terms involving both $p(\boldsymbol{r}_s, t)$ and $\partial p/\partial n(\boldsymbol{r}_s, t)$ which are approximated by using (40) and (41), respectively. For strict rigid body scattering, on the other hand, $v_j^k \equiv 0$ by default, *i.e.*, $\partial p/\partial n(\boldsymbol{r}_s, t) = 0$ as previously stated in Chapter 2. The Burton-Miller reformulation is then reduced to terms involving $p(\boldsymbol{r}_s, t)$ only which are approximated by using (40).

Let the spatial and temporal basis functions be defined as follows:

$$\phi_j(\boldsymbol{r}_s) = \left\{ \begin{array}{ll} 1, & \boldsymbol{r}_s \text{ on element } E_j \text{ that contains collocation point } \boldsymbol{r}_j \\ 0, & \text{otherwise} \end{array} \right\} \tag{42}$$

and

$$\psi_k(t) = \Psi\left(\frac{t-t_k}{\Delta t}\right),\ \Psi(\tau) = \left\{\begin{array}{ll} 1+\frac{11}{6}\tau+\tau^2+\frac{1}{6}\tau^3, & -1<\tau\leq 0 \\ 1+\frac{1}{2}\tau-\tau^2-\frac{1}{2}\tau^3, & 0<\tau\leq 1 \\ 1-\frac{1}{2}\tau-\tau^2+\frac{1}{2}\tau^3, & 1<\tau\leq 2 \\ 1-\frac{11}{6}\tau+\tau^2-\frac{1}{6}\tau^3, & 2<\tau\leq 3 \\ 0, & \text{otherwise} \end{array}\right\}. \tag{43}$$

The spatial basis functions (42) are zeroth-order, *i.e.*, constant over each element E_j, and the integrations are computed by high-order Gauss quadrature on a 6×6 grid. The temporal basis functions (43) are third-order Lagrange functions whose contribution from any node to the solution at collocation point $\boldsymbol{r}_j$ and time step t_n reduces to a summation of four terms, *i.e.*, the solution at t_n is interpolated using time steps $t_{n-3}, t_{n-2}, t_{n-1}, t_n$. For order K Lagrange functions, in general, the solution at t_n is interpolated using time steps $t_{n-K}, t_{n-(K-1)}, \ldots, t_{n-2}, t_{n-1}, t_n$ and (43) simplifies to:

$$\psi_{n-k}(t_n) = \Psi(k), \psi'_{n-k}(t_n) = \frac{\Psi'(k)}{\Delta t},\ \text{and}\ \psi''_{n-k}(t_n) = \frac{\Psi''(k)}{\Delta t^2}$$

for all $k = 0, 1, \ldots, K$, *i.e.*,

$$\Psi(k) = \left\{\begin{array}{ll} 1, & k=0 \\ 0, & k\neq 0 \end{array}\right\}, \Psi'(k) = \left\{\begin{array}{ll} 11/6, & k=0 \\ -3, & k=1 \\ 3/2, & k=2 \\ -1/3, & k=3 \\ 0, & \text{other} \end{array}\right\},\ \text{and}\ \Psi''(k) = \left\{\begin{array}{ll} 2, & k=0 \\ -5, & k=1 \\ 4, & k=2 \\ -1, & k=3 \\ 0, & \text{other} \end{array}\right\}. \tag{44}$$

By evaluating the discretized Burton-Miller-type reformulation at collocation points $\boldsymbol{r}_j$ on elements $E_j, j = 1, \ldots, N_e$ and at time step t_n using basis functions (42) and (43), (37) is cast into the following system of equations:

$$\boldsymbol{B_0 u^n + C_0 v^n = q^n - B_1 u^{n-1} - C_1 v^{n-1} - B_2 u^{n-2} - C_2 v^{n-2} - \ldots - B_J u^{n-J} - C_J v^{n-J}} \tag{45}$$

where $\boldsymbol{u}^k$ and $\boldsymbol{v}^k$ denote the vector that contains all unknowns $\left\{u_j^k,\ j = 1, ..., N_e\right\}$ and $\left\{v_j^k,\ j = 1, ..., N_e\right\}$, respectively, at time level t_k. Equation (45) is a March-On-in-Time scheme which, when solved iteratively, provides solutions $\boldsymbol{u}^n$ and $\boldsymbol{v}^n$ on rigid and soft surfaces, respectively. Due to the limited temporal stencil width of the basis function, the $\boldsymbol{B}$ and $\boldsymbol{C}$ matrices are sparse. Additionally, the index J denotes the maximum time history of the solution required for (45) and is dependent on the dimensions of the scattering surface

and the mean flow [75]. The non-zero entries for $\boldsymbol{B}$ are given by:

$$\{\boldsymbol{B_k}\}_{ij} = 2\pi a\,\delta_{ij}\psi'_{n-k}(t_n) + a\int_{E_j}\frac{\partial G_0}{\partial \overline{n}}\left(\psi'_{n-k}(t_R^n) + \frac{\overline{R}}{c\alpha^2}\psi''_{n-k}(t_R^n)\right)d\boldsymbol{r}_s$$
$$-bc\,\delta_{ij}\,\delta_{k0}\int_{S-E_i}\frac{\partial^2 G_0}{\partial\overline{n}'\partial\overline{n}}(\boldsymbol{r}_s,\boldsymbol{r}_i)d\boldsymbol{r_s} + \frac{b}{c\alpha^4}\int_{E_j}\overline{R}^3\frac{\partial G_0}{\partial\overline{n}'}\frac{\partial G_0}{\partial\overline{n}}\psi''_{n-k}(t_R^n)d\boldsymbol{r}_s$$
$$+bc\int_{E_j}\frac{\partial^2 G_0}{\partial\overline{n}'\partial\overline{n}}\left(\psi_{n-k}(t_R^n) - \delta_{ij}\psi_{n-k}(t_n) + \frac{\overline{R}}{c\alpha^2}\psi'_{n-k}(t_R^n)\right)d\boldsymbol{r}_s$$

and the non-zero entries for $\boldsymbol{C}$ are given by:

$$\{\boldsymbol{C_k}\}_{ij} = 2\pi bc\,\delta_{ij}\psi_{n-k}(t_n) - a\int_{E_j}G_0(\boldsymbol{r}_s,\boldsymbol{r}'_s)\psi'_{n-k}(t'_R)d\boldsymbol{r}_s$$
$$-bc\int_{E_j}\frac{\partial G_0}{\partial\overline{n}'}\left(\psi_{n-k}(t_R^n) + \frac{\overline{R}}{c\alpha^2}\psi'_{n-k}(t_R^n)\right)d\boldsymbol{r}_s$$

where δ_{ij} and δ_{k0} are Kronecker delta functions, a and b are the Burton-Miller stability parameters, and a prime denotes a derivative with respect to time. If the entire scattering surface is rigid, a solution to (45) can be obtained for $\boldsymbol{u}^n$. When the scattering body also includes soft surfaces, (45) must be coupled with a suitable boundary condition. A suitable boundary condition for soft, or deformable, surfaces is discussed in Chapter 5.

In [53], Fourier analysis of the temporal basis functions demonstrated that as the spatial discretization becomes more refined, it is more efficient to use higher-order basis functions in time. For the third-order basis functions (43) used herein, accuracy within 0.5% is achieved using a minimum of 22 points-per-wave period. In this work, the spatial resolution of the time-domain boundary element method with respect to the surface element basis functions $\phi_j(\boldsymbol{r}_s)$ in (42) is studied by considering instead the points-per-wavelength, PPW.

The spatial resolution is assessed by considering the scattering of an acoustic point source by prototype geometric bodies with rigid surfaces. Geometries include a flat plate and sphere. The flat plate has dimension $[-0.5, 0.5]\times[-0.5, 0.5]\times[-0.1, 0.1]$ and the sphere is centered at $\boldsymbol{x} = (x, y, z) = (0, 0, 0)$ with a radius of 0.5. For both geometries, a point source located at $\boldsymbol{x} = (0, 0, 1)$ is centered directly above the body as illustrated in Figure 3a for the flat plate and Figure 4a for the sphere. The point source is non-dimensionalized with amplitude of unity. To investigate whether the location of the point source affects the accuracy of the solution, a shifted point source located at $\boldsymbol{x} = (0.5, 0, 1)$ is considered for the flat plate as illustrated in Figure 3b. To investigate whether the orientation of the surface elements with respect to the wave direction affects the accuracy, the meshed sphere is rotated as illustrated in Figure 4b. Note that Figures 3 and 4 are not drawn to scale.

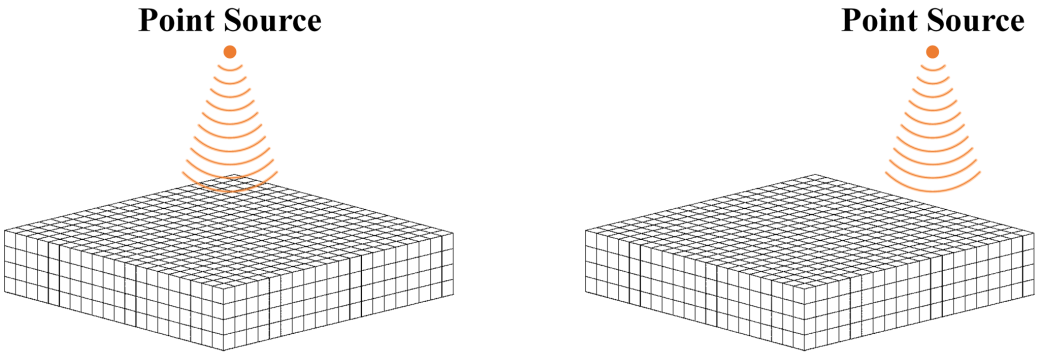

(a) Standard Point Source (b) Shifted Point Source

Fig. 3: Orientation of the flat plate surface elements with relation to the location of the acoustic point source.

(a) Standard Orientation (b) Rotated Orientation

Fig. 4: Orientation of the spherical surface elements with relation to the location of the acoustic point source.

The study is limited to the observed far field solution for rigid body scattering. Although structured quad-elements are used for both the flat plate and sphere, unstructured grids of triangles, or a combination of triangles and quads, are allowable for the methods used herein. The elements are defined using nine nodes and the collocation points are located at the center of each element E_j. Figure 5 illustrates the location of the nodes and collocation points for each element on the surface of the flat plate discretized by five elements along the x- and y-axes and one element along the z-axis. In the figure, the nodes on each element E_j are denoted by solid circles and the collocation point is denoted by an open circle.

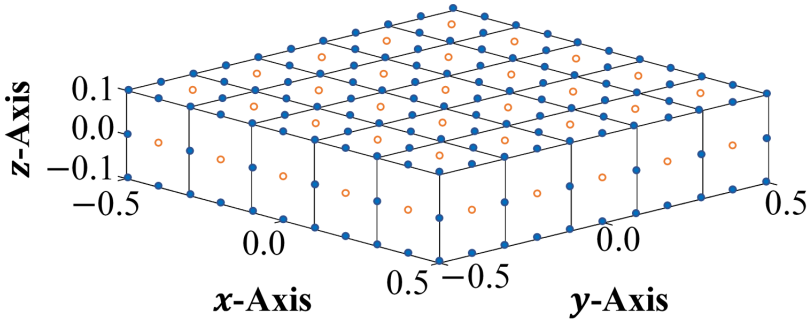

Fig. 5: Illustration of nodes (blue circles) and collocation points (open circles) for each surface element E_j from discretizing the surface of the flat plate with quad-elements.

3.2 FLAT PLATE WITH RIGID BODY

The surface of the flat plate is discretized in the x-, y-, and z- directions with N_x, N_y, and N_z elements, respectively. A series of computations is carried out by increasing the number of elements used from $N_x \times N_y \times N_z = 20 \times 20 \times 4$ $(1,120$ elements) to $100 \times 100 \times 20$ $(28,000$ elements). The number of boundary elements, N, is calculated by $N = 2(N_x N_y + N_y N_z + N_x N_z)$. For scattering visualization purposes at multiple frequencies, the frequency-domain solution converted from the time-domain at $\omega = 5\pi, 10\pi, 15\pi$, and 20π is illustrated in Figures 6, 8, 10, and 12 for the standard point source. These examples are for the linear convective wave equation with no mean flow, *i.e.*, $\boldsymbol{U} = 0$. For cases when $\boldsymbol{U} \neq 0$, a Prandtl-Glauert transformation can be applied to remove the mean flow as demonstrated in [77]. Here, ω is a non-dimensionalized value such that, for a specific frequency, $\omega = 2\pi c/L$ for a body with arbitrary length L. In general, ω is scaled by c/L. In Figures 6, 8, 10, and 12, the vertical axis is the magnitude of sound pressure. The horizontal axis indicates the solution along a field line of coordinates, $-2.5 \leq x \leq 2.5, y = 0, z = -2.5$. All discretizations are indicated in the legend.

The corresponding contour graphs of the frequency-domain solutions are illustrated in Figures 7, 9, 11, 13. In the contour graphs, the color-scale indicates the real part of the acoustic pressure. For scattering solutions at frequencies, $\omega = 5\pi, 6\pi, ...20\pi$, refer to Appendix A. As observed in the figures, the fluctuations in magnitude of sound pressure increase with increasing frequencies. Also, the deviation in numerical results between coarse and fine grids increases with increasing frequencies.

The spatial resolution with respect to the surface element basis functions is measured

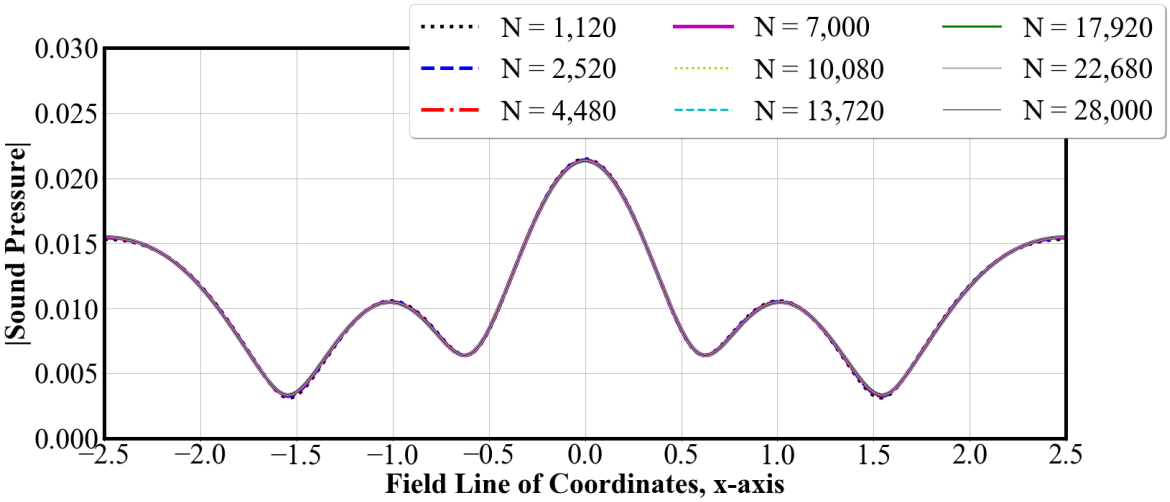

Fig. 6: Frequency-domain solution converted from the time-domain at $\omega = 5\pi$ for rigid body flat plate scattering along the field line of coordinates, $-2.5 \leq x \leq 2.5, y = 0, z = -2.5$.

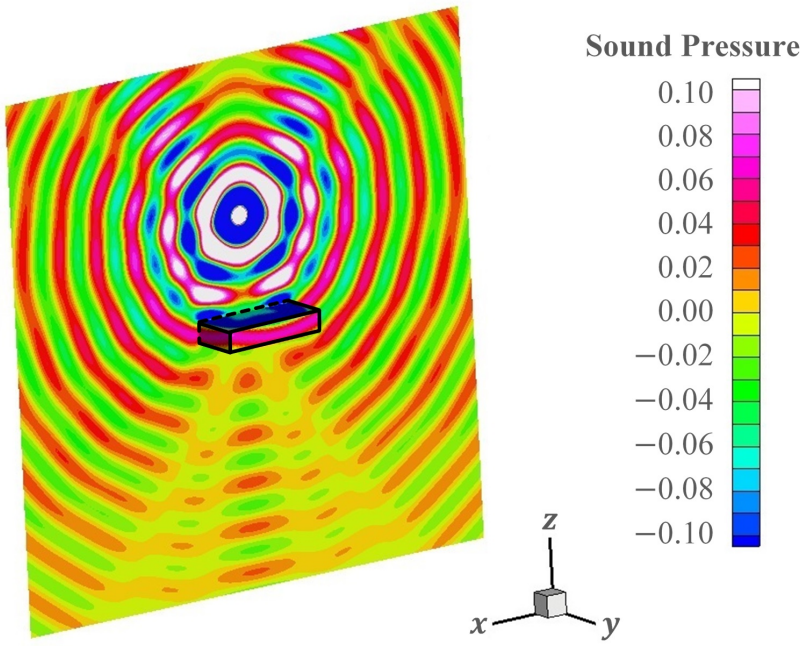

Fig. 7: Contour graph of the frequency-domain solution converted from the time-domain solution at $\omega = 5\pi$ for rigid body flat plate scattering. The visualization plane is located along the x-axis, centered at $y = 0, z = 0$.

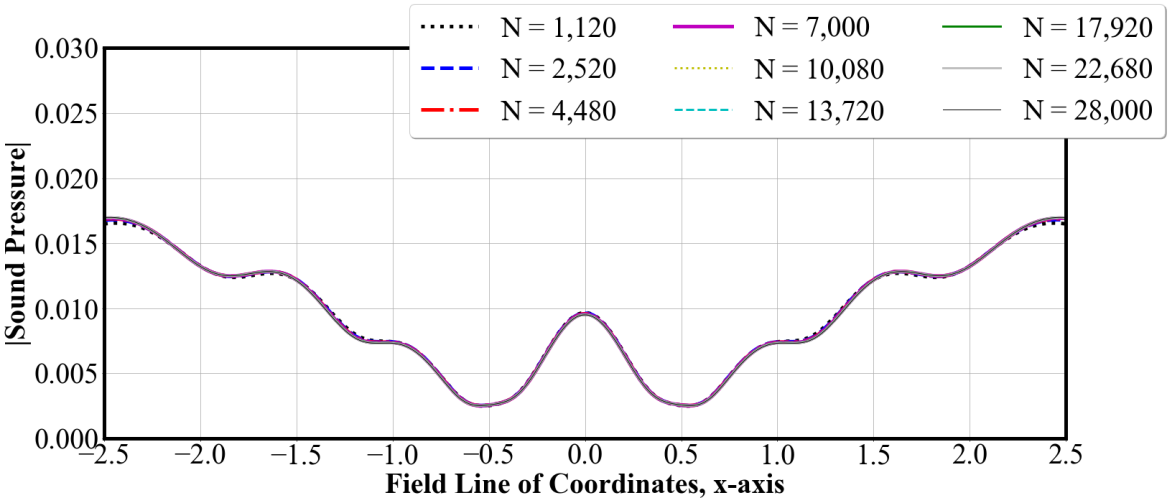

Fig. 8: Frequency-domain solution converted from the time-domain at $\omega = 10\pi$ for rigid body flat plate scattering along the field line of coordinates, $-2.5 \leq x \leq 2.5, y = 0, z = -2.5$.

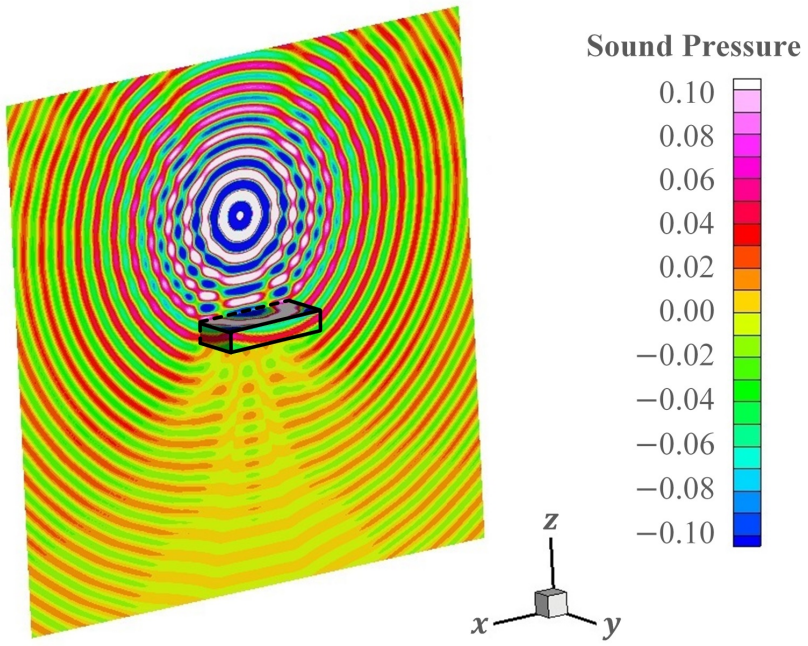

Fig. 9: Contour graph of the frequency-domain solution converted from the time-domain solution at $\omega = 10\pi$ for rigid body flat plate scattering. The visualization plane is located along the x-axis, centered at $y = 0, z = 0$.

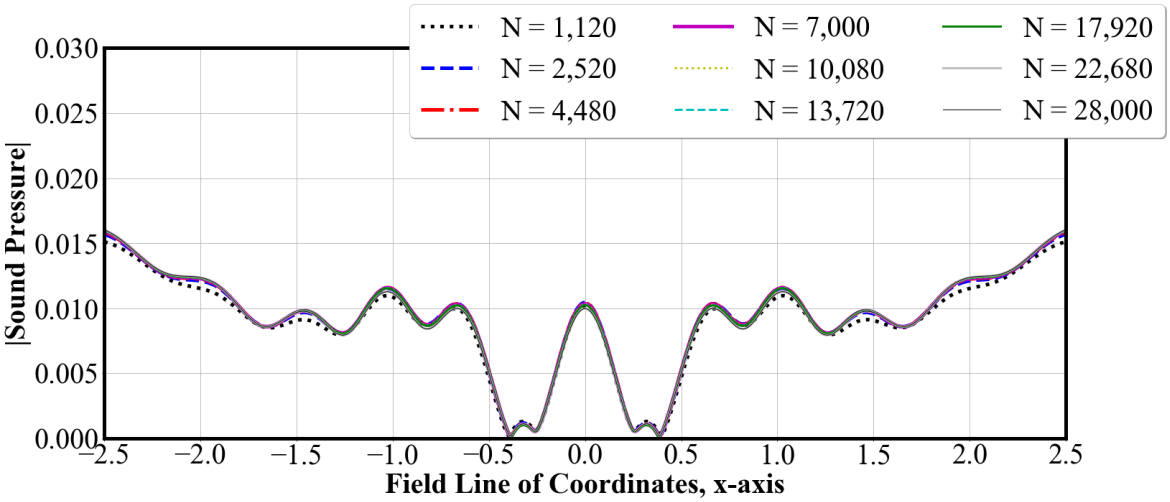

Fig. 10: Frequency-domain solution converted from the time-domain at $\omega = 15\pi$ for rigid body flat plate scattering along the field line of coordinates, $-2.5 \leq x \leq 2.5, y = 0, z = -2.5$.

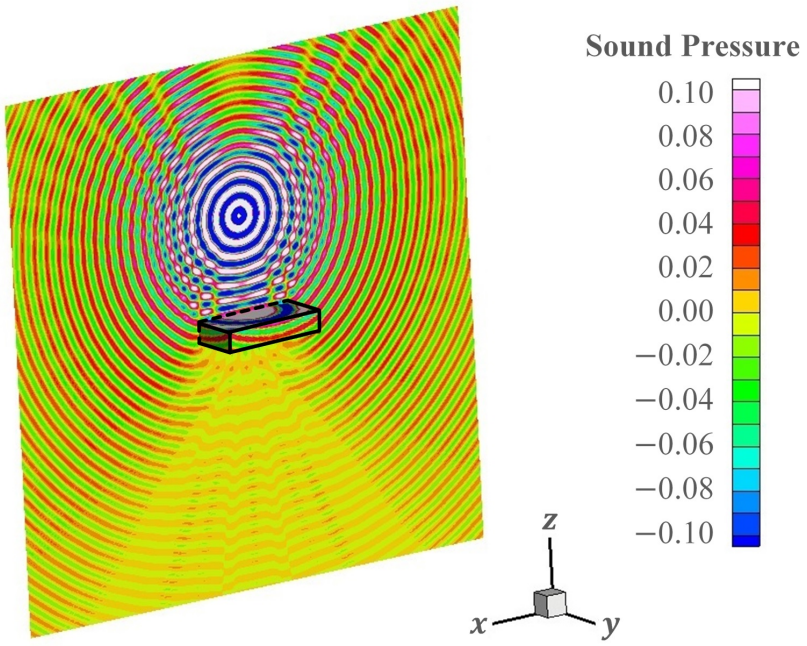

Fig. 11: Contour graph of the frequency-domain solution converted from the time-domain solution at $\omega = 15\pi$ for rigid body flat plate scattering. The visualization plane is located along the x-axis, centered at $y = 0, z = 0$.

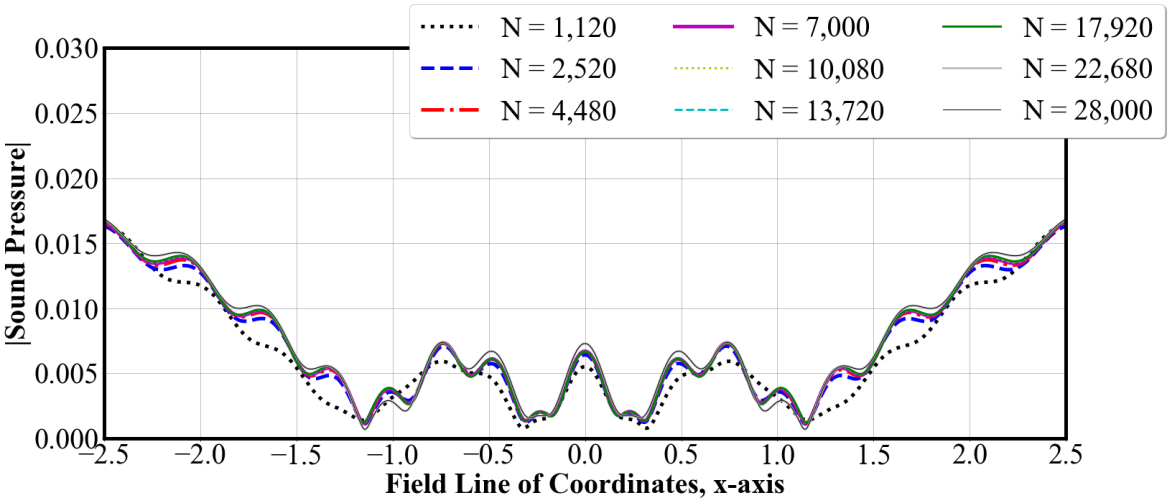

Fig. 12: Frequency-domain solution converted from the time-domain at $\omega = 20\pi$ for rigid body flat plate scattering along the field line of coordinates, $-2.5 \leq x \leq 2.5, y = 0, z = -2.5$.

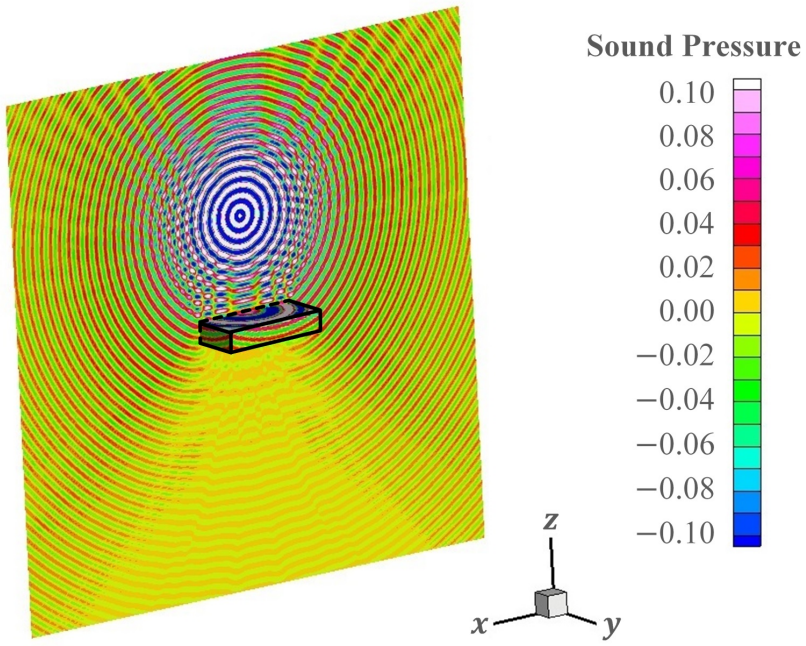

Fig. 13: Contour graph of the frequency-domain solution converted from the time-domain solution at $\omega = 20\pi$ for rigid body flat plate scattering. The visualization plane is located along the x-axis, centered at $y = 0, z = 0$.

along the x-direction on the surface using the metric of points-per-wavelength. Points-per-wavelength is computed by:

$$\text{PPW} = \frac{2\pi(p+1)N_x}{kL_x} \tag{46}$$

where p is the order of the basis function, $k = \omega/c$ is the wavenumber, and L_x is the plate length along the x-direction. Recall that the basis function is constant, so $p = 0$. For each discretization, $20 \times 20 \times 04$ to $90 \times 90 \times 18$ ($1,120$ elements to $22,680$ elements), the points-per-wavelength is calculated along the far field line of coordinates, $-2.5 \leq x \leq 2.5$, $y = 0$, $z = -2.5$ and compared against a reference solution. The L_2 norm of the relative error between the computational solution and reference solution is then calculated and graphed as a function of points-per-wavelength. When an exact solution is known, the exact solution is used as a reference. There is no exact solution for a flat plate with finite dimension, thus the solution computed by discretization of $100 \times 100 \times 20$ is used the reference solution. As demonstrated in Figures 49 to 64 in Appendix A, the solutions converge for all frequencies as the surface elements become smaller and thus it can be assumed the discretization of $100 \times 100 \times 20$ is an accurate approximation for the exact solution.

The results of the far field solution are shown in Figure 14 for the standard point source location and Figure 15 for the shifted point source location. As demonstrated in each of the figures, the relative error for all discretizations is less than 2% with only 5 points-per-wavelength. The excellent spatial accuracy is likely due to the high-order Gauss quadrature integration over a closed, hence periodic, domain. Further, the graphs indicate that the spatial accuracy is not dependent on the location of the point source in relation to the surface elements.

The spatial resolution is also measured along the x-direction on the surface using the metric of points-per-wavelength-squared, PPW2:

$$\text{PPW2} = \frac{4\pi^2(p+1)^2[2N_xN_y + 2(N_x+N_y)N_z]}{k^2[2L_xL_y + 2(L_x+L_y)L_z]} \tag{47}$$

where L_y and L_z are the plate lengths along the y- and z- directions. Equation (47) is equivalent to ($4\pi^2$ $\times$ degrees of freedom) divided by (k^2 $\times$ surface area). As such, PPW2 is a useful metric for shapes when only surface area is known rather than a specified length in one direction: a sphere, *e.g.* Evaluating PPW2 for the flat plate provides a comparative metric for how it relates to PPW. For each discretization, $20 \times 20 \times 04$ to $90 \times 90 \times 18$ ($1,120$ elements to $22,680$ elements), the points-per-wavelength-squared is calculated along the far field line of coordinates, $-2.5 \leq x \leq 2.5, y = 0, z = -2.5$ and compared against a reference

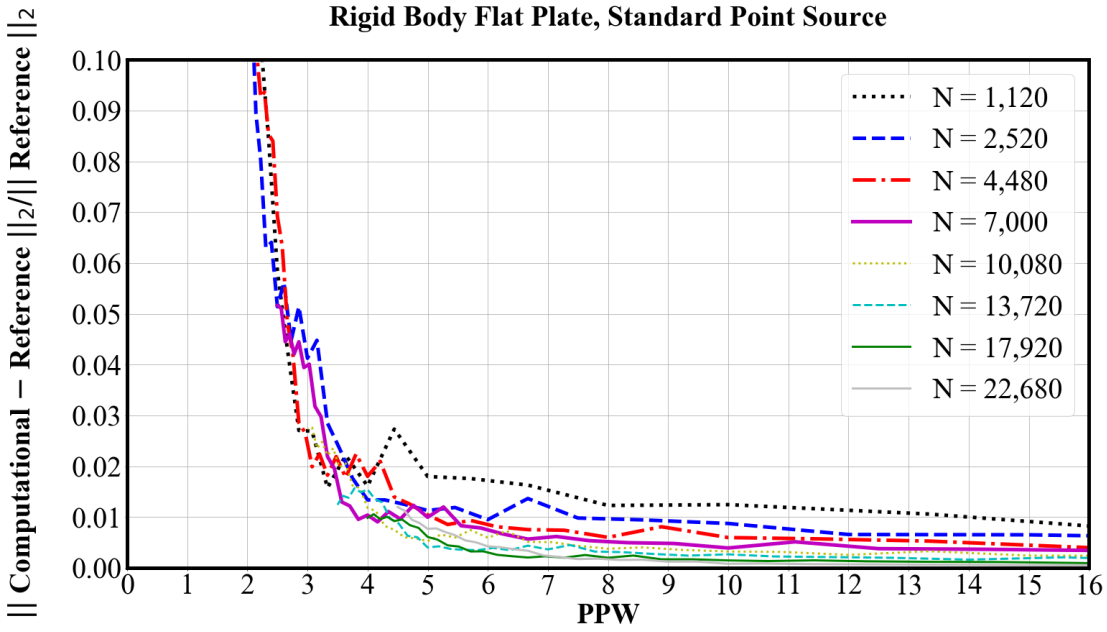

Fig. 14: Points-per-wavelength results of the flat plate (standard point source) with rigid body far field scattering solution obtained with constant basis functions.

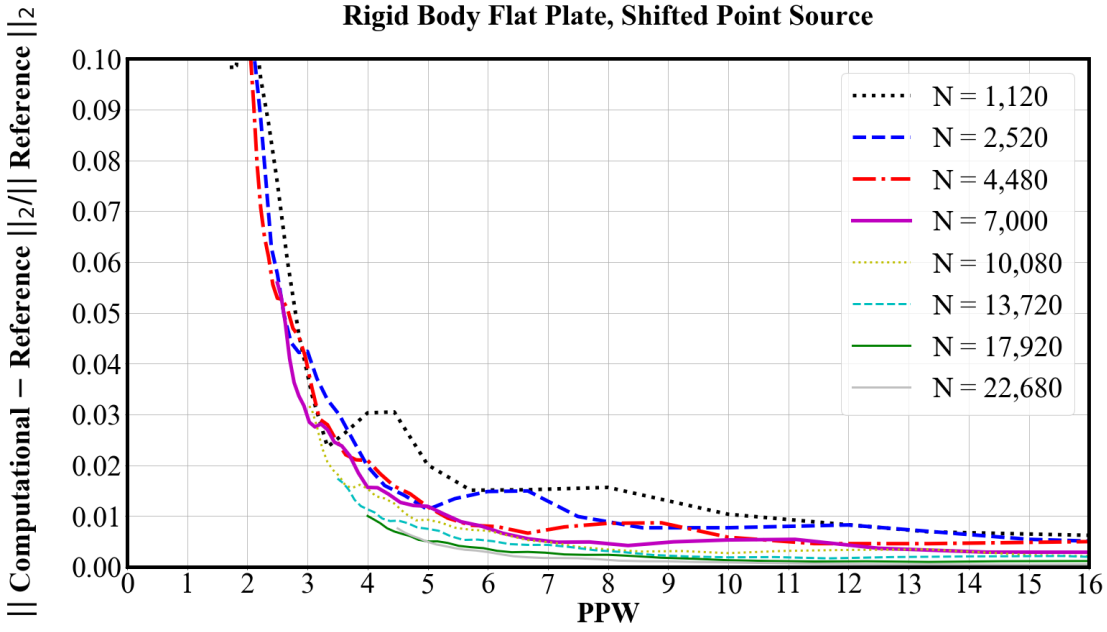

Fig. 15: Points-per-wavelength results of the flat plate (shifted point source) with rigid body far field scattering solution obtained with constant basis functions.

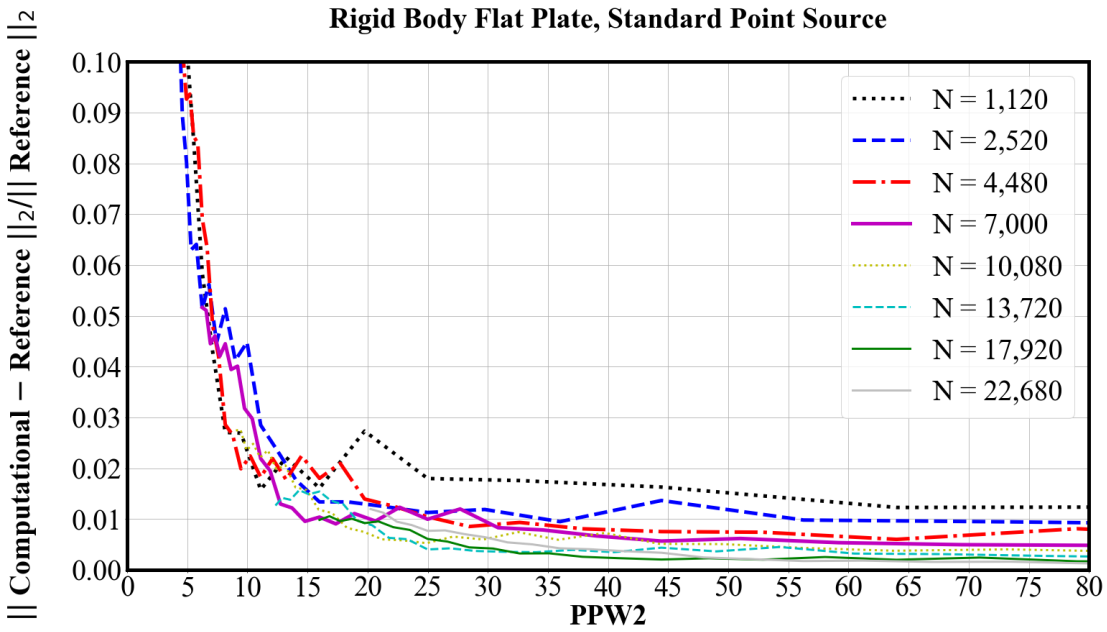

Fig. 16: Points-per-wavelength-squared results of the flat plate (standard point source) with rigid body far field scattering solution obtained with constant basis functions.

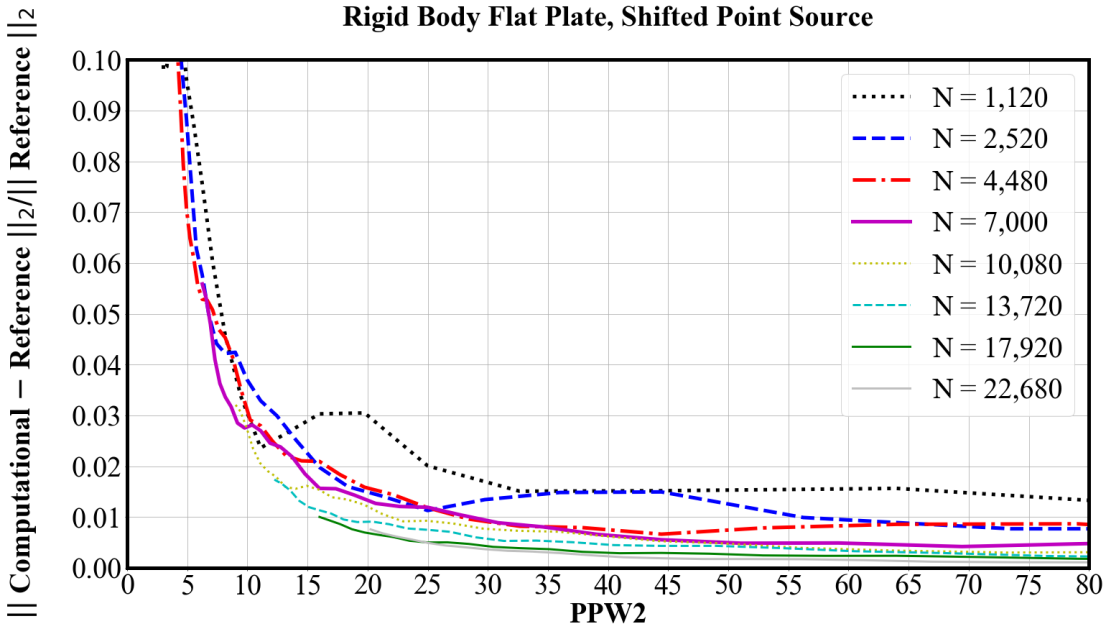

Fig. 17: Points-per-wavelength-squared results of the flat plate (shifted point source) with rigid body far field scattering solution obtained with constant basis functions.

solution from discretization $100 \times 100 \times 20$. The L_2 norm of the relative error between the computational solution and reference solution is then calculated and graphed as a function of points-per-wavelength-squared.

The results of the far field solution are illustrated in Figure 16 for the standard point source location and Figure 17 for the shifted point source location. As demonstrated in each of the figures, the relative error becomes less than 2% for all discretizations with only 25 points-per-wavelength-squared. These results agree with those of points-per-wavelength and further indicate that the spatial resolution is not dependent on the location of the point source in relation to the surface elements.

In the graphs of points-per-wavelength (Figures 14 and 15) and points-per-wavelength-squared (Figures 16 and 17), there is a slight loss of accuracy for coarser grids with small values of PPW and PPW2. This is likely due to the resolution along the edges of the flat plate. These results indicate that a finer resolution along the edges of finite bodies with sharp edges may help to maintain high spatial accuracy.

3.3 SPHERE WITH RIGID BODY

The surface of the sphere is also discretized, and a series of computations is carried out by increasing the number of elements from $N = 729$ to $72,091$. Both the standard and rotated orientations are considered as illustrated in Figures 4a and 4b, respectively. The frequency-domain solution converted from the time-domain at $\omega = 5\pi$ is illustrated in Figure 18 for the standard orientation, recalling that ω is a non-dimensionalized value. Moreover, Figures 19 through 21 illustrate solutions at $\omega = 10\pi, 15\pi$, and 20π, respectively, for all discretizations allowing for the visualization of rigid body scattering at higher frequencies. Included on each graph is the exact solution for unlike the flat plate with finite dimension, an exact solution is known for spherical bodies. All discretizations are indicated in the legend. The y-axis is the magnitude of sound pressure. The x-axis indicates the solution along a field line of coordinates, $-2.5 \leq x \leq 2.5, y = 0, z = -2.5$. For solutions at all frequencies, $\omega = 5\pi, 6\pi, ...20\pi$, refer to Appendix B. As with the flat plate results, the fluctuations in magnitude of sound pressure increase with increasing frequencies. Also, the deviation in numerical results from the exact solution increases with increasing frequencies.

The spatial resolution is measured along the x-direction using the metric of points-per-wavelength-squared. For each discretization, $N = 729$ to $72,091$ elements, the points-per-wavelength-squared is calculated along the field line of coordinates $-2.5 \leq x \leq 2.5$, $y = 0$, $z = -2.5$ using (47) and compared against the known, exact solution. The L_2 norm of the

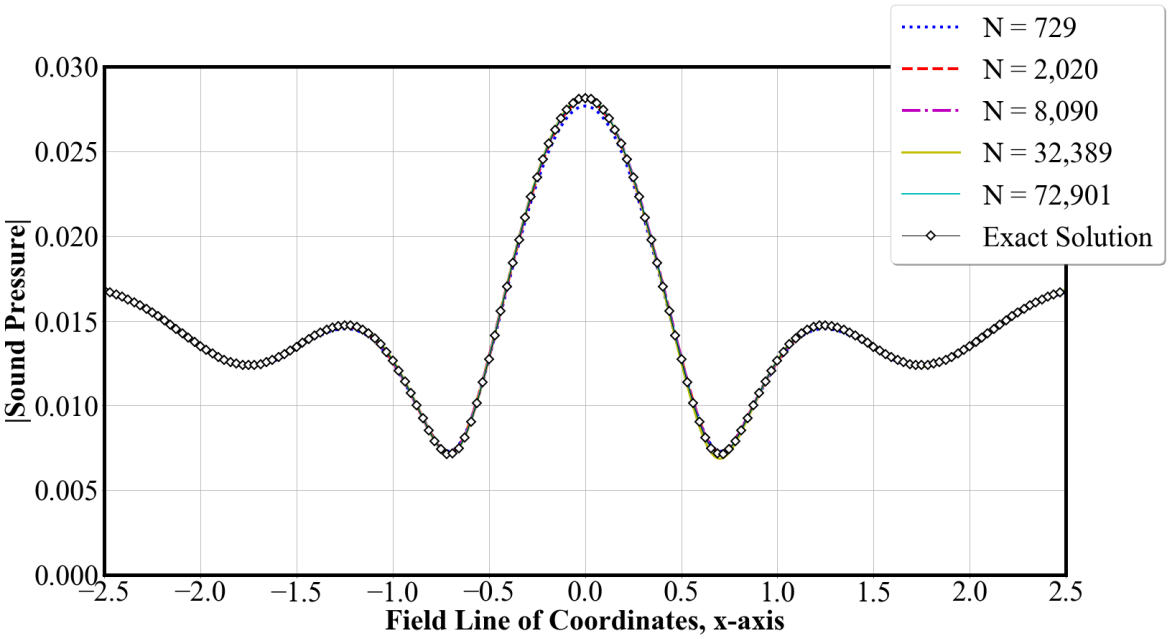

Fig. 18: Frequency-domain solution converted from the time-domain at $\omega = 5\pi$ for rigid body sphere scattering along the field line of coordinates, $-2.5 \leq x \leq 2.5, y = 0, z = -2.5$.

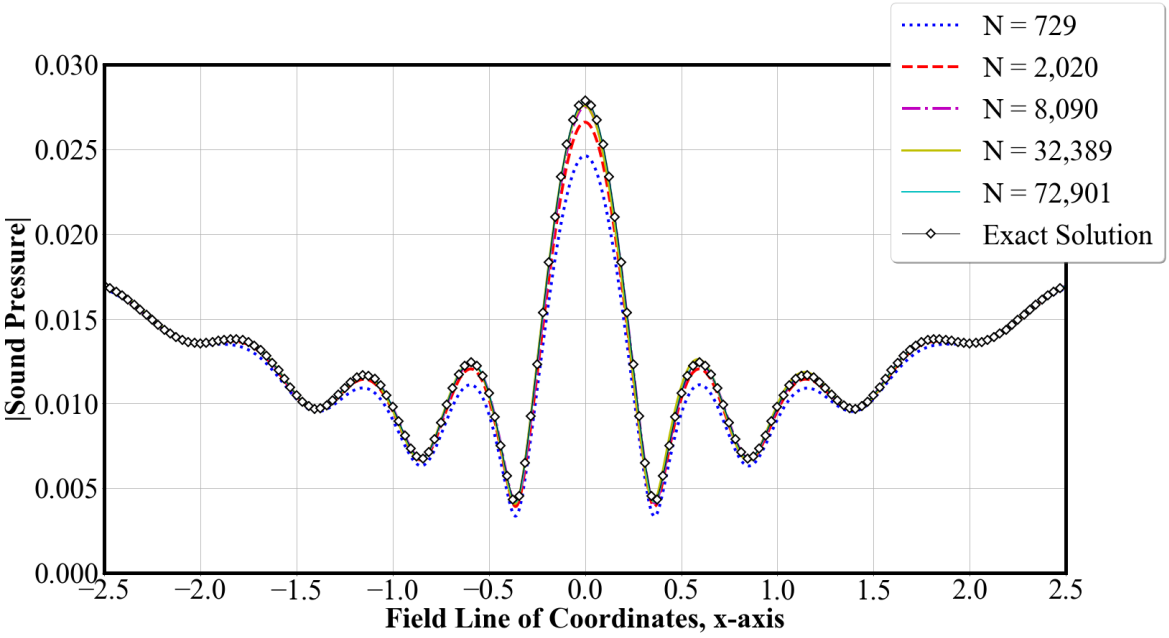

Fig. 19: Frequency-domain solution converted from the time-domain at $\omega = 10\pi$ for rigid body sphere scattering along the field line of coordinates, $-2.5 \leq x \leq 2.5, y = 0, z = -2.5$.

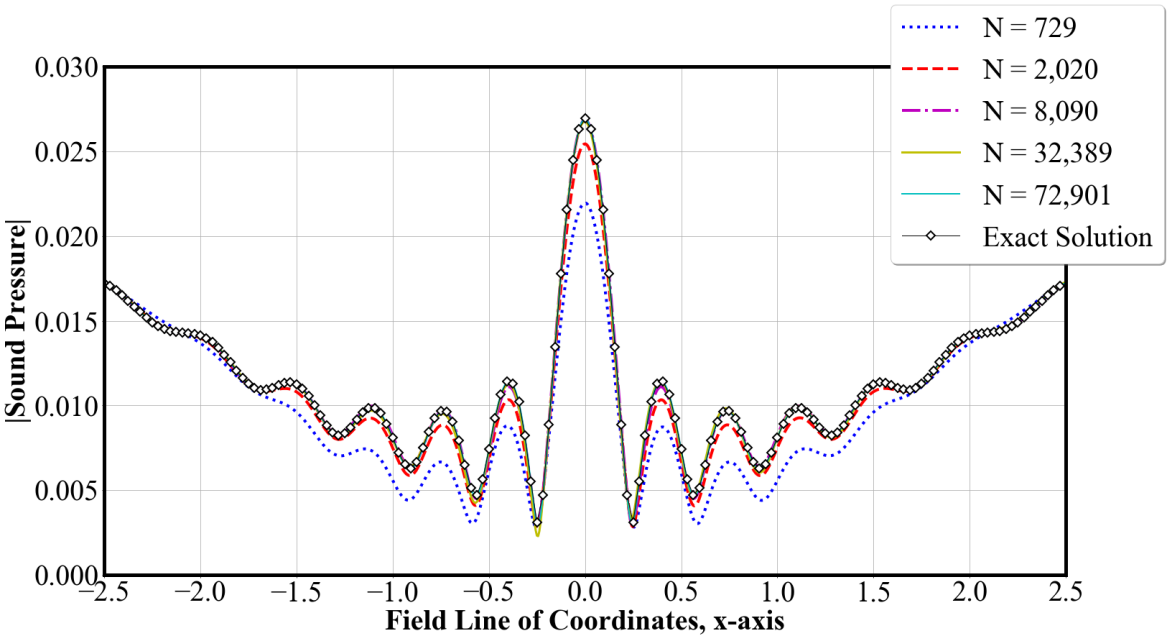

Fig. 20: Frequency-domain solution converted from the time-domain at $\omega = 15\pi$ for rigid body sphere scattering along the field line of coordinates, $-2.5 \leq x \leq 2.5, y = 0, z = -2.5$.

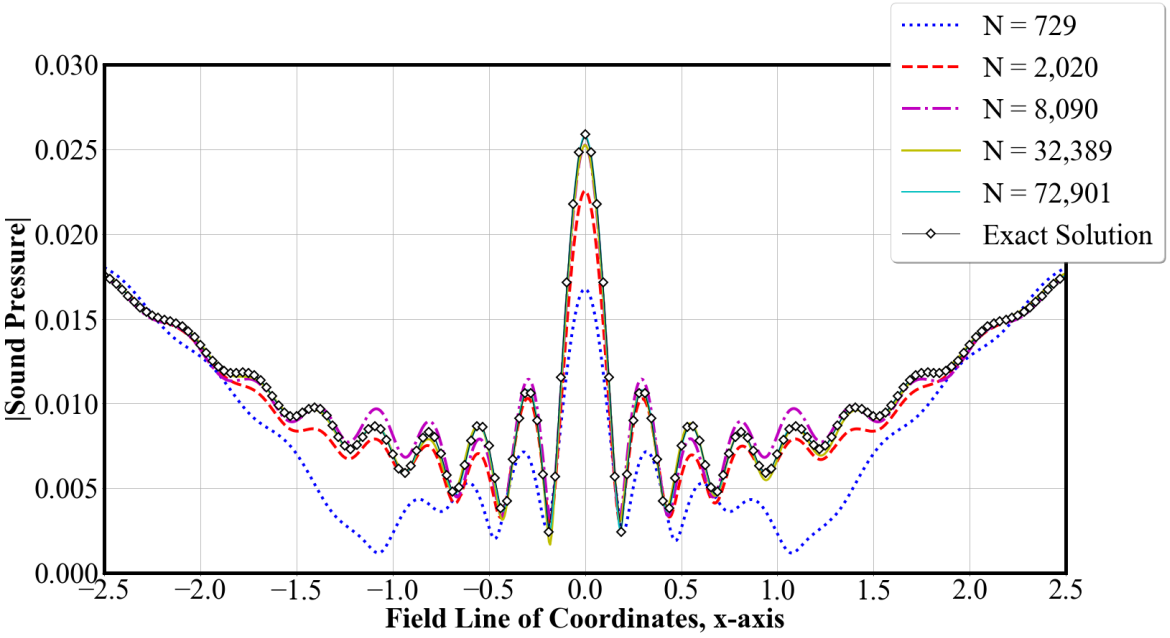

Fig. 21: Frequency-domain solution converted from the time-domain at $\omega = 20\pi$ for rigid body sphere scattering along the field line of coordinates, $-2.5 \leq x \leq 2.5, y = 0, z = -2.5$.

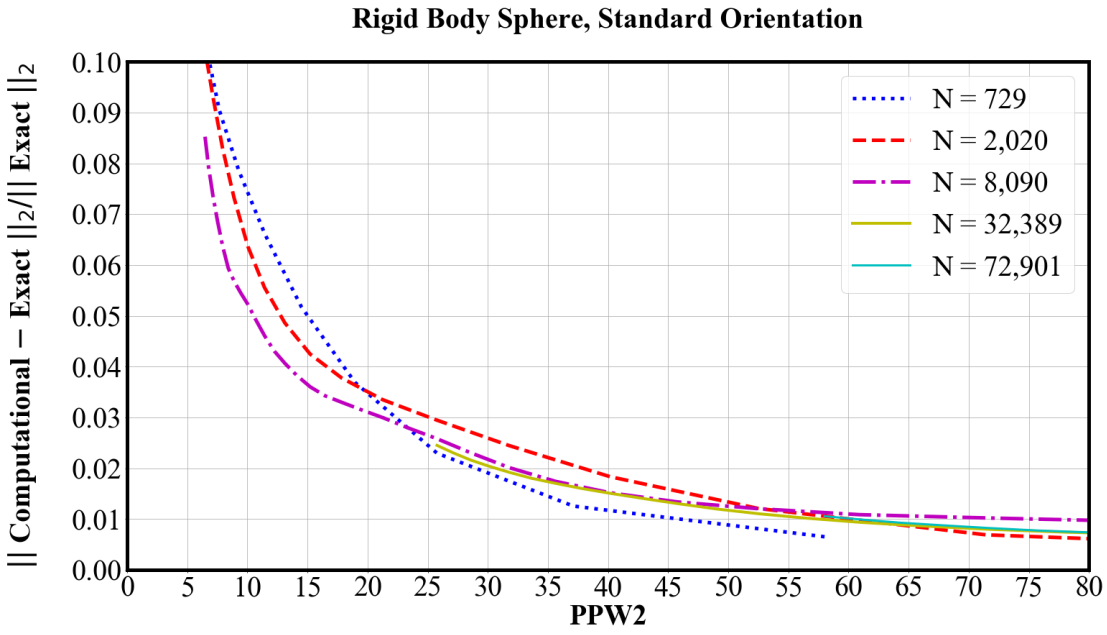

Fig. 22: Points-per-wavelength-squared results of the standard orientation sphere with rigid body far field scattering solution obtained with constant basis functions.

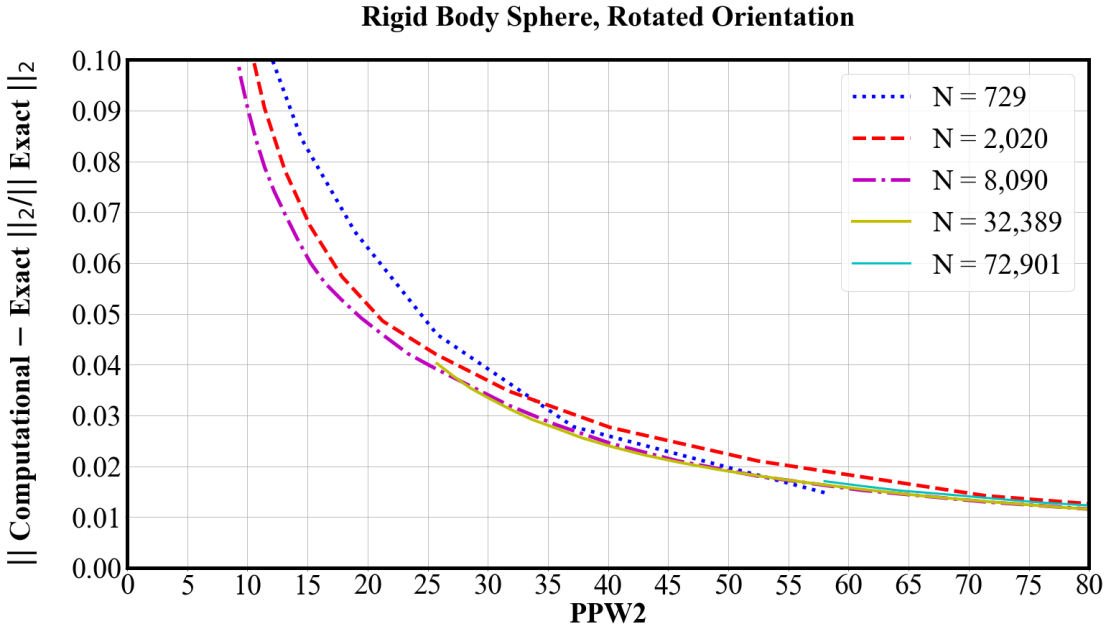

Fig. 23: Points-per-wavelength-squared results of the rotated orientation sphere with rigid body far field scattering solution obtained with constant basis functions.

relative error between the computational solution and reference solution is then calculated and graphed as a function of points-per-wavelength-squared.

The results of the far field solution with constant basis functions are illustrated in Figure 22 for the standard orientation and Figure 23 for the rotated orientation. As demonstrated in the figures, the relative error becomes as small as 3% for the standard orientation and as small as 5% for the rotated orientation when points-per-wavelength-squared is only 25. These results indicate that the spatial resolution is likely dependent on the orientation of the surface elements with respect to the wave direction. The standard orientation has smaller error at the same spatial resolution, likely a result of the sound wave being evenly distributed across all surface elements as it propagates around the sphere. It should be noted, however, that even though the rotated orientation has a higher error than the original, the error in both cases is still quite low when points-per-wavelength-squared is only 25. It appears that like the flat plate, at least for the far field problem, the use of constant spatial basis functions can keep the overall problem size small while the high-order integration helps to maintain accuracy.

CHAPTER 4

SCALABILITY AND PERFORMANCE USING CPUS

The Burton-Miller reformulation (37) of the time-domain boundary integral equation derived in Chapter 2 has been implemented in TD-FAST, a fast numerical solver that allows for the time-domain prediction of acoustic wave scattering with and without mean flow for up to full scale aircraft. TD-FAST has the capability of performing large-scale parallel computations using either central processing units (CPUs) or graphics processing units (GPUs). A CPU is a multi-core processor with local, private memory. A typical CPU has anywhere from two to thirty-two cores and is designed for sequential serial processing [78]. A GPU is a many-core processor containing hundreds to thousands of cores. A single CPU core has a higher clock speed and is more powerful than a single CPU core. However, GPUs, designed for high-throughput processing, can exploit massive parallelism [79, 80] and demonstrate orders of magnitude speedups over traditional low-latency CPU computing [1, 81–83].

4.1 PREVIOUS WORK ON GPUS

In [81], Geng and Jacob solve the linear Poisson-Boltzmann equation with a boundary integral method and achieved a 120-150X speedup when using one GPU versus one CPU. In [82] Guan, Yan, and Jin solve a three-dimensional electromagnetic scattering problem with a hybrid finite element-boundary integral method and achieved a 24-26X speedup when using two GPUs versus executing eight threads on one CPU; and in [83] Takahashi and Hamada solve the three-dimensional Helmholtz equation using boundary element methods and achieved a 6-23X speedup.

In [1], Hu studied the parallelization of TD-FAST with GPUs: "GPU computing favors intrinsically parallel algorithms. It is most effective when a time consuming computation can be efficiently divided into independent small computations. Such massive parallelism is naturally abundant in the time-domain boundary element methods. At each time step, computations on each element can be carried out independently, resulting in a high degree of parallelism. This makes the time-domain boundary element method a good application for GPU computing." Results of this study demonstrated a 30X speedup when using one GPU versus one CPU due to a loss of efficiency from inter-nodal message passing communications.

4.2 SCALABILITY OF CPUS

Though TD-FAST has significant speedup when utilizing GPU architecture, the code maintains the ability to exploit parallelism with CPUs for instances when GPU hardware may be unavailable to the user. It is therefore important to study the performance of TD-FAST when utilizing CPU architecture only. In this chapter, the CPU performance is investigated by considering both strong and weak scaling as well as parallel efficiency. Strong scaling indicates how the solution time varies with an increasing core count for a fixed problem size and weak scaling indicates how the solution time varies with an increasing problem size for a fixed core count. Both are derivatives of Amdahl's Law [84] and Gustafson's Law [85]. Amdahl's Law states that, for a fixed problem size, the maximum speedup is limited by $1/s$ as the core count approaches infinity such that s is the serial portion of the code. Gustafson's Law states that as core count increases with problem size, the speedup is linearly proportional to the problem size N [78].

The numerical algorithm performance using CPUs is studied by considering the scattering of an acoustic point source by a flat plate with rigid body as illustrated in Figure 3a in Chapter 3. The flat plate is discretized using N_x, N_y, and N_z elements in the x-, y-, and z-directions, respectively, yielding a total of $N = 2(N_xN_y + N_yN_z + N_xN_z)$ elements. A series of simulations are carried out using standard compute nodes available through the Old Dominion University Turing Cluster by increasing the number of elements used from $N_x \times N_y \times N_z = 5 \times 5 \times 1$ ($N = 70$ elements) to $50 \times 50 \times 10$ ($N = 7,000$ elements). As of January 2020, the Turing Cluster has 220 standard compute nodes with 128 GB of memory and between sixteen and thirty-two CPU cores each [86]. The processing power for each simulation is increased from one core to between thirty-two and 128 cores running exclusively on one, two, or four nodes as listed in Table I. All scattering problems are modeled for a total simulation time of $T = 6$ with time step of $\Delta t = 1/12$, both[1] non-dimensional.

Performance is assessed by first running three trials per simulation and then calculating the average clock time for each time step in the simulation for all three trials. The time used for exporting data to output files is not included in the reported time. The average trial clock time per simulation is illustrated in Figures 24 through 29 for element sizes $N = 70$ through $N = 7,000$, respectively. For each core count, the overall average clock time is denoted on the graphs by a horizontal line and its numerical value is listed in a gray

[1]A simulation time of $T = 6$ with time step of $\Delta t = 1/12$ was chosen to ensure that the scattering problem provided far field solutions over a wide range of frequencies. This combination of choices allows for the acoustic wave to propagate far beyond the scattering body over a broad frequency band.

TABLE I: Problem size with associated core and node counts

Number of Elements	**Processing Power**
$N = 70$ $(5 \times 5 \times 1)$	One Node: one, two, four, eight cores
$N = 280$ $(10 \times 10 \times 2)$	One Node: one, two, four, eight, sixteen, thirty-two cores
$N = 1,120$ $(20 \times 20 \times 4)$	One Node: one, four, eight, sixteen, thirty-two cores Two Nodes: sixty-four cores
$N = 2,520$ $(30 \times 30 \times 6)$	One Node: one, four, eight, sixteen, thirty-two cores Two Nodes: sixty-four cores
$N = 4,480$ $(40 \times 40 \times 8)$	One Node: one, sixteen, thirty-two cores Two Nodes: sixty-four cores Four Nodes: 128 cores
$N = 7,000$ $(50 \times 50 \times 10)$	One Node: one, sixteen, thirty-two cores Two Nodes: sixty-four cores Four Nodes: 128 cores

box with text "Average = ###". As the discretization becomes more refined and more processing power is used (specifically, Figures 26 through 29), it is increasingly difficult to differentiate between core counts of four, eight, *etc.* Therefore, Appendix C contains the graphs with data from one CPU core removed for purposes of better visualization.

Figures 24 through 29 each indicate a direct relationship between the decrease in clock time and the increase of processing power, *i.e.* as the processing power increases by a factor of two the average clock time decreases by approximately a factor of two. As shown in Figure 24, the average clock time per time step in the simulation for $N = 70$ elements is 0.0190 seconds when running with one CPU core, 0.0102 seconds with two CPU cores, 0.0057 seconds with four CPU cores, and 0.0037 seconds with eight CPU cores. In Figure 25, the average clock time per time step in the simulation for $N = 280$ elements is 0.2653 seconds when running with one CPU core, 0.1365 seconds with two CPU cores, 0.0767 seconds with four CPU cores, 0.0431 seconds with eight CPU cores, 0.0252 seconds with sixteen CPU cores, and 0.0129 seconds with thirty-two CPU cores.

The scalability is investigated by considering the decrease in the average clock time with increasing CPU core count, shown for $N = 70$ through $N = 7,000$ elements in Figures 30a through 35a. The scalability is additionally investigated by calculating the speedup S_{CPU}

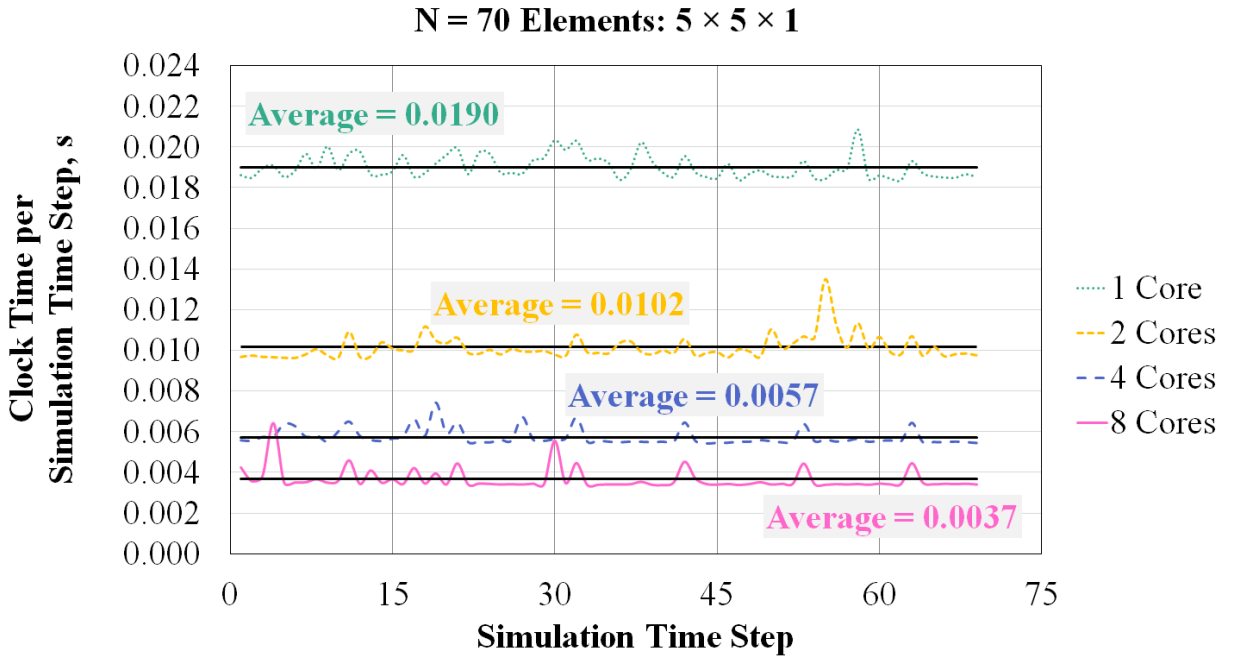

Fig. 24: Average clock time for $N = 70$ elements using one exclusive node with one, two, four, and eight cores.

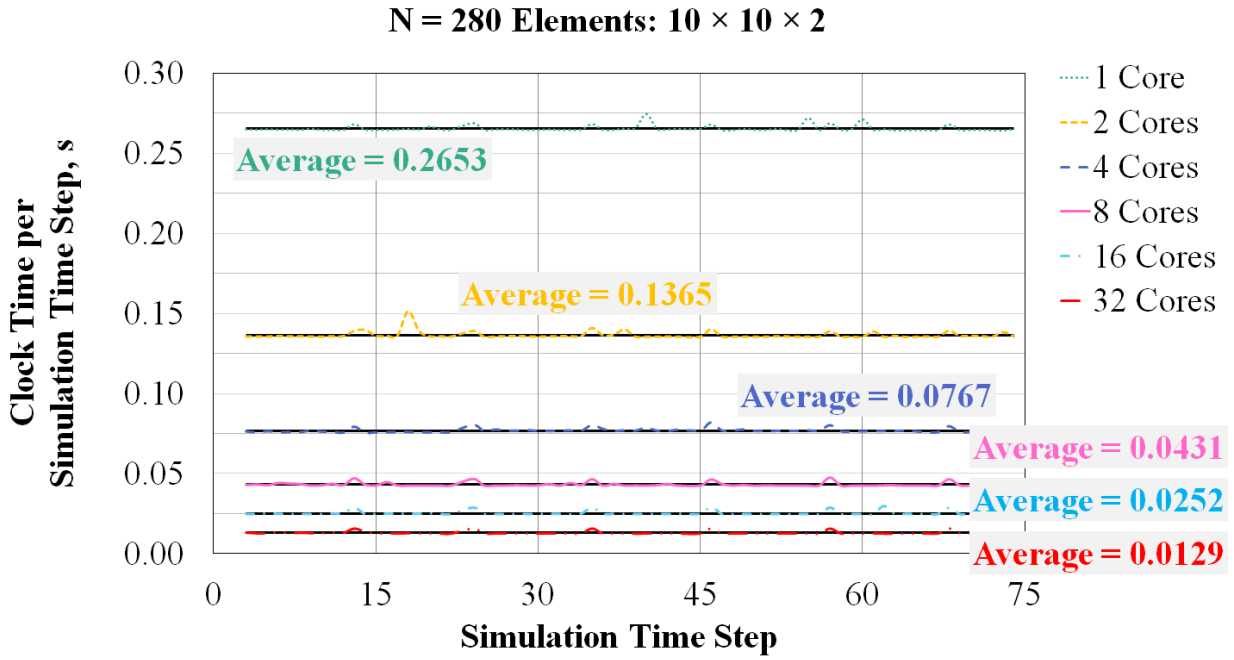

Fig. 25: Average clock time for $N = 280$ elements using one exclusive node with one, two, four, eight, sixteen, and thirty-two cores.

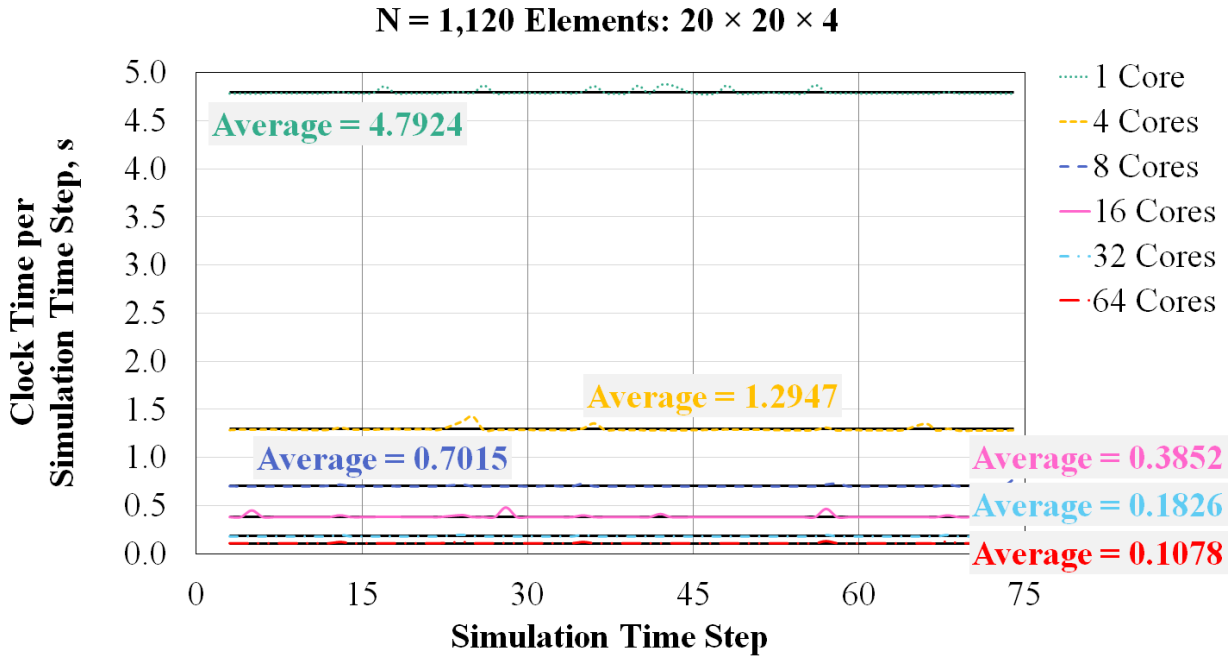

Fig. 26: Average clock time for $N = 1,120$ elements using one exclusive node with one, four, eight, sixteen, and thirty-two cores and using two exclusive nodes with sixty-four cores.

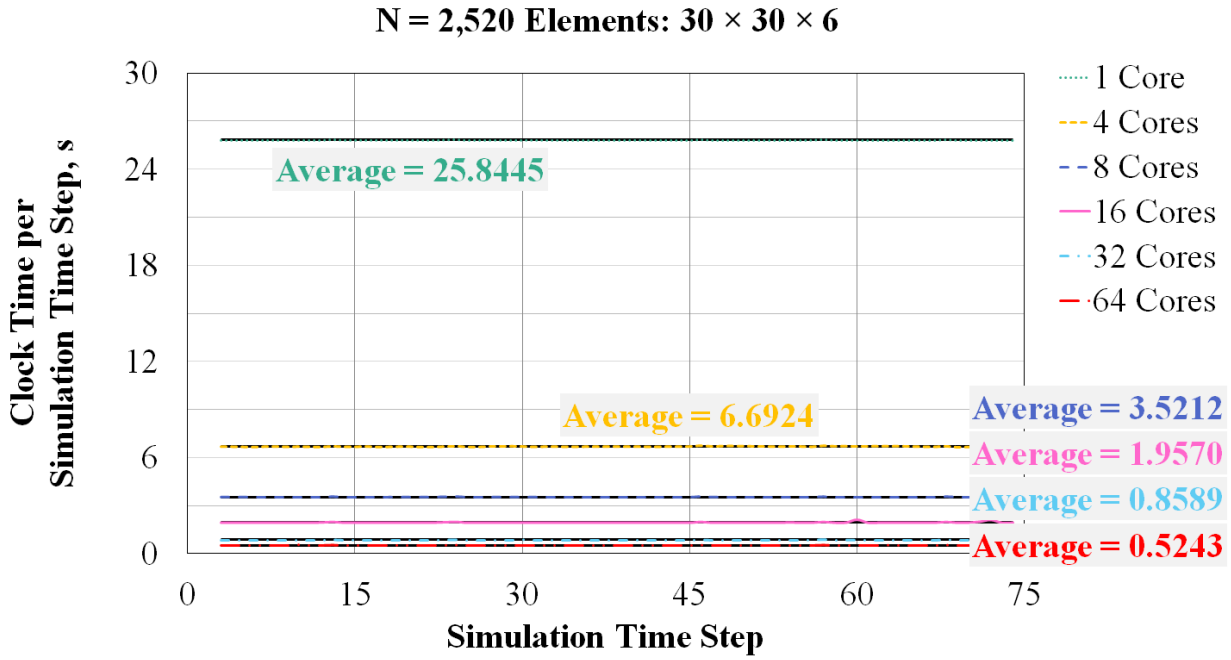

Fig. 27: Average clock time for $N = 2,520$ elements using one exclusive node with one, four, eight, sixteen, and thirty-two cores and using two exclusive nodes with sixty-four cores.

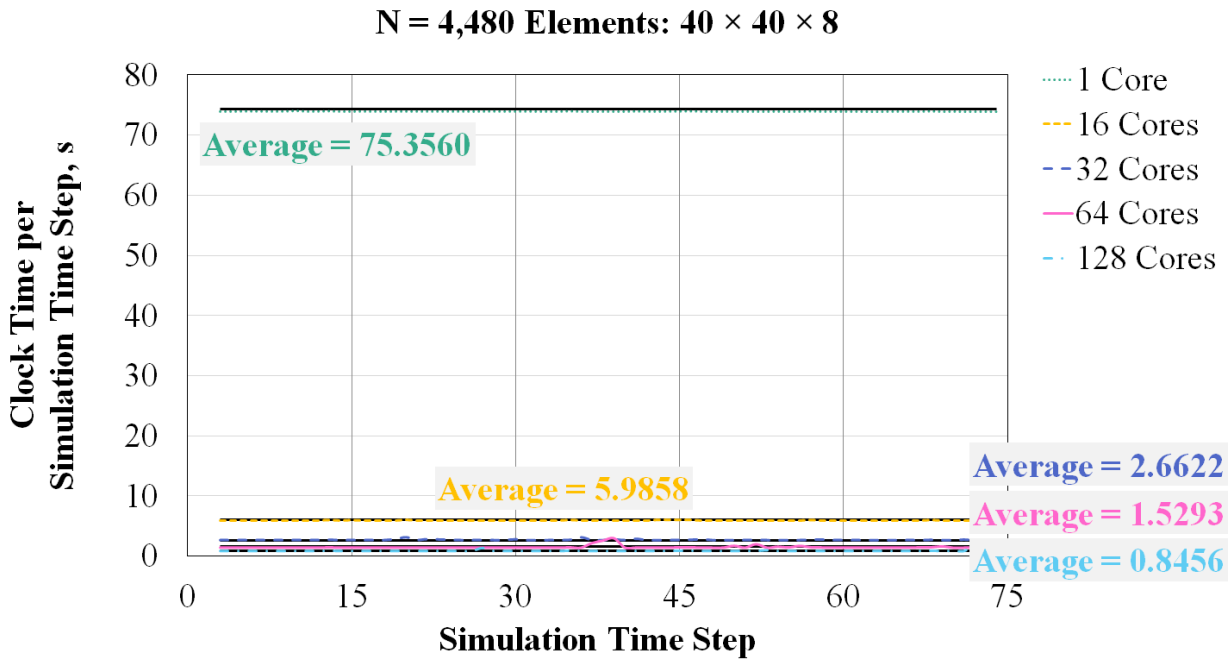

Fig. 28: Average clock time for $N = 4,480$ elements using one exclusive node with one, sixteen, and thirty-two cores, using two exclusive nodes with sixty-four cores, and using four exclusive nodes with 128 cores.

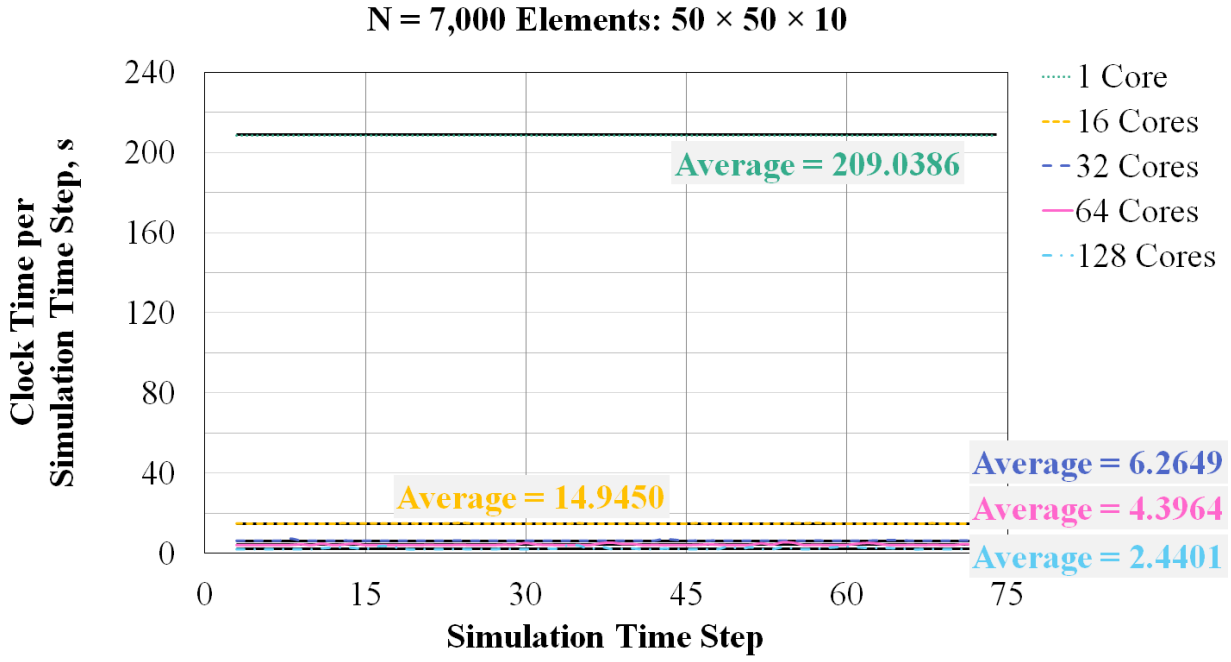

Fig. 29: Average clock time for $N = 7,000$ elements using one exclusive node with one, sixteen, and thirty-two cores, using two exclusive nodes with sixty-four cores, and using four exclusive nodes with 128 cores.

from C cores to D cores,

$$S_{\text{CPU}} = \frac{\text{Clock time per time step in the simulation using } C \text{ cores}}{\text{Clock time per time step in the simulation using } D \text{ cores}}$$

with increasing CPU core count. The results for $N = 70$ through $N = 7,000$ elements are shown in Figures 30b through 35b. In each of the figures, the actual scaling is indicated by a dotted line with marker (solid square for $N = 70$, solid circle for $N = 280$, solid triangle for $N = 1,120$, solid diamond for $N = 2,520$, open square for $N = 4,480$, and open circle for $N = 7,000$). The ideal scaling is indicated by a solid line. For a fixed problem size, ideal strong scaling dictates that the clock time is inversely proportional to the number of CPU cores. That is, if the processing power doubles from C to D cores, the clock time should be reduced by a factor of two and the speedup should double. If the processing power triples from C to D cores, the clock time should be reduced by a factor of three and the speedup should triple, etc.

As indicated in Figures 30a and 30b, the speedup is nearly ideal as processing power doubles from one to two cores. However, as the power is doubled again from two to four cores and from four to eight cores, the speedup is not linear. This is likely due to an increase in parallel overhead, *i.e.*, an increase in the time associated with performing inter-nodal message passing communications like that of GPUs in [1]. These results are also demonstrated in Figures 31a and 31b where the numerical results closely match the ideal when processing power increases from one to four cores then begins to taper, in Figures 32a and 32b where the numerical results closely match the ideal when processing power increases from one to eight cores then begins to taper, and in Figures 33a through 35b where the numerical results closely match the ideal when processing power increases from one to thirty-two cores then begins to taper.

The results from $7,000$ elements with thirty-two cores (refer to Figures 35a and 35b) indicate a super linear speedup due to the speedup being greater than that of ideal strong scaling. This is likely due to one of three possibilities: (1) not properly filtering out the time required for data export when calculating the average clock time, (2) one or more of the three trials for sixteen CPUs and/or thirty-two CPUs included outlier data thereby prompting a speedup greater than 2X as processing power is doubled from sixteen to thirty-two cores, and (3) thirty-two CPUs better accessed the memory within the node having fully-utilized the architecture whereas the sixteen CPUs, though running exclusively, were run on a single node with either sixteen cores or thirty-two cores depending on what nodes were available on Turing at the time of job submission. A combination of possibilities (2) and (3) are the

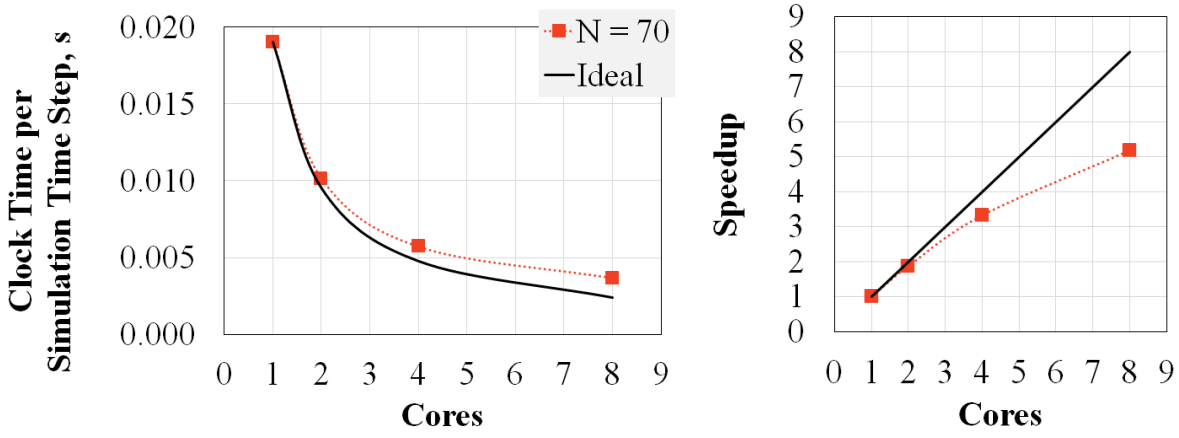

(a) Clock Time vs. CPU Cores (b) Speedup vs. CPU Cores

Fig. 30: Scalability results for $N = 70$ elements.

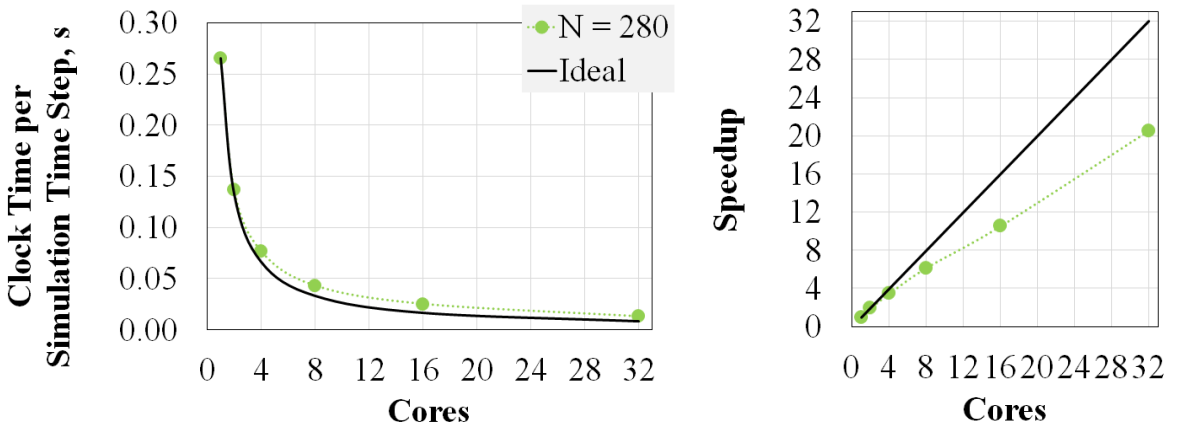

(a) Clock Time vs. CPU Cores (b) Speedup vs. CPU Cores

Fig. 31: Scalability results for $N = 280$ elements.

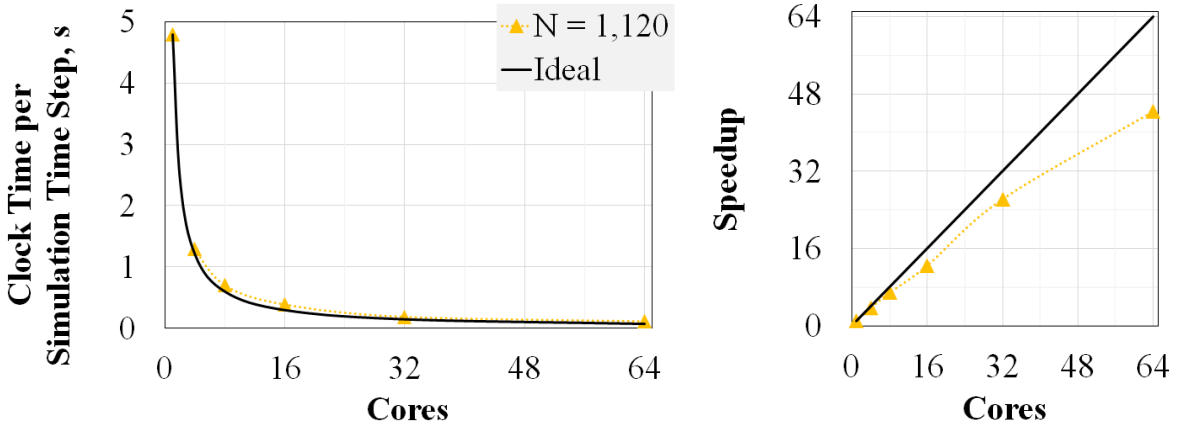

(a) Clock Time vs. CPU Cores (b) Speedup vs. CPU Cores

Fig. 32: Scalability results for $N = 1,120$ elements.

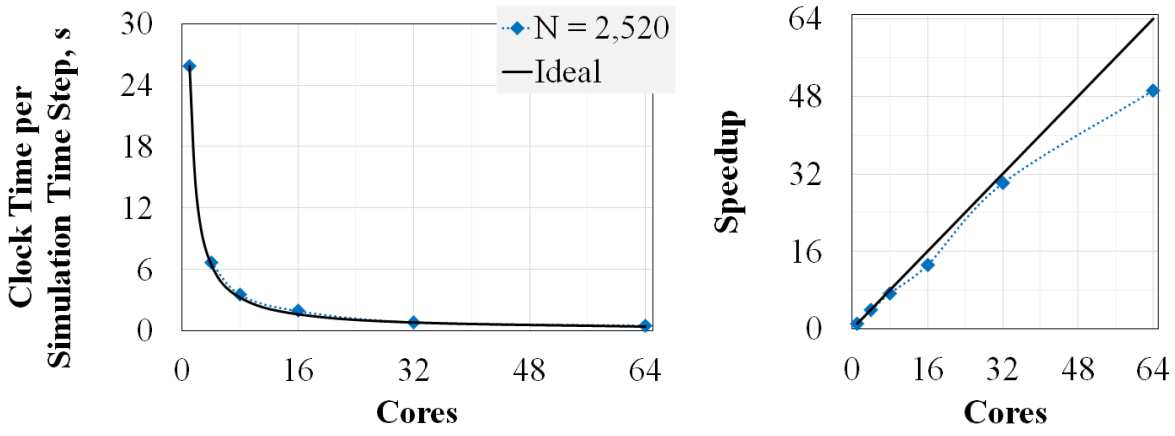

(a) Clock Time vs. CPU Cores (b) Speedup vs. CPU Cores

Fig. 33: Scalability results for $N = 2,520$ elements.

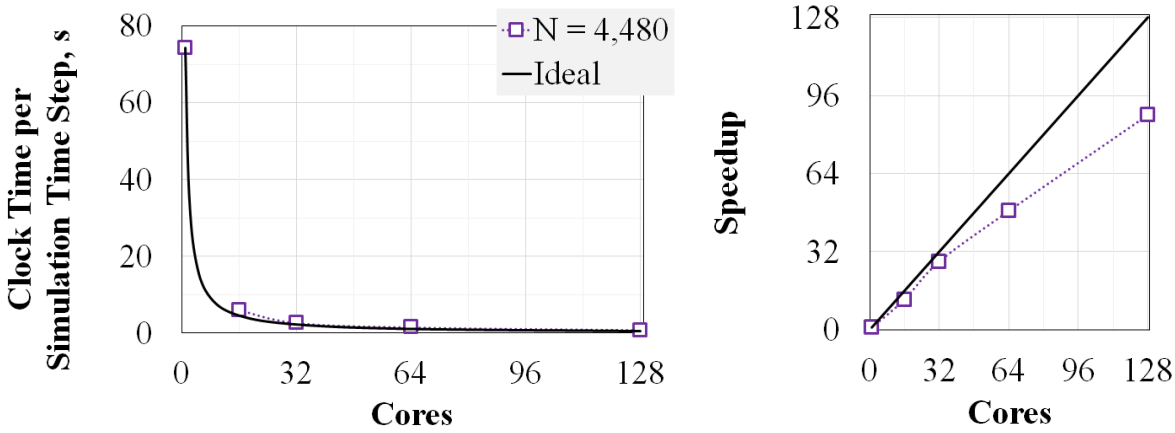

(a) Clock Time vs. CPU Cores (b) Speedup vs. CPU Cores

Fig. 34: Scalability results for $N = 4,480$ elements.

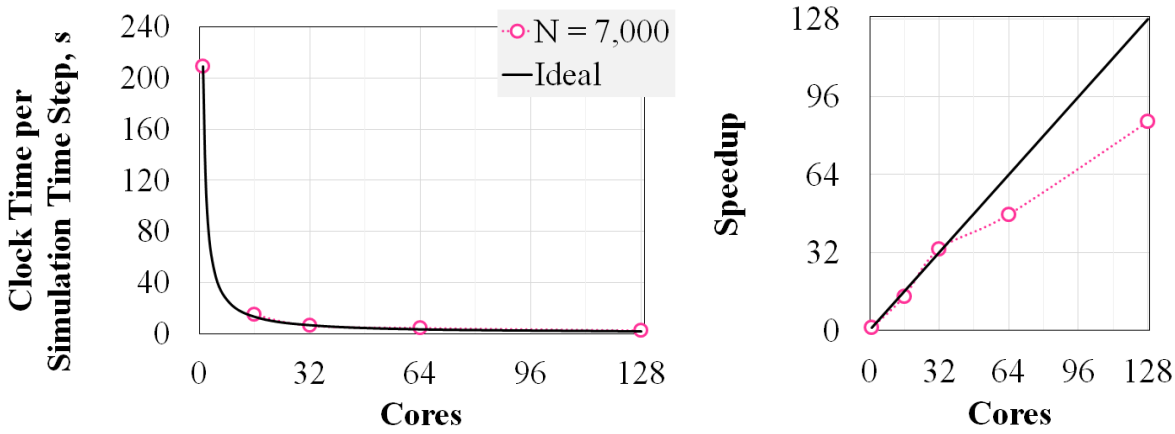

(a) Clock Time vs. CPU Cores (b) Speedup vs. CPU Cores

Fig. 35: Scalability results for $N = 7,000$ elements.

most likely culprit for this anomaly given that a speedup of greater than 2X occurred when doubling the processing power from sixteen to thirty-two cores for the simulations with $1,120$ elements (0.3852 seconds / 0.1826 seconds = 2.11X speedup), $2,520$ elements (1.9570 seconds / 0.8589 seconds = 2.28X speedup), and $4,480$ elements (5.9858 seconds / 2.6622 seconds = 2.29X speedup) using the clock time averages shown in Figures 26 through 29.

When running sixteen CPUs on one node, though exclusively, it is not guaranteed to fully-utilize the CPU architecture since the standard compute nodes on Turing have either sixteen or thirty-two cores. In any of the three trials the simulations could have occurred on either type of hardware thereby either under-utilizing or fully-utilizing the node. On the other hand, when running thirty-two CPUs exclusively on one node, sixty-four CPUs on two nodes, or 128 CPUs on four nodes, each of the simulations fully-utilized the hardware because the only possibility for job submission was for nodes with exactly thirty-two cores. Once fully-utilized, the speedup is less than 2X as processing power doubles from thirty-two to sixty-four cores and from sixty-four to 128 cores for each of the problem sizes: $1,120$ elements show a speedup of 1.69X from thirty-two to sixty-four cores, $2,520$ elements show a speedup of 1.64X from thirty-two to sixty-four cores, $4,480$ elements show a speedup of 1.74X from thirty-two to sixty-four cores and 1.81X from sixty-four to 128 cores, and $7,000$ elements show a speedup of 1.43X from thirty-two to sixty-four cores and 1.80X from sixty-four to 128 cores.

These results are also demonstrated in Figure 36 which compares the scaling results for all elements on the same graph. In this figure, $1,120$ through $7,000$ elements show a relationship greater than ideal scaling from sixteen to thirty-two cores, but then decreases to below ideal with core counts greater than thirty-two. The strong scaling study therefore demonstrates that as core count increases for a fixed problem size, there is an increase in the time associated with performing parallel communications. $N = 2,520$ elements, *e.g.*, scales linearly up to thirty-two cores but once doubled to sixty-four cores, the inter-nodal communication requirements become too large for the problem size and the scaling drops to 23% less than ideal. Similarly, $N = 4,480$ and $N = 7,000$ elements scale linearly up to thirty-two cores but then as processing power increases up to 128 cores, the required message passing outweighs the parallel performance and the scaling drops to 31% and 33% less than ideal, respectively. Moreover, the algorithm scales well with fewer CPUs for smaller problem sizes and performance suffers as the core count increases due to the costs associated with inter-nodal communication. Larger problem sizes, on the other hand, perform well with larger core counts. The results demonstrate that is better to fully-utilize all cores within each

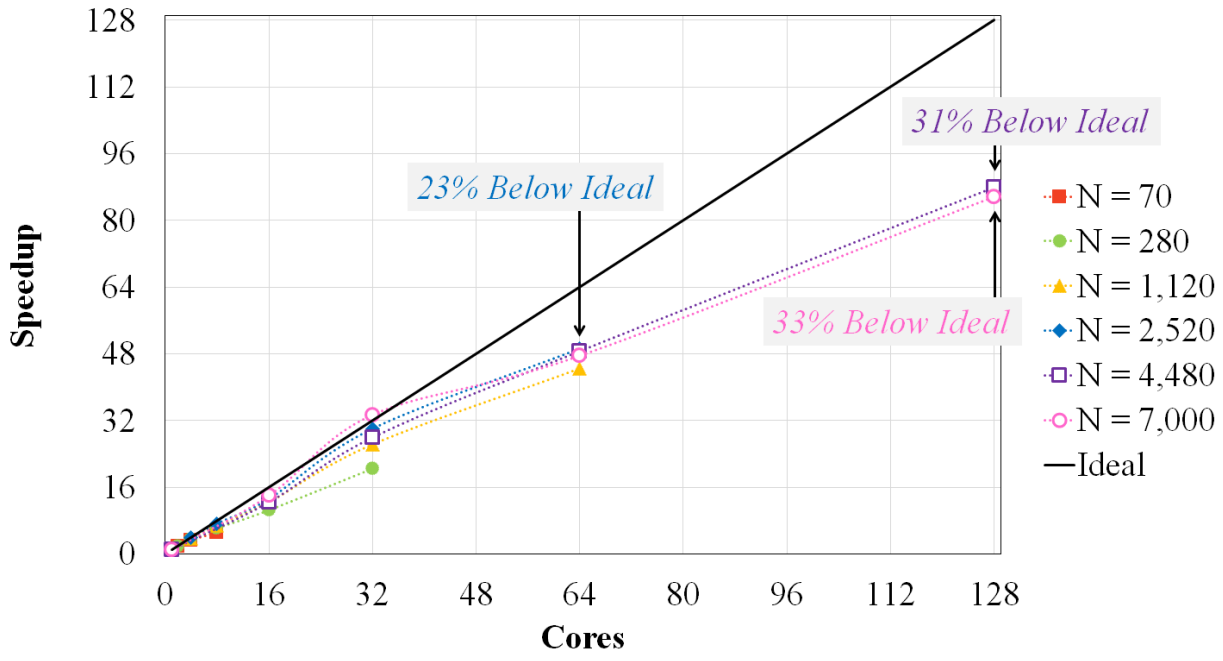

Fig. 36: Comparison of the speedup resulting from $N = 70$ to $N = 7,000$ elements.

node rather than using less cores than available per node if the message passage requirements do not outweigh the benefits of performing parallel operations.

The algorithm performance is further investigated by calculating the parallel efficiency P_{eff} from 1 core to C cores,

$$P_{\text{eff}} = \frac{S_{\text{CPU}} \text{ from 1 core to } C \text{ cores}}{C \text{ cores}}$$

and graphing against the problem size for the purpose of assessing the weak scaling with fixed core counts. The results are shown in Figure 37. For a comparison to strong scaling, the parallel efficiency is also graphed against the core count with fixed problem sizes as shown in Figure 38. Parallel efficiency is equal to 100% given ideal linear scaling as identified in each of the figures by a solid, horizontal line. The anomaly from $7,000$ elements with thirty-two cores is observed on each figure as the efficiency increases above 100% when $N = 7,000$ and $C = 32$. Once more, this result is numerically invalid and is likely due to outliers within the three trials and/or the under-utilization of a single node when using sixteen cores versus the full utilization when using thirty-two.

As indicated in Figure 37, when under-utilizing a single node, the algorithm scales well with fewer CPUs. For all problem sizes, four cores outperform eight and sixteen cores.

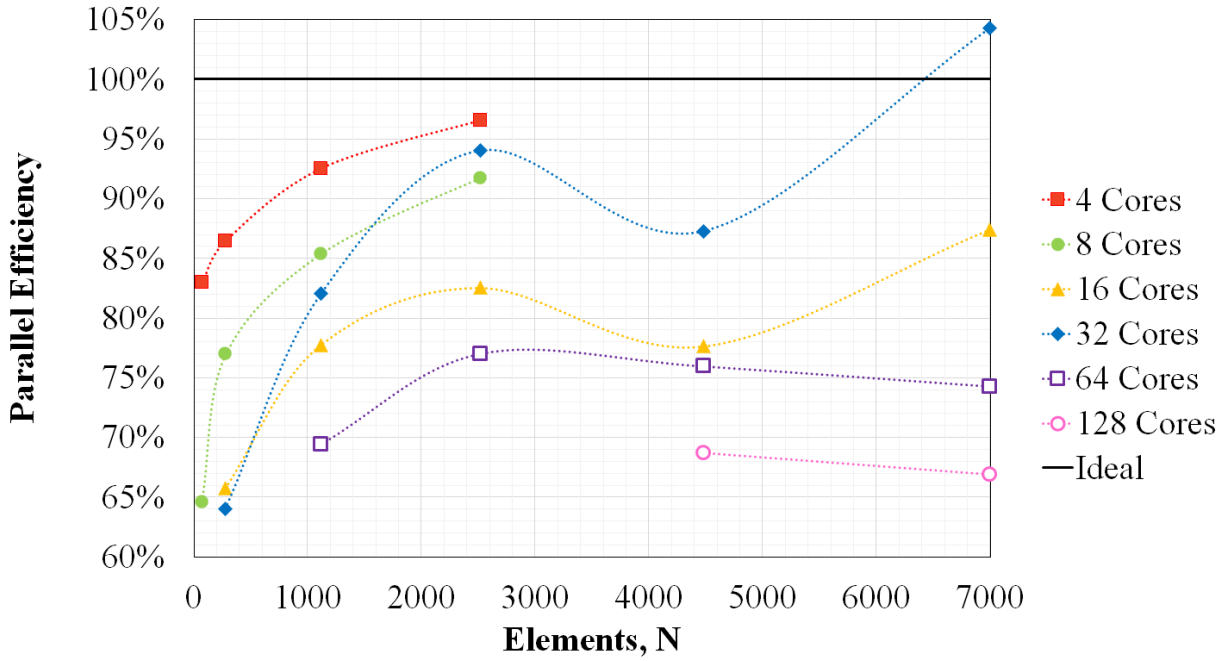

Fig. 37: Comparison of the parallel efficiency versus problem size resulting from increasing processing power for varying problem sizes.

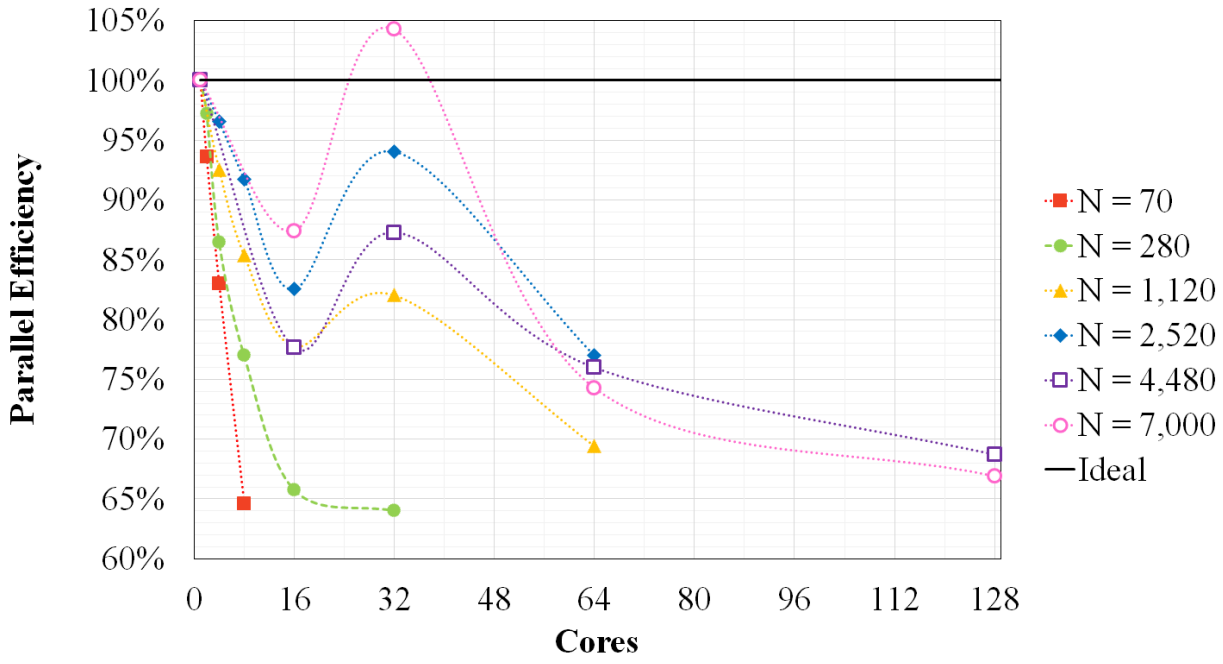

Fig. 38: Comparison of the parallel efficiency versus core count resulting from increasing processing power for varying problem sizes.

Given a problem size of $2,500$ elements, *e.g.*, the efficiency of four cores is 97% whereas eight cores is 92% and sixteen cores is 83%. Once fully-utilizing a single node, however, thirty-two cores outperforms that of eight and sixteen cores for all problem sizes larger than $1,000$ elements, *e.g.* given a problem size of $2,500$ elements, thirty-two cores has a parallel efficiency of 94%.

Figure 37 also demonstrates that when fully utilizing each compute node, the algorithm scales well with fewer CPUs given that the use of thirty-two cores is more efficient than sixty-four and sixty-four cores is more efficient than 128 for all problem sizes. These results are further demonstrated in Figure 38 where it is shown that, for all problem sizes greater than 280 elements, the use of sixteen cores is less efficient than thirty-two cores (due to the under-utilization of a single-node) and the use of thirty-two cores is more efficient than both sixty-four and 128 cores for all problem sizes (due to an increase in parallel overhead with increased parallelization). Therefore, by investigating the parallel efficiency and noting a significant decrease in efficiency as core counts increases, it is demonstrated that the algorithm performance suffers as the inter-nodal communication requirements increase for all problem sizes — the results of which agree with the strong scaling study.

CHAPTER 5

TIME-DOMAIN LINER IMPEDANCE BOUNDARY CONDITIONS

In Chapter 2, a time-domain boundary integral (30) with Burton-Miller reformulation (37) is derived from the linear convective wave equation with homogenous initial conditions. The solution predicts the acoustic pressure at an arbitrary observer point r' exterior to the scattering body using time-histories of pressure p and its derivatives on the surface. For lined bodies, the solution requires that the boundary condition $\partial p/\partial n$ is known.

This chapter introduces and derives suitable boundary conditions for pressure and its normal derivative on the surface. Boundary conditions are given for both impedance Z and admittance Y. Impedance and admittance are experimentally measured quantities; thus, the boundary conditions are dependent upon the specific type of acoustic liner installed on the surface of the scattering body. In this chapter, three acoustic liner models are introduced, and their applicable boundary conditions discussed including: the *Extended Helmholtz Resonator Model* [59], the *Three-Parameter Impedance Model* [29, 65], and the *Broadband Impedance Model* [62, 67, 68].

5.1 DERIVATION OF SUITABLE BOUNDARY CONDITIONS

Acoustic scattering of a sound field from a given noise source is predicted for objects in a stationary medium, *i.e.*, assuming a model with no mean flow $\boldsymbol{U}$. With no mean flow, the acoustic pressure in the frequency-domain $p(\boldsymbol{r_s}, \omega)$ is defined [65, 69, 87] as:

$$p(\boldsymbol{r_s}, \omega) = Z(\omega) v(\boldsymbol{r_s}, \omega) \tag{48}$$

where $v(\boldsymbol{r_s}, \omega) = \boldsymbol{v} \cdot \boldsymbol{n}$ is the volumetric flow of the acoustic wave, $\boldsymbol{v}$ is the acoustic velocity vector, $\boldsymbol{n}$ is the inward normal vector on the scattering body, and $Z(\omega)$ is the surface impedance. In the frequency-domain, v is represented [14] by:

$$v(\boldsymbol{r_s}, \omega) = \frac{1}{\rho_0 (i\omega)} \frac{\partial p}{\partial n}(\boldsymbol{r_s}, \omega) \tag{49}$$

where $\partial p/\partial n(\boldsymbol{r_s}, \omega)$ is the normal derivative of acoustic pressure, ρ_0 is the average fluid density, and i is the imaginary unit ($i^2 = -1$). Given (48) and (49), the acoustic pressure is related to frequency-domain impedance by:

$$\rho_0(i\omega)p(\boldsymbol{r_s}, \omega) = \frac{\partial p}{\partial n}(\boldsymbol{r_s}, \omega)Z(\omega).$$

It is assumed that the scattering surface S is decomposed into rigid and soft surfaces, S_0 and S_l, respectively, such that $S = S_0 \cup S_l$. On rigid surfaces, a Zero Energy Flux boundary condition [1] is imposed. On soft surfaces, $\partial p/\partial n$ is a non-zero term herein denoted by P_n. On S, the boundary condition is therefore given to be:

$$\frac{\partial p}{\partial n}(\boldsymbol{r_s}, \omega) = \left\{ \begin{array}{ll} 0, & \boldsymbol{r}_s \in S_0 \\ P_n(\boldsymbol{r_s}, \omega), & \boldsymbol{r}_s \in S_l \end{array} \right\}. \tag{50}$$

For time-domain analysis, (50) must be transformed from the frequency-domain to the time-domain using Fourier transforms. Define the Fourier transform $F(\omega)$ as:

$$F(\omega) = \frac{1}{2\pi}\int_{-\infty}^{\infty} f(t)e^{-i\omega t}dt \tag{51}$$

and inverse Fourier transform $f(t)$ as:

$$f(t) = \int_{-\infty}^{\infty} F(\omega)e^{i\omega t}d\omega.$$

With this definition, the inverse Fourier transform of $(i\omega)^n F(\omega)$ is equal to $d^n f(t)/dt^n$ and the inverse Fourier transform of $d^n F(\omega)/d\omega^n$ is equal to $(-it)^n f(t)$. Similarly, if $F(\omega)$ were defined to be

$$F(\omega) = \frac{1}{2\pi}\int_{-\infty}^{\infty} f(t)e^{i\omega t}dt, \tag{52}$$

the inverse Fourier transform of $(-i\omega)^n F(\omega)$ is equal to $d^n f(t)/dt^n$ and the inverse Fourier transform of $d^n F(\omega)/d\omega^n$ is equal to $(it)^n f(t)$. Moreover, given a Fourier transform of the form $H(\omega) = F(\omega)G(\omega)$, the Convolution Property [73] states that

$$h(t) = g(t) \star f(t) = \frac{1}{2\pi}\int_{-\infty}^{\infty} g(\tau)f(t-\tau)d\tau$$

where $g(t) \star f(t)$ is equivalent to $f(t) \star g(t)$. Taking the inverse Fourier transform of (50) using (51) and applying the Convolution Property gives:

$$\begin{aligned} F^{-1}\left[(i\omega)\rho_0 p(\boldsymbol{r_s}, \omega)\right] &= F^{-1}\left[P_n(\boldsymbol{r_s}, \omega)Z(\omega)\right] \\ \rho_0\frac{\partial p}{\partial t}(\boldsymbol{r_s}, t) &= \frac{1}{2\pi}\int_{-\infty}^{\infty} P_n(\boldsymbol{r_s}, \tau)z(t-\tau)d\tau \end{aligned}$$

where, by causality, $z(t-\tau)=0$ for all $t-\tau<0$. That is,

$$\rho_0\frac{\partial p}{\partial t}(\boldsymbol{r_s},t)=\frac{1}{2\pi}\int_{-\infty}^{t}P_n(\boldsymbol{r_s},\tau)z(t-\tau)d\tau. \tag{53}$$

Equation (53) satisfies the use of retarded time values which account for the effects of the surface experiencing acoustic signals at different times based on the motion of the body and location of the observer. Causality expresses the notion that if a source is turned on at any time in the past, then the pressure should be zero for all times prior [58, 69]. Equation (53) solves for the time derivative of acoustic pressure, $\partial p/\partial t$, using its normal derivative on soft surfaces, P_n, and the time-domain impedance, z, thus giving a suitable time-domain impedance boundary condition provided that impedance on the surface is known.

A time-domain admittance boundary condition is also suitable for predicting the acoustic pressure exterior to the scattering body. In the frequency-domain, the admittance $Y(\omega)$ is defined as:

$$Y(\omega)=\frac{1}{Z(\omega)} \tag{54}$$

such that

$$\frac{1}{\rho_0}\frac{\partial p}{\partial n}(\boldsymbol{r_s},\omega)=p(\boldsymbol{r_s},\omega)(i\omega)Y(\omega). \tag{55}$$

Equation (55) relates the normal derivative of acoustic pressure to the frequency-domain admittance. Taking the inverse Fourier transform of (55) using (51) and applying the Convolution Property gives:

$$F^{-1}\left[\frac{1}{\rho_0}P_n(\boldsymbol{r_s},\omega)\right]=F^{-1}\left[p(\boldsymbol{r_s},\omega)(i\omega)Y(\omega)\right]$$
$$\frac{1}{\rho_0}P_n(\boldsymbol{r_s},t)=\frac{1}{2\pi}\int_{-\infty}^{\infty}p(\boldsymbol{r_s},\tau)\frac{dy}{dt}(t-\tau)d\tau$$

where, by causality, $y(t-\tau)=0$ for all $t-\tau<0$. That is,

$$\frac{1}{\rho_0}P_n(\boldsymbol{r_s},t)=\frac{1}{2\pi}\int_{-\infty}^{t}p(\boldsymbol{r_s},\tau)\frac{dy}{dt}(t-\tau)d\tau. \tag{56}$$

Equation (56) solves for the normal derivative of acoustic pressure on soft surfaces, P_n, using the time-domain pressure, p, and the time derivative of admittance, dy/dt, thus giving a suitable time-domain admittance boundary condition provided that admittance on the surface is known and is differentiable. Using the convolution identity, $g(t)\star f(t)\equiv f(t)\star g(t)$, (56) can equivalently be written as:

$$\frac{1}{\rho_0}P_n(\boldsymbol{r_s},t)=\frac{1}{2\pi}\int_{-\infty}^{t}\frac{\partial p}{\partial t}(\boldsymbol{r_s},\tau)y(t-\tau)d\tau$$

which solves for the normal derivative of acoustic pressure on soft surfaces, P_n, using the time derivative of pressure, $\partial p/\partial t$, and the time-domain admittance, y.

The impedance (53) and admittance (56) boundary conditions are discretized by dividing the surface S into a set of N_e boundary elements $\{E_j, j = 1, \ldots, N_e\}$ where the collocation point $\boldsymbol{r}_j$ is located at the centroid of E_j. The time-domain is divided into N_t uniform time steps where $t_k = k\Delta t$. Series solutions of (53) and (56) are obtained by approximating terms involving $p(\boldsymbol{r}_s, t)$ and $\partial p/\partial n(\boldsymbol{r}_s, t)$ using surface element basis functions $\phi_j(\boldsymbol{r}_s)$ and temporal basis functions $\psi_k(t)$ defined by (42) and (43), respectively.

By evaluating the series solutions at collocation points $\boldsymbol{r}_j$ on elements $E_j, j = 1, \ldots, N_e$ and at time step t_n using basis functions (42) and (43), (53) and (56) are cast into the following system of equations:

$$\boldsymbol{D_0 u^n} + \boldsymbol{E_0 v^n} = -\boldsymbol{D_1 u^{n-1}} - \boldsymbol{E_1 v^{n-1}} - \cdots - \boldsymbol{D_K u^{n-K}} - \boldsymbol{E_K v^{n-K}} \tag{57}$$

where the matrices $\boldsymbol{D}$ and $\boldsymbol{E}$ are specific to the acoustic liner selected for modeling $Z(\omega)$ and $Y(\omega)$. Their non-zero entries are discussed in Section 5.2.

In (57), $\boldsymbol{u}^k$ and $\boldsymbol{v}^k$ denote the vector that contains all unknowns $\left\{u_j^k,\, j = 1, ..., N_e\right\}$ and $\left\{v_j^k,\, j = 1, ..., N_e\right\}$, respectively, at time level t_k. Equation (57) is a March-On-in-Time scheme which, when coupled with (45) and solved iteratively, provides solutions for $\boldsymbol{u}^n$ and $\boldsymbol{v}^n$ on rigid and soft surfaces, respectively. The coupled system can be expressed as:

$$\begin{aligned}\begin{bmatrix} \boldsymbol{B_0} & \boldsymbol{C_0} \\ \boldsymbol{D_0} & \boldsymbol{E_0} \end{bmatrix} \begin{bmatrix} \boldsymbol{u^n} \\ \boldsymbol{v^n} \end{bmatrix} = \begin{bmatrix} \boldsymbol{q^n} \\ \boldsymbol{0} \end{bmatrix} - \begin{bmatrix} \boldsymbol{B_1} & \boldsymbol{C_1} \\ \boldsymbol{D_1} & \boldsymbol{E_1} \end{bmatrix} \begin{bmatrix} \boldsymbol{u^{n-1}} \\ \boldsymbol{v^{n-1}} \end{bmatrix} - \cdots - \\ - \begin{bmatrix} \boldsymbol{B_K} & \boldsymbol{C_K} \\ \boldsymbol{D_K} & \boldsymbol{E_K} \end{bmatrix} \begin{bmatrix} \boldsymbol{u^{n-K}} \\ \boldsymbol{v^{n-K}} \end{bmatrix} - \cdots - \begin{bmatrix} \boldsymbol{B_J} & \boldsymbol{0} \\ \boldsymbol{0} & \boldsymbol{0} \end{bmatrix} \begin{bmatrix} \boldsymbol{u^{n-J}} \\ \boldsymbol{v^{n-J}} \end{bmatrix}\end{aligned} \tag{58}$$

where matrices $\boldsymbol{B}, \boldsymbol{C}, \boldsymbol{D}$ and $\boldsymbol{E}$ each have size $N \times N$ for a scattering body with N total surface elements.

For locally reacting liners, the liner boundary condition is given pointwise. It follows that, assuming the liner impedance (or admittance) is the same on all soft boundaries, $\boldsymbol{D}$ and $\boldsymbol{E}$ are diagonal coefficient matrices of the form $\boldsymbol{D_k} = d_k \boldsymbol{I}$ and $\boldsymbol{E_k} = e_k \boldsymbol{I}$ where $k = 0, 1, \ldots, K$ for order K Lagrange functions, $\boldsymbol{I}$ is the identity matrix, and d_k, e_k are the coefficients for the time-domain liner boundary condition that is the same for all liner elements. The derivations for d_k and e_k are specific to the type of acoustic liner modeled and are discussed in Section 5.2.

5.2 ACOUSTIC LINER MODELS

Both impedance and admittance boundary conditions are researched in literature, though impedance is most frequently used. Impedance is a complex quantity, generally expressed in the frequency-domain as $Z(\omega) = Z_R + iZ_I$. The real part of impedance, Z_R, is the specific acoustic resistance and the imaginary part of impedance, Z_I, is the specific acoustic reactance [69], quantities which account for the effect a soft body has on the damping and phase shift of an acoustic wave. Resistance and reactance values are educed from measured values. Resistance is a positive value and reactance can be either positive or negative [65]. Moreover, acoustic resonance occurs when the reactance is zero, *i.e.*, when $Z(\omega)$ has real parts only [87]. Admittance is also a complex quantity, generally expressed in the frequency-domain as $Y(\omega) = Y_R + iY_I$ for $Y(\omega) = 1/Z(\omega)$ where

$$Y_R = \frac{Z_R}{Z_R^2 + Z_I^2} \text{ and } Y_I = \frac{-Z_I}{Z_R^2 + Z_I^2}. \tag{59}$$

The acoustic impedance is the ratio of acoustic pressure to the volumetric flow of the acoustic wave and therefore, by (54), the acoustic admittance is the ratio of the volumetric flow of the acoustic wave to its pressure. With constant flow, admittance will tend towards infinity as pressure tends towards zero and with constant pressure, impedance will tend towards infinity as flow tends towards zero. Both quantities provide usefulness for studying suitable boundary conditions for the stable Burton-Miller reformulation (37) of the time-domain boundary integral (30), and both are studied in this work. Given that impedance and admittance are educed from measured values, the applied boundary condition is dependent not only on the frequency but also on the specific type of acoustic liner assumed to be installed on the scattering surface.

In this chapter, three different acoustic liner models are introduced, and their applicable boundary conditions discussed. Further, the boundary conditions are discretized and evaluated at collocation points $\boldsymbol{r}_j, j = 1, \ldots, N_e$ and time step t_n using basis functions (42) and (43) to allow for coupling with the discretized Burton-Miller reformulation (45). The liner models studied are the *Extended Helmholtz Resonator Model* [59], the *Three-Parameter Impedance Model* [29, 65], and the *Broadband Impedance Model* [62, 67, 68]. In the *Extended Helmholtz Resonator* and *Three-Parameter* models, both impedance and admittance boundary conditions are considered for analysis. In these models, impedance and admittance are specified at a single frequency. In the *Broadband Impedance Model*, only an impedance boundary condition is considered for analysis. In this model, multiple frequencies are investigated simultaneously.

5.3 EXTENDED HELMHOLTZ RESONATOR MODEL

In the *Extended Helmholtz Resonator Model* [59], the frequency-domain surface impedance is defined to be:

$$Z(\omega) = F_R + (i\omega)m - iF_\beta \cot\left(\frac{\omega\nu\Delta t}{2} - i\frac{\epsilon}{2}\right) \tag{60}$$

where, for an acoustic liner represented by a wall consisting of an array of Helmholtz resonators,

F_R is the face-sheet resistance

ωm is the face-sheet mass reactance

$-\cot\left(\frac{\omega\nu\Delta t}{2} - i\frac{\epsilon}{2}\right)$ is the cavity reactance

F_β is a parameter used for varying the cavity reactance

Δt is the time step

ϵ is the damping in the cavity's fluid, and

$\nu\Delta t = 2L/c$ is a multiple of the time step and is proportional to two times the cavity depth L divided by the speed of sound c

The poles of the cotangent term are located at

$$\omega = \frac{2n\pi + i\epsilon}{\nu\Delta t}, n \in \mathbb{Z}.$$

The model is causal [59] and thus for $\mathrm{Im}(\omega) < \dfrac{\epsilon}{\nu\Delta t}$, (60) becomes:

$$Z(\omega) = F_R + (i\omega)m + F_\beta + 2F_\beta \sum_{N=1}^{\infty} e^{-i\omega N\nu\Delta t - \epsilon N} \tag{61}$$

where $F_R, F_\beta, \epsilon > 0$. Equation (61) results by simplifying (60) using the exponential identity of cotangent:

$$\begin{aligned} -i\cot\left(\frac{\omega\nu\Delta t}{2} - i\frac{\epsilon}{2}\right) &= \frac{e^{i\left(\frac{\omega\nu\Delta t}{2} - i\frac{\epsilon}{2}\right)} + e^{-i\left(\frac{\omega\nu\Delta t}{2} - i\frac{\epsilon}{2}\right)}}{e^{i\left(\frac{\omega\nu\Delta t}{2} - i\frac{\epsilon}{2}\right)} - e^{-i\left(\frac{\omega\nu\Delta t}{2} - i\frac{\epsilon}{2}\right)}} = \frac{1 + e^{-(i\omega\nu\Delta t + \epsilon)}}{1 - e^{-(i\omega\nu\Delta t + \epsilon)}} \\ &= 1 + 2\frac{e^{-(i\omega\nu\Delta t + \epsilon)}}{1 - e^{-(i\omega\nu\Delta t + \epsilon)}} = 1 + 2\sum_{N=1}^{\infty} e^{-i\omega N\nu\Delta t - \epsilon N}. \end{aligned}$$

Figure 39 illustrates an acoustic liner represented by a wall consisting of an array of Helmholtz resonators [59].

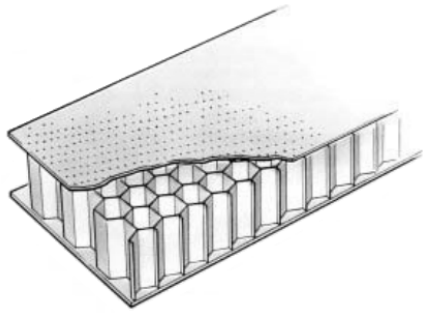

Fig. 39: Acoustic liner diagram consisting of an array of Helmholtz resonators.

Using Euler's formula ($e^{i\theta} = \cos\theta + i\sin\theta$), the even identity of cosine, and the odd identity of sine, (61) can be further simplified as follows:

$$\begin{aligned}
Z(\omega) &= F_R + (i\omega)m + F_\beta + 2F_\beta \sum_{N=1}^{\infty} e^{-i\omega N\nu\Delta t - \epsilon N} \\
&= F_R + (i\omega)m + F_\beta + 2F_\beta \sum_{N=1}^{\infty} e^{-\epsilon N} e^{i(-\omega N\nu\Delta t)} \\
&= F_R + (i\omega)m + F_\beta + 2F_\beta \sum_{N=1}^{\infty} e^{-\epsilon N} \left[\cos(\omega N\nu\Delta t) - i\sin(\omega N\nu\Delta t)\right] \\
&= F_R + F_\beta + 2F_\beta \sum_{N=1}^{\infty} e^{-\epsilon N} \cos(\omega N\nu\Delta t) + (i\omega)m - 2iF_\beta \sum_{N=1}^{\infty} e^{-\epsilon N} \sin(\omega N\nu\Delta t).
\end{aligned}$$

Hence,

$$\mathrm{Re}(Z) = F_R + F_\beta + 2F_\beta \sum_{N=1}^{\infty} e^{-\epsilon N} \cos(\omega N\nu\Delta t) \tag{62}$$

and

$$\mathrm{Im}(Z) = \omega m - 2F_\beta \sum_{N=1}^{\infty} e^{-\epsilon N} \sin(\omega N\nu\Delta t). \tag{63}$$

From the exponential identity of cosine, the real part of impedance (62) is written as follows:

$$\mathrm{Re}(Z) = F_R + F_\beta + 2F_\beta \sum_{N=1}^{\infty} e^{-\epsilon N} \cos(\omega N\nu\Delta t) = F_R + F_\beta \frac{\sinh(\epsilon)}{\cosh(\epsilon) - \cos(\omega\nu\Delta t)}, \tag{64}$$

which indicates that in addition to being causal, the *Extended Helmholtz Resonator* model is also passive [59]:

$$\mathrm{Re}(Z) = F_R + F_\beta \frac{\sinh\epsilon}{\cosh\epsilon - \cos(\omega\nu\Delta t)} > 0$$

because $\sinh\epsilon, \cosh\epsilon > 1$ for all $\epsilon > 1$, $|\cos(\omega\nu\Delta t)| \leq 1$, and thus $\cosh(\epsilon) - \cos(\omega\nu\Delta t) > 0$. Furthermore, (64) results from using the exponential identity of cosine and the simplification:

$$\begin{aligned}
2F_\beta \sum_{N=1}^{\infty} e^{-\epsilon N} \cos(\omega N\nu\Delta t) &= F_\beta \sum_{N=1}^{\infty} e^{-\epsilon N} \left[e^{i(\omega N\nu\Delta t)} + e^{-i(\omega N\nu\Delta t)}\right] \\
&= F_\beta \left[\frac{e^{-(\epsilon - i\omega\nu\Delta t)}}{1 - e^{-(\epsilon - i\omega\nu\Delta t)}} + \frac{e^{-(\epsilon + i\omega\nu\Delta t)}}{1 - e^{-(\epsilon + i\omega\nu\Delta t)}}\right] \\
&= F_\beta \left[\frac{e^{i\omega\nu\Delta t} + e^{-i\omega\nu\Delta t} - 2e^{-\epsilon}}{e^{\epsilon} - e^{i\omega\nu\Delta t} - e^{-i\omega\nu\Delta t} + e^{-\epsilon}}\right] \\
&= F_\beta \left[\frac{\left(e^{i\omega\nu\Delta t} + e^{-i\omega\nu\Delta t}\right) - (e^{\epsilon} + e^{-\epsilon}) + (e^{\epsilon} - e^{-\epsilon})}{(e^{\epsilon} + e^{-\epsilon}) - (e^{i\omega\nu\Delta t} + e^{-i\omega\nu\Delta t})}\right] \\
&= F_\beta \left[\frac{\cos(\omega\nu\Delta t) - \cosh\epsilon + \sinh\epsilon}{\cosh\epsilon - \cos(\omega\nu\Delta t)}\right] \\
&= -F_\beta + F_\beta \frac{\sinh\epsilon}{\cosh\epsilon - \cos(\omega\nu\Delta t)}.
\end{aligned}$$

Similarly, from the exponential identity of sine, the imaginary part of impedance (63) is written as follows:

$$\mathrm{Im}(Z) = \omega m - 2F_\beta \sum_{N=1}^{\infty} e^{-\epsilon N} \sin(\omega N\nu\Delta t) = \omega m - F_\beta \frac{\sin(\omega\nu\Delta t)}{\cosh\epsilon - \cos(\omega\nu\Delta t)}. \tag{65}$$

Taking the inverse Fourier transform of (61) using (51) leads to a time-domain representation of surface impedance:

$$z(t) = 2\pi \left[F_R\delta(t) + m\delta'(t) + F_\beta\delta(t) + 2F_\beta \sum_{N=1}^{\infty} e^{-\epsilon N}\delta(t - N\nu\Delta t)\right]. \tag{66}$$

Substituting (66) into (53) and using the identities of the Dirac delta function yields an impedance boundary condition for soft surfaces:

$$\begin{aligned}
\rho_0 \frac{\partial p}{\partial t}(\boldsymbol{r_s}, t) &= \frac{1}{2\pi} \int_{-\infty}^{t} P_n(\boldsymbol{r_s}, \tau) z(t - \tau) d\tau \\
&= \int_{-\infty}^{t} P_n(\boldsymbol{r_s}, \tau) \left[F_R\delta(t - \tau) + m\delta'(t - \tau) + F_\beta\delta(t - \tau)\right] d\tau \\
&+ \int_{-\infty}^{t} P_n(\boldsymbol{r_s}, \tau) \left[2F_\beta \sum_{N=1}^{\infty} e^{-\epsilon N}\delta((t - \tau) - N\nu\Delta(t - \tau))\right] d\tau \\
&= F_R P_n(\boldsymbol{r_s}, t) + m\frac{\partial P_n}{\partial t}(\boldsymbol{r_s}, t) + F_\beta P_n(\boldsymbol{r_s}, t) + 2F_\beta \sum_{N=1}^{\infty} e^{-\epsilon N} P_n(\boldsymbol{r_s}, t - N\nu\Delta t) \\
&= (F_R + F_\beta) P_n(\boldsymbol{r}_s, t) + m\frac{\partial P_n}{\partial t}(\boldsymbol{r}_s, t) + 2F_\beta \sum_{N=1}^{\infty} e^{-\epsilon N} P_n(\boldsymbol{r}_s, t - N\nu\Delta t).
\end{aligned} \tag{67}$$

In this model, the coefficients F_R and F_β are specified at a single frequency $\omega = \omega_0 > 0$. Provided impedance is of the form $Z(\omega) = Z_R + iZ_I$, F_R and F_β are determined by (64) and (65) to be:

$$F_R = Z_R + Z_I \frac{\sinh(\epsilon)}{\sin(\omega_0 \nu \Delta t)} \text{ and } F_\beta = -Z_I \frac{\cosh(\epsilon) - \cos(\omega_0 \nu \Delta t)}{\sin(\omega_0 \nu \Delta t)} \tag{68}$$

for arbitrary Z_R and Z_I constants measured experimentally.

Evaluating the impedance boundary condition (67) at collocation points $\boldsymbol{r}_j, j = 1, \ldots, N_e$ and time step t_n using basis functions (42) and (43), yields the following discretized impedance boundary condition:

$$\begin{aligned} \rho_0 \sum_{k=0}^{N_t} \sum_{j=1}^{N_e} u_j^k \delta_{ij} \psi_k'(t_n) = \\ \sum_{k=0}^{N_t} \sum_{j=1}^{N_e} v_j^k \delta_{ij} \left[(F_R + F_\beta)\, \psi_k(t_n) + m\psi_k'(t_n) + 2F_\beta \sum_{N=1}^{\infty} e^{-\epsilon N} \psi_k(t_n - N\nu\Delta t) \right]. \end{aligned} \tag{69}$$

Casting (69) into matrix form (57), the non-zero entries for $\boldsymbol{D}$ and $\boldsymbol{E}$ are found to be, respectively:

$$\begin{aligned} \{\boldsymbol{D_k}\}_{ij} &= \delta_{ij} \left[\rho_0 \psi_{n-k}'(t_n) \right] \text{ and} \\ \{\boldsymbol{E_k}\}_{ij} &= \delta_{ij} \left[(F_R + F_\beta)\, \psi_{n-k}(t_n) + m\psi_{n-k}'(t_n) + 2F_\beta \sum_{N=1}^{\infty} e^{-\epsilon N} \psi_{n-k}(t_n - N\nu\Delta t) \right] \end{aligned} \tag{70}$$

where δ_{ij} is a Kronecker delta function and a prime denotes a derivative with respect to time. The matrices are diagonally dominant and of the form $\boldsymbol{D_k} = d_k \boldsymbol{I}$ and $\boldsymbol{E_k} = e_k \boldsymbol{I}$. The coefficients d_k and e_k simplify using (44) and (70) to:

$$d_k = \rho_0 \begin{Bmatrix} \frac{11}{6\Delta t}, & k = 0 \\ \frac{-3}{\Delta t}, & k = 1 \\ \frac{3}{2\Delta t}, & k = 2 \\ \frac{-1}{3\Delta t}, & k = 3 \\ 0, & \text{other} \end{Bmatrix} \text{ and}$$

$$e_k = (F_R + F_\beta) \begin{Bmatrix} 1, & k = 0 \\ 0, & k \neq 0 \end{Bmatrix} + m \begin{Bmatrix} \frac{11}{6\Delta t}, & k = 0 \\ \frac{-3}{\Delta t}, & k = 1 \\ \frac{3}{2\Delta t}, & k = 2 \\ \frac{-1}{3\Delta t}, & k = 3 \\ 0, & \text{other} \end{Bmatrix} + 2F_\beta \sum_{N=1}^{\infty} e^{-\epsilon N} \begin{Bmatrix} 1, & k - N\nu = 0 \\ 0, & k - N\nu \neq 0 \end{Bmatrix}.$$

Similarly, an admittance boundary condition is obtained by defining the frequency-domain surface admittance to be:

$$Y(\omega) = \overline{F_R} + (i\omega)m + \overline{F_\beta} + 2\overline{F_\beta}\sum_{N=1}^{\infty} e^{-i\omega N\nu\Delta t - \epsilon N} \tag{71}$$

where $\overline{F_R}, \overline{F_\beta}, \epsilon > 0$. For a measured admittance value $Y(\omega) = Y_R + iY_I$, $\overline{F_R}$ and $\overline{F_\beta}$ are determined by (59) and (68) to be:

$$\overline{F_R} = Y_R + Y_I\frac{\sinh(\epsilon)}{\sin(\omega_0\nu\Delta t)} \text{ and } \overline{F_\beta} = -Y_I\frac{\cosh(\epsilon) - \cos(\omega_0\nu\Delta t)}{\sin(\omega_0\nu\Delta t)}.$$

Taking the inverse Fourier transform of (71) using (51) leads to a time-domain representation of surface admittance:

$$y(t) = 2\pi\left[\overline{F_R}\delta(t) + m\delta'(t) + \overline{F_\beta}\delta(t) + 2\overline{F_\beta}\sum_{N=1}^{\infty} e^{-\epsilon N}\delta(t - N\nu\Delta t)\right]. \tag{72}$$

Further substituting (72) into (56), taking a derivative in time, and using the identities of the Dirac delta function yields an admittance boundary condition for soft surfaces:

$$\frac{1}{\rho_0}\frac{\partial p}{\partial n}(\boldsymbol{r_s}, t) = \left(\overline{F_R} + \overline{F_\beta}\right)\frac{\partial p}{\partial t}(\boldsymbol{r_s}, t) - m\frac{\partial^2 p}{\partial t^2}(\boldsymbol{r_s}, t) + 2\overline{F_\beta}\sum_{N=1}^{\infty} e^{-\epsilon N}\frac{\partial p}{\partial t}(\boldsymbol{r_s}, t - N\nu\Delta t). \tag{73}$$

Evaluating the impedance boundary condition (73) at collocation points $\boldsymbol{r}_j, j = 1, \ldots, N_e$ and time step t_n using basis functions (42) and (43), yields the following discretized admittance boundary condition:

$$\begin{aligned}\frac{1}{\rho_0}\sum_{k=0}^{N_t}\sum_{j=1}^{N_e} v_j^k\delta_{ij}\psi_k(t_n) = \\ \sum_{k=0}^{N_t}\sum_{j=1}^{N_e} u_j^k\delta_{ij}\left[\left(\overline{F_R} + \overline{F_\beta}\right)\psi_k'(t_n) - m\psi_k''(t_n) + 2\overline{F_\beta}\sum_{N=1}^{\infty} e^{-\epsilon N}\psi_k'(t_n - N\nu\Delta t)\right].\end{aligned} \tag{74}$$

Casting (74) into matrix form (57), the non-zero entries for $\boldsymbol{D}$ and $\boldsymbol{E}$ are found to be, respectively:

$$\begin{aligned}\{\boldsymbol{D_k}\}_{ij} &= \delta_{ij}\left[\left(\overline{F_R} + \overline{F_\beta}\right)\psi_{n-k}'(t_n) - m\psi_{n-k}''(t_n) + 2\overline{F_\beta}\sum_{N=1}^{\infty} e^{-\epsilon N}\psi_{n-k}'(t_n - N\nu\Delta t)\right] \\ \text{and } \{\boldsymbol{E_k}\}_{ij} &= \delta_{ij}\left[\frac{1}{\rho_0}\psi_{n-k}(t_n)\right].\end{aligned} \tag{75}$$

The matrices are diagonally dominant and of the form $\boldsymbol{D_k} = d_k\boldsymbol{I}$ and $\boldsymbol{E_k} = e_k\boldsymbol{I}$. The coefficients d_k and e_k simplify using (44) and (75) to:

$$d_k = \left(\overline{F_R} + \overline{F_\beta}\right)\begin{Bmatrix} \frac{11}{6\Delta t}, & k=0 \\ \frac{-3}{\Delta t}, & k=1 \\ \frac{3}{2\Delta t}, & k=2 \\ \frac{-1}{3\Delta t}, & k=3 \\ 0, & \text{other} \end{Bmatrix} - m\begin{Bmatrix} \frac{2}{\Delta t^2}, & k=0 \\ \frac{-5}{\Delta t^2}, & k=1 \\ \frac{4}{\Delta t^2}, & k=2 \\ \frac{-1}{\Delta t^2}, & k=3 \\ 0, & \text{other} \end{Bmatrix} + 2\overline{F_\beta}\sum_{N=1}^{\infty} e^{-\epsilon N}\begin{Bmatrix} \frac{11}{6\Delta t}, & k-N\nu=0 \\ \frac{-3}{\Delta t}, & k-N\nu=1 \\ \frac{3}{2\Delta t}, & k-N\nu=2 \\ \frac{-1}{3\Delta t}, & k-N\nu=3 \\ 0, & \text{other} \end{Bmatrix}$$

and $e_k = \dfrac{1}{\rho_0}\begin{Bmatrix} 1, & k=0 \\ 0, & k\neq 0 \end{Bmatrix}$.

5.4 THREE-PARAMETER IMPEDANCE MODEL

In the *Three-Parameter Impedance Model* [29,65], the frequency-domain surface impedance is defined to be:

$$Z(\omega) = R_0 + h_0(-i\omega) + \frac{A_0}{(-i\omega)}, \tag{76}$$

where $R_0, h_0, A_0 > 0$ are constants that fit an impedance value $Z(\omega) = Z_R + iZ_I$ at $\omega = \omega_0 > 0$. This model is simpler than the *Extended Helmholtz Resonator Model* and is both causal and passive. The acoustic resistance Z_R is equal to R_0 and the acoustic reactance Z_I is a function of both h_0 and A_0. Numerical values for R_0 are determined using a measured resistance. Numerical values for h_0 and A_0 are determined by choosing a positive constant for one and, using a measured acoustic reactance, subsequently solving for the other. Let c_0 be an arbitrary positive constant, *e.g.*,

- if $Z_I < 0$ then $R_0 = Z_R$, $A_0 = c_0$, and $h_0 = (A_0/\omega_0 - Z_I)/\omega_0$, and
- if $Z_I > 0$ then $R_0 = Z_R$, $h_0 = c_0$, and $A_0 = (Z_I + h_0\omega_0)\omega_0$.

Taking the inverse Fourier transform of (76) using (52) and substituting into (53) yields a time-domain impedance boundary condition for soft surfaces:

$$\rho_0\frac{\partial^2 p}{\partial t^2}(\boldsymbol{r}_s, t) = R_0\frac{\partial P_n}{\partial t}(\boldsymbol{r}_s, t) + h_0\frac{\partial^2 P_n}{\partial t^2}(\boldsymbol{r}_s, t) + A_0 P_n(\boldsymbol{r}_s, t). \tag{77}$$

Evaluating the impedance boundary condition (77) at collocation points $\boldsymbol{r}_j, j = 1, \ldots, N_e$ and time step t_n using basis functions (42) and (43), yields the following discretized impedance boundary condition:

$$\rho_0\sum_{k=0}^{N_t}\sum_{j=1}^{N_e} u_j^k\delta_{ij}\psi_k''(t_n) = \sum_{k=0}^{N_t}\sum_{j=1}^{N_e} v_j^k\delta_{ij}\left[R_0\psi_k'(t_n) + h_0\psi_k''(t_n) + A_0\psi_k(t_n)\right]. \tag{78}$$

Casting (78) into matrix form (57), the non-zero entries for $\boldsymbol{D}$ and $\boldsymbol{E}$ are found to be, respectively:

$$\{\boldsymbol{D_k}\}_{ij} = \delta_{ij}\rho_0\psi''_{n-k}(t_n) \text{ and } \{\boldsymbol{E_k}\}_{ij} = \delta_{ij}\left[R_0\psi'_{n-k}(t_n) + h_0\psi''_{n-k}(t_n) + A_0\psi_{n-k}(t_n)\right] \quad (79)$$

where δ_{ij} is a Kronecker delta function and a prime denotes a derivative with respect to time. The matrices are diagonally dominant and of the form $\boldsymbol{D_k} = d_k\boldsymbol{I}$ and $\boldsymbol{E_k} = e_k\boldsymbol{I}$. The coefficients d_k and e_k simplify using (44) and (79) to:

$$d_k = \rho_0 \begin{Bmatrix} \frac{2}{\Delta t^2}, & k=0 \\ \frac{-5}{\Delta t^2}, & k=1 \\ \frac{4}{\Delta t^2}, & k=2 \\ \frac{-1}{\Delta t^2}, & k=3 \\ 0, & \text{other} \end{Bmatrix} \text{ and } e_k = R_0 \begin{Bmatrix} \frac{11}{6\Delta t}, & k=0 \\ \frac{-3}{\Delta t}, & k=1 \\ \frac{3}{2\Delta t}, & k=2 \\ \frac{-1}{3\Delta t}, & k=3 \\ 0, & \text{other} \end{Bmatrix} + h_0 \begin{Bmatrix} \frac{2}{\Delta t^2}, & k=0 \\ \frac{-5}{\Delta t^2}, & k=1 \\ \frac{4}{\Delta t^2}, & k=2 \\ \frac{-1}{\Delta t^2}, & k=3 \\ 0, & \text{other} \end{Bmatrix} + A_0 \begin{Bmatrix} 1, & k=0 \\ 0, & k\neq 0 \end{Bmatrix}.$$

Similarly, an admittance boundary condition is obtained by defining the frequency-domain surface admittance to be:

$$Y(\omega) = \overline{R_0} + \overline{h_0}(-i\omega) + \frac{\overline{A_0}}{(-i\omega)}, \quad (80)$$

where $\overline{R_0}, \overline{h_0}, \overline{A_0} > 0$ are constants that fit an admittance value $Y(\omega) = Y_R + iY_I$ at $\omega = \omega_0 > 0$ where Y_R and Y_I are as defined in (59). Given an arbitrary positive constant c_0, *e.g.*,

- if $Y_I < 0$ then $\overline{R_0} = Y_R$, $\overline{A_0} = c_0$, and $\overline{h_0} = (\overline{A_0}/\omega_0 - Y_I)/\omega_0$, and
- if $Y_I > 0$ then $\overline{R_0} = Y_R$, $\overline{h_0} = c_0$, and $\overline{A_0} = (Y_I + \overline{h_0}\omega_0)\omega_0$.

Taking the inverse Fourier transform of (80) using (52) and substituting into (53) yields a time-domain admittance boundary condition for soft surfaces:

$$P_n(\boldsymbol{r}_s, t) = \rho_0\left[\overline{R_0}\frac{\partial p}{\partial t}(\boldsymbol{r}_s, t) + \overline{h_0}\frac{\partial^2 p}{\partial t^2}(\boldsymbol{r}_s, t) + \overline{A_0}p(\boldsymbol{r}_s, t)\right]. \quad (81)$$

Evaluating the impedance boundary condition (81) at collocation points $\boldsymbol{r}_j, j = 1, \ldots, N_e$ and time step t_n using basis functions (42) and (43), yields the following discretized admittance boundary condition:

$$\sum_{k=0}^{N_t}\sum_{j=1}^{N_e} v_j^k\delta_{ij}\psi_k(t_n) = \rho_0\sum_{k=0}^{N_t}\sum_{j=1}^{N_e} u_j^k\delta_{ij}\left[\overline{R_0}\psi'_k(t_n) + \overline{h_0}\psi''_k(t_n) + \overline{A_0}\psi_k(t_n)\right]. \quad (82)$$

Casting (82) into matrix form (57), the non-zero entries for $\boldsymbol{D}$ and $\boldsymbol{E}$ are found to be:

$$\{\boldsymbol{D_k}\}_{ij} = \delta_{ij}\rho_0\left[\overline{R_0}\psi'_{n-k}(t_n) + \overline{h_0}\psi''_{n-k}(t_n) + \overline{A_0}\psi_{n-k}(t_n)\right] \text{ and } \{\boldsymbol{E_k}\}_{ij} = \delta_{ij}\psi_k(t_n). \quad (83)$$

The matrices are diagonally dominant and of the form $\boldsymbol{D_k} = d_k\boldsymbol{I}$ and $\boldsymbol{E_k} = e_k\boldsymbol{I}$. The coefficients d_k and e_k simplify using (44) and (83) to:

$$d_k = \rho_0\overline{R_0}\begin{Bmatrix} \frac{11}{6\Delta t}, & k=0 \\ \frac{-3}{\Delta t}, & k=1 \\ \frac{3}{2\Delta t}, & k=2 \\ \frac{-1}{3\Delta t}, & k=3 \\ 0, & \text{other} \end{Bmatrix} + \rho_0\overline{h_0}\begin{Bmatrix} \frac{2}{\Delta t^2}, & k=0 \\ \frac{-5}{\Delta t^2}, & k=1 \\ \frac{4}{\Delta t^2}, & k=2 \\ \frac{-1}{\Delta t^2}, & k=3 \\ 0, & \text{other} \end{Bmatrix} + \rho_0\overline{A_0}\begin{Bmatrix} 1, & k=0 \\ 0, & k\neq 0 \end{Bmatrix} \text{ and } e_k = \begin{Bmatrix} 1, & k=0 \\ 0, & k\neq 0 \end{Bmatrix}.$$

5.5 BROADBAND IMPEDANCE MODEL

In the *Broadband Impedance Model* [62,67,68], the frequency-domain surface impedance is defined to be:

$$Z(\omega) = (-i\omega)h_0 + R_0 + \sum_{\ell=1}^{J_1}\frac{A_\ell}{\gamma_\ell - i\omega} + \frac{1}{2}\sum_{\ell=1}^{J_2}\left[\frac{B_\ell + iC_\ell}{\alpha_\ell + i\beta_\ell - i\omega} + \frac{B_\ell - iC_\ell}{\alpha_\ell - i\beta_\ell - i\omega}\right], \tag{84}$$

where causality, passivity, and stability lead to $h_0, R_0 > 0$, $\gamma_k > 0$ for all $\ell = 1,\ldots,J_1$, and $\alpha_k > 0$ for all $\ell = 1,\ldots,J_2$. Here, the impedance $Z(\omega)$ is non-dimensionalized by $\rho_0 c$ where ρ_0 is the average fluid density and c is the speed of sound. When $J_1 = 1, \gamma_1 = 0$ and $B_\ell, C_\ell = 0$ for all $\ell = 1,\ldots,J_2$, (84) reduces to the *Three-Parameter Model* (76). Rearranging (84) yields:

$$\begin{aligned} Z(\omega) &= (-i\omega)h_0 + R_0 + \sum_{\ell=1}^{J_1}\frac{A_\ell}{\gamma_\ell - i\omega} + \frac{1}{2}\sum_{\ell=1}^{J_2}\left[\frac{B_\ell(2\alpha_\ell - 2i\omega)}{(\alpha_\ell - i\omega)^2 + \beta_\ell^2} + \frac{iC_\ell(-2i\beta_\ell)}{(\alpha_\ell - i\omega)^2 + \beta_\ell^2}\right] \\ &= (-i\omega)h_0 + R_0 + \sum_{\ell=1}^{J_1}\frac{A_\ell}{\gamma_\ell - i\omega} + \sum_{\ell=1}^{J_2}\frac{B_\ell(\alpha_\ell - i\omega)}{(\alpha_\ell - i\omega)^2 + \beta_\ell^2} + \sum_{\ell=1}^{J_2}\frac{C_\ell\beta_\ell}{(\alpha_\ell - i\omega)^2 + \beta_\ell^2} \\ &= (-i\omega)h_0 + R_0 + \sum_{\ell=1}^{J_1}A_\ell\left[\frac{1}{\gamma_\ell - i\omega}\right] \\ &\qquad + \sum_{\ell=1}^{J_2}B_\ell\left[\frac{\alpha_\ell - i\omega}{(\alpha_\ell - i\omega)^2 + \beta_\ell^2}\right] + \sum_{\ell=1}^{J_2}C_\ell\left[\frac{\beta_\ell}{(\alpha_\ell - i\omega)^2 + \beta_\ell^2}\right]. \end{aligned} \tag{85}$$

Substituting (85) into (50) yields:

$$\begin{aligned} \rho_0(i\omega)p(\boldsymbol{r_s},\omega) &= (-i\omega)h_0P_n(\boldsymbol{r_s},\omega) + R_0P_n(\boldsymbol{r_s},\omega) + \sum_{\ell=1}^{J_1}A_\ell\left[\frac{1}{\gamma_\ell - i\omega}P_n(\boldsymbol{r_s},\omega)\right] \\ &\quad + \sum_{\ell=1}^{J_2}B_\ell\left[\frac{\alpha_\ell - i\omega}{(\alpha_\ell - i\omega)^2 + \beta_\ell^2}P_n(\boldsymbol{r_s},\omega)\right] + \sum_{\ell=1}^{J_2}C_\ell\left[\frac{\beta_\ell}{(\alpha_\ell - i\omega)^2 + \beta_\ell^2}P_n(\boldsymbol{r_s},\omega)\right]. \end{aligned} \tag{86}$$

To facilitate the conversion of (85) to the time-domain, the following frequency-domain terms are defined:

$$p_\ell^{(0)}(\boldsymbol{r}_s,\omega) = \frac{1}{\gamma_\ell - i\omega} P_n(\boldsymbol{r}_s,\omega) \text{ for all } \ell = 1,\ldots,J_1, \tag{87}$$

$$p_\ell^{(1)}(\boldsymbol{r}_s,\omega) = \frac{\alpha_\ell - i\omega}{(\alpha_\ell - i\omega)^2 + \beta_\ell^2} P_n(\boldsymbol{r_s},\omega) \text{ for all } \ell = 1,\ldots,J_2, \text{ and} \tag{88}$$

$$p_\ell^{(2)}(\boldsymbol{r}_s,\omega) = \frac{\beta_\ell}{(\alpha_\ell - i\omega)^2 + \beta_\ell^2} P_n(\boldsymbol{r_s},\omega) \text{ for all } \ell = 1,\ldots,J_2. \tag{89}$$

Substituting (87), (88), and (89) into (86) yields:

$$\begin{aligned}\rho_0(i\omega)p(\boldsymbol{r_s},\omega) = (-i\omega)h_0 P_n(\boldsymbol{r_s},\omega) + R_0 P_n(\boldsymbol{r_s},\omega) \\ + \sum_{\ell=1}^{J_1} A_\ell p_\ell^{(0)}(\boldsymbol{r}_s,\omega) + \sum_{\ell=1}^{J_2} B_\ell p_\ell^{(1)}(\boldsymbol{r}_s,\omega) + \sum_{\ell=1}^{J_2} C_\ell p_\ell^{(2)}(\boldsymbol{r}_s,\omega).\end{aligned} \tag{90}$$

Taking the inverse Fourier transform of (90) using (52) yields a time-domain impedance boundary condition for soft surfaces:

$$\begin{aligned}0 = \rho_0 \frac{\partial p}{\partial t}(\boldsymbol{r_s},t) + h_0 \frac{\partial P_n}{\partial t}(\boldsymbol{r_s},t) + R_0 P_n(\boldsymbol{r_s},t) \\ + \sum_{\ell=1}^{J_1} A_\ell p_\ell^{(0)}(\boldsymbol{r}_s,t) + \sum_{\ell=1}^{J_2} B_\ell p_\ell^{(1)}(\boldsymbol{r}_s,t) + \sum_{\ell=1}^{J_2} C_\ell p_\ell^{(2)}(\boldsymbol{r}_s,t).\end{aligned} \tag{91}$$

Moreover, taking the inverse Fourier transform of (87) using (51) yields the following time-domain partial-differential equation given by (92). For all $\ell = 1,\ldots,J_1$:

$$0 = P_n(\boldsymbol{r_s},t) - \frac{\partial p_\ell^{(0)}}{\partial t}(\boldsymbol{r_s},t) - \gamma_\ell p_\ell^{(0)}(\boldsymbol{r_s},t). \tag{92}$$

Then, adding $(\alpha_\ell - i\omega) \times p_\ell^{(1)}$ to $\beta_\ell \times p_\ell^{(2)}$ using (88) and (89) and taking the inverse Fourier transform using (51) yields a second time-domain partial-differential equation given by (93). For all $\ell = 1,\ldots,J_2$ yields:

$$0 = P_n(\boldsymbol{r_s},t) - \frac{\partial p_\ell^{(1)}}{\partial t}(\boldsymbol{r}_s,t) - \alpha_\ell p_\ell^{(1)}(\boldsymbol{r}_s,t) - \beta_\ell p_\ell^{(2)}(\boldsymbol{r}_s,t). \tag{93}$$

Finally, substituting (89) into (88) and taking the inverse Fourier transform using (51) yields a third time-domain partial-differential equation given by (93). For all $\ell = 1,\ldots,J_2$ yields:

$$0 = \beta_\ell p_\ell^{(1)}(\boldsymbol{r}_s,t) - \frac{\partial p_\ell^{(2)}}{\partial t}(\boldsymbol{r}_s,t) - \alpha_\ell p_\ell^{(2)}(\boldsymbol{r}_s,t). \tag{94}$$

The time-domain broadband model (91) and subsequent partial differential equations (92) through (94) are discretized by dividing the surface S into a set of N_e boundary

elements. Series solutions are obtained by approximating terms involving $p(\boldsymbol{r}_s, t)$ and $\partial p/\partial n(\boldsymbol{r}_s, t)$ using surface element basis functions $\phi_j(\boldsymbol{r}_s)$ and temporal basis functions $\psi_k(t)$ defined by (42) and (43), respectively, and by approximating terms involving $p_\ell^{(m)}(\boldsymbol{r}_s, t)$ by:

$$p_\ell^{(m)}(\boldsymbol{r}_s, t) = \sum_{k=0}^{N_t} \sum_{j=1}^{N_e} \left(p_\ell^{(m)}\right)_j^k \phi_j(\boldsymbol{r}_s)\psi_k(t), m = 0, 1, 2.$$

Evaluating the series solutions at collocation points $\boldsymbol{r}_j, j = 1, \ldots, N_e$ and time step t_n yields the following discretized impedance boundary condition:

$$\begin{aligned} 0 = &\sum_{k=0}^{N_t} \sum_{j=1}^{N_e} \delta_{ij} \left[u_j^k \rho_0 \psi_k'(t_n) + v_j^k \left(h_0 \psi_k'(t_n) + R_0 \psi_k(t_n)\right)\right] \\ &+ \sum_{k=0}^{N_t} \sum_{j=1}^{N_e} \delta_{ij} \left[\sum_{\ell=1}^{J_1} \left(p_\ell^{(0)}\right)_j^k A_\ell \psi_k(t_n) + \sum_{\ell=1}^{J_2} \left(p_\ell^{(1)}\right)_j^k B_\ell \psi_k(t_n) + \sum_{\ell=1}^{J_2} \left(p_\ell^{(2)}\right)_j^k C_\ell \psi_k(t_n)\right] \end{aligned} \tag{95}$$

and subsequent partial differential equations:

$$0 = \sum_{k=0}^{N_t} \sum_{j=1}^{N_e} \delta_{ij} \left[v_j^k \psi_k(t_n) - \sum_{\ell=1}^{J_1} \left(p_\ell^{(0)}\right)_j^k \left(\psi_k'(t_n) + \gamma_\ell \psi_k(t_n)\right)\right] \tag{96}$$

$$0 = \sum_{k=0}^{N_t} \sum_{j=1}^{N_e} \delta_{ij} \left[v_j^k \psi_k(t_n) - \sum_{\ell=1}^{J_2} \left(p_\ell^{(1)}\right)_j^k \left(\psi_k'(t_n) + \alpha_\ell \psi_k(t_n)\right) - \sum_{\ell=1}^{J_2} \left(p_\ell^{(2)}\right)_j^k \beta_\ell \psi_k(t_n)\right] \tag{97}$$

$$0 = \sum_{k=0}^{N_t} \sum_{j=1}^{N_e} \delta_{ij} \left[\sum_{\ell=1}^{J_2} \left(p_\ell^{(1)}\right)_j^k \beta_\ell \psi_k(t_n) - \sum_{\ell=1}^{J_2} \left(p_\ell^{(2)}\right)_j^k \left(\psi_k'(t_n) + \alpha_\ell \psi_k(t_n)\right)\right]. \tag{98}$$

Unlike with the *Extended Helmholtz Resonator* and *Three-Parameter* models where the discretized liner boundary condition is cast into a single equation (57) and coupled with the Burton-Miller reformulation (45), the *Broadband Impedance Model* has three additional equations that must be included in the coupled system. Thus, for the *Broadband* system, the following vectors are additionally defined:

$$\boldsymbol{P}_{(0)} = [\boldsymbol{p}_1^{(0)} \boldsymbol{p}_2^{(0)} \cdots \boldsymbol{p}_{J_1}^{(0)}]^T, \boldsymbol{P}_{(1)} = [\boldsymbol{p}_1^{(1)} \boldsymbol{p}_2^{(1)} \cdots \boldsymbol{p}_{J_1}^{(1)}]^T, \text{ and } \boldsymbol{P}_{(2)} = [\boldsymbol{p}_1^{(2)} \boldsymbol{p}_2^{(2)} \cdots \boldsymbol{p}_{J_1}^{(2)}]^T \tag{99}$$

where $\boldsymbol{p}_j^{(0)}, \boldsymbol{p}_j^{(1,2)}$ denote the vectors that contains the auxiliary variables from all points where the impedance boundary condition is applied. Using (99), the discretizations (95) through (98) are then written as the following system of equations with a finite number of K time steps:

$$\begin{aligned} &\boldsymbol{D_0 u^n} + \boldsymbol{E_0 v^n} + \boldsymbol{F_0} \boldsymbol{P}_{(0)}^n + \boldsymbol{G_0} \boldsymbol{P}_{(1)}^n + \boldsymbol{H_0} \boldsymbol{P}_{(2)}^n \\ &\quad = \boldsymbol{0} - \boldsymbol{D_1 u^{n-1}} - \boldsymbol{E_1 v^{n-1}} - \boldsymbol{F_1} \boldsymbol{P}_{(0)}^{n-1} - \boldsymbol{G_1} \boldsymbol{P}_{(1)}^{n-1} - \boldsymbol{H_1} \boldsymbol{P}_{(2)}^{n-1} - \cdots - \\ &\qquad - \boldsymbol{D_K u^{n-K}} - \boldsymbol{E_K v^{n-K}} - \boldsymbol{F_K} \boldsymbol{P}_{(0)}^{n-K} - \boldsymbol{G_K} \boldsymbol{P}_{(1)}^{n-K} - \boldsymbol{H_K} \boldsymbol{P}_{(2)}^{n-K} \end{aligned} \tag{100}$$

$$\boldsymbol{\mathcal{J}_0 v^n} + \boldsymbol{\mathcal{K}_0 P}^n_{(0)} = \mathbf{0} - \boldsymbol{\mathcal{J}_1 v^{n-1}} - \boldsymbol{\mathcal{K}_1 P}^{n-1}_{(0)} - \cdots - \boldsymbol{\mathcal{J}_K v^{n-K}} - \boldsymbol{\mathcal{K}_K P}^{n-K}_{(0)} \tag{101}$$

$$\begin{aligned}\boldsymbol{\mathcal{L}_0 v^n} + \boldsymbol{\mathcal{M}_0 P}^n_{(1)} + \boldsymbol{\mathcal{N}_0 P}^n_{(2)} = \mathbf{0} &- \boldsymbol{\mathcal{L}_1 v^{n-1}} - \boldsymbol{\mathcal{M}_1 P}^{n-1}_{(1)} - \boldsymbol{\mathcal{N}_1 P}^{n-1}_{(2)} - \cdots - \\ &- \boldsymbol{\mathcal{L}_K v^{n-K}} - \boldsymbol{\mathcal{M}_K P}^{n-K}_{(1)} - \boldsymbol{\mathcal{N}_K P}^{n-K}_{(2)}\end{aligned} \tag{102}$$

$$\boldsymbol{\mathcal{P}_0 P}^n_{(1)} + \boldsymbol{\mathcal{Q}_0 P}^n_{(2)} = \mathbf{0} - \boldsymbol{\mathcal{P}_1 P}^{n-1}_{(1)} - \boldsymbol{\mathcal{Q}_1 P}^{n-1}_{(2)} - \cdots - \boldsymbol{\mathcal{P}_K P}^{n-K}_{(1)} - \boldsymbol{\mathcal{Q}_K P}^{n-K}_{(2)} \tag{103}$$

where, like with the *Extended Helmholtz Resonator* and *Three-Parameter* models, $\boldsymbol{u}^k$ and $\boldsymbol{v}^k$ denote the vector that contains all unknowns $\left\{u_j^k, j = 1, \ldots, N_e\right\}$ and $\left\{v_j^k, j = 1, \ldots, N_e\right\}$, respectively, at time level t_k. For the third-order time basis functions, $k = 3$.

Given N total surface elements, the non-zero entries of (100) are given by:

$$\begin{aligned}
\boldsymbol{D_k} &= \left[\left\{\boldsymbol{D_k}\right\}_{ij}\right]_{N\times N} \\
\boldsymbol{E_k} &= \left[\left\{\boldsymbol{E_k}\right\}_{ij}\right]_{N\times N} \\
\boldsymbol{F_k} &= \left[\left\{\boldsymbol{F_k^{A_1}}\right\}_{ij} \quad \cdots \quad \left\{\boldsymbol{F_k^{A_{J_1}}}\right\}_{ij}\right]_{N\times J_1 N} \\
\boldsymbol{G_k} &= \left[\left\{\boldsymbol{G_k^{B_1}}\right\}_{ij} \quad \cdots \quad \left\{\boldsymbol{G_k^{B_{J_2}}}\right\}_{ij}\right]_{N\times J_2 N} \\
\boldsymbol{H_k} &= \left[\left\{\boldsymbol{H_k^{C_1}}\right\}_{ij} \quad \cdots \quad \left\{\boldsymbol{H_k^{C_{J_2}}}\right\}_{ij}\right]_{N\times J_2 N}
\end{aligned}$$

such that all matrices are diagonally dominant. By (44) and (96), $\left\{\boldsymbol{D_k}\right\}_{ij} = \delta_{ij}\rho_0\psi'_{n-k}(t_n)$ where

$$\boldsymbol{D_k} \text{ has coefficients: } \rho_0 \begin{Bmatrix} \frac{11}{6\Delta t}, & k = 0 \\ \frac{-3}{\Delta t}, & k = 1 \\ \frac{3}{2\Delta t}, & k = 2 \\ \frac{-1}{3\Delta t}, & k = 3 \\ 0, & \text{other} \end{Bmatrix},$$

$\left\{\boldsymbol{E_k}\right\}_{ij} = \delta_{ij}\left(h_0\psi'_{n-k}(t_n) + R_0\psi_{n-k}(t_n)\right)$ where

$$\boldsymbol{E_k} \text{ has coefficients: } h_0 \begin{Bmatrix} \frac{11}{6\Delta t}, & k = 0 \\ \frac{-3}{\Delta t}, & k = 1 \\ \frac{3}{2\Delta t}, & k = 2 \\ \frac{-1}{3\Delta t}, & k = 3 \\ 0, & \text{other} \end{Bmatrix} + R_0 \begin{Bmatrix} 1, & k = 0 \\ 0, & k \neq 0 \end{Bmatrix},$$

$\left\{\boldsymbol{F}_{\boldsymbol{k}}^{\boldsymbol{A_\ell}}\right\}_{ij} = \delta_{ij} A_\ell \psi_{n-k}(t_n)$ where

$$\boldsymbol{F}_{\boldsymbol{k}}^{\boldsymbol{A_\ell}} \text{ has coefficients: } A_\ell \begin{Bmatrix} 1, & k=0 \\ 0, & k \neq 0 \end{Bmatrix} \text{ for all } \ell = 1, \ldots, J_1,$$

$\left\{\boldsymbol{G}_{\boldsymbol{k}}^{\boldsymbol{B_\ell}}\right\}_{ij} = \delta_{ij} B_\ell \psi_{n-k}(t_n)$ where

$$\boldsymbol{G}_{\boldsymbol{k}}^{\boldsymbol{B_\ell}} \text{ has coefficients: } B_\ell \begin{Bmatrix} 1, & k=0 \\ 0, & k \neq 0 \end{Bmatrix} \text{ for all } \ell = 1, \ldots, J_2,$$

and $\left\{\boldsymbol{H}_{\boldsymbol{k}}^{\boldsymbol{C_\ell}}\right\}_{ij} = \delta_{ij} C_\ell \psi_{n-k}(t_n)$ where

$$\boldsymbol{H}_{\boldsymbol{k}}^{\boldsymbol{C_\ell}} \text{ has coefficients: } C_\ell \begin{Bmatrix} 1, & k=0 \\ 0, & k \neq 0 \end{Bmatrix} \text{ for all } \ell = 1, \ldots, J_2.$$

Similarly, the non-zero entries of (101) are given by:

$$\boldsymbol{\mathcal{J}}_{\boldsymbol{k}} = \begin{bmatrix} \{\boldsymbol{\mathcal{J}}_{\boldsymbol{k}}\}_{ij} \\ \mathbf{0} \\ \vdots \\ \mathbf{0} \end{bmatrix}_{J_1 N \times N}$$

$$\boldsymbol{\mathcal{K}}_{\boldsymbol{k}} = \begin{bmatrix} \{\boldsymbol{\mathcal{K}}_{\boldsymbol{k}}^{\boldsymbol{\gamma_1}}\}_{ij} & & \\ & \ddots & \\ & & \left\{\boldsymbol{\mathcal{K}}_{\boldsymbol{k}}^{\boldsymbol{\gamma_{J_1}}}\right\}_{ij} \end{bmatrix}_{J_1 N \times J_1 N}$$

such that all matrices are diagonally dominant, and, in $\boldsymbol{\mathcal{J}}_{\boldsymbol{k}}$, there are $(J_1 - 1)$ zero matrices $\mathbf{0}$, each with size $N \times N$. By (44) and (96), $\{\boldsymbol{\mathcal{J}}_{\boldsymbol{k}}\}_{ij} = \delta_{ij} \psi_{n-k}(t_n)$ where

$$\boldsymbol{\mathcal{J}}_{\boldsymbol{k}} \text{ has coefficients: } \begin{Bmatrix} 1, & k=0 \\ 0, & k \neq 0 \end{Bmatrix}$$

and $\{\boldsymbol{\mathcal{K}}_{\boldsymbol{k}}^{\boldsymbol{\gamma_\ell}}\}_{ij} = -\delta_{ij} \left(\psi'_{n-k}(t_n) + \gamma_\ell \psi_{n-k}(t_n)\right)$ where

$$\boldsymbol{\mathcal{K}}_{\boldsymbol{k}}^{\boldsymbol{\gamma_\ell}} \text{ has coefficients: } -\begin{Bmatrix} \frac{11}{6\Delta t}, & k=0 \\ \frac{-3}{\Delta t}, & k=1 \\ \frac{3}{2\Delta t}, & k=2 \\ \frac{-1}{3\Delta t}, & k=3 \\ 0, & \text{other} \end{Bmatrix} - \gamma_\ell \begin{Bmatrix} 1, & k=0 \\ 0, & k \neq 0 \end{Bmatrix} \text{ for all } \ell = 1, \ldots, J_1.$$

The non-zero entries of (102) are given by:

$$\boldsymbol{\mathcal{L}_k} = \begin{bmatrix} \{\boldsymbol{\mathcal{L}_k}\}_{ij} \\ \mathbf{0} \\ \vdots \\ \mathbf{0} \end{bmatrix}_{J_2N\times N}$$

$$\boldsymbol{\mathcal{M}_k} = \begin{bmatrix} \{\boldsymbol{\mathcal{M}_k^{\alpha_1}}\}_{ij} & & \\ & \ddots & \\ & & \{\boldsymbol{\mathcal{M}_k^{\alpha_{J_2}}}\}_{ij} \end{bmatrix}_{J_2N\times J_2N}$$

$$\boldsymbol{\mathcal{N}_k} = \begin{bmatrix} \left\{\boldsymbol{\mathcal{N}_k^{\beta_1}}\right\}_{ij} & & \\ & \ddots & \\ & & \left\{\boldsymbol{\mathcal{N}_k^{\beta_{J_2}}}\right\}_{ij} \end{bmatrix}_{J_2N\times J_2N}$$

such that all matrices are diagonally dominant, and, in $\boldsymbol{\mathcal{L}_k}$, there are (J_2-1) zero matrices $\mathbf{0}$, each with size $N\times N$. By (44) and (97), $\{\boldsymbol{\mathcal{L}_k}\}_{ij} = \delta_{ij}\psi_{n-k}(t_n)$ where

$$\boldsymbol{\mathcal{L}_k} \text{ has coefficients: } \begin{Bmatrix} 1, & k=0 \\ 0, & k\neq 0 \end{Bmatrix},$$

$\{\boldsymbol{\mathcal{M}_k^{\alpha_\ell}}\}_{ij} = -\delta_{ij}\left(\psi'_{n-k}(t_n) + \alpha_\ell\psi_{n-k}(t_n)\right)$ where

$$\boldsymbol{\mathcal{M}_k^{\alpha_\ell}} \text{ has coefficients: } -\begin{Bmatrix} \frac{11}{6\Delta t}, & k=0 \\ \frac{-3}{\Delta t}, & k=1 \\ \frac{3}{2\Delta t}, & k=2 \\ \frac{-1}{3\Delta t}, & k=3 \\ 0, & \text{other} \end{Bmatrix} - \alpha_\ell \begin{Bmatrix} 1, & k=0 \\ 0, & k\neq 0 \end{Bmatrix} \text{ for all } \ell = 1,\ldots,J_2,$$

and $\left\{\boldsymbol{\mathcal{N}_k^{\beta_\ell}}\right\}_{ij} = -\delta_{ij}\beta_\ell\psi_{n-k}(t_n)$ where

$$\boldsymbol{\mathcal{N}_k^{\beta_\ell}} \text{ has coefficients: } -\beta_\ell \begin{Bmatrix} 1, & k=0 \\ 0, & k\neq 0 \end{Bmatrix} \text{ for all } \ell = 1,\ldots,J_2.$$

Finally, the non-zero entries of (103) are given by:

$$\boldsymbol{\mathcal{P}_k} = \begin{bmatrix} \left\{\boldsymbol{\mathcal{P}_k^{\beta_1}}\right\}_{ij} & & \\ & \ddots & \\ & & \left\{\boldsymbol{\mathcal{P}_k^{\beta_{J_2}}}\right\}_{ij} \end{bmatrix}_{J_2N\times J_2N}$$

$$\boldsymbol{\mathcal{Q}_k} = \begin{bmatrix} \{\boldsymbol{\mathcal{Q}_k^{\alpha_1}}\}_{ij} & & \\ & \ddots & \\ & & \{\boldsymbol{\mathcal{Q}_k^{\alpha_{J_2}}}\}_{ij} \end{bmatrix}_{J_2N\times J_2N}$$

such that all matrices are diagonally dominant. By (44) and (98), $\left\{\boldsymbol{\mathcal{P}_k^{\beta_\ell}}\right\}_{ij} = \delta_{ij}\beta_\ell\psi_{n-k}(t_n)$ where

$$\boldsymbol{\mathcal{P}_k^{\beta_\ell}} \text{ has coefficients: } \beta_\ell \begin{Bmatrix} 1, & k=0 \\ 0, & k\neq 0 \end{Bmatrix} \text{ for all } \ell = 1,\ldots,J_2$$

and $\{\boldsymbol{\mathcal{Q}_k^{\alpha_\ell}}\}_{ij} = -\delta_{ij}\left(\psi'_{n-k}(t_n) + \alpha_\ell\psi_{n-k}(t_n)\right)$ where

$$\boldsymbol{\mathcal{Q}_k^{\alpha_\ell}} \text{ has coefficients: } -\begin{Bmatrix} \frac{11}{6\Delta t}, & k=0 \\ \frac{-3}{\Delta t}, & k=1 \\ \frac{3}{2\Delta t}, & k=2 \\ \frac{-1}{3\Delta t}, & k=3 \\ 0, & \text{other} \end{Bmatrix} - \alpha_\ell \begin{Bmatrix} 1, & k=0 \\ 0, & k\neq 0 \end{Bmatrix} \text{ for all } \ell = 1,\ldots,J_2.$$

Coupling (100) through (98) with (45) forms a March-On-in-Time scheme for the Burton-Miller-type time-domain boundary integral equation using a broadband impedance boundary condition. Comparable to the March-On-in-Time scheme (58) developed for the *Extended Helmholtz Resonator* and *Three-Parameter* models, this coupled system has dimension $N(2+J_1+2J_2)\times N(2+J_1+2J_2)$ and is expressed as shown in (104). When solved iteratively, (104) provides solutions for $\boldsymbol{u}^k$ and $\boldsymbol{v}^k$ on rigid and soft surfaces.

$$
\begin{bmatrix} \boldsymbol{B_0} & \boldsymbol{C_0} & \boldsymbol{0} & \boldsymbol{0} & \boldsymbol{0} \\ \boldsymbol{D_0} & \boldsymbol{E_0} & \boldsymbol{F_0} & \boldsymbol{G_0} & \boldsymbol{H_0} \\ \boldsymbol{0} & \boldsymbol{\mathcal{J}_0} & \boldsymbol{\mathcal{K}_0} & \boldsymbol{0} & \boldsymbol{0} \\ \boldsymbol{0} & \boldsymbol{\mathcal{L}_0} & \boldsymbol{0} & \boldsymbol{\mathcal{M}_0} & \boldsymbol{\mathcal{N}_0} \\ \boldsymbol{0} & \boldsymbol{0} & \boldsymbol{0} & \boldsymbol{\mathcal{P}_0} & \boldsymbol{\mathcal{Q}_0} \end{bmatrix} \begin{bmatrix} \boldsymbol{u^n} \\ \boldsymbol{v^n} \\ \boldsymbol{P^n_{(0)}} \\ \boldsymbol{P^n_{(1)}} \\ \boldsymbol{P^n_{(2)}} \end{bmatrix} = \begin{bmatrix} \boldsymbol{q^n} \\ \boldsymbol{0} \\ \boldsymbol{0} \\ \boldsymbol{0} \\ \boldsymbol{0} \end{bmatrix} - \begin{bmatrix} \boldsymbol{B_1} & \boldsymbol{C_1} & \boldsymbol{0} & \boldsymbol{0} & \boldsymbol{0} \\ \boldsymbol{D_1} & \boldsymbol{E_1} & \boldsymbol{F_1} & \boldsymbol{G_1} & \boldsymbol{H_1} \\ \boldsymbol{0} & \boldsymbol{\mathcal{J}_1} & \boldsymbol{\mathcal{K}_1} & \boldsymbol{0} & \boldsymbol{0} \\ \boldsymbol{0} & \boldsymbol{\mathcal{L}_1} & \boldsymbol{0} & \boldsymbol{\mathcal{M}_1} & \boldsymbol{\mathcal{N}_1} \\ \boldsymbol{0} & \boldsymbol{0} & \boldsymbol{0} & \boldsymbol{\mathcal{P}_1} & \boldsymbol{\mathcal{Q}_1} \end{bmatrix} \begin{bmatrix} \boldsymbol{u^{n-1}} \\ \boldsymbol{v^{n-1}} \\ \boldsymbol{P^{n-1}_{(0)}} \\ \boldsymbol{P^{n-1}_{(1)}} \\ \boldsymbol{P^{n-1}_{(2)}} \end{bmatrix}
$$

$$
- \begin{bmatrix} \boldsymbol{B_2} & \boldsymbol{C_2} & \boldsymbol{0} & \boldsymbol{0} & \boldsymbol{0} \\ \boldsymbol{D_2} & \boldsymbol{E_2} & \boldsymbol{F_2} & \boldsymbol{G_2} & \boldsymbol{H_2} \\ \boldsymbol{0} & \boldsymbol{\mathcal{J}_2} & \boldsymbol{\mathcal{K}_2} & \boldsymbol{0} & \boldsymbol{0} \\ \boldsymbol{0} & \boldsymbol{\mathcal{L}_2} & \boldsymbol{0} & \boldsymbol{\mathcal{M}_2} & \boldsymbol{\mathcal{N}_2} \\ \boldsymbol{0} & \boldsymbol{0} & \boldsymbol{0} & \boldsymbol{\mathcal{P}_2} & \boldsymbol{\mathcal{Q}_2} \end{bmatrix} \begin{bmatrix} \boldsymbol{u^{n-2}} \\ \boldsymbol{v^{n-2}} \\ \boldsymbol{P^{n-2}_{(0)}} \\ \boldsymbol{P^{n-2}_{(1)}} \\ \boldsymbol{P^{n-2}_{(2)}} \end{bmatrix}
$$

$$
- \cdots -
$$

$$
- \begin{bmatrix} \boldsymbol{B_K} & \boldsymbol{C_K} & \boldsymbol{0} & \boldsymbol{0} & \boldsymbol{0} \\ \boldsymbol{D_K} & \boldsymbol{E_K} & \boldsymbol{F_K} & \boldsymbol{G_K} & \boldsymbol{H_K} \\ \boldsymbol{0} & \boldsymbol{\mathcal{J}_K} & \boldsymbol{\mathcal{K}_K} & \boldsymbol{0} & \boldsymbol{0} \\ \boldsymbol{0} & \boldsymbol{\mathcal{L}_K} & \boldsymbol{0} & \boldsymbol{\mathcal{M}_K} & \boldsymbol{\mathcal{N}_K} \\ \boldsymbol{0} & \boldsymbol{0} & \boldsymbol{0} & \boldsymbol{\mathcal{P}_K} & \boldsymbol{\mathcal{Q}_K} \end{bmatrix} \begin{bmatrix} \boldsymbol{u^{n-K}} \\ \boldsymbol{v^{n-K}} \\ \boldsymbol{P^{n-K}_{(0)}} \\ \boldsymbol{P^{n-K}_{(1)}} \\ \boldsymbol{P^{n-K}_{(2)}} \end{bmatrix}
$$

$$
- \cdots -
$$

$$
- \begin{bmatrix} \boldsymbol{B_J} & \boldsymbol{C_J} & \boldsymbol{0} & \boldsymbol{0} & \boldsymbol{0} \\ \boldsymbol{0} & \boldsymbol{0} & \boldsymbol{0} & \boldsymbol{0} & \boldsymbol{0} \\ \boldsymbol{0} & \boldsymbol{0} & \boldsymbol{0} & \boldsymbol{0} & \boldsymbol{0} \\ \boldsymbol{0} & \boldsymbol{0} & \boldsymbol{0} & \boldsymbol{0} & \boldsymbol{0} \\ \boldsymbol{0} & \boldsymbol{0} & \boldsymbol{0} & \boldsymbol{0} & \boldsymbol{0} \end{bmatrix} \begin{bmatrix} \boldsymbol{u^{n-J}} \\ \boldsymbol{v^{n-J}} \\ \boldsymbol{P^{n-J}_{(0)}} \\ \boldsymbol{P^{n-J}_{(1)}} \\ \boldsymbol{P^{n-J}_{(2)}} \end{bmatrix} \tag{104}
$$

CHAPTER 6

STABILITY ANALYSIS AND NUMERICAL RESULTS

Direct numerical simulation of the time-domain boundary integral equation (30) without Burton-Miller reformulation is prone to numerical instabilities due to resonant frequencies resulting from non-trivial solutions in the interior domain. In Chapter 2, a Burton-Miller reformulation is introduced so that resonant frequencies can be eliminated, and stability achieved. Coupled with an impedance (or admittance) boundary condition on the scattering surface, a March-On-in-Time scheme in introduced in Chapter 5 which, when solved iteratively, provides predictions for the scattering solution on both rigid and soft bodies. This chapter now studies the time-domain boundary integral equation with Burton-Miller reformulation to ensure stability of the coupled system with either an impedance (53) or an admittance boundary condition (56).

6.1 EIGENVALUE ANALYSIS

Two March-On-in-Time schemes are introduced in Chapter 5 for predicting acoustic scattering around a body from a given noise source. Equation (58) is used when modeling either a *Helmholtz Resonator* or a *Three-Parameter* acoustic liner on the scattering surface and (104) is used when modeling a *Broadband* acoustic liner. To assess the stability of each system, a numerical eigenvalue study is conducted.

The systems are first denoted by:

$$\boldsymbol{A_0 w^n = q_0^n - A_1 w^{n-1} - A_2 w^{n-2} - ... - A_K w^{n-K} - ... - A_J w^{n-J}} \tag{105}$$

where

$$\boldsymbol{A_k} = \begin{bmatrix} \boldsymbol{B_k} & \boldsymbol{C_k} \\ \boldsymbol{D_k} & \boldsymbol{E_k} \end{bmatrix}_{k=0,...,K} \quad \boldsymbol{A_k} = \begin{bmatrix} \boldsymbol{B_k} & \boldsymbol{0} \\ \boldsymbol{0} & \boldsymbol{0} \end{bmatrix}_{k=K+1,...,J} \quad \boldsymbol{w^n} = \begin{bmatrix} \boldsymbol{u^n} \\ \boldsymbol{v^n} \end{bmatrix} \boldsymbol{q_0^n} = \begin{bmatrix} \boldsymbol{q^n} \\ \boldsymbol{0} \end{bmatrix}$$

given in (58) and where

$$\boldsymbol{A_k} = \begin{bmatrix} \boldsymbol{B_K} & \boldsymbol{C_K} & \boldsymbol{0} & \boldsymbol{0} & \boldsymbol{0} \\ \boldsymbol{D_K} & \boldsymbol{E_K} & \boldsymbol{F_K} & \boldsymbol{G_K} & \boldsymbol{H_K} \\ \boldsymbol{0} & \boldsymbol{\mathcal{J}_K} & \boldsymbol{\mathcal{K}_K} & \boldsymbol{0} & \boldsymbol{0} \\ \boldsymbol{0} & \boldsymbol{\mathcal{L}_K} & \boldsymbol{0} & \boldsymbol{\mathcal{M}_K} & \boldsymbol{\mathcal{N}_K} \\ \boldsymbol{0} & \boldsymbol{0} & \boldsymbol{0} & \boldsymbol{\mathcal{P}_K} & \boldsymbol{\mathcal{Q}_K} \end{bmatrix}_{k=0,...,K}$$

$$\boldsymbol{A_k} = \begin{bmatrix} \boldsymbol{B_K} & \mathbf{0} & \mathbf{0} & \mathbf{0} & \mathbf{0} \\ \mathbf{0} & \mathbf{0} & \mathbf{0} & \mathbf{0} & \mathbf{0} \\ \mathbf{0} & \mathbf{0} & \mathbf{0} & \mathbf{0} & \mathbf{0} \\ \mathbf{0} & \mathbf{0} & \mathbf{0} & \mathbf{0} & \mathbf{0} \\ \mathbf{0} & \mathbf{0} & \mathbf{0} & \mathbf{0} & \mathbf{0} \end{bmatrix}_{k=K+1,\ldots,J} \qquad \boldsymbol{w^n} = \begin{bmatrix} \boldsymbol{u^n} \\ \boldsymbol{v^n} \\ \boldsymbol{P^n_{(0)}} \\ \boldsymbol{P^n_{(1)}} \\ \boldsymbol{P^n_{(2)}} \end{bmatrix} \; \boldsymbol{q_0^n} = \begin{bmatrix} \boldsymbol{q^n} \\ \mathbf{0} \\ \mathbf{0} \\ \mathbf{0} \\ \mathbf{0} \end{bmatrix}$$

given in (104). Seeking solutions of the form

$$\boldsymbol{w^n} = \lambda^n \boldsymbol{e_0} \tag{106}$$

to the corresponding homogeneous system (105), a polynomial eigenvalue problem is obtained:

$$\left[\boldsymbol{A_0}\lambda^J + \boldsymbol{A_1}\lambda^{J-1} + \boldsymbol{A_2}\lambda^{J-2} + \cdots + \boldsymbol{A_{J-1}}\lambda + \boldsymbol{A_J}\right] \boldsymbol{e_0} = 0. \tag{107}$$

Note that the homogeneous system[1] is representative of when the source, or incident wave, has traveled far beyond the scattering body and it is often when numerical instability occurs. Equation (107) is cast into a generalized eigenvalue problem (see Appendix D) with eigenvectors $\boldsymbol{e}_j = \lambda^j \boldsymbol{e}_0 = \lambda \boldsymbol{e}_{j-1}$. The largest eigenvalue $\lambda_{\max}$ of the generalized eigenvalue problem is then calculated by using a matrix power iteration method as detailed in Appendix D. The matrix power method is run using code written in Matlab and is repeated until the iterative scheme has converged to the largest eigenvalue, $|\lambda|_{\max}$, *i.e.*, when $|\lambda^{(k)} - \lambda^{(k-1)}|/|\lambda^{(k)}| < \delta$ for a given tolerance δ. If the numerical scheme given by (105) is stable, it is necessary that $|\lambda_{\max}| \leq 1$ for all λ in (107) [2, 39, 44, 51, 72].

The stability of the numerical algorithm is investigated by considering the scattering of an acoustic point source by a flat plate with dimension $[-0.5, 0.5] \times [-0.5, 0.5] \times [-0.1, 0.1]$ where the point source, located at $\boldsymbol{x} = (0, 0, 1)$, is centered directly above the body as illustrated in Figure 3a in Chapter 3. The surface of the flat plate is discretized in the x-, y-, and z- directions with N_x, N_y, and N_z elements, respectively, giving a total number of $N = 2(N_xN_y + N_yN_z + N_xN_z)$ surface elements. Four problem sizes are considered: $5 \times 5 \times 1$ ($N = 70$ elements), $10 \times 10 \times 2$ ($N = 280$ elements), $20 \times 20 \times 4$ ($N = 1,120$ elements), and $30 \times 30 \times 6$ ($N = 2,520$ elements) as illustrated in Figures 40a through 40d.

Furthermore, two different time steps[2] are considered: $\Delta t = 1/12$ and $\Delta t = 1/24$. When using Burton-Miller reformulation with the given basis functions (42), stability has been demonstrated using as little as 22 points-per-wave period [53], translating to a minimum

[1] For the stability study, the eigenvalue analyses is concerned only with the homogeneous system.

[2] A time step of $\Delta t = 1/12$ was chosen to ensure that the scattering problem provided solutions over a wide range of frequencies. This choice is consistent with the scalability assessment in Chapter 4. A time step of $\Delta t = 1/24$ was additionally chosen to assess the dependence of time step on stability.

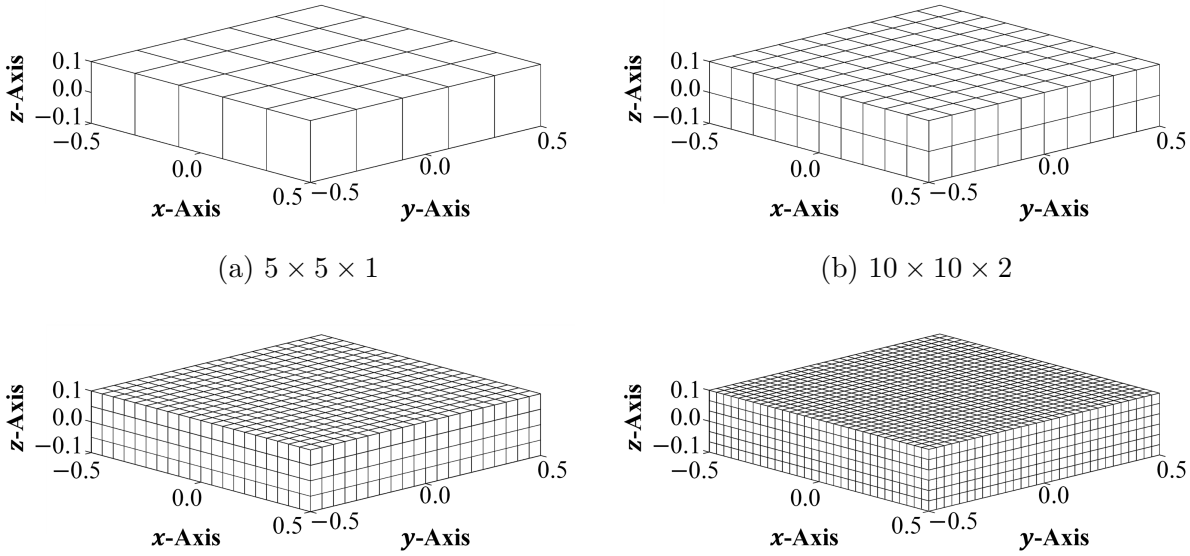

(a) $5 \times 5 \times 1$

(b) $10 \times 10 \times 2$

(c) $20 \times 20 \times 4$

(d) $30 \times 30 \times 6$

Fig. 40: Schematic diagrams illustrating the respective discretization for the flat plate with dimension $[-0.5, 0.5] \times [-0.5, 0.5] \times [-0.1, 0.1]$ used for modeling the acoustic scattering of a point source located at $(x, y, z) = (0, 0, 1)$.

time step requirement of $\Delta t \approx \Delta x$. When $\Delta t > \Delta x$, matrix $\boldsymbol{B_0}$ is banded leading to increased stability. For each selected time step, spatial resolutions of $N_x = 20$ and $N_x = 30$ are sufficiently fine for the third-order temporal basis function given in (42) and stability is expected for all analyses. For the coarser grids, $N_x = 5$ and $N_x = 10$, analyses may indicate a necessity for larger time steps, *i.e.* greater than 1/5 and 1/10, respectively.

6.2 ACOUSTIC LINER MODELS

For the *Extended Helmholtz Resonator Model*, the liner boundary condition is modeled using numerical data from [59]. In [59], eighteen different resistance and reactance curves are proposed for varying combinations of $Z(\omega)$ and ν within the range $0 \leq \omega \Delta t \leq \pi/5$. The constant ν is defined such that the cavity depth is equal to a multiple of time step:

$$\frac{2L}{c} = \nu \Delta t$$

where L is the cavity depth and c is the speed of sound. Three of the eighteen curves are illustrated in Figure 41. In this example, all three curves of $Z(\omega)$ and $\nu = 1, 5, 9$ intersect

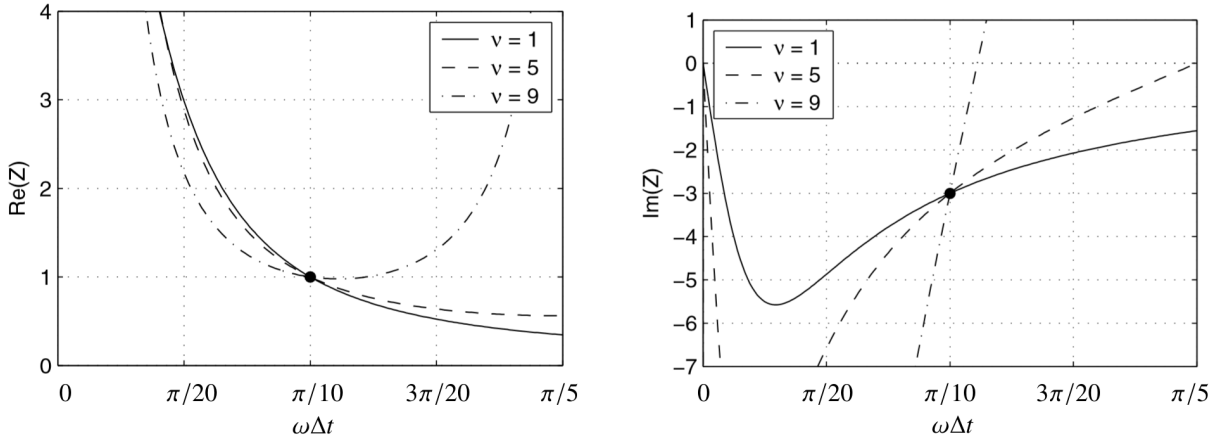

Fig. 41: Resistance and reactance curves for Cases 1, 2, 3 indicating an intersection for each ν at the non-dimensional frequency $\omega_0\Delta t = \pi/10$. At this frequency, $Z(\omega_0\Delta t) = 1 - 3i$.

at the non-dimensional frequency $\omega_0\Delta t = \pi/10$ giving an impedance of $Z(\omega_0\Delta t) = 1 - 3i$. These cases are herein referred to as Cases 1, 2, 3 respectively. Appendix E further illustrates all eighteen cases for the *Extended Helmholtz Resonator Model*.

To assess the stability of (105), all eighteen cases are considered and $\omega_0\Delta t$ is chosen to be $\omega_0\Delta_t = \pi/10$. At this frequency, the resistance and reactance curves intersect at the given $Z(\omega_0\Delta t)$ and ν combinations listed in Table II. These eighteen cases yield the impedance boundary condition (69) constants ϵ, F_R, F_β and the admittance boundary condition (74) constants ϵ, $\overline{F_R}$, $\overline{F_\beta}$ listed in Table III. By choosing a non-dimensional frequency, all constants are independent of time step. Moreover, it is assumed that $\rho_0 = 1$ and $m = 0$ in (69).

For the *Three-Parameter Impedance Model* analysis, the liner boundary condition is also modeled using numerical data from [59]. In this model, the impedance and admittance boundary condition constants, R_0, h_0, A_0 and $\overline{R_0}, \overline{h_0}, \overline{A_0}$ respectively, are independent of ν. Choosing $\omega_0\Delta t = \pi/10$, only the six cases corresponding to the first of each $Z(\omega)$ and ν combination listed in Table II are considered for analysis, herein referred to as Cases 1, 4, 7, 10, 13, 16 respectively. These six cases yield the constants listed in Table IV.

Finally, for the *Broadband Impedance Model*, the liner boundary condition is modeled using experimental data. Two acoustic liners, named CT57 and GE03, were tested in the Grazing Flow Impedance Tube at the NASA Langley Research Center Liner Technology Facility [88]. During the tests [89], impedance values were measured along a broad range of frequencies. Using the measured data, twenty-five different numerical models were generated

TABLE II: Eighteen different cases of $Z(\omega)$ and ν at the specified frequency $\omega_0\Delta t = \pi/10$ used in the *Extended Helmholtz Resonator Model* analysis.

Case	$Z(\omega_0\Delta t) = Z_R + iZ_I$	ν	**Case**	$Z(\omega_0\Delta t) = Z_R + iZ_I$	ν	**Case**	$Z(\omega_0\Delta t) = Z_R + iZ_I$	ν
1		1	**7**		1	**13**		19
2	$1 - 3i$	5	**8**	$1 - i$	5	**14**	$1 + 2i$	15
3		9	**9**		9	**15**		11
4		1	**10**		19	**16**		19
5	$1 - 2i$	5	**11**	$1 + i$	15	**17**	$1 + 3i$	15
6		9	**12**		11	**18**		11

TABLE III: Constants used for the *Extended Helmholtz Resonator Model*.

Case	ν	ϵ	*Impedance Boundary Condition Constants*			*Admittance Boundary Condition Constants*		
			$Z(\omega_0\Delta t) = Z_R + iZ_I$	F_R	F_β	$Y(\omega_0) = Y_R + iY_I$	$\overline{F_R}$	$\overline{F_\beta}$
1	1	0.092542		0.100301	0.516754		0.189970	-0.051675
2	5	0.294705	1 - 3i	0.103031	3.131222	0.1 + 0.3i	0.189697	-0.313122
3	9	0.092542		0.100301	18.982855		0.189970	-1.898285
4	1	0.138510		0.100674	0.378952		0.379865	-0.075790
5	5	0.433091	1 - 2i	0.106486	2.190518	0.2 + 0.4i	0.378703	-0.438104
6	9	0.138510		0.100674	12.689687		0.379865	-2.537937
7	1	0.273869		0.102621	0.280504		0.948690	-0.140252
8	5	0.793236	1 - i	0.120920	1.331459	0.5 + 0.5i	0.939540	-0.665729
9	9	0.273869		0.102621	6.435871		0.948690	-3.217936
10	19	0.273869		0.102621	0.280504		0.948690	-0.140252
11	15	0.793236	1 + i	0.120920	1.331459	0.5 - 0.5i	0.939540	-0.665729
12	11	0.273869		0.102621	6.435871		0.948690	-3.217936
13	19	0.138510		0.100674	0.378952		0.379865	-0.075790
14	15	0.433091	1 + 2i	0.106486	2.190518	0.2 - 0.4i	0.378703	-0.438104
15	11	0.138510		0.100674	12.689687		0.379865	-2.537937
16	19	0.092542		0.100301	0.516754		0.189970	-0.051675
17	15	0.294705	1 + 3i	0.103031	3.131222	0.1 - 0.3i	0.189697	-0.313122
18	11	0.092542		0.100301	18.982855		0.189970	-1.898285

using least squares regression giving values for the parameters which define the surface impedance (84). In each of the broadband cases, herein referred to as Cases 1 through 25, the parameters yield $\mathrm{Re}(Z) > 0$, thus preserving causality and stability. These twenty-five cases represent both zero and non-zero h_0 and R_0 as well as different amounts of poles, *i.e.*, $J_1 = 1, 2$ and $J_2 = 2, 4, 6, 8$. This representation is not unique and merely represents twenty-five possible options. Table V lists the constants generated for the *Broadband* model.

TABLE IV: Constants used for the *Three-Parameter Impedance Model*.

Case	*Impedance Boundary Condition Constants*				*Admittance Boundary Condition Constants*			
	$Z(\omega_0\Delta t) = Z_R + iZ_I$	R_0	h_0	A_0	$Y(\omega_0\Delta t) = Y_R + iY_I$	$\overline{R_0}$	$\overline{h_0}$	$\overline{A_0}$
1	$1-3i$	1	0.802811	0.1	$0.1+0.3i$	0.1	0.1	2.552196
4	$1-2i$	1	0.537553	0.1	$0.2+0.4i$	0.2	0.1	2.929188
7	$1-i$	1	0.272294	0.1	$0.5+0.5i$	0.5	0.1	3.306179
10	$1+i$	1	0.1	5.191134	$0.5-0.5i$	0.5	0.139665	0.1
13	$1+2i$	1	0.1	8.961045	$0.2-0.4i$	0.2	0.113139	0.1
16	$1+3i$	1	0.1	12.730957	$0.1-0.3i$	0.1	0.086614	0.1

TABLE V: Constants used for the *Broadband Impedance Model*.

Case	h_0	R_0	J_1	A_ℓ	γ_ℓ	J_2	B_ℓ	C_ℓ	α_ℓ	β_ℓ
				$\ell = 1,\ldots,J_1$			$\ell = 1,\ldots,J_2$			
1	0.010873	0.177655	1	18.467174	0.985273	2	43.919202	-0.571804	4.887694	37.631479
							23.611034	-8.511097	7.670216	-66.460858
2	0	0	1	18.422293	1.091586	2	98.624933	-3.063868	6.641055	81.958998
							44.048396	-0.696846	4.871120	37.450376
3	0	0.068743	1	18.421975	1.075243	2	99.855347	-9.968384	7.952528	82.203159
							44.089363	-0.709128	4.879110	37.451098
4	0.011775	0.001514	1	32.573728	1.896347	2	0.001101	-9.910991	22.599229	16.476064
							75.213211	-9.915633	7.374808	82.791519
5	0	0	1	27.493859	0.470593	3	99.686994	1.823551	10.638159	96.074097
							99.672009	-9.863166	0.080378	97.146410
							1.066955	0.959000	1.137323	7.645146
6	0.015544	0.308273	1	18.180913	0.755022	2	37.665098	-4.408271	4.407188,	36.919111
							37.665098	4.408271	4.407188	-36.919111
7	0	0.000665	1	4.337323	0.215576	4	37.817445	-3.544474	4.337323	37.084072
							37.817445	3.544474	4.337323	-37.084072
							3757.735850	-193.214362	47.096939	476.960753
							3757.735850	193.214362	47.096939	-476.960753
8	0.010183	0.711158	1	16.686886	0.364459	8	0.796373	-8.866594	8.842337	56.643991
							0.796373	8.866594	8.842337	-56.643991
							-12.892626	9.953336	13.57575	12.238280
							-12.892626	-9.953336	13.57575	-12.238280
							35.493978	0.290887	4.550649	38.683505
							35.493978	-0.290887	4.550649	-38.683505
							3.879810	2.735772	1.545798	36.4536010
							3.879810	-2.735772	1.545798	-36.453610

continuation of Table V

Case	h_0	R_0	J_1	A_ℓ	γ_ℓ	J_2	B_ℓ	C_ℓ	α_ℓ	β_ℓ
				$\ell = 1, \ldots, J_1$			$\ell = 1, \ldots, J_2$			
9	0.005862	0.028692	1	30.915827	1.274166	2	560.351405	-39.926136	10.924474	164.483463
							560.351405	39.926136	10.924474	-164.483463
10	0.014599	0.003611	1	29.835155	1.319666	2	62.349090	-6.861790	7.816387	82.405591
							62.349090	6.861790	7.816387	-82.405591
11	0.026522	0.171544	1	26.468841	0.213259	4	22.682684	-40.629046	102.846227	105.275362
							22.682684	40.629046	102.846227	-105.275362
							3.219713	3.598788	3.608834	7.438713
							3.219713	-3.598788	3.608834	-7.438713
12	0.028230	0.058915	1	31.621031	1.101980	6	0.024059	-87.819346	0.004878	2648.812896
							0.024059	87.819346	0.004878	-2648.812896
							0	-64.591284	62.149306	4.493802
							0	64.591284	62.149306	-4.493802
							6.729911	175.898561	483.872273	58.532344
							6.729911	-175.898561	483.872273	-58.532344
13	0.013599	0.232571	1	26.919465	0.959544	6	260.766647	34.068538	28.447787	28.447787
							260.766647	-34.068538	28.447787	28.447787
							0.062505	16.725016	8.165089	8.165089
							0.062505	-16.725016	8.165089	8.165089
							3.180330	-21.212760	15.149207	15.149207
							3.180330	21.212760	15.149207	15.149207
14	0	0.028694	1	22.036983	0.824364	6	96.302181	1.422601	2.493450	79.997260
							96.302181	-1.422601	2.493450	-79.997260
							5.497760	20.768558	6.380633	3.003809
							5.497760	-20.768558	6.380633	-3.003809
							341.395138	-38.680703	19.136511	296.497672
							341.395138	38.680703	19.136511	-296.497672
15	0.000225	0.013971	1	2.534543	1562.572387	8	0.035679	-11.486752	38.696225	29.277588
							0.035679	11.486752	38.696225	-29.277588
							183.798072	-1.216857	2.625280	97.864923
							183.798072	1.216857	2.625280	-97.864923
							792.465405	12.644471	26.921543	4007.367566
							792.465405	-12.644471	26.921543	-4007.367566
							29.010084	1.705372	1.381639	2.063757
							29.010084	-1.705372	1.381639	-2.063757

continuation of Table V

Case	h_0	R_0	J_1	A_ℓ	γ_ℓ	J_2	B_ℓ	C_ℓ	α_ℓ	β_ℓ
				$\ell = 1, \ldots, J_1$			$\ell = 1, \ldots, J_2$			
16	0.013175	0.272720	1	107.146330	788.823443	8	11.059494	-16.009196	38.533751	66.689894
							11.059494	16.009196	38.533751	-66.689894
							14.060655	-23.749053	51.115956	104.286524
							14.060655	23.749053	51.115956	-104.286524
							28.616386	9.158041	1.962748	2.604681
							28.616386	-9.158041	1.962748	-2.604681
							64.914129	-33.751278	17.387868	100.423185
							64.914129	33.751278	17.387868	-100.423185
17	0.000203	0.621728	2	6.318130	23.497365	6	1854.492719	12.461307	0.052354	388.900938
							1854.492719	-12.461307	0.052354	-388.900938
							10.631933	28.161879	4.603434	4.185982
				10.503281	0.102745		10.631933	-28.161879	4.603434	4.185982
							0.000564	-39.262791	20.931904	59.674410
							0.000564	39.262791	20.931904	-59.674410
18	0.012782	0.248469	2	16.145435	0.709115	6	4.700128	-28.224184	47.148624	31.626755
							4.700128	28.224184	47.148624	-31.626755
							35.031678	-15.414300	6.793332	72.753857
				15.326936	2.161501		35.031678	15.414300	6.793332	-72.753857
							407.091329	10.823413	13.057666	1192.072526
							407.091329	-10.823413	13.057666	-1192.072526
19	0.024000	0.038000	1	30.300000	0.120000	2	3.150000	0.980000	1.290000	57.200000
							3.150000	-0.980000	1.290000	-57.200000
20	0.012112	0.380870	1	16.251535	0.020422	2	37.970796	-1.844678	4.482321	37.613785
							37.970796	1.844678	4.482321	-37.613785
21	0.016253	0.151567	1	872.368067	3928.026719	4	38.379756	0.156211	4.436313	37.537987
							38.379756	-0.156211	4.436313	-37.537987
							12.751961	40.30577	4.118517	2.435390
							12.751961	-40.30577	4.118517	-2.435290
22	0.004711	0.191272	1	16.704306	0.073500	6	125.978567	-40.900615	35.784243	94.874392
							125.978567	40.900615	35.784243	-94.874392
							34.728391	1.601956	3.961033	37.649632
							34.728391	-1.601956	3.961033	-37.649632
							515.400396	-3036.103688	727.105191	123.424421
							15.400396	3036.103688	727.105191	-123.424421
23	0.025644	0.071884	1	20.063286	0.633995	2	45.349058	2.686075	5.094989	37.880208
							45.349058	-2.686075	5.094989	-37.880208
24	0.000255	0.574000	1	19.829038	1.171253	4	65.804633	-50.070590	9.352923	74.181396
							65.804633	50.070590	9.352923	-74.181396
							51.596007	-3.775851	5.600285	37.234242
							51.596007	3.775851	5.600285	-37.234242

continuation of Table V

Case	h_0	R_0	J_1	A_ℓ	γ_ℓ	J_2	B_ℓ	C_ℓ	α_ℓ	β_ℓ
				$\ell = 1, \ldots, J_1$			$\ell = 1, \ldots, J_2$			
25	0.008159	0.316180	1	17.178531	0.001534	6	10.182474	1.914140	2.407176	36.315770
							10.182474	-1.914140	2.407176	-36.315770
							30.083492	-0.729202	5.124423	39.025518
							30.083492	0.729202	5.124423	-39.025518
							517.347902	-0.204553	0.085969	217.264825
							517.347902	0.204553	0.085969	-217.264825

Figures 42a and 42b illustrate two examples of the *Broadband* model, Cases 1 and 4. Figure 42a depicts experimental data from the CT57 liner and Figure 42b depicts experimental data from the GE03. In each figure, the experimental data is graphed using solid circles and the numerical model is graphed with a dotted line. For illustrations of all twenty-five cases, refer to Appendix F.

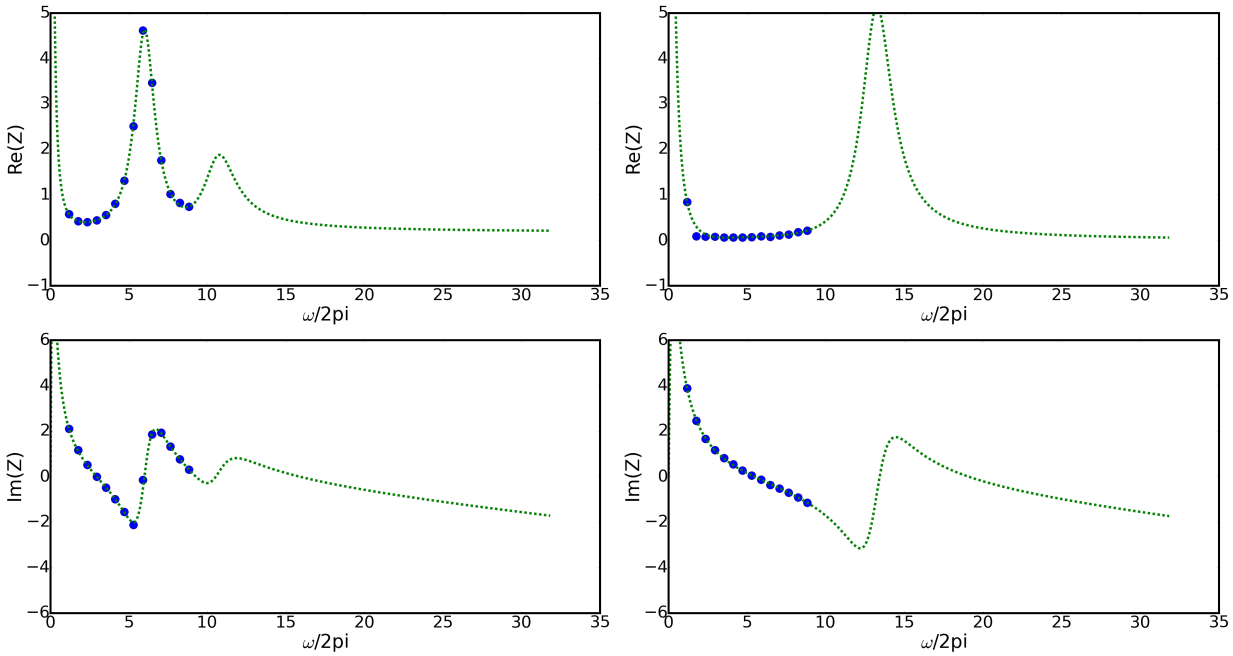

(a) Broadband Case 1

(b) Broadband Case 4

Fig. 42: Illustration of the *Broadband Impedance Model* curves generated for resistance and reactance using least squares regression of experimental data. The experimental data is graphed using solid circles and the numerical model is graphed with a dotted line.

6.3 EIGENVALUE COMPUTATION

For the stability assessment of each liner model, surface discretization, and time step, it is assumed that the acoustic liner is installed on all scattering surfaces. The fully-lined configuration is herein referred to as "*soft*" whereas an un-lined configuration is herein referred to as "*rigid*." An illustration comparing *rigid* versus *soft* bodies for each discretization is shown in Figure 43. Using the rigid body as a baseline, the stability of the numerical algorithm is tested assuming no liner boundary condition on any scattering surface. Then, soft body liner applications are assessed for their stability in solving the system (105). With no liner installed on the scattering surface, all baseline cases are expected to yield eigenvalues no greater than unity. For the baseline assessment, all matrices associated with the liner boundary condition are equivalently set equal to zero.

The values of the maximum eigenvalue for both the *rigid* and *soft* bodies are calculated using a code written in Matlab for each liner model, surface discretization, and time step. For the soft body *Extended Helmholtz Resonator* and *Three-Parameter Impedance* models, all impedance boundary condition eigenvalue results are listed in Table VI and all admittance boundary condition eigenvalue results are listed in Table VII. Further, for the soft body *Broadband Impedance Model*, all impedance boundary condition eigenvalue results are listed in Table VIII. The rigid body results are not listed in table form because, as expected, all baseline cases yield a maximum eigenvalue of 1.000000 for discretizations $5 \times 5 \times 1$, $10 \times 10 \times 2$, $20 \times 20 \times 4$, and $30 \times 30 \times 6$ and time steps $\Delta t = 1/12$ and $\Delta t = 1/24$. Since $|\lambda_{\max}| \leq 1$ for all λ, the baseline study validates that the Burton-Miller reformulation of the time-domain integral equation provides numerical stability by successfully eliminating resonant frequencies.

In Tables VI through VIII, all eigenvalues converge to a tolerance $\delta < 10^{-9}$ within $5,000$ iterations[3] unless denoted by *dnc*. Moreover, any eigenvalues greater than unity are listed in **bold** and if greater than two are listed as $\star\star\star$. For the *Broadband* model on the finest grid, $30 \times 30 \times 6$, several matrices are too large and exceed the memory bandwidth in Matlab.

[3]When deciding the maximum number of iterations to use before considering the solution non-convergent within a tolerance $\delta < 10^{-9}$, several steps were taken. First, the total number of iterations was monitored, and it was found that, for the convergent solutions, most cases converged to a tolerance $\delta < 10^{-9}$ within $3,000$ iterations though nearly all converged within 500. It was then decided to set a limit of $5,000$ iterations for all scenarios. To ensure $5,000$ was sufficient, several of the cases that did not converge were re-run up to 10^6 iterations including all $5 \times 5 \times 1$ and $10 \times 10 \times 2$ cases as well as half of all $20 \times 20 \times 4$. It was found that in all scenarios, the cases that did not converge to a tolerance $\delta < 10^{-9}$ within $5,000$ iterations were still non-convergent by 10^6. It was therefore decided that $5,000$ iterations was sufficient for reaching a converged solution. The cases that were re-run up to 10^6 iterations are denoted by *dnc* † in each table.

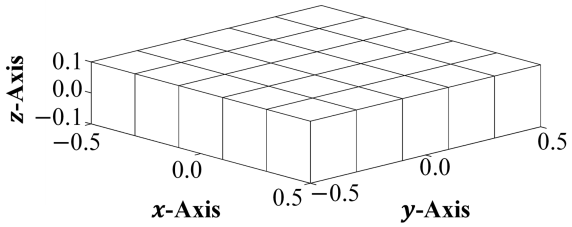

(a) Rigid Body, $5 \times 5 \times 1$

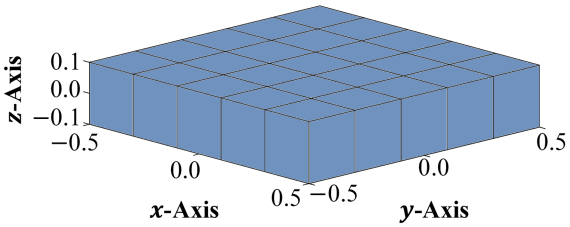

(b) Soft Body, $5 \times 5 \times 1$

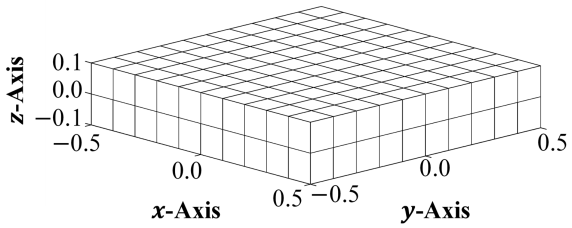

(c) Rigid Body, $10 \times 10 \times 2$

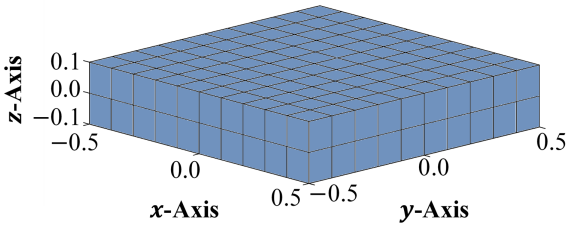

(d) Soft Body, $10 \times 10 \times 2$

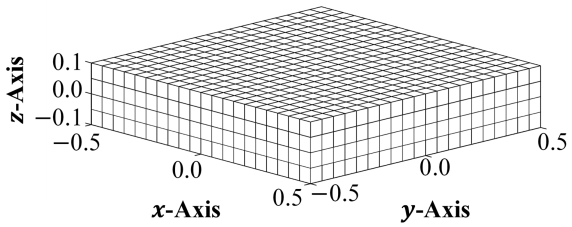

(e) Rigid Body, $20 \times 20 \times 4$

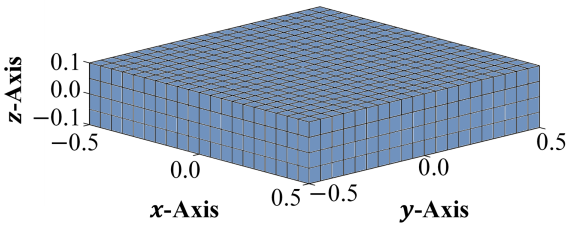

(f) Soft Body, $20 \times 20 \times 4$

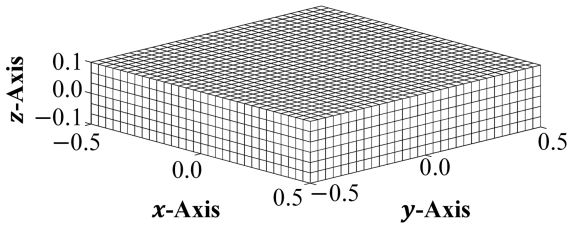

(g) Rigid Body, $30 \times 30 \times 6$

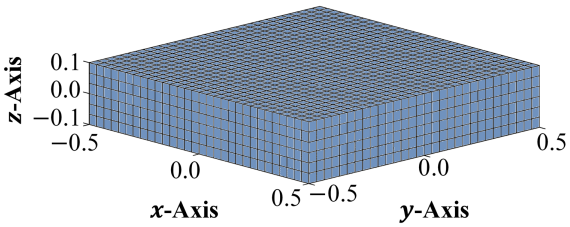

(h) Soft Body, $30 \times 30 \times 6$

Fig. 43: Schematic diagrams illustrating a comparison between un-lined and fully-lined scattering bodies for all discretizations.

These cases are not included in the stability assessment and are denoted by *emb*.

The *Three-Parameter Impedance Model* analysis demonstrates stability for soft body scattering given both an impedance and admittance boundary condition in all six numerical cases. Apart from $5 \times 5 \times 1$, all analyses yield a maximum eigenvalue no greater than unity. As indicated in Table VI, the coarsest grid with impedance boundary condition is unstable for Cases 1, 4, 7 when $\Delta t = 1/12$ and Case 1 when $\Delta t = 1/24$. Also as indicated in Table VII, the coarsest grid with admittance boundary condition did not converge within 10^6 iterations for any case when $\Delta t = 1/24$. While the unstable impedance cases in Table VI may due to round-off error, being that the eigenvalues are 1.000001, 1.000003, 1.000008, and 1.000004, it is more likely that the *Three-Parameter* model provides numerical stability for fine grids, only, using either an impedance or admittance boundary condition especially when considering that $\Delta t < \Delta x$ for each time step with discretization of $5 \times 5 \times 1$. It can therefore be concluded that the *Three-Parameter Impedance Model* is sufficient for predicting scattering by fully-lined bodies such that, at a minimum, the condition $\Delta t \approx \Delta x$ is satisfied.

The *Broadband Impedance Model* analysis demonstrates stability for soft body scattering given an impedance boundary condition in fifteen out of twenty-five numerical cases. Apart from Cases 7, 20, 22, 25 (CT57) and Cases 4, 5, 9, 11, 15, 19 (GE03), all analyses yield a maximum eigenvalue no greater than unity. As indicated in Table VIII, Cases 20 and 25 are unstable for all discretizations and time steps, Cases 5, 9, 11, 19, and 22 are unstable for coarse grids only with Case 11 showing stability for just $30 \times 30 \times 6$, and Cases 4, 7, and 15 favor one time step over the other.

As with the *Three-Parameter* model, there are several instances where the unstable *Broadband* cases may be due to round-off error (*e.g.*, Case 5: 1.000006, Case 8: 1.000006, Case 11: 1.000001, 1.000001, Case 19: 1.000006, Case 20: 1.000001, 1.000003, 1.000009, 1.000002, and Case 22: 1.000003). However, for this model, it is more likely that stability is dependent on the specific numerical parameters developed from the experimental data especially when considering that both acoustic liners yield stable results. It can therefore be concluded that the *Broadband* model is sufficient for predicting scattering by fully-lined bodies due to the fact that, for the numerical cases given, only Cases 1-3, 6, 8, 10, 12-14, 16-18, 21, and 23-24 be used. If additional acoustic liners are tested experimentally and numerical models developed, it is pertinent that each case is assessed for its stability prior to predicting the acoustic wave scattering using the *Broadband Impedance Model* while noting that for stability, it is required that resistance is a positive value. These results indicate that eigenvalue analysis, though not a sufficient condition for stability, is necessary.

TABLE VI: Maximum eigenvalues calculated for the *Extended Helmholtz Resonator Model* and *Three-Parameter Impedance Model* given discretizations $5\times5\times1$, $10\times10\times2$, $20\times20\times4$, and $30\times30\times6$ and time steps $\Delta t = 1/12$ and $\Delta t = 1/24$, assuming an impedance boundary condition is applied on all scattering surfaces, *i.e.*, soft body scattering.

Case	*Extended Helmholtz Resonator Model*, Impedance Boundary Condition, Soft Body							
	$\Delta t = 1/12$				$\Delta t = 1/24$			
	$5\times5\times1$	$10\times10\times2$	$20\times20\times4$	$30\times30\times6$	$5\times5\times1$	$10\times10\times2$	$20\times20\times4$	$30\times30\times6$
1	1.000000	1.000000	1.000000	1.000000	*dnc* †	1.000000	1.000000	1.000000
2	**1.017881**	*dnc* †	*dnc* †	*dnc*	0.999772	1.000000	0.999999	0.999999
3	*dnc* †	*dnc* †	*dnc* †	*dnc*	*dnc* †	*dnc* †	*dnc* †	*dnc*
4	1.000000	1.000000	1.000000	1.000000	*dnc* †	1.000000	1.000000	1.000000
5	1.000000	1.000000	0.999990	1.000000	*dnc* †	1.000000	1.000000	1.000000
6	*dnc* †	*dnc* †	*dnc* †	*dnc*	*dnc* †	*dnc* †	*dnc* †	*dnc*
7	1.000000	1.000000	1.000000	1.000000	*dnc* †	1.000000	1.000000	1.000000
8	1.000000	1.000000	1.000000	1.000000	*dnc* †	1.000000	1.000000	0.999999
9	*dnc* †	*dnc* †	*dnc* †	*dnc*	*dnc* †	*dnc* †	*dnc* †	*dnc*
10	**1.002829**	*dnc* †	*dnc* †	*dnc*	*dnc* †	**1.0006875**	*dnc* †	*dnc*
11	1.000000	1.000000	1.000000	1.000000	*dnc* †	1.000000	**1.000001**	0.999999
12	*dnc* †	*dnc* †	*dnc* †	*dnc*	*dnc* †	*dnc* †	*dnc* †	*dnc*
13	*dnc* †	*dnc* †	*dnc* †	*dnc*	*dnc* †	*dnc* †	*dnc* †	*dnc*
14	*dnc* †	*dnc* †	*dnc* †	*dnc*	*dnc* †	0.999999	*dnc* †	*dnc*
15	*dnc* †	*dnc* †	*dnc* †	*dnc*	*dnc* †	*dnc* †	*dnc* †	*dnc*
16	*dnc* †	*dnc* †	*dnc* †	*dnc*	*dnc* †	*dnc* †	*dnc* †	*dnc*
17	*dnc* †	*dnc* †	*dnc* †	*dnc*	*dnc* †	*dnc* †	*dnc* †	*dnc*
18	*dnc* †	*dnc* †	*dnc* †	*dnc*	*dnc* †	0.997547	*dnc* †	*dnc*
Case	*Three-Parameter Impedance Model*, Impedance Boundary Condition, Soft Body							
	$\Delta t = 1/12$				$\Delta t = 1/24$			
	$5\times5\times1$	$10\times10\times2$	$20\times20\times4$	$30\times30\times6$	$5\times5\times1$	$10\times10\times2$	$20\times20\times4$	$30\times30\times6$
1	**1.000001**	1.000000	1.000000	1.000000	**1.000004**	1.000000	1.000000	0.995652
4	**1.000003**	1.000000	1.000000	1.000000	0.995680	0.995693	0.995715	0.995715
7	**1.000008**	1.000000	1.000000	1.000000	1.000000	0.995758	0.995777	0.995780
10	1.000000	1.000000	1.000000	1.000000	1.000000	1.000000	1.000000	1.000000
13	1.000000	1.000000	1.000000	1.000000	1.000000	1.000000	1.000000	1.000000
16	1.000000	1.000000	1.000000	1.000000	1.000000	1.000000	1.000000	1.000000

TABLE VII: Maximum eigenvalues calculated for the *Extended Helmholtz Resonator Model* and *Three-Parameter Impedance Model* given discretizations $5\times5\times1$, $10\times10\times2$, $20\times20\times4$, and $30\times30\times6$ and time steps $\Delta t = 1/12$ and $\Delta t = 1/24$, assuming an admittance boundary condition is applied on all scattering surfaces, *i.e.*, soft body scattering.

Case	*Extended Helmholtz Resonator Model*, Admittance Boundary Condition, Soft Body							
	$\Delta t = 1/12$				$\Delta t = 1/24$			
	$5\times5\times1$	$10\times10\times2$	$20\times20\times4$	$30\times30\times6$	$5\times5\times1$	$10\times10\times2$	$20\times20\times4$	$30\times30\times6$
1	**1.001179**	**1.000641**	**1.000344**	**1.000237**	**1.000257**	**1.000128**	**1.000067**	**1.000047**
2	*dnc* †	*dnc* †	*dnc*	*dnc*	*dnc* †	*dnc* †	*dnc*	*dnc*
3	⋆⋆⋆	⋆⋆⋆	⋆⋆⋆	⋆⋆⋆	**1.398807**	⋆⋆⋆	*dnc*	⋆⋆⋆
4	**1.000673**	**1.000367**	**1.000197**	**1.000136**	**1.000070**	**1.000028**	**1.000019**	**1.000012**
5	*dnc* †	*dnc* †	*dnc*	*dnc*	*dnc* †	*dnc* †	*dnc*	*dnc*
6	**1.746528**	⋆⋆⋆	⋆⋆⋆	⋆⋆⋆	*dnc* †	**1.762173**	*dnc*	*dnc*
7	**1.000083**	**1.000045**	**1.000025**	**1.000017**	**1.000001**	**1.000009**	1.000000	1.000000
8	*dnc* †	*dnc* †	*dnc*	*dnc*	*dnc* †	*dnc* †	*dnc*	*dnc*
9	**1.679646**	⋆⋆⋆	⋆⋆⋆	⋆⋆⋆	*dnc* †	**1.693648**	*dnc*	*dnc*
10	**1.041789**	**1.037838**	**1.035973**	**1.035262**	0.999942	1.000000	1.000000	1.000000
11	*dnc* †	*dnc* †	*dnc*	*dnc*	*dnc* †	*dnc* †	*dnc*	*dnc*
12	**1.694827**	⋆⋆⋆	⋆⋆⋆	⋆⋆⋆	**1.218656**	**1.708369**	*dnc*	*dnc*
13	**1.028602**	**1.024535**	**1.021663**	**1.020462**	1.000000	1.000000	1.000000	1.000000
14	*dnc* †	*dnc* †	*dnc*	*dnc*	*dnc* †	*dnc* †	*dnc*	*dnc*
15	**1.758448**	⋆⋆⋆	⋆⋆⋆	⋆⋆⋆	**1.258092**	**1.773645**	*dnc*	*dnc*
16	**1.019933**	**1.015423**	**1.011951**	**1.010342**	1.000000	0.999999	1.000000	1.000000
17	*dnc* †	*dnc* †	*dnc*	*dnc*	*dnc* †	*dnc* †	*dnc*	*dnc*
18	⋆⋆⋆	⋆⋆⋆	⋆⋆⋆	⋆⋆⋆	**1.442119**	⋆⋆⋆	*dnc*	⋆⋆⋆
Case	*Three-Parameter Impedance Model*, Admittance Boundary Condition, Soft Body							
	$\Delta t = 1/12$				$\Delta t = 1/24$			
	$5\times5\times1$	$10\times10\times2$	$20\times20\times4$	$30\times30\times6$	$5\times5\times1$	$10\times10\times2$	$20\times20\times4$	$30\times30\times6$
1	0.994385	0.996788	0.998212	0.998745	*dnc* †	0.997762	0.998633	0.999024
4	0.994052	0.996584	0.998092	0.998658	*dnc* †	0.997570	0.998600	0.998999
7	0.993775	0.996411	0.997988	0.998583	*dnc* †	0.997527	0.998570	0.998976
10	0.999535	0.999739	0.999857	0.999901	*dnc* †	0.999869	0.999929	0.999951
13	0.999527	0.999736	0.999857	0.999901	*dnc* †	0.999868	0.999928	0.999944
16	0.999525	0.999736	0.999857	0.999901	*dnc* †	0.999868	0.999928	0.999950

TABLE VIII: Maximum eigenvalues calculated for the *Broadband Impedance Model* given discretizations $5 \times 5 \times 1$, $10 \times 10 \times 2$, $20 \times 20 \times 4$, and $30 \times 30 \times 6$ and time steps $\Delta t = 1/24$ and $\Delta t = 1/24$, assuming an impedance boundary condition is applied on all scattering surfaces, *i.e.*, soft body scattering.

Case	*Broadband Impedance Model*, Impedance Boundary Condition, Soft Body							
	$\Delta t = 1/12$				$\Delta t = 1/24$			
	$5 \times 5 \times 1$	$10 \times 10 \times 2$	$20 \times 20 \times 4$	$30 \times 30 \times 6$	$5 \times 5 \times 1$	$10 \times 10 \times 2$	$20 \times 20 \times 4$	$30 \times 30 \times 6$
1	1.000000	1.000000	1.000000	1.000000	1.000000	1.000000	1.000000	1.000000
2	1.000000	1.000000	1.000000	1.000000	1.000000	1.000000	1.000000	1.000000
3	1.000000	1.000000	1.000000	1.000000	1.000000	1.000000	1.000000	1.000000
4	0.999976	**1.000231**	**1.000079**	**1.000029**	**1.000017**	0.999965	0.999958	0.999994
5	**1.000006**	1.000000	1.000000	1.000000	**1.000026**	1.000000	1.000000	1.000000
6	1.000000	1.000000	1.000000	1.000000	1.000000	1.000000	1.000000	1.000000
7	1.000000	1.000000	1.000000	1.000000	*dnc* †	1.000000	**1.000041**	1.000000
8	1.000000	1.000000	1.000000	*emb*	1.000000	1.000000	1.000000	*emb*
9	1.000000	1.000000	1.000000	1.000000	**1.000006**	1.000000	1.000000	1.000000
10	1.000000	1.000000	1.000000	1.000000	1.000000	1.000000	1.000000	1.000000
11	1.000000	**1.000056**	**1.000001**	1.000000	**1.000056**	**1.000001**	0.997911	1.000000
12	0.997825	0.999678	0.998873	0.999674	0.999630	0.999641	0.999758	0.999650
13	1.000000	1.000000	1.000000	1.000000	1.000000	1.000000	1.000000	1.000000
14	1.000000	1.000000	1.000000	1.000000	1.000000	1.000000	1.000000	1.000000
15	0.999965	1.000000	1.000000	*emb*	*dnc* †	**1.001096**	1.000000	*emb*
16	1.000000	1.000000	1.000000	*emb*	0.999999	1.000000	1.000000	*emb*
17	1.000000	1.000000	1.000000	*emb*	1.000000	1.000000	1.000000	*emb*
18	1.000000	1.000000	1.000000	*emb*	1.000000	1.000000	1.000000	*emb*
19	**1.000065**	1.000000	1.000000	1.000000	**1.000006**	1.000000	1.000000	1.000000
20	**1.000001**	**1.000165**	**1.000023**	**1.000003**	**1.000165**	**1.000076**	**1.000009**	**1.000002**
21	1.000000	1.000000	1.000000	1.000000	1.000000	1.000000	1.000000	1.000000
22	**1.000060**	**1.000003**	1.000000	1.000000	**1.000045**	1.000000	1.000000	1.000000
23	1.000000	1.000000	1.000000	1.000000	1.000000	1.000000	1.000000	1.000000
24	1.000000	1.000000	1.000000	1.000000	1.000000	1.000000	1.000000	1.000000
25	**1.000134**	**1.000102**	**1.000091**	**1.000091**	**1.000077**	**1.000048**	**1.000043**	**1.000043**

In contrast to both the *Three-Parameter* and *Broadband* models, the *Extended Helmholtz Resonator Model* analysis demonstrates that the majority of eigenvalues are greater than unity. Though an impedance boundary condition yields some[4] stable results for time steps $\Delta t = 1/12, 1/24$ and discretizations $10 \times 10 \times 2$, $20 \times 20 \times 4$, $30 \times 30 \times 6$, the majority of cases do not. Using an admittance boundary condition, on the other hand, yields no[5] stable or convergent results for $\Delta 1 = 1/12$ and very few for $\Delta t = 1/24$. These results further indicate that eigenvalue analysis, though not a sufficient condition for stability, is necessary.

Referring back to the eighteen curves whose data are listed in Table II, stability tends to occur for an impedance boundary condition with negative reactance and small ν, *e.g.* in Cases 1, 4-5, 7-8 defined by $Z_I = -3$ and $\nu = 1$, $Z_I = -2$ and $\nu = 1, 5$, and $Z_I = -1$ and $\nu = 1, 5$, respectively. Case 11 is also stable for impedance, and in this case, $Z_I = 1$ and $\nu = 15$. Moreover, stability tends to occur for an admittance boundary condition, $\Delta t = 1/24$ only, with positive reactance and large ν, *e.g.* in Cases 10, 13, 16 defined by $Z_I = 1$ and $\nu = 19$, $Z_I = 2$ and $\nu = 19$, and $Z_I = 3$ and $\nu = 19$, respectively. Case 7 is also stable for admittance, $\Delta t = 1/24$ only, and in this case, $Z_I = -1$ and $\nu = 1$.

For both impedance and admittance, the *Helmholtz* model cases with neither convergence nor stability largely occur when there is a high variability at the chosen frequency $\omega_0 \Delta t$ or when near resonance. These results follow the observation in [59] where it is stated: "for $\mathrm{Im}(z_0) < 0$ the best choice, *i.e.*, where Z varies not too much near Z_0, is for $\nu = 1$" and "for $\mathrm{Im}(z_0) > 0$ on the other hand, it is better to be halfway between $\nu = N/2$ and N" while noting that, here, $N = 20$. A study by Richter *et. al.* [66] also found that instability could occur in some cases. Given the results listed in Tables VI and VII, it is a more logical choice to model an impedance or admittance boundary condition at a single frequency using the *Three-Parameter Impedance Model* instead of the *Extended Helmholtz Resonator Model*. There are significantly less restrictions for ensuring stability with the *Three-Parameter* model. The *Helmholtz* model, for both impedance and admittance, is largely insufficient for predicting scattering by fully-lined bodies.

6.4 CONVERGENCE CRITERIA

It should be noted that in [2], the *Helmholtz* and *Three-Parameter* models were assessed using both impedance and admittance boundary conditions with less strict convergence

[4]Only six of eighteen cases are stable: Cases 1, 4-5, 7-8, 11 are stable assuming that, in Case 11, the eigenvalue 1.000001 is a result of rounding error.

[5]Only four of eighteen cases are stable: Cases 7, 10, 13, 16 are stable, assuming that, in Case 7, the eigenvalues 1.000001 and 1.000009 are results of rounding error.

criterion for the tolerance δ: if iterations $< 5,000$ then $\delta = 10^{-9}$, if $5,000 \leq$ iterations $< 10,000$ then $\delta = 10^{-6}$, if $10,000 \leq$ iterations $< 15,000$ then $\delta = 10^{-4}$, and if iterations $\geq 15,000$ then the solution is considered non-convergent. With this criterion, more cases are considered stable for the *Helmholtz* model. However, several of these cases are either non-convergent or yield eigenvalues greater than unity given the stricter tolerance limitation defined herein: $\delta < 10^{-9}$ within $5,000$ iterations. If, *e.g.*, reducing the tolerance after 5,000 iterations, the $10 \times 10 \times 2$, $\Delta t = 1/12$ *Helmholtz* model with impedance boundary condition yields maximum eigenvalues of:

- Case 1: $\lambda_{\max} = 0.999999993$ such that $\delta = 10^{-9}$ after 355 iterations
- Case 2: $\lambda_{\max} = 0.83147$ such that $\delta = 10^{-5}$ after 6,820 iterations
- Case 3: $\lambda_{\max} = 0.57459$ such that $\delta = 10^{-5}$ after 267,465 iterations
- Case 4: $\lambda_{\max} = 1.000000003$ such that $\delta = 10^{-9}$ after 220 iterations
- Case 5: $\lambda_{\max} = 1.000000010$ such that $\delta = 10^{-9}$ after 685 iterations
- Case 6: $\lambda_{\max} = 0.619165$ such that $\delta = 10^{-6}$ after 907,925 iterations
- Case 7: $\lambda_{\max} = 1.000000013$ such that $\delta = 10^{-9}$ after 145 iterations
- Case 8: $\lambda_{\max} = 1.000000050$ such that $\delta = 10^{-9}$ after 160 iterations
- Case 9: $\lambda_{\max} = 0.6072157$ such that $\delta = 10^{-7}$ after 528,555 iterations
- Case 10: $\lambda_{\max} = 0.9884644$ such that $\delta = 10^{-7}$ after 7,190 iterations
- Case 11: $\lambda_{\max} = 0.999999772$ such that $\delta = 10^{-9}$ after 595 iterations
- Case 12: $\lambda_{\max} = 1.0146873$ such that $\delta = 10^{-7}$ after 49,525 iterations
- Case 13: $\lambda_{\max} = 0.9882871$ such that $\delta = 10^{-7}$ after 143,665 iterations
- Case 14: $\lambda_{\max} = 1.0027441$ such that $\delta = 10^{-7}$ after 18,305 iterations
- Case 15: $\lambda_{\max} = 1.006487$ such that $\delta = 10^{-6}$ after 5,310 iterations
- Case 16: $\lambda_{\max} = 1.0219033$ such that $\delta = 10^{-7}$ after 201,475 iterations
- Case 17: $\lambda_{\max} = 0.9912392$ such that $\delta = 10^{-7}$ after 255,905 iterations
- Case 18: $\lambda_{\max} = 1.06011996$ such that $\delta = 10^{-8}$ after 662,8000 iterations

where each of the listed eigenvalues are from the smallest tolerance obtained between 5,000 and 10^6 iterations and the number of decimal places shown are indicative of the significant digits between consecutive iterations. As demonstrated by the results above, the tightest tolerance obtained for all eighteen cases is $\delta = 10^{-5}$. Had the convergence criteria rather been defined with a tolerance of $\delta = 10^{-5}$, the $10 \times 10 \times 2$, $\Delta t = 1/12$ *Helmholtz* model with impedance boundary condition would therefore have yielded eigenvalues of:

- Case 1: $\lambda_{\max} = 0.99986$ after 175 iterations
- Case 2: $\lambda_{\max} = 0.83147$ after 6,820 iterations
- Case 3: $\lambda_{\max} = 0.57459$ after 267,465 iterations
- Case 4: $\lambda_{\max} = 0.99997$ after 115 iterations
- Case 5: $\lambda_{\max} = 0.99964$ after 385 iterations
- Case 6: $\lambda_{\max} = 0.61917$ after 246,150 iterations
- Case 7: $\lambda_{\max} = 0.99992$ after 65 iterations
- Case 8: $\lambda_{\max} = 0.99941$ after 65 iterations
- Case 9: $\lambda_{\max} = 0.60144$ after 16,670 iterations
- Case 10: $\lambda_{\max} = 0.98821$ after 1,135 iterations
- Case 11: $\lambda_{\max} = 0.99995$ after 365 iterations
- Case 12: $\lambda_{\max} = \mathbf{1.00890}$ after 2,985 iterations
- Case 13: $\lambda_{\max} = 0.99660$ after 6,800 iterations
- Case 14: $\lambda_{\max} = \mathbf{1.01150}$ after 1,405 iterations
- Case 15: $\lambda_{\max} = \mathbf{1.00491}$ after 5,080 iterations
- Case 16: $\lambda_{\max} = \mathbf{1.01475}$ after 1,630 iterations
- Case 17: $\lambda_{\max} = 0.98861$ after 2,575 iterations
- Case 18: $\lambda_{\max} = 0.97277$ after 1,650 iterations

In this example, all analyses for the $10 \times 10 \times 2$, $\Delta t = 1/12$ *Helmholtz* model with impedance boundary condition are stable except for Cases 12, 14-16 unlike with the stricter tolerance defined herein when only Cases 1, 4-5, 7-8, 11 are stable and Cases 2-3, 6, 9-10, 12-18 are non-convergent (see Table VI). Further, it should be noted that many of the unstable analyses in Table VI, *e.g.*, Cases 2-3, 6, 9, 13, require more than 5,000 iterations to achieve a tolerance less than 10^{-5}. Similar results are obtained for all scenarios investigated.

Though a less strict convergence criterion identifies more stable models, it is decided that a stricter tolerance is ideal for assessing stability of the numerical algorithm and for the results presented herein. This stricter tolerance provides a more succinct list of cases that provide stable results given either a *Helmholtz*, *Three-Parameter*, or *Broadband* model for simulating an acoustic liner on scattering surfaces.

6.5 STABILITY OF PARTIALLY-LINED BODIES

To further assess stability of the *Helmholtz*, *Three-Parameter*, and *Broadband* models,

a partially-lined body is also considered. Herein referred to as "*mixed*," it is assumed for this configuration that an acoustic liner is installed on the top-surface of the flat plate nearest the point source (refer to Figure 3a). Only discretizations $5 \times 5 \times 1$ and $10 \times 10 \times 2$ are considered for this analysis. The partially-lined bodies for these discretizations are illustrated in Figure 44. Since stability parameters have been previously identified for each model with fully-lined bodies given both coarse and fine grids and large and small time steps, all discretizations need not be used to assess numerical stability for *mixed* bodies. For this assessment, all matrices associated with un-lined surface elements are equivalently set equal to zero. The eigenvalue results are listed in Table IX for $\Delta t = 1/12$ and Table X for $\Delta t = 1/24$.

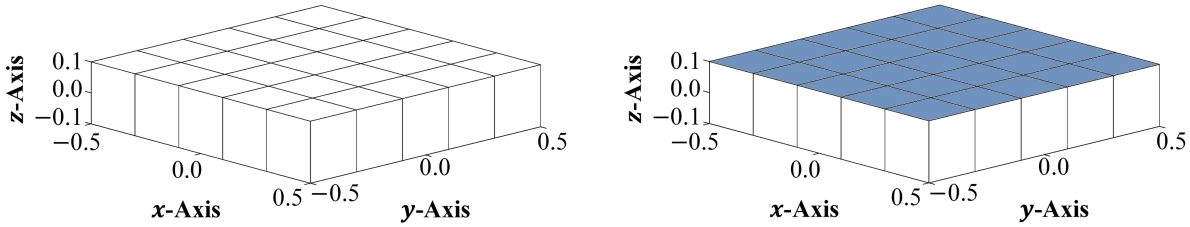

(a) Rigid Body, $5 \times 5 \times 1$

(b) Mixed Body, $5 \times 5 \times 1$

(c) Rigid Body, $10 \times 10 \times 2$

(d) Mixed Body, $10 \times 10 \times 2$

Fig. 44: Schematic diagrams illustrating the partially-lined scattering bodies for discretizations $5 \times 5 \times 1$ and $10 \times 10 \times 2$, compared with un-lined bodies.

Similar to the soft body analyses, the *Three-Parameter Impedance Model* further demonstrates stability for mixed body scattering given both an impedance and admittance boundary condition in all six numerical cases for time steps $\Delta t = 1/12, 1/24$ and discretizations $10 \times 10 \times 2$, $20 \times 20 \times 4$, $30 \times 30 \times 6$. Apart from $5 \times 5 \times 1$, all analyses yield a maximum eigenvalue no greater than unity. While there are some instances where round-off error may contribute to eigenvalues greater than unity (*e.g.*, 1.000001, 1.000002, 1.000002 for Cases 1, 4, 7 with $\Delta t = 1/24$), it is more likely that the *Three-Parameter* model yields numerical

stability for fine grids when $\Delta t \approx \Delta x$. The mixed body scattering results are consistent with the soft body, thus demonstrating that the *Three-Parameter Impedance Model* is sufficient for predicting scattering by both partially- and fully-lined bodies when, at a minimum, the condition $\Delta t \approx \Delta x$ is satisfied.

TABLE IX: Maximum eigenvalues calculated for discretizations $5 \times 5 \times 1$ and $10 \times 10 \times 2$ (*Helmholtz, Three-Parameter, Broadband*) with $\Delta t = 1/12$, assuming a partially-lined body.

Case	*Broadband, Impedance*		**Case**	*Helmholtz, Impedance*		*Helmholtz, Admittance*	
	$5 \times 5 \times 1$	$10 \times 10 \times 2$		$5 \times 5 \times 1$	$10 \times 10 \times 2$	$5 \times 5 \times 1$	$10 \times 10 \times 2$
1	1.000000	1.000000	**1**	1.000000	1.000000	**1.000292**	**1.0000641**
2	1.000000	1.000000	**2**	*dnc* †	*dnc* †	*dnc* †	*dnc* †
3	1.000000	1.000000	**3**	*dnc* †	*dnc* †	⋆⋆⋆	⋆⋆⋆
4	**1.000148**	**1.000173**	**4**	1.000000	1.000000	**1.000169**	**1.000367**
5	1.000000	0.993455	**5**	1.000000	1.000000	*dnc* †	*dnc* †
6	1.000000	1.000000	**6**	*dnc* †	*dnc* †	**1.739504**	⋆⋆⋆
7	1.000000	1.000000	**7**	1.000000	1.000000	**1.000021**	**1.000045**
8	0.989167	1.000000	**8**	1.000000	1.000000	*dnc* †	*dnc* †
9	1.000000	1.000000	**9**	*dnc* †	*dnc* †	**1.672663**	⋆⋆⋆
10	1.000000	1.000000	**10**	0.971815	*dnc* †	**1.029051**	**1.037838**
11	**1.000111**	**1.000056**	**11**	1.000000	1.000000	0.999950	*dnc* †
12	0.999540	0.999678	**12**	*dnc* †	*dnc* †	**1.688297**	⋆⋆⋆
13	1.000000	1.000000	**13**	*dnc* †	*dnc* †	**1.014432**	**1.024535**
14	1.000000	1.000000	**14**	*dnc* †	*dnc* †	*dnc* †	*dnc* †
15	1.000000	1.000000	**15**	*dnc* †	*dnc* †	**1.751776**	⋆⋆⋆
16	1.000000	1.000000	**16**	*dnc* †	*dnc* †	**1.007172**	**1.015423**
17	1.000000	1.000000	**17**	*dnc* †	*dnc* †	*dnc* †	*dnc* †
18	1.000000	1.000000	**18**	*dnc* †	*dnc* †	⋆⋆⋆	⋆⋆⋆
19	**1.000004**	1.000000	**Case**	*Three-Parameter, Impedance*		*Three-Parameter, Admittance*	
20	0.998459	**1.000165**	**1**	1.000000	1.000000	0.998224	0.996788
21	1.000000	1.000000	**4**	1.000000	1.000000	0.998092	0.996584
22	1.000000	**1.000003**	**7**	1.000000	1.000000	0.997977	0.996411
23	1.000000	1.000000	**10**	1.000000	1.000000	0.999874	0.999739
24	1.000000	1.000000	**13**	1.000000	1.000000	0.999873	0.999736
25	**1.000099**	**1.000102**	**16**	1.000000	1.000000	0.999873	0.999736

TABLE X: Maximum eigenvalues calculated for discretizations $5 \times 5 \times 1$ and $10 \times 10 \times 2$ (*Helmholtz, Three-Parameter, Broadband*) with $\Delta t = 1/24$, assuming a partially-lined body.

Case	*Broadband, Impedance*		**Case**	*Helmholtz, Impedance*		*Helmholtz, Admittance*	
	$5 \times 5 \times 1$	$10 \times 10 \times 2$		$5 \times 5 \times 1$	$10 \times 10 \times 2$	$5 \times 5 \times 1$	$10 \times 10 \times 2$
1	1.000000	1.000000	**1**	*dnc* †	1.000000	**1.000064**	**1.000128**
2	1.000000	1.000000	**2**	0.999999	1.000000	*dnc* †	*dnc* †
3	1.000000	1.000000	**3**	*dnc* †	*dnc* †	**1.394840**	⋆⋆⋆
4	0.999999	0.999981	**4**	*dnc* †	1.000000	**1.000017**	**1.000028**
5	1.000000	1.000000	**5**	0.999999	1.000000	*dnc* †	*dnc* †
6	1.000000	1.000000	**6**	*dnc* †	*dnc* †	*dnc* †	**1.762173**
7	0.999994	1.000000	**7**	*dnc* †	1.000000	**1.000001**	**1.000009**
8	1.000000	1.000000	**8**	1.000000	1.000000	*dnc* †	*dnc* †
9	1.000000	1.000000	**9**	**1.014022**	*dnc* †	*dnc* †	**1.693648**
10	1.000000	1.000000	**10**	*dnc* †	**1.006875**	1.000000	1.000000
11	**1.000006**	**1.000001**	**11**	1.000000	1.000000	*dnc* †	*dnc* †
12	0.999200	0.999641	**12**	*dnc* †	*dnc* †	**1.213335**	**1.708369**
13	1.000000	1.000000	**13**	*dnc* †	*dnc* †	1.000000	1.000000
14	1.000000	1.000000	**14**	0.999976	0.999999	*dnc* †	*dnc* †
15	*dnc* †	**1.001096**	**15**	*dnc* †	*dnc* †	**1.253654**	**1.7773645**
16	1.000000	1.000000	**16**	*dnc* †	*dnc* †	1.000000	0.999999
17	1.000000	1.000000	**17**	*dnc* †	*dnc* †	*dnc* †	*dnc* †
18	1.000000	1.000000	**18**	*dnc* †	0.997547	**1.439175**	⋆⋆⋆
19	1.000000	1.000000	**Case**	*Three-Parameter, Impedance*		*Three-Parameter, Admittance*	
20	0.999999	**1.000076**	**1**	**1.000001**	1.000000	*dnc* †	0.997620
21	1.000000	1.000000	**4**	**1.000002**	0.995693	*dnc* †	0.997570
22	0.997424	1.000000	**7**	**1.000002**	0.995758	*dnc* †	0.997527
23	1.000000	1.000000	**10**	1.000000	1.000000	0.569258	0.999869
24	1.000000	1.000000	**13**	1.000000	1.000000	0.999935	0.999868
25	**1.000057**	**1.000048**	**16**	1.000000	1.000000	0.999937	0.999868

The *Broadband Impedance Model* mixed body analysis is also consistent with the soft body results. For both time steps, as with rigid body scattering, Cases 1-3, 6, 8, 10, 12-14, 16-18, 21, and 23-24 are stable and yield eigenvalues no greater than unity. This further demonstrates that the *Broadband* model is sufficient for predicting scattering by both partially- and fully-lined bodies such that, each numerical case is assessed prior. Further, the *Extended Helmholtz Resonator Model* mixed body analysis is also consistent with the soft body results given that stability tends to occur for an impedance boundary condition with

negative reactance and small ν (for both time steps $\Delta t = 1/12, 1/24$) and for an admittance boundary condition with positive reactance and large ν (for $\Delta t = 1/24$). These results further demonstrate that not only is eigenvalue analysis necessary for assessing stability, but also that the *Helmholtz* model is largely insufficient for predicting scattering by both partially- and fully-lined bodies and the *Three-Parameter Impedance Model* is preferable for modeling an acoustically treated surface at a single frequency.

6.6 NUMERICAL EXAMPLE OF POINT SOURCE REFLECTION

In this section, a numerical example of a point source reflection by a flat plate with a *Three-Parameter* impedance boundary condition is presented and compared to an analytical solution. The flat plate has dimension $[-2, 2] \times [-2, 2] \times [-0.02, 0]$ and is discretized on the surface by $201 \times 201 \times 4$ giving a total of $N = 84,018$ elements. The point source is centered above the flat plate at $\boldsymbol{r}_0 = (0.0, 0.0, 1.0)$. Further, the source term is defined by:

$$q(\boldsymbol{r}, t) = e^{-\sigma t^2} \delta(\boldsymbol{r} - \boldsymbol{r}_0)$$

where $\sigma = 1.42/(6\Delta t)^2$ and $\Delta t = 1/160$.

On the scattering surface, the *Three-Parameter* impedance model (76) is applied on all elements with $R_0 = 0.5$, $h_0 = 0.1$, and $A_0 = (0.2 + \omega_0 h_0)\omega_0$ such that A_0 is evaluated at a given frequency ω_0. These parameters yield an impedance of $Z(\omega_0) = 0.5 + 0.2i$. Figure 45 illustrates two instantaneous solutions at $t = 280\Delta t$ such that $\omega_0 = 12\pi$. The effect of lined surfaces on the absorption of the pulse is clearly visualized by the weakened reflection (right of Figure 45) as compared to the reflection by the solid surface (left of Figure 45).

The time-domain solution can be converted to the frequency-domain by either using a fast Fourier transform algorithm or the following summation:

$$p(\boldsymbol{r}, \omega) = \Delta t \left[p(\boldsymbol{r}, t_1) e^{-i\omega t_1} + p(\boldsymbol{r}, t_2) e^{-i\omega t_2} + p(\boldsymbol{r}, t_3) e^{-i\omega t_3} + \cdots + p(\boldsymbol{r}, t_{N_t}) e^{-i\omega t_{N_t}} \right]$$

where Δt is the time step of the March-On-in-Time scheme and N_t is the total number of time steps. Figure 46 illustrates the frequency-domain solution at $\omega = 6\pi$ and $\omega = 12\pi$. In the figure, the dotted line identifies a field line of coordinates located at $-2.5 \leq x \leq 2.5$, $y = 0$, and $z = 0.5$. Moreover, the point source is visualized directly above the flat plate.

To validate the numerical solution, the frequency-domain computational results are compared with the frequency-domain analytic solution for a flat plate of infinite length, derived herein. For reference, a time-domain analytic solution can be found in [90]. For the derivation of the frequency-domain analytic solution, consider the solution in terms of velocity

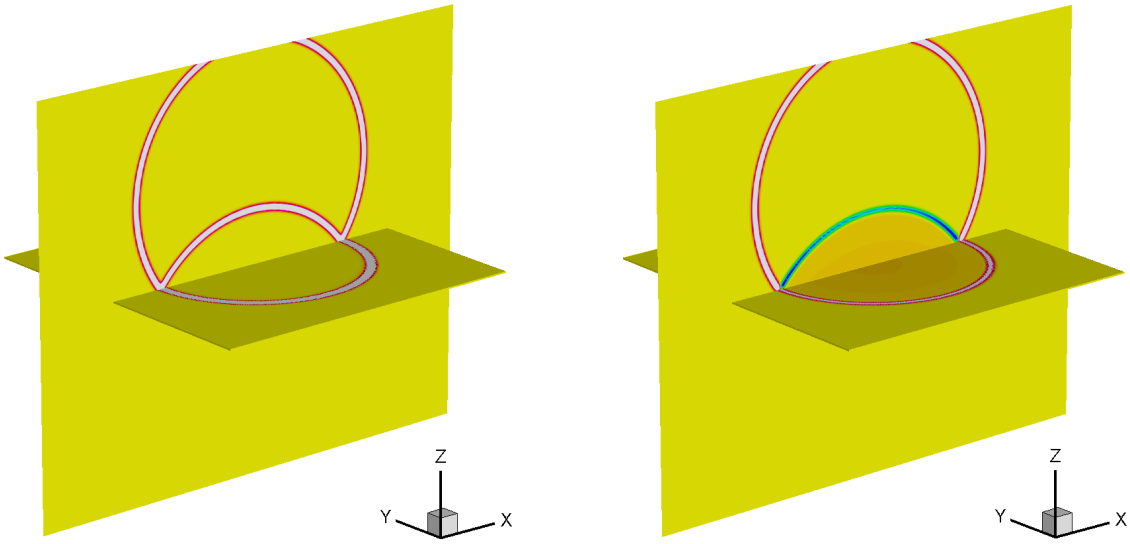

Fig. 45: Illustration of instantaneous solution contours comparing the reflection of a point source by an un-lined surface (left) to a fully-lined surface (right).

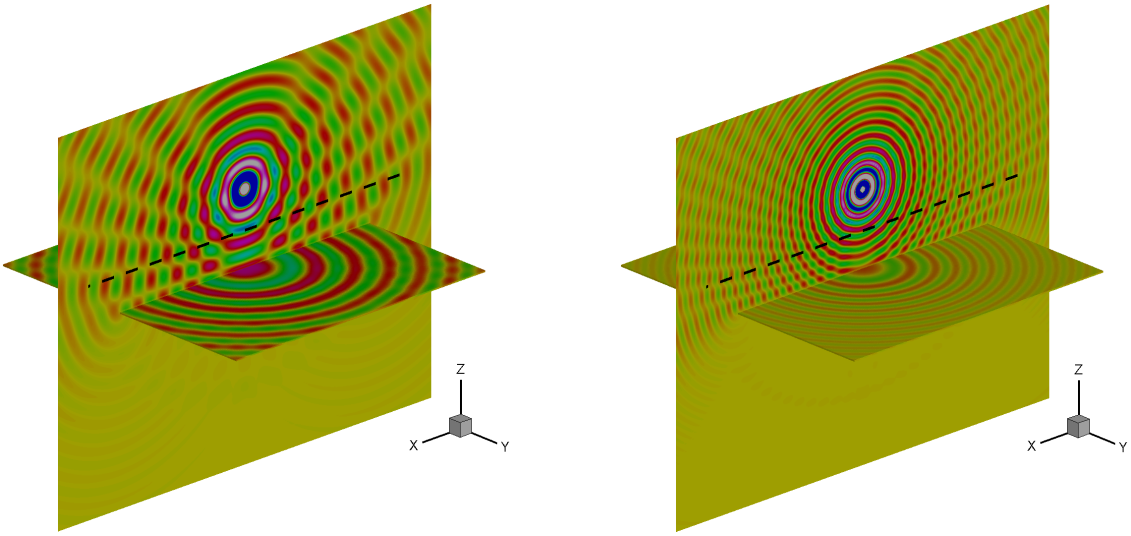

Fig. 46: Illustration of the frequency-domain solution for the reflection of a point source by a fully-lined flat plate at $\omega = 6\pi$ (left) and $\omega = 12\pi$ (right).

potential ϕ where:

$$p = -\rho_0 \frac{\partial \phi}{\partial t} \text{ and } \boldsymbol{u} = \nabla \phi.$$

Assume that the scattering surface is located at $z = 0$ and the point source is located at $\boldsymbol{r}_0 = (x_0, y_0, z_0)$ for all $z_0 > 0$. By the Weyl Identity [91], the frequency-domain solution for the wave equation by a point source is expressed in plane waves as follows:

$$\phi_{\text{inc}} = \frac{\exp\left[ik|\boldsymbol{r} - \boldsymbol{r}_0|\right]}{4\pi|\boldsymbol{r} - \boldsymbol{r}_0|} = \frac{i}{8\pi^2} \int_{-\infty}^{\infty} \int_{-\infty}^{\infty} \frac{\exp\left[i(k_x(x - x_0) + k_y(y - y_0) + \gamma|z - z_0|)\right]}{\gamma} \, dk_x \, dk_y$$

where $\gamma = \sqrt{k^2 - k_x^2 - k_y^2}$.

The time-dependency is assumed to be $e^{-i\omega t}$ and a dispersion relation $\omega = ck$ is assumed for the case without mean flow. The plane wave incident on the lined surface, denoted by a hat, is of the form:

$$\hat{\phi}_{\text{inc}}(x, y, z) = A_{\text{inc}} \exp\left[i(k_x(x - x_0) + k_y(y - y_0) - \gamma(z - z_0))\right]. \tag{108}$$

Further, the wave reflected by the surface at $z = 0$ is expressed as:

$$\hat{\phi}_{\text{ref}}(x, y, z) = A_{\text{ref}} \exp\left[i(k_x(x - x_0) + k_y(y - y_0) + \gamma(z + z_0))\right]. \tag{109}$$

Adding (108) and (109) results in a total field at $z = 0$ such that $\hat{\phi} = \hat{\phi}_{\text{inc}} + \hat{\phi}_{\text{ref}}$, or:

$$\begin{aligned} \hat{\phi}(x, y, z) = {} & A_{\text{inc}} \exp\left[i(k_x(x - x_0) + k_y(y - y_0) - \gamma(z - z_0))\right] \\ & + A_{\text{ref}} \exp\left[i(k_x(x - x_0) + k_y(y - y_0) + \gamma(z + z_0))\right]. \end{aligned}$$

The impedance boundary condition is defined in terms of velocity potential ϕ to be:

$$Z(\omega) = \frac{p}{\rho_0 c v_n} = -\frac{i\omega\hat{\phi}}{c\frac{\partial \hat{\phi}}{\partial z}} = -\frac{ik\hat{\phi}}{\frac{\partial \hat{\phi}}{\partial z}} \tag{110}$$

where v_n is the normal velocity with direction into the surface. Applying (110) to $\hat{\phi}(x, y, z)$ at $z = 0$ gives an impedance boundary condition of:

$$Z = \frac{ik\left(A_{\text{inc}} + A_{\text{ref}}\right)\exp\left[i(k_x(x - x_0) + k_y(y - y_0) + \gamma(z_0))\right]}{i\gamma\left(A_{\text{inc}} - A_{\text{ref}}\right)\exp\left[i(k_x(x - x_0) + k_y(y - y_0) + \gamma(z_0))\right]} = \frac{k\left(A_{\text{inc}} + A_{\text{ref}}\right)}{\gamma\left(A_{\text{inc}} - A_{\text{ref}}\right)}.$$

By letting $\hat{A} = A_{\text{ref}}/A_{\text{inc}}$, it is straightforward to show that $\hat{A} = (\gamma Z - k)/(\gamma Z + k)$. Hence, the reflected wave of the point source is given by:

$$\phi_{\text{ref}}(x, y, z) = \frac{i}{8\pi^2} \int_{-\infty}^{\infty} \int_{-\infty}^{\infty} \frac{\hat{A} \exp\left[i(k_x(x - x_0) + k_y(y - y_0) + \gamma(z + z_0))\right]}{\gamma} \, dk_x \, dk_y.$$

For direct numerical evaluation, a change of variables from (k_x, k_y) to (u, v) is introduced such that $k_x = u\cos v$ and $k_y = u\sin v$. This change of variables gives:

$$\begin{aligned}\phi_{\text{ref}}(x,y,z) &= \frac{i}{8\pi^2}\int_0^{2\pi}\int_0^{\infty}\frac{\hat{A}\exp\left[i(k_x(x-x_0)+k_y(y-y_0)+\gamma(z+z_0))\right]}{\gamma}\,u\,du\,dv \\ &= \frac{i}{8\pi^2}\int_0^{2\pi}\int_0^{\infty}\frac{\hat{A}\exp\left[i(u\cos v(x-x_0)+u\sin v(y-y_0)+\sqrt{k^2-u^2}(z+z_0))\right]}{\gamma}\,u\,du\,dv,\end{aligned}$$

where $\gamma = \sqrt{k^2-k_x^2-k_y^2} = \sqrt{k^2-u^2}$. Further simplifications yield:

$$\int_0^{2\pi}\exp\left[iu(\cos v(x-x_0)+\sin v(y-y_0))\right]\,dv = \int_0^{2\pi}\exp\left[iur'\cos(v-\theta')\right]\,dv = 2\pi J_0(ur')$$

such that $x - x_0 = r'\cos\theta'$, $y - y_0 = r'\sin\theta'$, and J_0 is a Bessel Function of the First Kind. Hence, ϕ_{ref} is given to be:

$$\phi_{\text{ref}} = \frac{i}{4\pi}\int_0^{\infty}\frac{\hat{A}\exp\left[i\gamma(z+z_0)\right]}{\gamma}J_0(ur')\,u\,du.$$

Furthermore, by considering a change of variables for $0 < u < k$:

$$\xi = \frac{\gamma}{k}, u = k\sqrt{1-\xi^2}, du = -\frac{k^2}{u}\xi\,d\xi$$

and a change of variables for $k < u < \infty$:

$$\xi = -\frac{i\gamma}{k}, u = k\sqrt{1+\xi^2}, du = \frac{k^2}{u}\xi\,d\xi,$$

the following analytical expression is obtained for the reflected wave:

$$\begin{aligned}\phi_{\text{ref}}(x,y,z) = &\frac{ik}{4\pi}\int_0^1\hat{A}(\xi)\exp\left[ik\xi(z+z_0)\right]J_0(kr'\sqrt{1-\xi^2})\,d\xi \\ &+\frac{k}{4\pi}\int_0^{\infty}\hat{A}(i\xi)\exp\left[-k\xi(z+z_0)\right]J_0(kr'\sqrt{1+\xi^2})\,d\xi\end{aligned}$$

such that

$$\hat{A}(\xi) = \frac{\xi Z - 1}{\xi Z + 1} \text{ and } \hat{A}(i\xi) = \frac{i\xi Z - 1}{i\xi Z + 1}.$$

The frequency-domain solutions along the field line of coordinates $-2.5 \le x \le 2.5$, $y = 0$, and $z = 0.5$, shown as dotted lines in Figure 46, are graphed with a solid line in Figures 47 and 48. Also graphed with solid markers is the analytic solution derived herein for the incident ϕ_{inc} and reflected ϕ_{ref} waves. As demonstrated by Figures 47 and 48, very good agreements are observed for the solutions at frequencies $\omega = 6\pi$ and $\omega = 12\pi$, respectively.

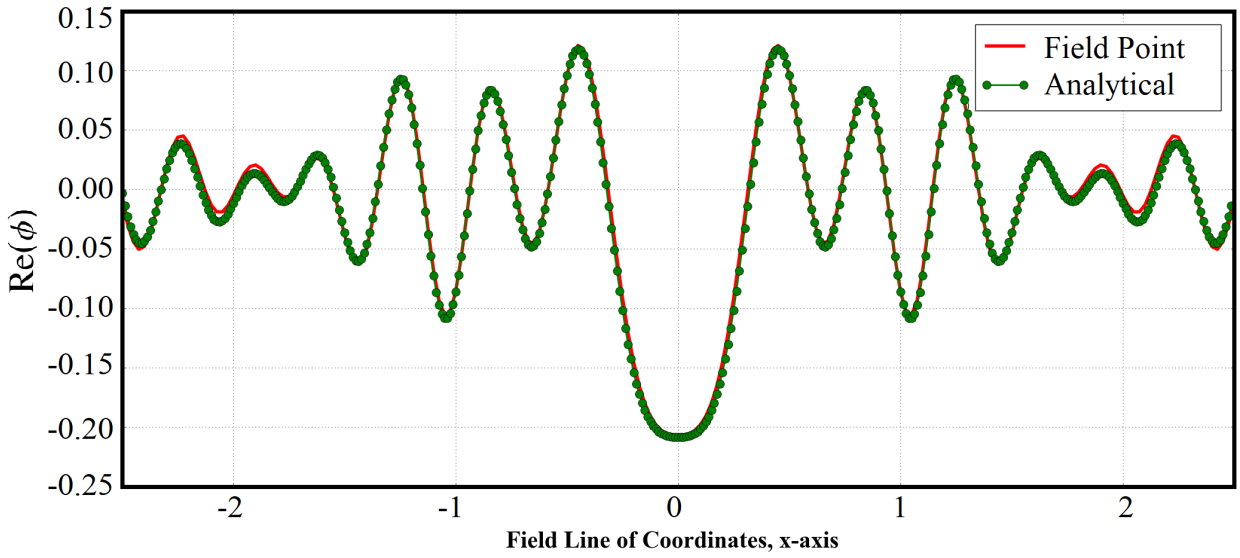

Fig. 47: Comparison of the numerical frequency-domain solution along the field line specified by $-2.5 \leq x \leq 2.5$ (as depicted in Figure 46) to the analytical solution such that $\omega = 6\pi$.

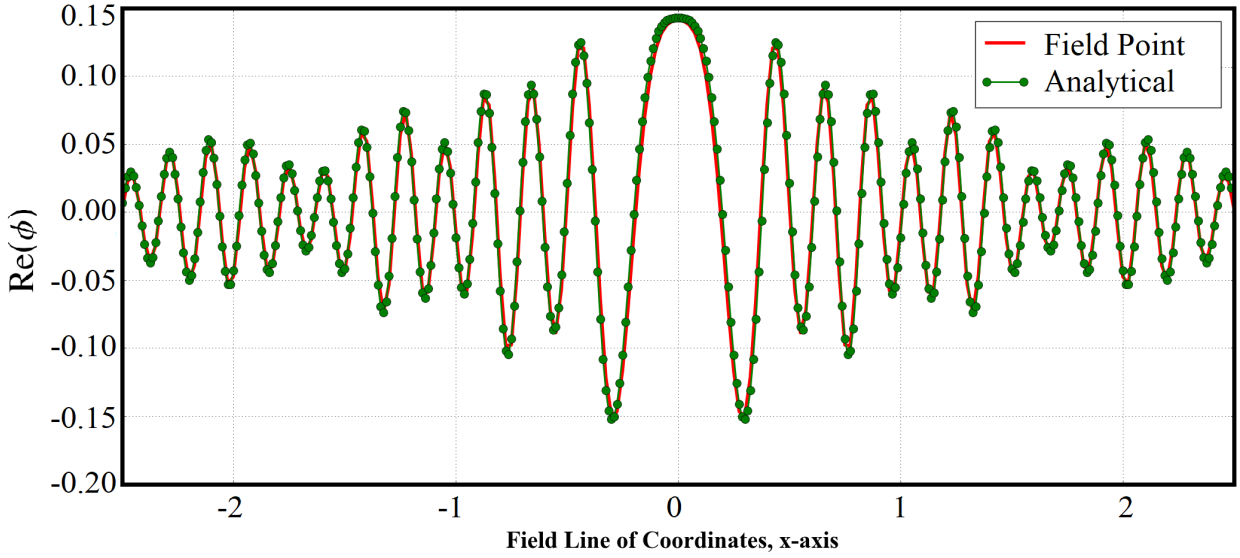

Fig. 48: Comparison of the numerical frequency-domain solution along the field line specified by $-2.5 \leq x \leq 2.5$ (as depicted in Figure 46) to the analytical solution such that $\omega = 12\pi$.

CHAPTER 7

CONCLUDING REMARKS

Reducing aircraft noise is a major objective in the field of computational aeroacoustics. When designing next generation quiet aircraft, it is important to be able to accurately and efficiently predict the acoustic scattering by an aircraft body from a given noise source. Acoustic scattering problems can be modeled using boundary element methods by reformulating the linear convective wave equation as a boundary integral equation, both in the frequency-domain and the time-domain. Boundary element methods reduce the spatial dimension by one by allowing for the integration over a surface instead of a volume. They also effectively handle singular and infinite fields which ultimately saves computing memory and maintains high computational efficiency [1, 10, 20, 21].

Though frequency-domain solvers are the most commonly used and researched within literature, there are several distinct advantages to using a time-domain solver. Time-domain solvers allow for the simulation and study of broadband sources and time-dependent transient signals, whereas studying broadband sources in the frequency-domain, on the other hand, carry a high computational cost. Time-domain solvers also allow for the scattering solutions at all frequencies to be obtained within a single computation and avoid needing to invert a large dense linear system as is required in the frequency-domain. Moreover, a time-domain solution is more naturally coupled with a nonlinear computational fluid dynamics simulation of noise sources.

Time-domain boundary integral equations unfortunately have an intrinsic numerical instability. This instability is observed across multiple disciplines and is a result of internal modes of resonance corresponding to time harmonic solutions of the integral equation [42]. These resonant modes yield an ill-conditioned matrix in the frequency-domain due to the existence of non-unique solutions which results in numerical instability in the time-domain [11, 43]. In recent years, numerical techniques for modeling acoustic wave scattering using time-domain boundary integral equations have been under development [1, 53–55]. It has been shown that stability can be realized through implementing a Burton-Miller-type reformulation of the time-domain boundary integral equation and both computational cost and computational time can be reduced using fast algorithms and high performance computing.

The objective of this study was to investigate the feasibility and stability for modeling acoustic wave scattering using a Burton-Miller-type time-domain boundary integral equation with impedance boundary condition. In Chapter 2, the derivation of a time-domain boundary integral equation, stabilized through Burton-Miller reformulation, was presented. The formulation used an adjoint free space Green's function and hypersingularities associated with the Burton-Miller reformulation were reduced via method of regularization.

In Chapter 3, the Burton-Miller reformulation was discretized using collocation methods and approximated using constant spatial and third-order Lagrange temporal basis functions. The spatial resolution of the time-domain boundary element method with respect to the spatial basis functions was studied by considering two metrics: the points-per-wavelength and the points-per-wavelength-squared. Analysis was conducted for both flat plate and spherical geometries. The flat plate had dimension $[-0.5, 0.5] \times [-0.5, 0.5] \times [-0.1, 0.1]$ and the sphere was centered at $\boldsymbol{x} = (x, y, z) = (0, 0, 0)$ with a radius of 0.5. For both geometries, a point source located at $\boldsymbol{x} = (0, 0, 1)$ was centered directly above each body. To investigate whether the location of the point source affected the accuracy of the solution, a shifted point source located at $\boldsymbol{x} = (0.5, 0, 1)$ was also considered for the flat plate. In addition, to investigate whether the orientation of the surface elements with respect to the wave direction affected the accuracy, the meshed sphere was also rotated along its axis.

The flat plate analysis demonstrated excellent spatial accuracy with the relative error for all discretizations being less than 2% with only 5 points-per-wavelength. The relative error was also less than 2% with only 25 points-per-wavelength-squared. The excellent spatial accuracy is likely due to using high-order Gauss quadrature integration over a closed, hence periodic, domain. Further, the analysis indicated that the spatial accuracy is not dependent on the location of the acoustic point source in relation to the surface elements. The sphere analysis demonstrated that the relative error becomes as small as 3% and 5%, for non-rotated and rotated orientations respectively, with only 25 points-per-wavelength-squared. These results demonstrated that the spatial accuracy is likely dependent on the orientation of the surface elements with respect to wave direction. Further, both the flat plate and sphere analyses indicate that, at least for the far field problem, the use of constant spatial basis functions can keep the overall problem size small while the high-order integration helps to maintain accuracy.

In Chapter 4, the numerical algorithm performance using CPUs was studied by once more considering the scattering of an acoustic point source by a flat plate with rigid body.

The purpose of this study was to gain an understanding of the computational complexity of time-domain acoustic solvers and for developing skills required in the field of high performance computing. It is important to understand the stability of such solvers because time-domain boundary element methods with Burton-Miller reformulation carry a high computational cost. As with the spatial resolution study, the flat plate had dimension $[-0.5, 0.5] \times [-0.5, 0.5] \times [-0.1, 0.1]$ and the point source located at $\boldsymbol{x} = (0, 0, 1)$ was centered directly above the body. The performance was studied by investigating both the strong and weak scaling capabilities of the numerical algorithm. The strong scaling results demonstrated that as core count increases for a fixed problem size, there was in increase in the time associated with performing parallel communications. The algorithm scaled well with fewer CPUs for small problem sizes and performance suffered as processing power increased due to the costs associated with parallel overhead. Larger problem sizes, on the other hand, performed well with larger core counts.

Super linear speedup was observed in the results using 7,000 elements with thirty-two cores, likely due to one of three possibilities: (1) not properly filtering out the time required for data export when calculating the average clock time, (2) one or more of the three trials for sixteen CPUs and/or thirty-two CPUs included outlier data thereby prompting a speedup greater than 2X as processing power is doubled from sixteen to thirty-two cores, and (3) thirty-two CPUs better accessed the memory within the node having fully-utilized the architecture whereas the sixteen CPUs, though running exclusively, were run on a single node with either sixteen cores or thirty-two cores depending on what nodes were available at the time of job submission. Possibilities (2) and (3) were the most likely culprits for the super linear speedup. It was therefore concluded that it is better to fully-utilize all cores within each node rather than using less cores than available per node as long as the inter-nodal communication requirements do not outweigh the benefits that massive parallelization provides.

When studying the diffraction of acoustic waves around a scattering body, boundary conditions on the scattering surface must be properly defined. For rigid bodies, the normal derivative of pressure is equal to zero. For acoustically treated, or soft bodies, the normal derivative of pressure is non-zero and is defined by an impedance, or admittance, boundary condition. Acoustically treated boundaries of scattering bodies are surfaces in which an acoustic liner is applied. Typically composed of an array of Helmholtz resonators, acoustic liners are incredibly effective at suppressing noise by "inducing vortex shedding at the mouths of resonators" [65].

In Chapter 5, time-domain liner boundary conditions were derived for pressure and its normal derivative on the surface. Three acoustic liner models were also introduced, and their applicable boundary conditions discussed including: the *Extended Helmholtz Resonator Model* [59], the *Three-Parameter Impedance Model* [29, 65], and the *Broadband Impedance Model* [62, 67, 68]. Each model satisfied the requirement of being real, causal, and passive. In Chapter 6, the stability of the Burton-Miller-type time-domain boundary integral equation coupled with a liner boundary condition was assessed. In literature, stability analysis has proven convolution quadrature methods second-order convergent for basis functions constant in space and linear in time [71], but no theoretical proof has yet been provided for other methods. Eigenvalue analysis is the current standard for studying the stability of time-domain boundary integral equations [39, 44, 51]. In this work, eigenvalue analysis was conducted for each liner model assuming both fully-lined and partially-lined bodies. Though not a sufficient condition for proving stability, it is necessary that the magnitude of all eigenvalues is no greater than unity for stability to be achieved.

Given either an impedance or an admittance boundary condition, the *Three-Parameter Impedance Model* provided numerical stability for both fully-lined and partially-lined bodies with fine grids. On the coarsest grid, stability was realized only when $\Delta t < \Delta x$. It was therefore concluded that the *Three-Parameter Impedance Model* is stable when, at a minimum, the condition $\Delta t \approx \Delta x$ is satisfied.

The *Broadband Impedance Model* analysis demonstrated stability for fully-lined bodies given an impedance boundary condition in fifteen out of twenty-five cases. It also demonstrated stability for partially-lined bodies in twenty out of twenty-five cases. These results reinforce that eigenvalue analysis is necessary the stability of a numerical scheme.

Unlike the *Three-Parameter* and *Broadband* models, which both offer many instances of stable solutions, the *Extended Helmholtz Resonator Model* demonstrated that the majority of all eigenvalues are greater than unity considering either fully-lined or partially-lined bodies. These results once more reinforce that eigenvalue analysis is necessary to assess if a numerical scheme is stable. When considering looser convergence criteria, more cases were shown to be stable. However, it was decided that a stricter tolerance is ideal for assessing the stability. For the results presented, a stricter convergence tolerance provided a succinct list of stable *Helmholtz* model.

For the *Helmholtz* model, it was demonstrated that instability largely occurs for an impedance boundary condition with negative reactance and small ν and for an admittance boundary condition with positive reactance and large ν. These results follow the observation

in [59] where it is stated: "for $\mathrm{Im}(z_0) < 0$ the best choice, *i.e.*, where Z varies not too much near Z_0, is for $\nu = 1$" and "for $\mathrm{Im}(z_0) > 0$ on the other hand, it is better to be halfway between $\nu = N/2$ and N" while noting that, here, $N = 20$.

The derivations of the time-domain boundary integral equation with Burton-Miller reformulation in Chapter 2 followed the cited references as they evolved over time, for completeness. Derivations for the impedance and admittance boundary conditions for each liner model in Chapter 5 were individual, yet trivial, contributions of the present work specific to the constant spatial and third-order temporal basis functions used for approximation. The spatial resolution analyses in Chapter 3 represent new, individual contributions of the present work. The performance study analyses in Chapter 4 also represent another contribution of the present work though not unique in the field of research. Furthermore, the acoustic liner assessment in Chapter 6 represents a major, individual contribution of the present work. The eigenvalue results presented are paramount to understanding the stability of using a liner boundary condition.

Though interesting results were observed in the *Extended Helmholtz Resonator Model* and the *Three-Parameter Impedance Model* studies, including having demonstrated the necessity for conducting an eigenvalue study, these models have the downfall of being strictly limited to analysis at a single frequency. The study of the *Broadband Impedance Model*, on the other hand, allows for the investigation of multiple frequencies simultaneously. Understanding the stability of such a model improves the capabilities of designing next generation quieter aircraft.

REFERENCES

[1] F. Q. Hu, "An efficient solution of time-domain boundary integral equations for acoustic scattering and its acceleration by graphics processing units," in *19th AIAA/CEAS Aeroacoustics Conference*, (AIAA paper 2013–2018), American Institute of Aeronautics and Astronautics, 2013.

[2] M. E. Rodio, F. Q. Hu, and D. M. Nark, "Investigating the numerical stability of a time-domain boundary integral equation with impedance boundary condition for simulating sound absorption of lined bodies," in *25th AIAA/CEAS Aeroacoustics Conference*, (AIAA paper 2018–2416), American Institute of Aeronautics and Astronautics, 2019.

[3] W. L. Meyer, W. A. Bell, B. T. Zinn, and M. P. Stallybrass, "Boundary integral solutions of three-dimensional acoustic radiation problems," *Journal of Sound and Vibration*, vol. 59, no. 2, pp. 245–262, 1978.

[4] D. Blokhintzev, "The propagation of sound in an inhomogeneous and moving medium I," *Journal of the Acoustical Society of America*, vol. 18, no. 2, pp. 322–328, 1946.

[5] J. E. Ffowcs-Williams and D. L. Hawkings, "Sound generation by turbulence and surfaces in arbitrary motion," *Philosophical Transactions of the Royal Society of London*, vol. 264, no. 1151, pp. 321–342, 1969.

[6] M. J. Lighthill, "On sound generated aerodynamically, I. general theory," *Proceedings of the Royal Society of London*, vol. 211, no. 1107, pp. 564–587, 1952.

[7] F. Farassat, "Discontinuities in aerodynamics and aeroacoustics: The concept and applications of generalized derivatives," *Journal of Sound and Vibration*, vol. 55, no. 2, pp. 165–193, 1977.

[8] F. Farassat and M. K. Meyers, "Extension of Kirchhoff's formula to radiation from moving surfaces," *Journal of Sound and Vibration*, vol. 123, no. 3, pp. 451–460, 1988.

[9] Y. W. Lee and D. J. Lee, "Derivation and implementation of the boundary integral formula for the convective wave equation in time-domain," *Journal of the Acoustical Society of America*, vol. 136, no. 6, pp. 2959–2967, 2014.

[10] D. J. Chappell, P. J. Harris, D. Henwood, and R. Chakrabarti, "A stable boundary element method for modeling transient acoustic radiation," *Journal of the Acoustical Society of America*, vol. 120, no. 1, pp. 74–80, 2006.

[11] A. A. Ergin, B. Shankar, and E. Michielssen, "Analysis of transient wave scattering from rigid bodies using a Burton-Miller approach," *Journal of the Acoustical Society of America*, vol. 106, no. 5, pp. 2396–2404, 1999.

[12] A. D. Jones and F. Q. Hu, "A three-dimensional time-domain boundary element method for the computation of exact Greens functions in acoustic analogy," in *13th AIAA/CEAS Aeroacoustics Conference*, (AIAA paper 2007–3479), American Institute of Aeronautics and Astronautics, 2007.

[13] S. Marburg, "The Burton and Miller method: Unlocking another mystery of its coupling parameter," *Journal of Computational Acoustics*, vol. 23, no. 1550016, 2015.

[14] S. Marburg and S. Schneider, "Influence of element types on numeric error for acoustic boundary elements," *Journal of Computational Acoustics*, vol. 11, no. 3, pp. 363–386, 2001.

[15] R. J. Astley and G. J. Macaulay, "Three-dimensional wave-envelope elements of variable order for acoustic radiation and scattering, Part i: Formulation in the frequency-domain," *Journal of the Acoustical Society of America*, vol. 103, no. 1, pp. 49–63, 1998.

[16] R. J. Astley and J. G. Bain, "A three-dimensional boundary element scheme for acoustic radiation in low Mach number flows," *Journal of Sound and Vibration*, vol. 109, no. 3, pp. 445–465, 1986.

[17] R. L. Johnston and G. Fairweather, "The method of fundamental solutions for problems in potential flow," *Applied Mathematical Modelling*, vol. 8, no. 4, pp. 265–270, 1984.

[18] S. F. Wu and J. Yu, "Reconstructing interior acoustic pressure fields via Helmholtz equation least-squares method," *Journal of the Acoustical Society of America*, vol. 104, no. 4, pp. 2054–2060, 1998.

[19] Z. Wang and S. F. Wu, "Helmholtz equation least squares method for reconstructing the acoustic pressure field," *Journal of the Acoustical Society of America*, vol. 102, no. 4, pp. 2020–2032, 1997.

[20] N. Kamiya, E. Andoh, and K. Nogae, "Eigenvalue analysis by the boundary element method: New developments," *Engineering Analysis with Boundary Elements*, vol. 12, no. 3, pp. 151–162, 1993.

[21] W. H. Tsao and W. S. Hwang, "Regularized boundary integral methods for three-dimensional potential flows," *Engineering Analysis with Boundary Elements*, vol. 77, no. 1, pp. 49–60, 2017.

[22] R. P. Shaw, "Transient scattering by a circular cylinder," *Journal of Sound and Vibration*, vol. 42, no. 3, pp. 295–304, 1975.

[23] D. P. Lockard, "An efficient, two-dimensional implementation of the Ffowcs Williams and Hawkings equation," *Journal of Sound and Vibration*, vol. 229, no. 4, pp. 897–911, 2000.

[24] P. M. Morse and K. U. Ingard, *Theoretical Acoustics*. New Jersey, USA: Princeton University Press, 1 ed., 1986.

[25] M. K. Meyers and J. S. Hausmann, "On the application of the Kirchhoff formula for moving surfaces," *Journal of Sound and Vibration*, vol. 139, no. 1, pp. 174–178, 1990.

[26] M. K. Meyers and J. S. Hausmann, "Computation of acoustic scattering from a moving rigid surface," *Journal of the Acoustical Society of America*, vol. 91, no. 5, pp. 174–178, 1990.

[27] A. Kierkegaard, S. Boij, and G. Efraimsson, "A frequency-domain linearized Navier-Stokes equations approach to acoustic propagation in flow ducts with sharp edges," *Journal of the Acoustical Society of America*, vol. 142, no. 4, pp. 710–719, 2010.

[28] A. Iob, R. Arina, and C. Schipani, "Frequency-domain linearized Euler model for turbomachinery noise radiation through engine exhaust," *American Institute of Aeronautics and Astronautics Journal*, vol. 48, no. 4, pp. 848–858, 2010.

[29] C. K. W. Tam and L. Auriault, "Time-domain impedance boundary conditions for computational aeroacoustics," *American Institute of Aeronautics and Astronautics Journal*, vol. 34, no. 5, pp. 917–923, 1996.

[30] Y. Reymen, M. Baelmans, and W. Desmet, "Efficient implementation of Tam and Auriaults time-domain impedance boundary condition," *American Institute of Aeronautics and Astronautics Journal*, vol. 24, no. 9, pp. 2368–2376, 2008.

[31] M. B. Friedman and R. P. Shaw, "Diffraction of pulses by cylindrical obstacles of arbitrary cross section," *Journal of Applied Mechanics*, vol. 29, no. 1, pp. 40–46, 1962.

[32] R. P. Shaw, "Diffraction of acoustic pulses by obstacles of arbitrary shape with Robin boundary condition," *Journal of the Acoustical Society of America*, vol. 41, no. 1, pp. 855–859, 1967.

[33] R. P. Banaugh and W. Goldsmith, "Diffraction of steady acoustic waves by surfaces of arbitrary shape," *Journal of the Acoustical Society of America*, vol. 35, no. 10, pp. 1590–1601, 1963.

[34] K. M. Mitzner, "Acoustic scattering from an interface between media of greatly different density," *Journal of the Acoustical Society of America*, vol. 39, no. 6, p. 1260, 1966.

[35] K. M. Mitzner, "Numerical solution for transient scattering from a hard surface of arbitrary shape – retarded potential technique," *Journal of the Acoustical Society of America*, vol. 42, no. 2, pp. 391–397, 1967.

[36] B. Birgisson, E. Siebrits, and A. P. Peirce, "Elastodynamic direct boundary element methods with enhanced numerical stability properties," *International Journal for Numerical Methods in Engineering*, vol. 46, no. 6, pp. 871–888, 1999.

[37] P. J. Davies, "A stability analysis of a time marching scheme for the general surface electric field integral equation," *Applied Numerical Mathematics*, vol. 27, no. 1, pp. 33–57, 1998.

[38] P. J. Davies and D. B. Duncan, "Averaging technique for time-marching schemes for retarded potential integral equations," *Applied Numerical Mathematics*, vol. 23, no. 3, pp. 291–310, 1997.

[39] S. J. Dodson, S. P. Walker, and M. J. Bluck, "Implicitness and stability of time-domain integral equation scattering analysis," *Applied Computational Electromagnetics Society Journal*, vol. 13, pp. 291–301, 1998.

[40] J. L. Hu and C. H. Chan, "Improved temporal basis function for time-domain electric field integral equation method acceleration for 3-D electromagnetic analysis," *Electronics Letters*, vol. 35, no. 11, pp. 883–885, 1999.

[41] G. X. Jiang, H. B. Zhu, G. Q. Ji, and W. Cao, "Improved stable scheme for the time-domain integral equation method," *IEEE Microwave and Wireless Components Letters*, vol. 17, no. 1, pp. 1–3, 2007.

[42] B. P. Rynne and P. D. Smith, "Stability of time marching algorithms for the electric field integral equation," *Journal of Electromagnetic Waves and Applications*, vol. 4, no. 12, pp. 1181–1205, 1990.

[43] P. D. Smith, "Instabilities in time marching methods for scattering: Cause and rectification," *Electromagnetics*, vol. 10, no. 4, pp. 439–451, 1990.

[44] H. Wang, D. J. Henwood, P. J. Harris, and R. Chakrabarti, "Concerning the cause of instability in time-stepping boundary element methods applied to the exterior acoustic problem," *Journal of Sound and Vibration*, vol. 305, no. 1, pp. 289–297, 2007.

[45] A. Geranmayeh, W. Ackermann, and T. Weiland, "Temporal discretization choices for stable boundary element methods in electromagnetic scattering problems," *Applied Numerical Mathematics*, vol. 59, pp. 2751–2773, 2008.

[46] M. J. Bluck and S. P. Walker, "Analysis of three-dimensional transient acoustic wave propagation using the boundary integral equation method," *International Journal for Numerical Methods in Engineering*, vol. 39, no. 8, pp. 1419–1431, 1996.

[47] A. Geranmayeh, W. Ackermann, and T. Weiland, "Proper combination of integrators and interpolators for stable marching-on-in time schemes," in *10th IEEE International Conference on Electromagnetism in Advanced Applications*, vol. 415, (Torino, Italy), The Institute of Electrical and Electronics Engineers, 2007.

[48] T. Ha-Duong and B. Ludwig, "A Galerkin BEM for transient acoustic scattering by an absorbing obstacle," *International Journal for Numerical Methods in Engineering*, vol. 57, no. 13, pp. 1845–1882, 2003.

[49] G. Unger, "Analysis of boundary element methods for Laplacian eigenvalue problems." Dissertation, 2009. Institute of Computational Mathematics.

[50] G. Yu, W. J. Mansur, J. A. M. Carrer, and L. Gong, "Stability of Galerkin and collocation time domain boundary element methods as applied to the scalar wave equation," *Computers and Structures*, vol. 74, no. 4, pp. 495–506, 2000.

[51] H.-W. Jang and J.-G. Ih, "Stabilization of time domain acoustic boundary element method for the exterior problem avoiding the nonuniqueness," *Journal of the Acoustical Society of America*, vol. 133, no. 3, pp. 1237–1244, 2013.

[52] A. J. Burton and G. F. Miller, "The application of integral equation methods to the numerical solution of some exterior boundary problems," *Proceedings of the Royal Society of London*, vol. 323, no. 1553, pp. 201–210, 1971.

[53] F. Q. Hu, "Further development of a time-domain boundary integral equation method for aeroacoustic scattering computations," in *20th AIAA/CEAS Aeroacoustics Conference*, (AIAA paper 2014–3194), American Institute of Aeronautics and Astronautics, 2014.

[54] F. Q. Hu, M. E. Pizzo, and D. M. Nark, "On the assessment of acoustic scattering and shielding by time-domain boundary integral equation solutions," in *22nd AIAA/CEAS Aeroacoustics Conference*, (AIAA paper 2016–2779), American Institute of Aeronautics and Astronautics, 2016.

[55] F. Q. Hu, M. E. Pizzo, and D. M. Nark, "A new formulation of time-domain boundary integral equation for acoustic wave scattering in the presence of a uniform mean flow," in *23rd AIAA/CEAS Aeroacoustics Conference*, (AIAA paper 2017–3510), American Institute of Aeronautics and Astronautics, 2017.

[56] C.-J. Zheng, H.-B. Chen, H.-F. Gao, and L. Du, "Is the Burton-Miller formulation really free of fictitious eigenfrequencies?," *Engineering Analysis with Boundary Elements*, vol. 59, no. 1, pp. 43–51, 2015.

[57] L. Long, "The compressible aerodynamics of rotating blades based on an acoustic formulation." NASA Technical Paper, 1983. 2197.

[58] K.-Y. Fung and H. Ju, "Time-domain impedance boundary conditions for computational acoustics and aeroacoustics," *International Journal of Computational Fluid Dynamics*, vol. 18, no. 6, pp. 503–511, 2004.

[59] S. W. Rienstra, "Impedance models in time-domain including the extended Helmholtz resonator model," (AIAA paper 2006–2686), American Institute of Aeronautics and Astronautics, 2006.

[60] A. M. N. Spillere, A. A. Medeiros, and J. S. Cordiolo, "An improved impedance education technique based on impedance models and the mode matching method," *Applied Acoustics*, vol. 129, no. 2018, pp. 322–334, 2017.

[61] A. H. Nayfeh, J. E. Kaiser, and D. P. Telionis, "Acoustics of aircraft engine-duct systems," *American Institute of Aeronautics and Astronautics Journal*, vol. 13, no. 3, pp. 130–153, 1975.

[62] X. Y. Li, X. D. Li, and C. K. W. Tam, "Improved multipole broadband and time-domain impedance boundary condition," *American Institute of Aeronautics and Astronautics Journal*, vol. 50, no. 2, pp. 980–984, 2012.

[63] Q. Zhang and D. J. Bodony, "Numerical simulation of two-dimensional acoustic liners with high-speed grazing flow," *American Institute of Aeronautics and Astronautics Journal*, vol. 49, no. 2, pp. 365–382, 2011.

[64] S. Allam and M. Abom, "Experimental characterization of acoustic liners with extended reaction," in *14th AIAA/CEAS Aeroacoustics Conference*, (AIAA paper 2008–3074), American Institute of Aeronautics and Astronautics, 2008.

[65] C. K. W. Tam, *Computational Aeroacoustics: A Wave Number Approach*. New York, USA: Cambridge University Press, 1 ed., 2012.

[66] C. Richter, F. H. Thiele, X. Li, and M. Zhuang, "Comparison of time-domain impedance boundary conditions for lined duct flows," *American Institute of Aeronautics and Astronautics Journal*, vol. 45, no. 6, pp. 1333–1345, 2007.

[67] D. Dragna, P. Pineau, and P. Blanc-Benon, "A generalized recursive convolution method for time-domain propagation in porous media," *Journal of the Acoustical Society of America*, vol. 138, no. 2, pp. 1030–1042, 2015.

[68] R. Troian, D. Dragna, C. C. Bailly, and M. A. Galland, "Broadband liner impedance eduction for multimodal acoustic propagation in the presence of a mean flow," *Journal of Sound and Vibration*, vol. 392, no. 1, pp. 200–216, 2017.

[69] A. D. Pierce, *Acoustics: An Introduction to Its Physical Principles and Applications*. New York, USA: Acoustical Society of America, 3 ed., 1994.

[70] A. Selamet and I. Lee, "Helmholtz resonator with extended neck," *Journal of the Acoustical Society of America*, vol. 113, no. 4, pp. 1975–1985, 2003.

[71] P. J. Davies and D. B. Duncan, "Stability and convergence of collocation schemes for retarded potential integral equations," *Society for Industrial and Applied Mathematics Journal on Numerical Analysis*, vol. 42, no. 3, pp. 1167–1188, 2004.

[72] M. E. Pizzo, F. Q. Hu, and D. M. Nark, "Simulation of sound absorption by scattering bodies treated with acoustic liners using a time-domain boundary element method," in *24th AIAA/CEAS Aeroacoustics Conference*, (AIAA paper 2018–3456), American Institute of Aeronautics and Astronautics, 2018.

[73] R. Haberman, *Applied Partial Differential Equations with Fourier Series and Boundary Value Problems*. New Jersey, USA: Pearson Education, Inc., 5 ed., 2013.

[74] L. Morino, "Is there a difference between aeroacoustics and aerodynamics? An aeroelasticians viewpoint," *American Institute of Aeronautics and Astronautics Journal*, vol. 41, no. 7, pp. 1209–1223, 2003.

[75] F. Q. Hu, M. E. Pizzo, and D. M. Nark, "On a time-domain boundary integral equation formulation for acoustic scattering by rigid bodies in uniform mean flow," *Journal of the Acoustical Society of America*, vol. 142, no. 6, pp. 3624–3636, 2017.

[76] M. Guiggiani and A. Gigante, "Cauchy principal value integrals in the boundary element method," *Journal of Applied Mechanics*, vol. 57, no. 4, pp. 906–915, 1990.

[77] F. Q. Hu, M. E. Pizzo, and D. M. Nark, "On the use of a Prandtl-Glauert-Lorentz transformation for acoustic scattering by rigid bodies with a uniform flow," *Journal of the Sound and Vibration*, vol. 443, no. 22, pp. 2594–2605, 1992.

[78] G. Hager and G. Wellein, *Introduction to High Performance Computing for Scientists and Engineers*. New York, USA: Taylor and Francis Group, LLC, 1 ed., 2011.

[79] K. Fatahalian and M. Houston, "A closer look at GPUs," *Communications of the ACM*, vol. 51, no. 10, pp. 50–57, 2008.

[80] M. Garland and D. B. Kirk, "Understanding throughput-oriented architectures," *Communications of the ACM*, vol. 53, no. 11, pp. 58–66, 2010.

[81] W. Geng and F. Jacob, "A GPU-accelerated direct-sum boundary integral Poisson-Boltzmann solver," *Computer Physics Communications*, vol. 184, no. 6, pp. 1490–1496, 2013.

[82] J. Guan, S. Yan, and J.-M. Jin, "An accurate and efficient finite element-boundary integral method with GPU acceleration for 3-D electromagnetic analysis," *IEEE Transactions on Antennas and Propagation*, vol. 62, no. 12, pp. 6325–6336, 2014.

[83] T. Takahashi and T. Hamada, "GPU-accelerated boundary element method for Helmholtz' equation in three dimensions," *International Journal for Numerical Methods in Engineering*, vol. 80, no. 10, pp. 1295–1321, 2009.

[84] G. M. Amdahl, "Validity of the single processor approach to achieving large scale computing capabilities, reprinted from the AFIPS conference proceedings," in *Proceedings of the April 18-20, 1967, Spring Joint Computer Conference*, vol. 483–485, (New York, USA), Association for Computing Machinery, 1967.

[85] J. L. Gustafson, "Reevaluating Amdahl's Law," *Communications of the ACM*, vol. 31, no. 5, pp. 532–533, 1988.

[86] J. Pratt, "Turing cluster." `www.odu.edu/facultystaff/research/resources/computing/high-performance-computing/compute`, 2020. Accessed 20 Jan. 2020.

[87] R. H. Randall, *An Introduction to Acoustics*. Massachusetts, USA: Addison-Wesley Press, Inc., 1 ed., 1951.

[88] M. G. Jones, "Liner technology facility, NASA Langley Research Center." `stab.larc.nasa.gov/facilities/liner-technology-facility`, 2020. Accessed 22 Feb. 2020, Last Modified 30 Apr. 2014.

[89] D. M. Nark and M. G. Jones, "Assessment of axial wave number and mean flow uncertainty on acoustic liner impedance eduction," (AIAA paper 2018–3444), American Institute of Aeronautics and Astronautics, 2018.

[90] S. Zheng and M. Zhuang, "Three-dimensional benchmark problem for broadband time-domain impedance boundary conditions," *American Institute of Aeronautics and Astronautics Journal*, vol. 42, no. 2, pp. 405–407, 2004.

[91] J. D. Jackson, *Classical Electrodynamics*. New York, USA: Wiley, 3 ed., 1998.

APPENDIX A

FREQUENCY-DOMAIN SOLUTIONS FOR RIGID BODY FLAT PLATE

This appendix illustrates the frequency-domain solutions converted from the time-domain solutions at $\omega = 5\pi, 6\pi, ..., 20\pi$ for the scattering of a rigid body flat plate where ω is a non-dimensionalized value. The flat plate has dimension $[-0.5, 0.5] \times [-0.5, 0.5] \times [-0.1, 0.1]$. The scattering solution results from an acoustic point source located at $\boldsymbol{x} = (0, 0, 1)$ as illustrated in Figure 3a. The surface of the flat plate is discretized in the x-, y-, and z- directions and a series of computations is carried out by increasing the number of elements used from $20 \times 20 \times 4$ $(1,120$ elements) to $100 \times 100 \times 20$ $(28,000$ elements). All discretizations are indicated in the legend. The vertical axis is the magnitude of sound pressure. The horizontal axis indicates the solution along a field line of coordinates, $-2.5 \leq x \leq 2.5, y = 0, z = -2.5$.

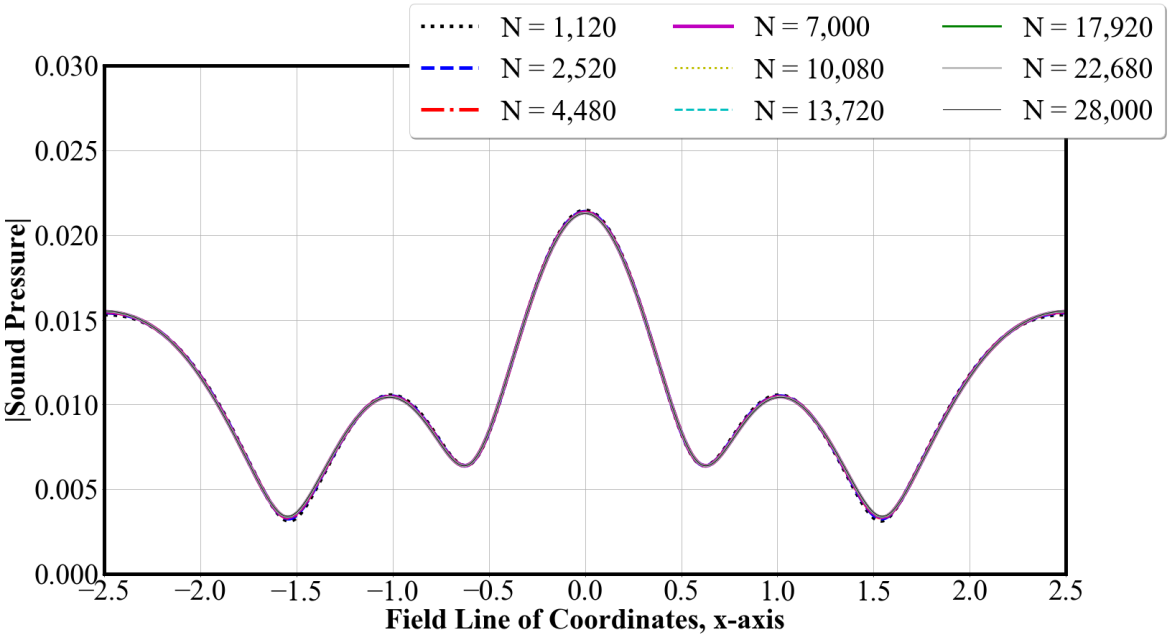

Fig. 49: Frequency-domain solution converted from the time-domain at $\omega = 5\pi$ for rigid body flat plate scattering along the field line of coordinates, $-2.5 \leq x \leq 2.5, y = 0, z = -2.5$.

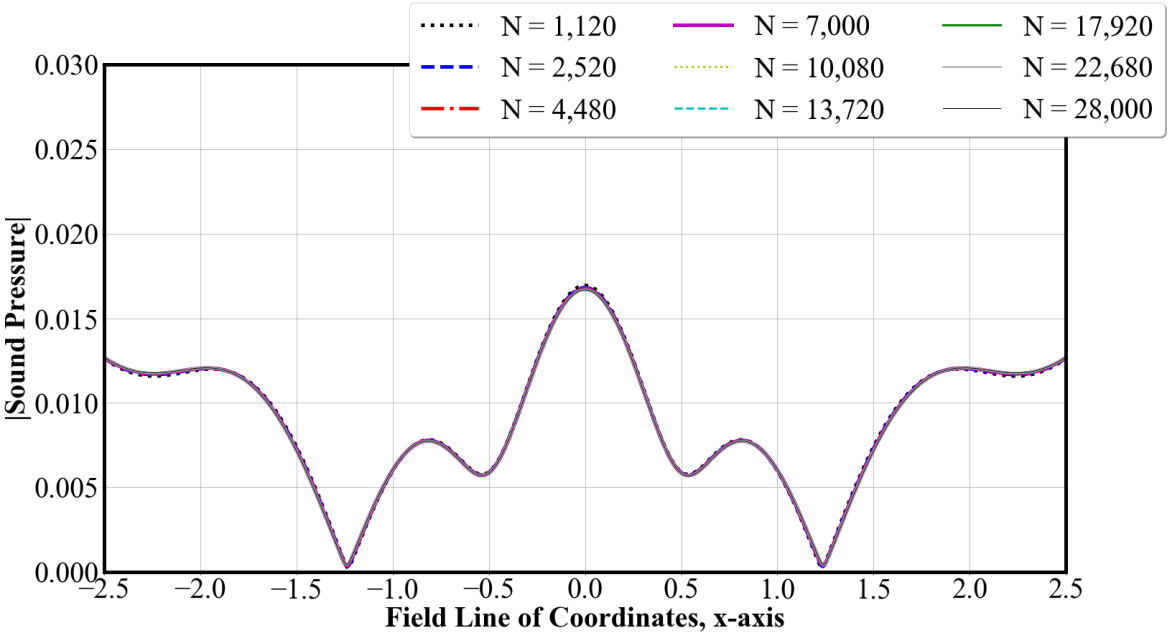

Fig. 50: Frequency-domain solution converted from the time-domain at $\omega = 6\pi$ for rigid body flat plate scattering along the field line of coordinates, $-2.5 \leq x \leq 2.5, y = 0, z = -2.5$.

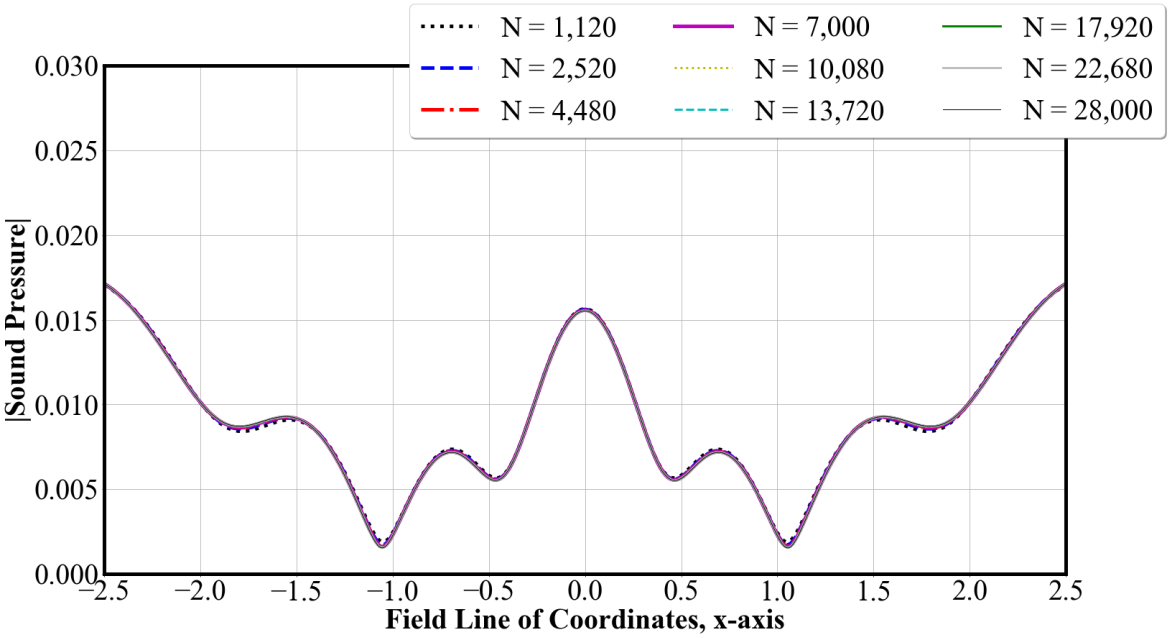

Fig. 51: Frequency-domain solution converted from the time-domain at $\omega = 7\pi$ for rigid body flat plate scattering along the field line of coordinates, $-2.5 \leq x \leq 2.5, y = 0, z = -2.5$.

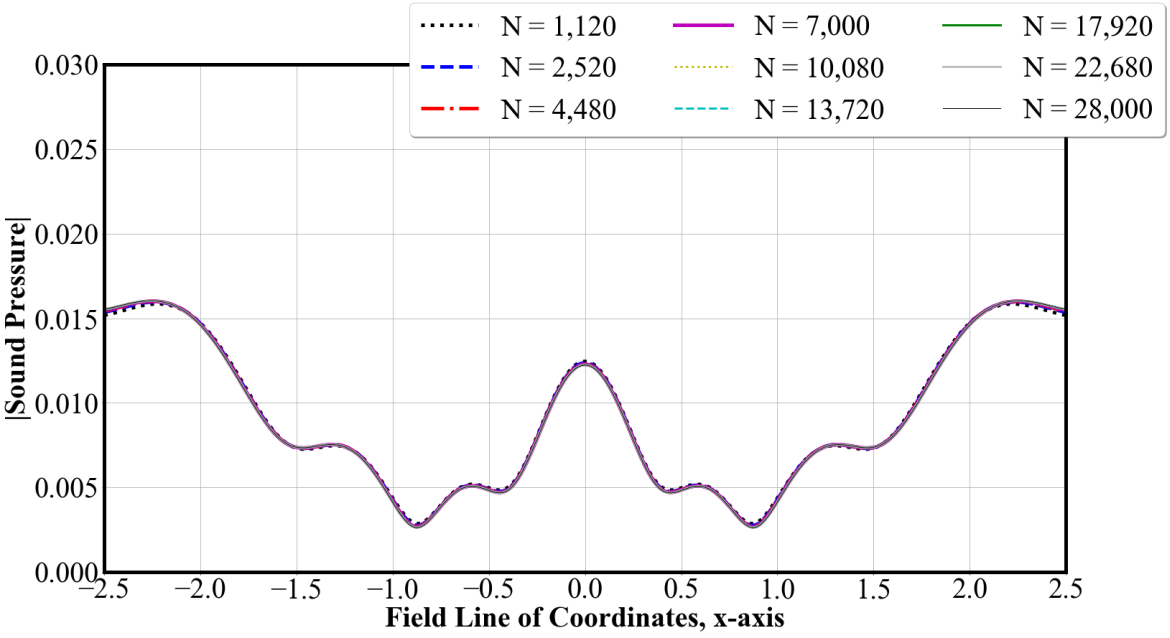

Fig. 52: Frequency-domain solution converted from the time-domain at $\omega = 8\pi$ for rigid body flat plate scattering along the field line of coordinates, $-2.5 \leq x \leq 2.5, y = 0, z = -2.5$.

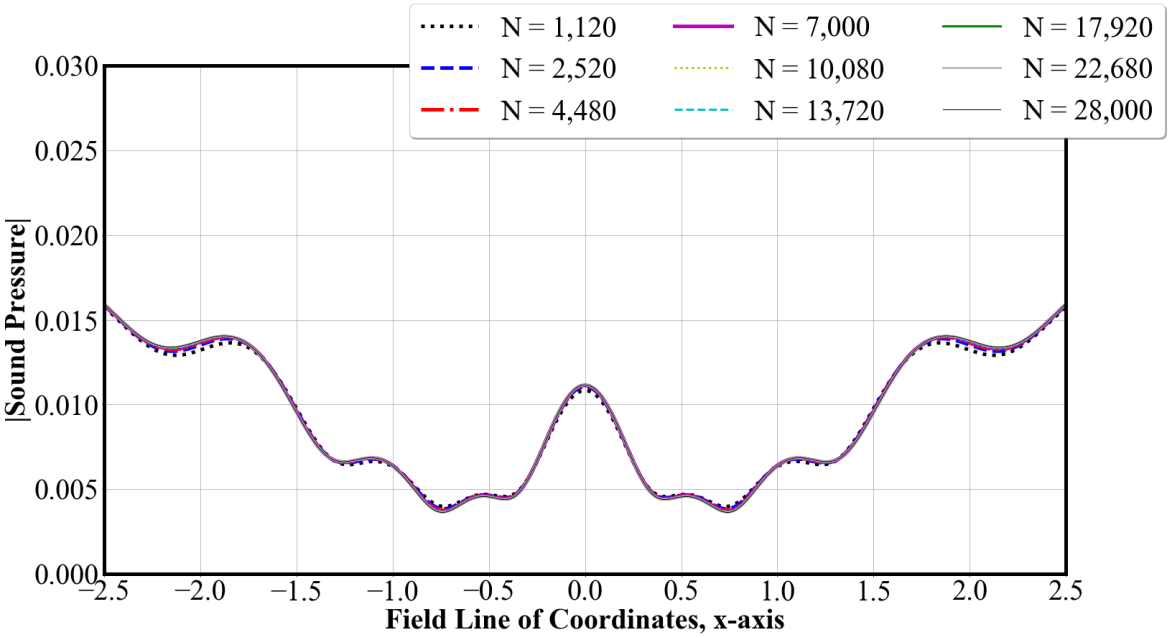

Fig. 53: Frequency-domain solution converted from the time-domain at $\omega = 9\pi$ for rigid body flat plate scattering along the field line of coordinates, $-2.5 \leq x \leq 2.5, y = 0, z = -2.5$.

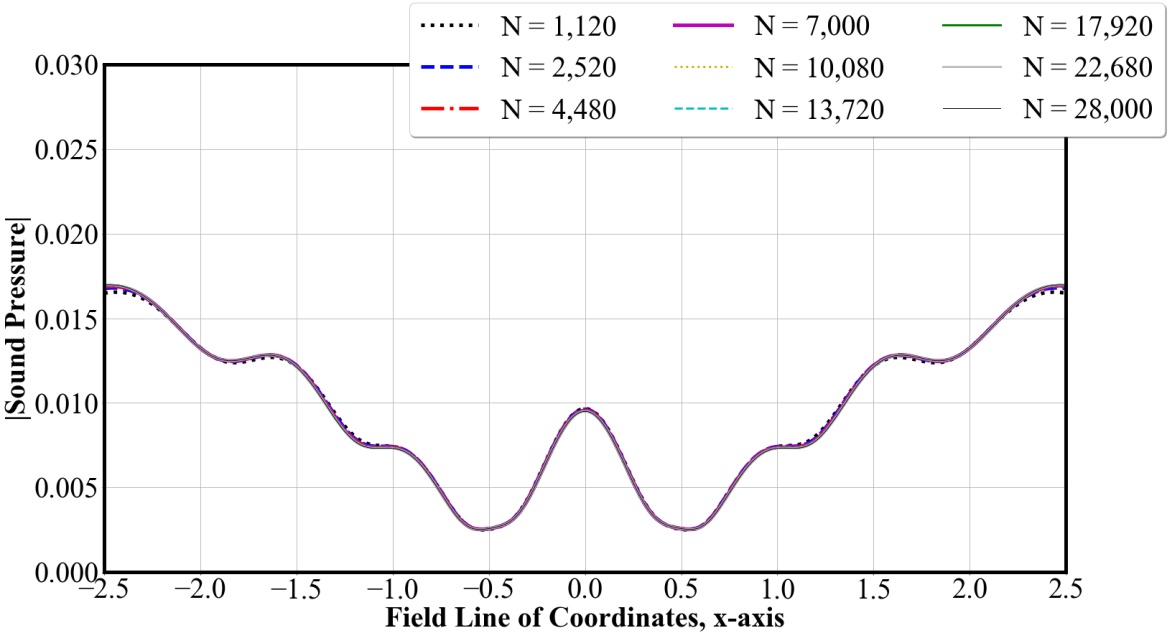

Fig. 54: Frequency-domain solution converted from the time-domain at $\omega = 10\pi$ for rigid body flat plate scattering along the field line of coordinates, $-2.5 \leq x \leq 2.5, y = 0, z = -2.5$.

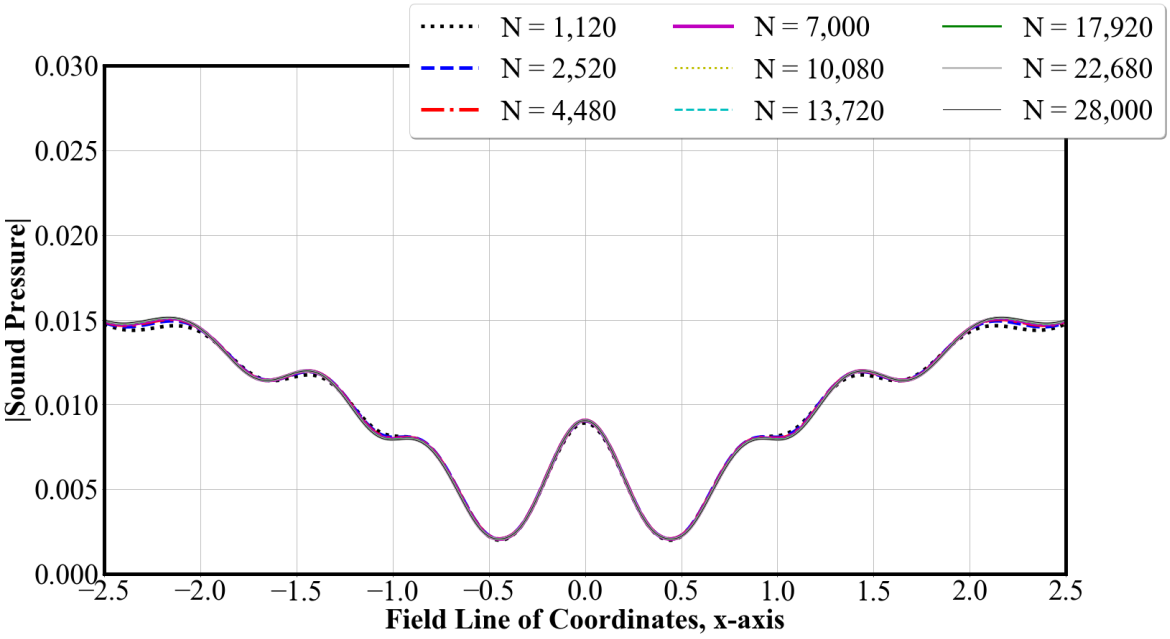

Fig. 55: Frequency-domain solution converted from the time-domain at $\omega = 11\pi$ for rigid body flat plate scattering along the field line of coordinates, $-2.5 \leq x \leq 2.5, y = 0, z = -2.5$.

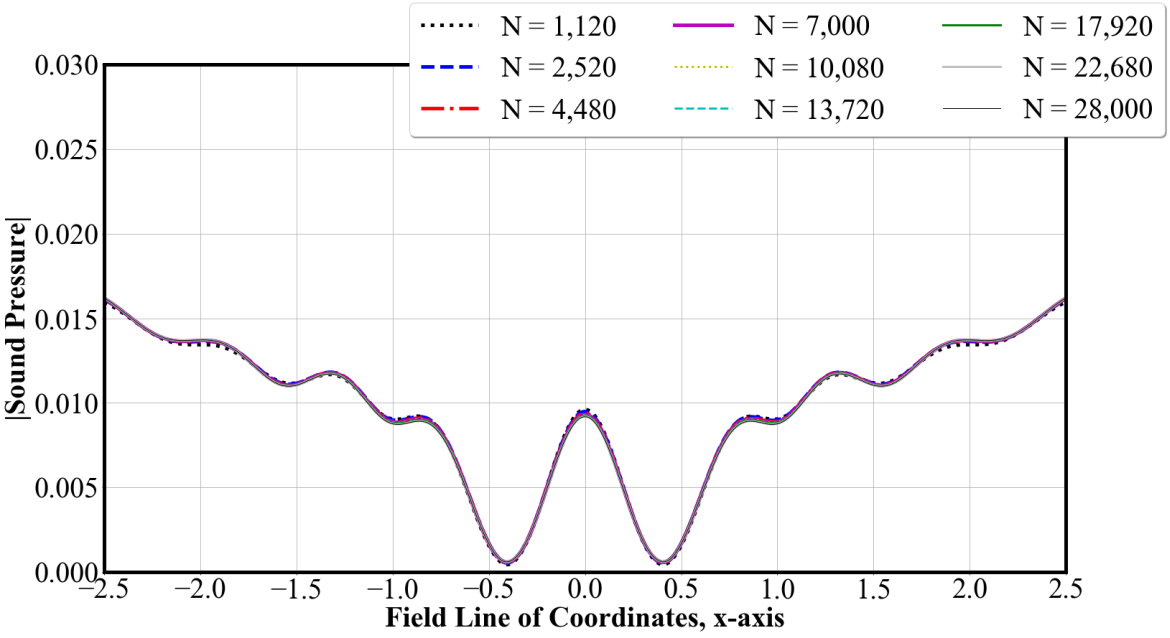

Fig. 56: Frequency-domain solution converted from the time-domain at $\omega = 12\pi$ for rigid body flat plate scattering along the field line of coordinates, $-2.5 \leq x \leq 2.5, y = 0, z = -2.5$.

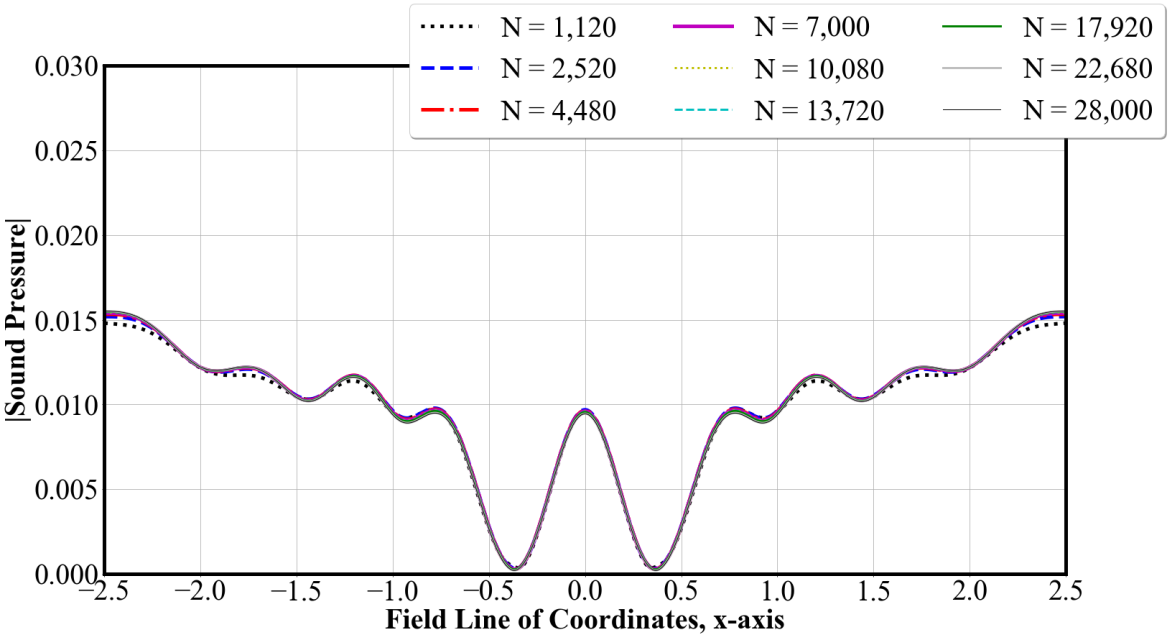

Fig. 57: Frequency-domain solution converted from the time-domain at $\omega = 13\pi$ for rigid body flat plate scattering along the field line of coordinates, $-2.5 \leq x \leq 2.5, y = 0, z = -2.5$.

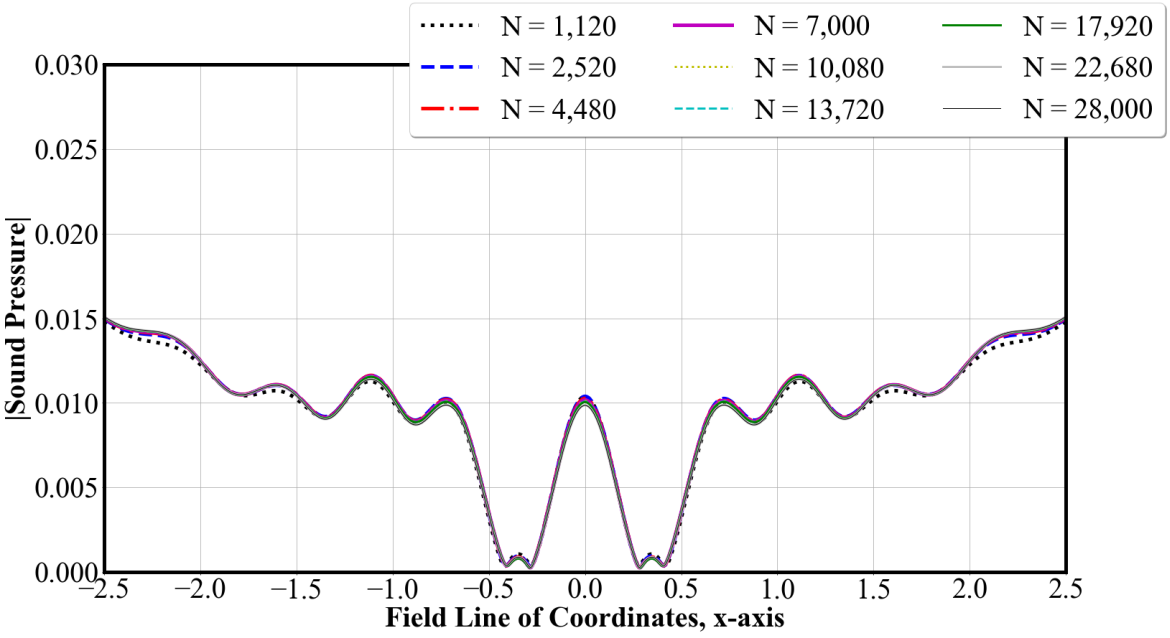

Fig. 58: Frequency-domain solution converted from the time-domain at $\omega = 14\pi$ for rigid body flat plate scattering along the field line of coordinates, $-2.5 \leq x \leq 2.5, y = 0, z = -2.5$.

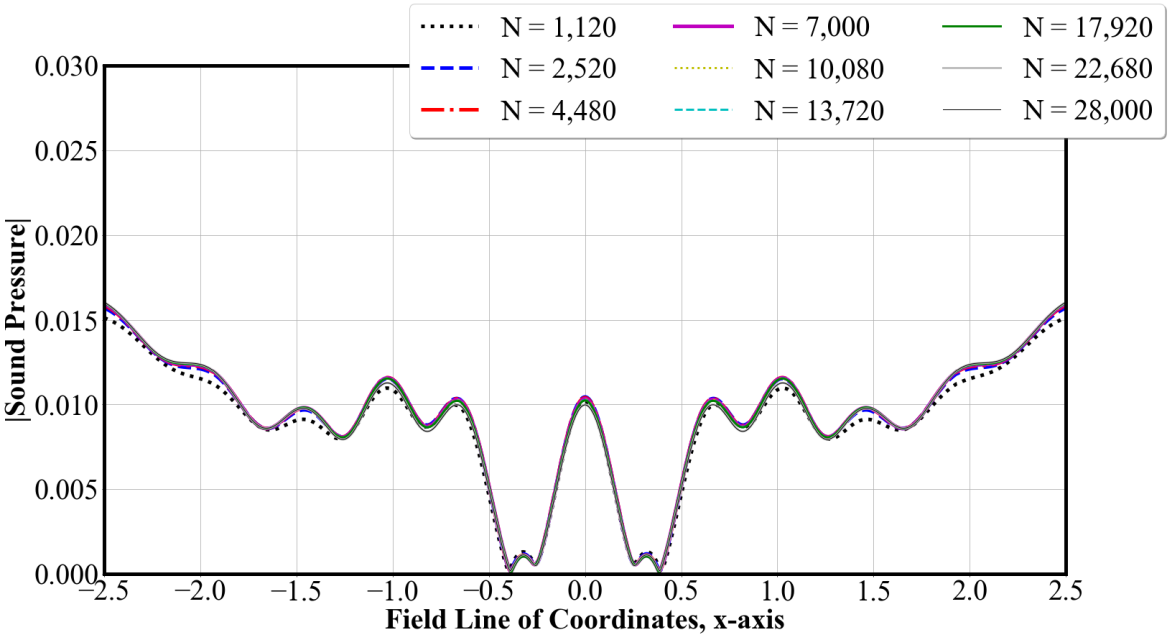

Fig. 59: Frequency-domain solution converted from the time-domain at $\omega = 15\pi$ for rigid body flat plate scattering along the field line of coordinates, $-2.5 \leq x \leq 2.5, y = 0, z = -2.5$.

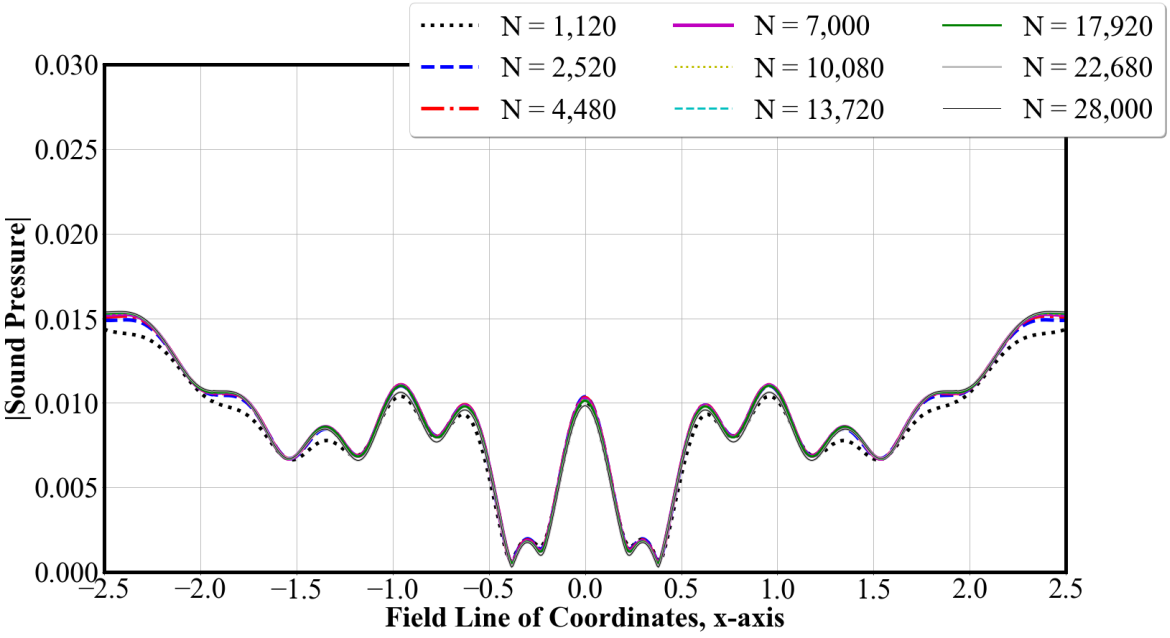

Fig. 60: Frequency-domain solution converted from the time-domain at $\omega = 16\pi$ for rigid body flat plate scattering along the field line of coordinates, $-2.5 \leq x \leq 2.5, y = 0, z = -2.5$.

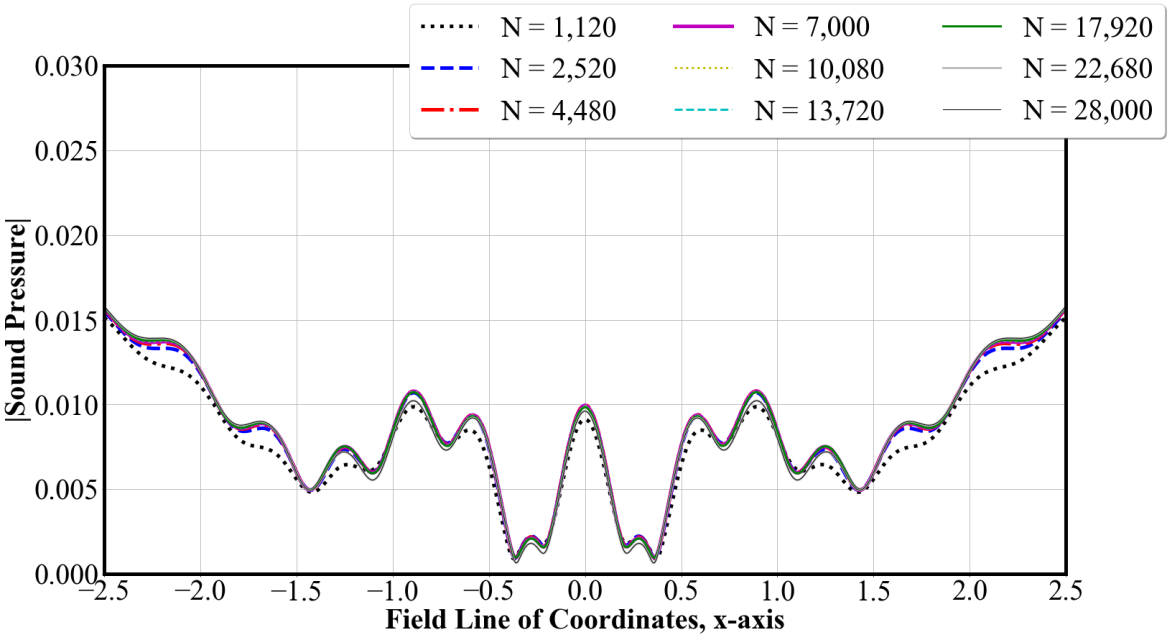

Fig. 61: Frequency-domain solution converted from the time-domain at $\omega = 17\pi$ for rigid body flat plate scattering along the field line of coordinates, $-2.5 \leq x \leq 2.5, y = 0, z = -2.5$.

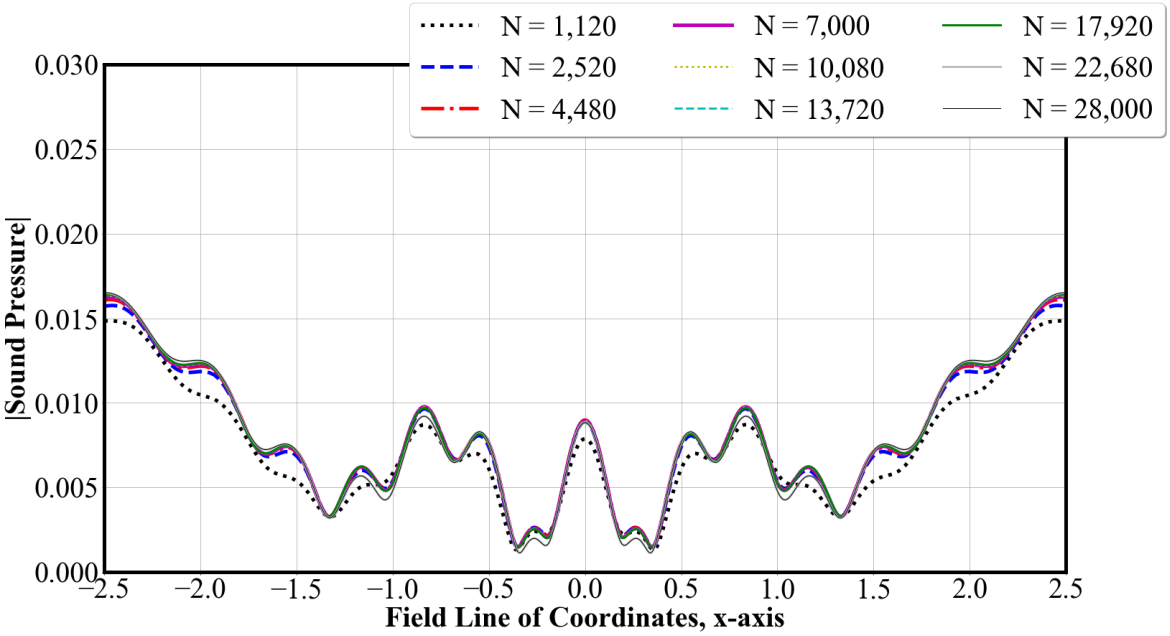

Fig. 62: Frequency-domain solution converted from the time-domain at $\omega = 18\pi$ for rigid body flat plate scattering along the field line of coordinates, $-2.5 \leq x \leq 2.5, y = 0, z = -2.5$.

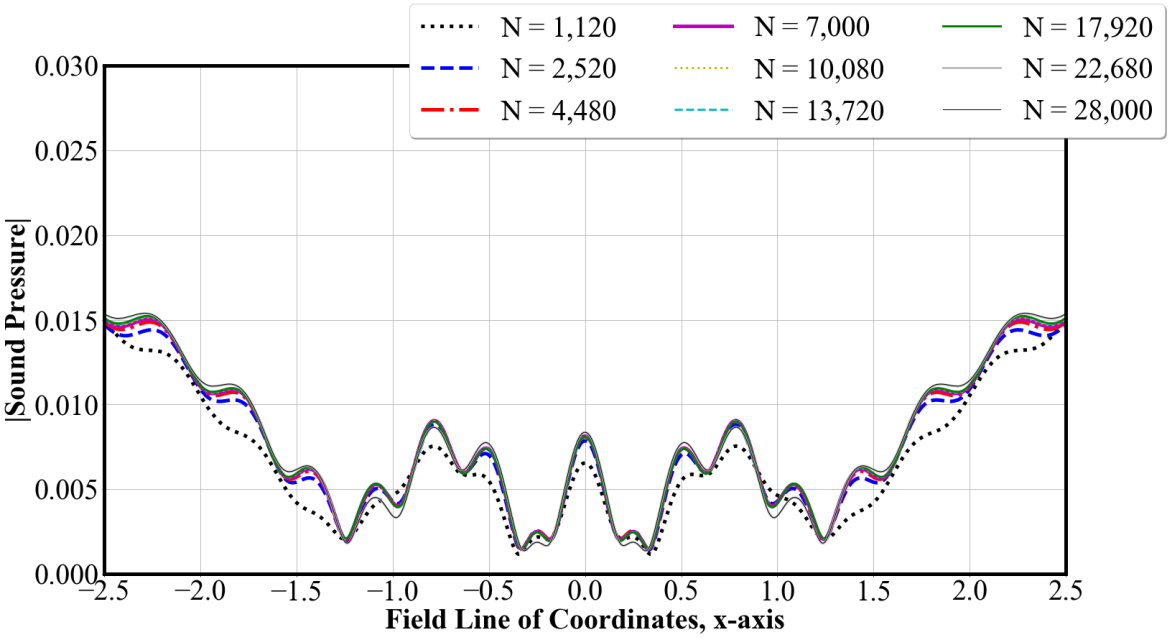

Fig. 63: Frequency-domain solution converted from the time-domain at $\omega = 19\pi$ for rigid body flat plate scattering along the field line of coordinates, $-2.5 \leq x \leq 2.5, y = 0, z = -2.5$.

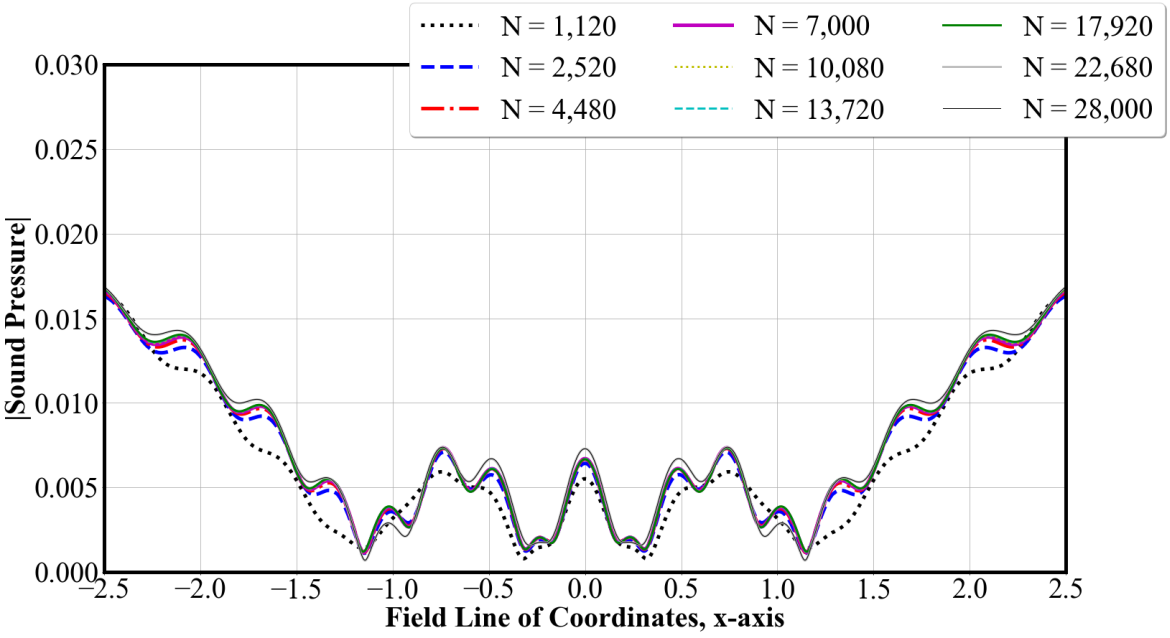

Fig. 64: Frequency-domain solution converted from the time-domain at $\omega = 20\pi$ for rigid body flat plate scattering along the field line of coordinates, $-2.5 \leq x \leq 2.5, y = 0, z = -2.5$.

APPENDIX B

FREQUENCY-DOMAIN SOLUTIONS FOR RIGID BODY SPHERE

This appendix illustrates the frequency-domain solutions converted from the time-domain solutions at $\omega = 5\pi, 6\pi, ..., 20\pi$ for the scattering of a rigid body sphere where ω is a non-dimensionalized value. The sphere is centered at $\boldsymbol{x} = (x, y, z) = (0, 0, 0)$ with a radius of 0.5. The scattering solution results from an acoustic point source located at $\boldsymbol{x} = (0, 0, 1)$ as illustrated in Figures 4a. The surface of the sphere is discretized, and a series of computations is carried out by increasing the number of elements from $N = 729$ to $N = 72,091$. All discretizations are indicated in the legend, including the exact solution. The vertical axis is the magnitude of sound pressure. The horizontal axis indicates the solution along a field line of coordinates, $-2.5 \leq x \leq 2.5, y = 0, z = -2.5$.

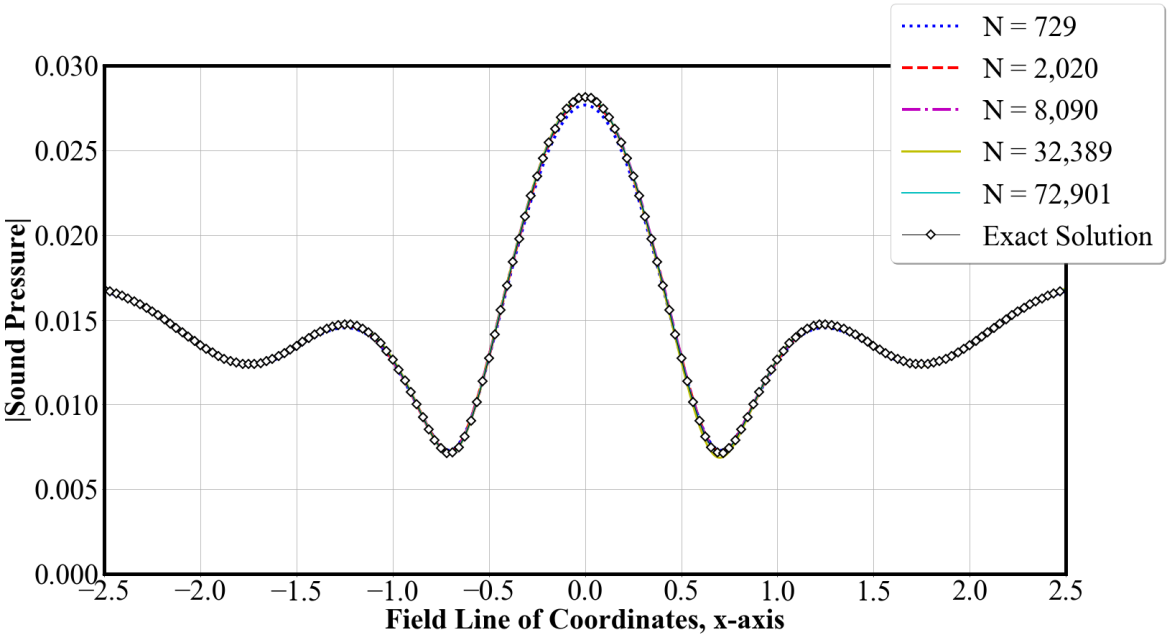

Fig. 65: Frequency-domain solution converted from the time-domain at $\omega = 5\pi$ for rigid body sphere scattering along the field line of coordinates, $-2.5 \leq x \leq 2.5, y = 0, z = -2.5$.

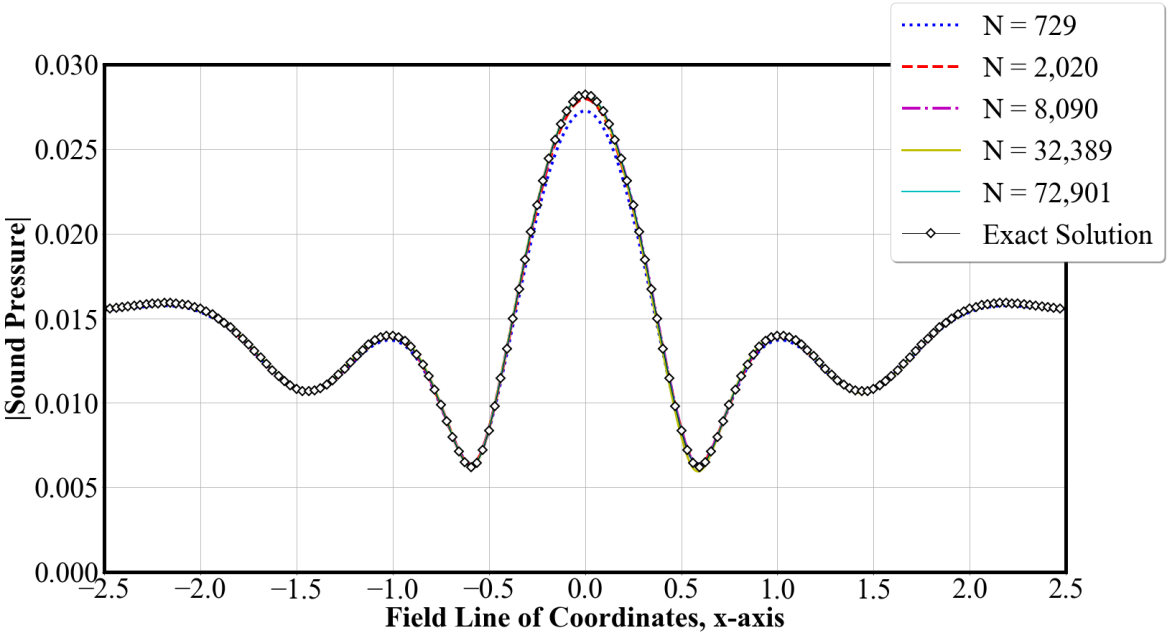

Fig. 66: Frequency-domain solution converted from the time-domain at $\omega = 6\pi$ for rigid body sphere scattering along the field line of coordinates, $-2.5 \leq x \leq 2.5, y = 0, z = -2.5$.

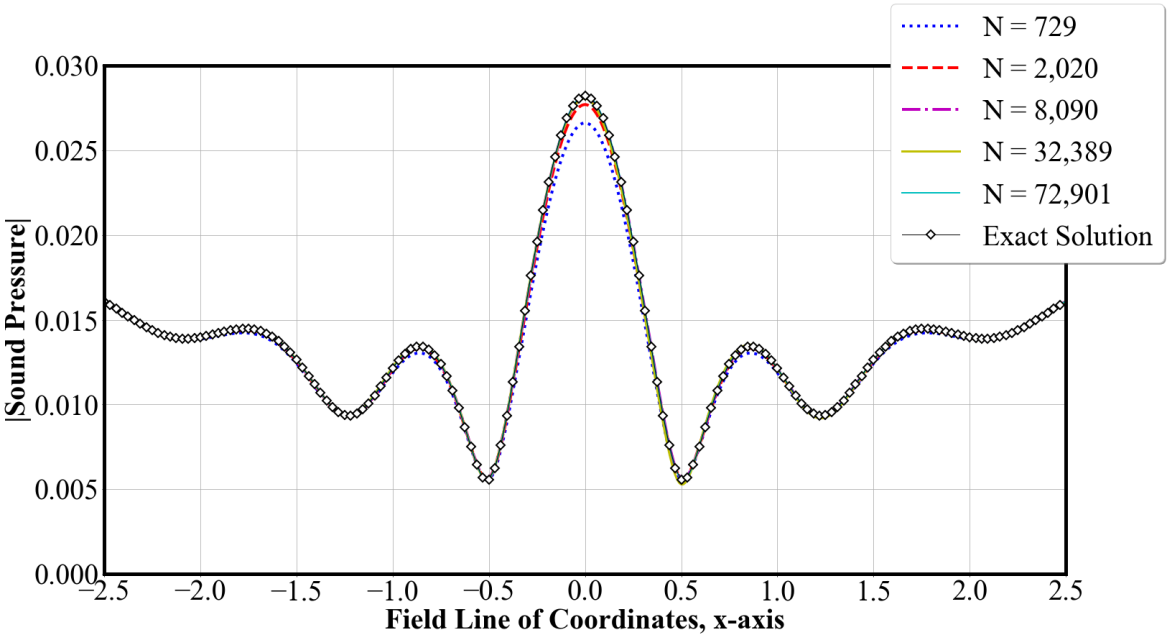

Fig. 67: Frequency-domain solution converted from the time-domain at $\omega = 7\pi$ for rigid body sphere scattering along the field line of coordinates, $-2.5 \leq x \leq 2.5, y = 0, z = -2.5$.

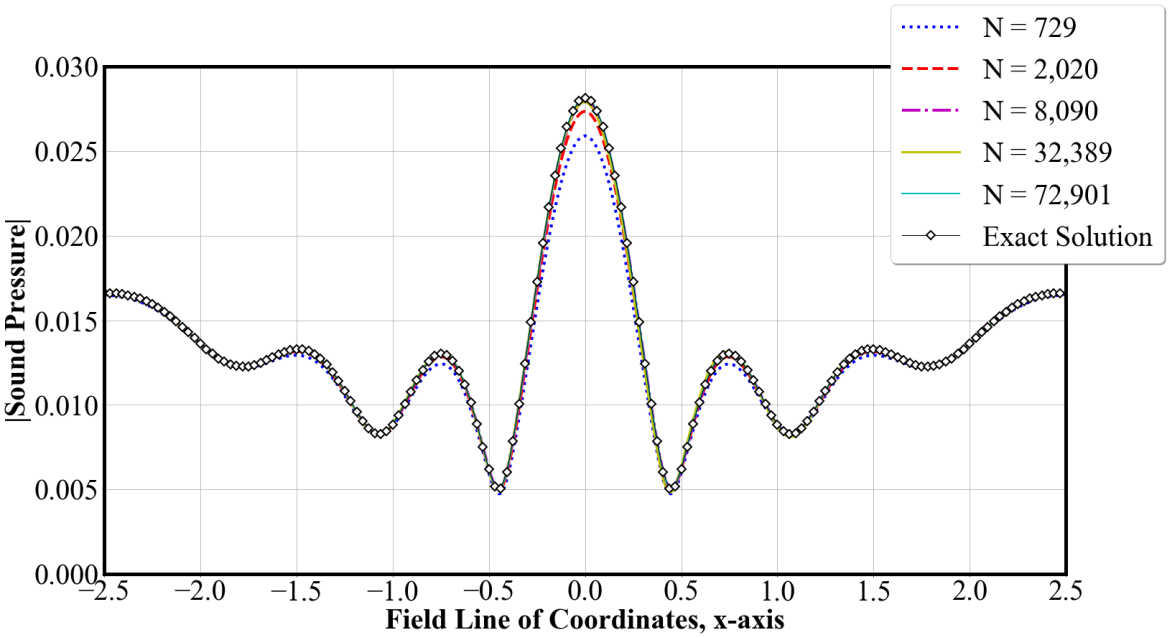

Fig. 68: Frequency-domain solution converted from the time-domain at $\omega = 8\pi$ for rigid body sphere scattering along the field line of coordinates, $-2.5 \leq x \leq 2.5, y = 0, z = -2.5$.

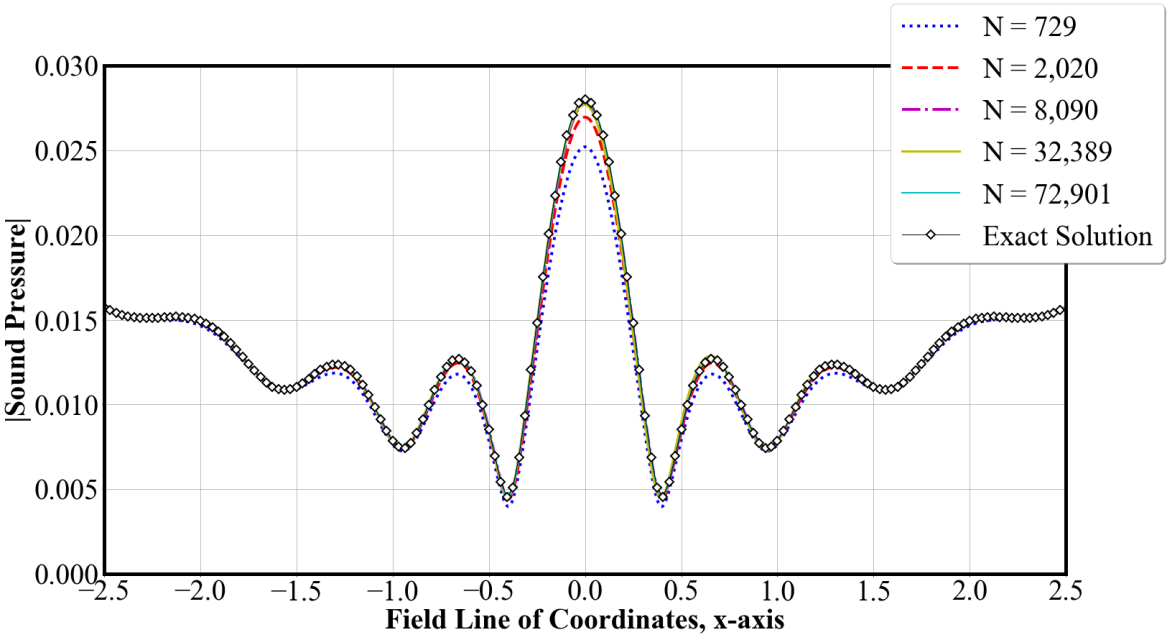

Fig. 69: Frequency-domain solution converted from the time-domain at $\omega = 9\pi$ for rigid body sphere scattering along the field line of coordinates, $-2.5 \leq x \leq 2.5, y = 0, z = -2.5$.

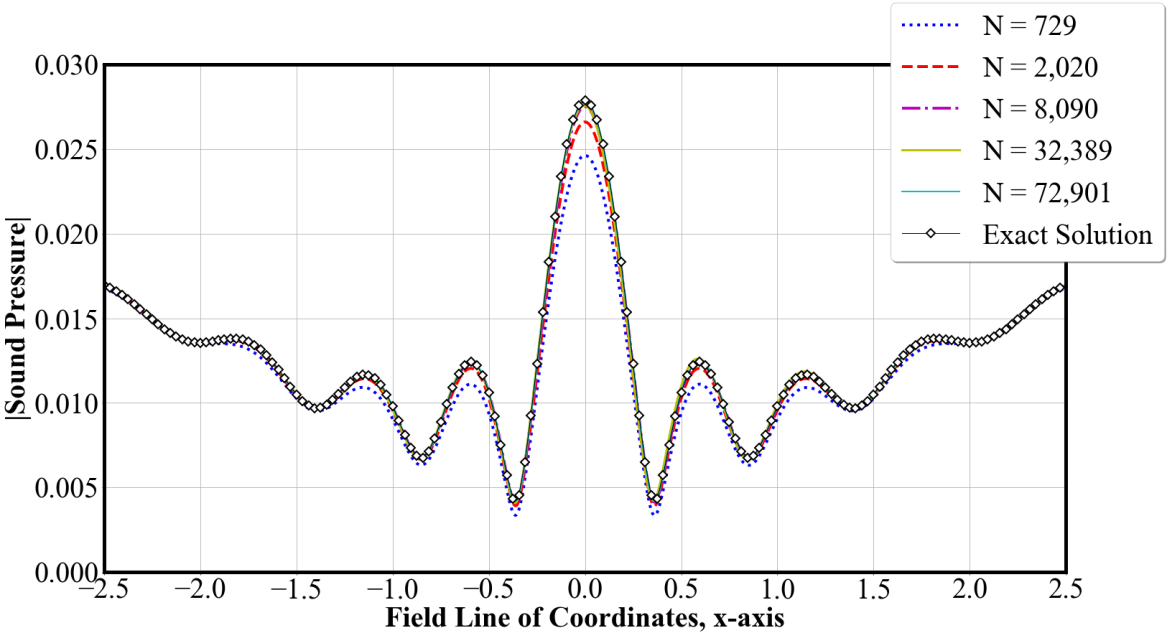

Fig. 70: Frequency-domain solution converted from the time-domain at $\omega = 10\pi$ for rigid body sphere scattering along the field line of coordinates, $-2.5 \leq x \leq 2.5, y = 0, z = -2.5$.

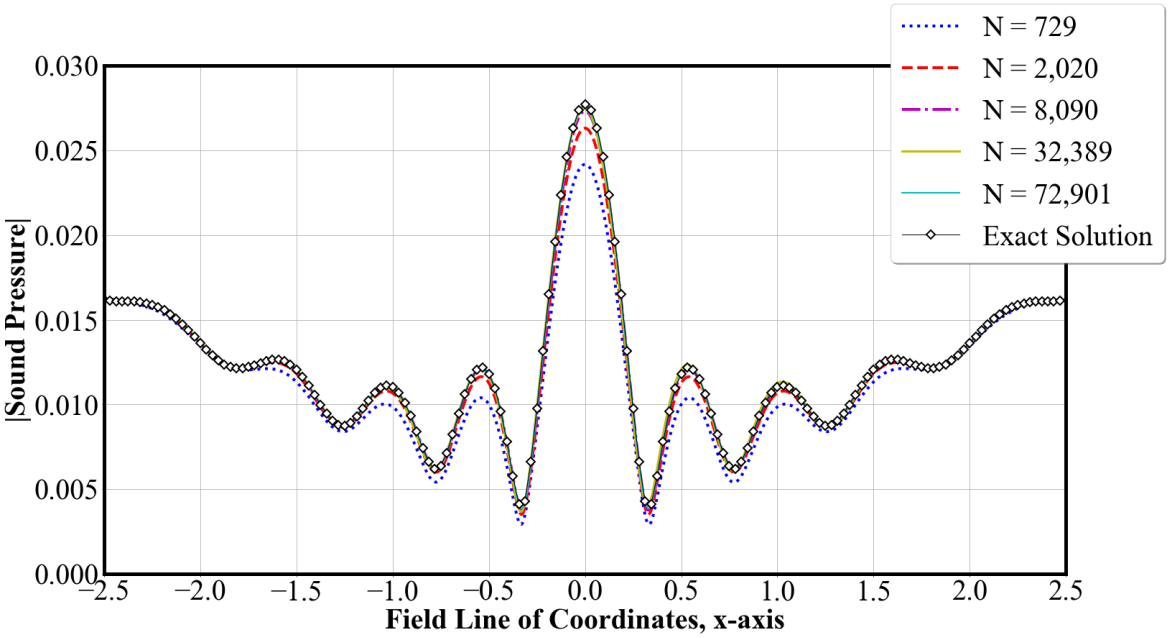

Fig. 71: Frequency-domain solution converted from the time-domain at $\omega = 11\pi$ for rigid body sphere scattering along the field line of coordinates, $-2.5 \leq x \leq 2.5, y = 0, z = -2.5$.

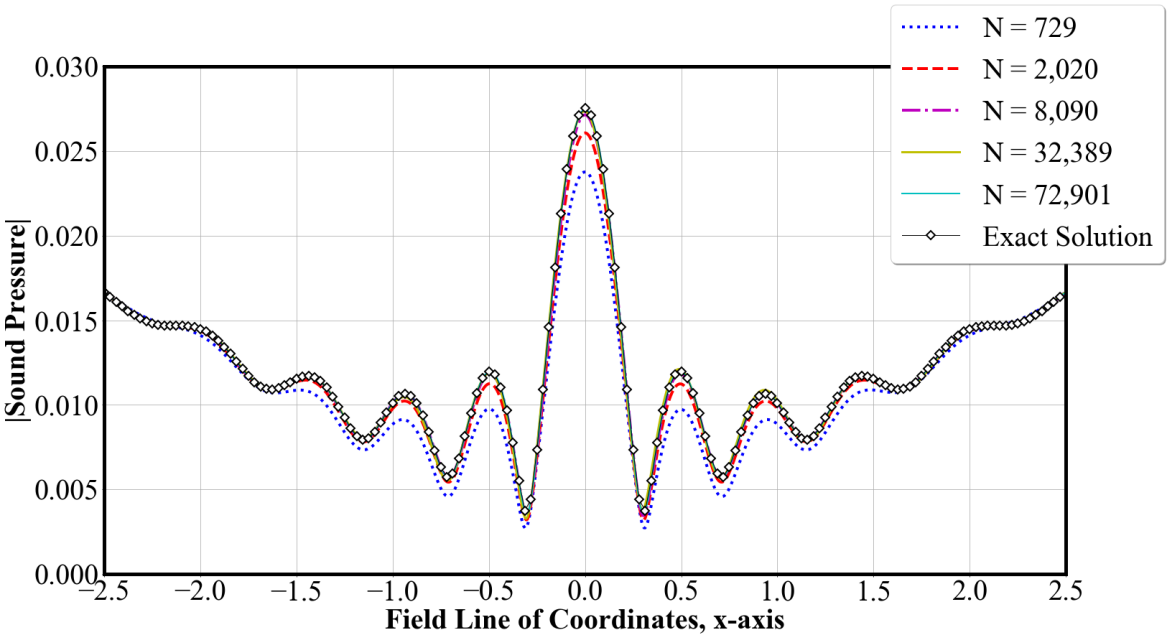

Fig. 72: Frequency-domain solution converted from the time-domain at $\omega = 12\pi$ for rigid body sphere scattering along the field line of coordinates, $-2.5 \leq x \leq 2.5, y = 0, z = -2.5$.

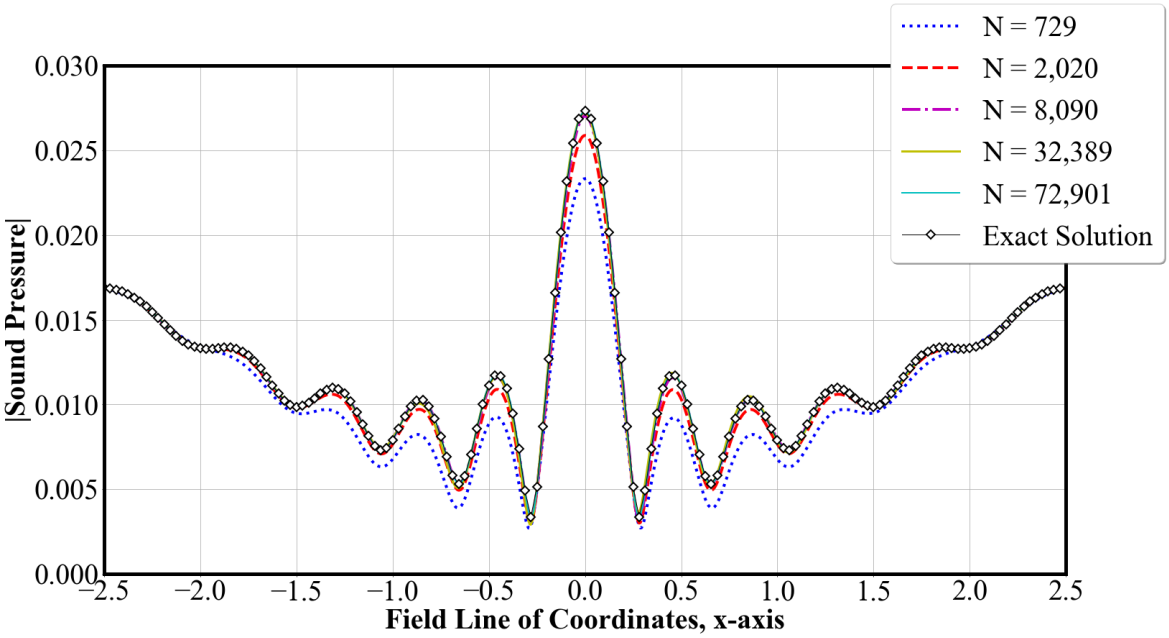

Fig. 73: Frequency-domain solution converted from the time-domain at $\omega = 13\pi$ for rigid body sphere scattering along the field line of coordinates, $-2.5 \leq x \leq 2.5, y = 0, z = -2.5$.

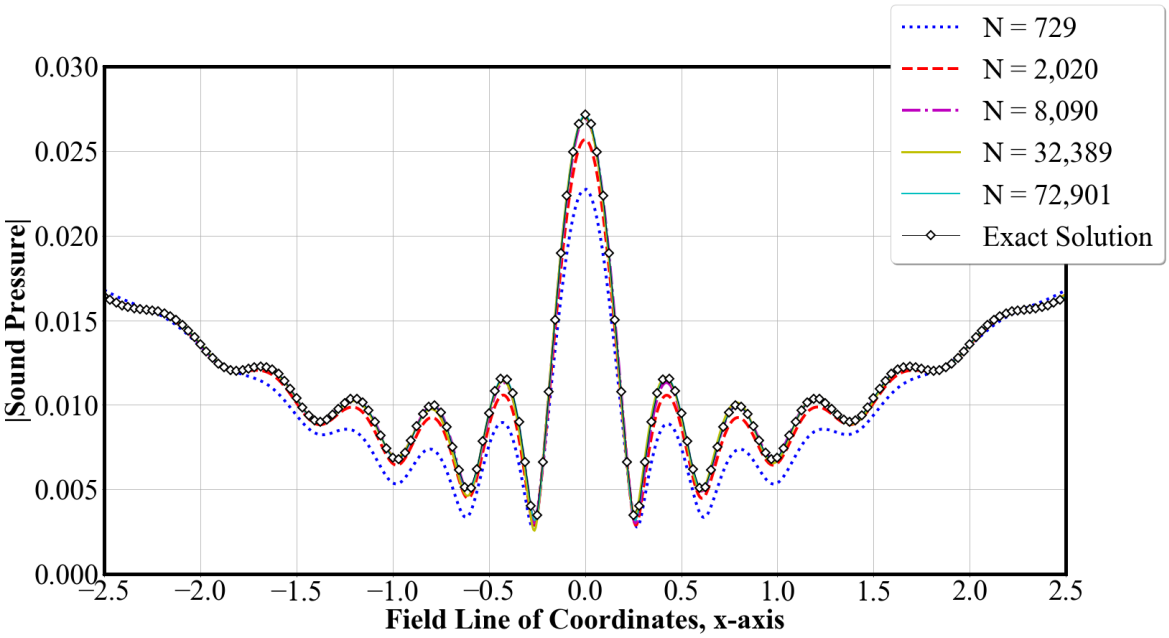

Fig. 74: Frequency-domain solution converted from the time-domain at $\omega = 14\pi$ for rigid body sphere scattering along the field line of coordinates, $-2.5 \leq x \leq 2.5, y = 0, z = -2.5$.

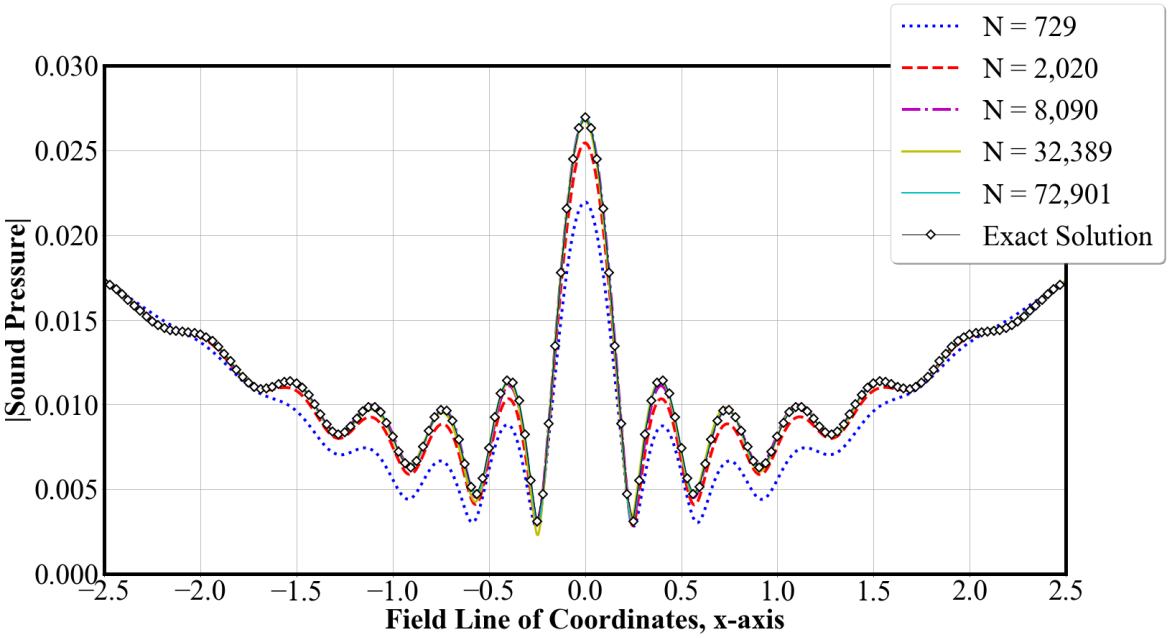

Fig. 75: Frequency-domain solution converted from the time-domain at $\omega = 15\pi$ for rigid body sphere scattering along the field line of coordinates, $-2.5 \leq x \leq 2.5, y = 0, z = -2.5$.

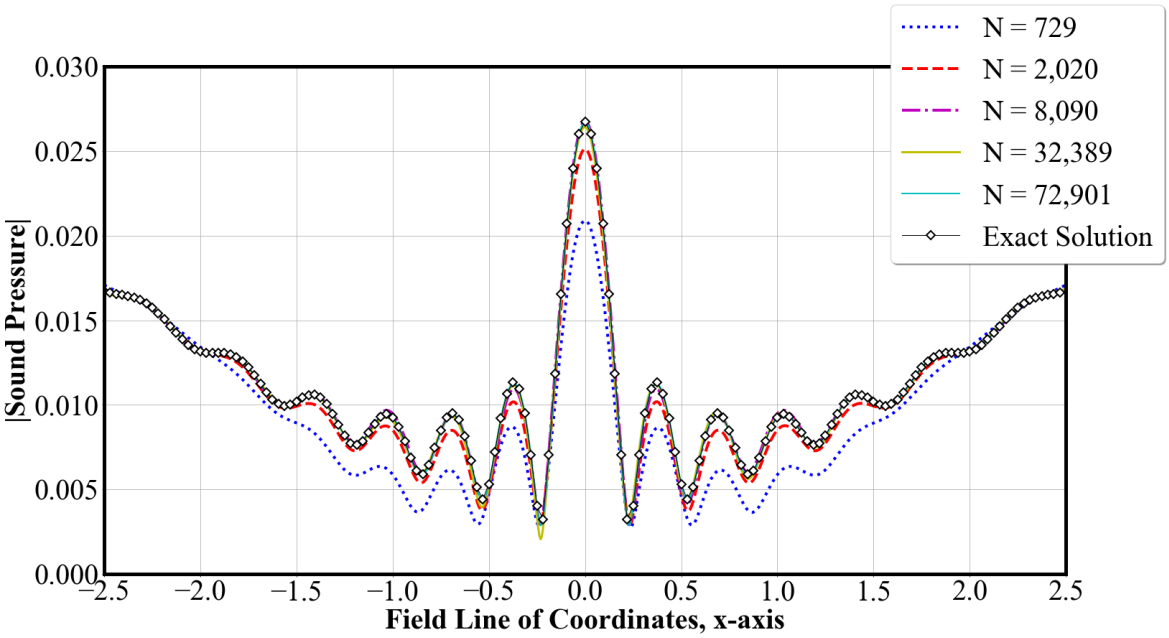

Fig. 76: Frequency-domain solution converted from the time-domain at $\omega = 16\pi$ for rigid body sphere scattering along the field line of coordinates, $-2.5 \leq x \leq 2.5, y = 0, z = -2.5$.

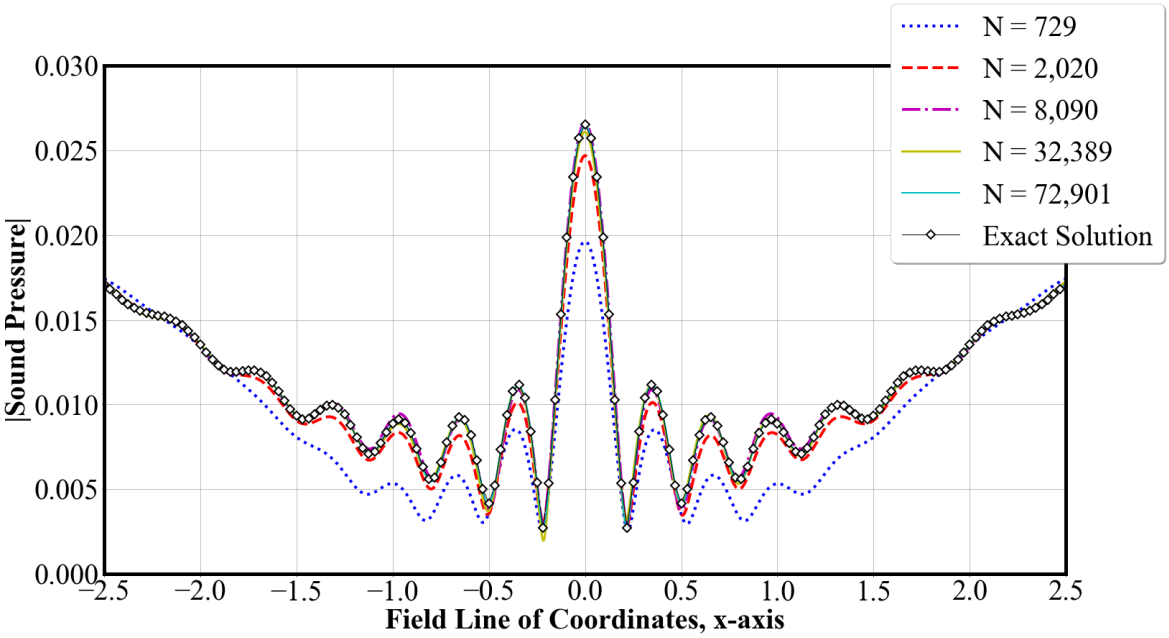

Fig. 77: Frequency-domain solution converted from the time-domain at $\omega = 17\pi$ for rigid body sphere scattering along the field line of coordinates, $-2.5 \leq x \leq 2.5, y = 0, z = -2.5$.

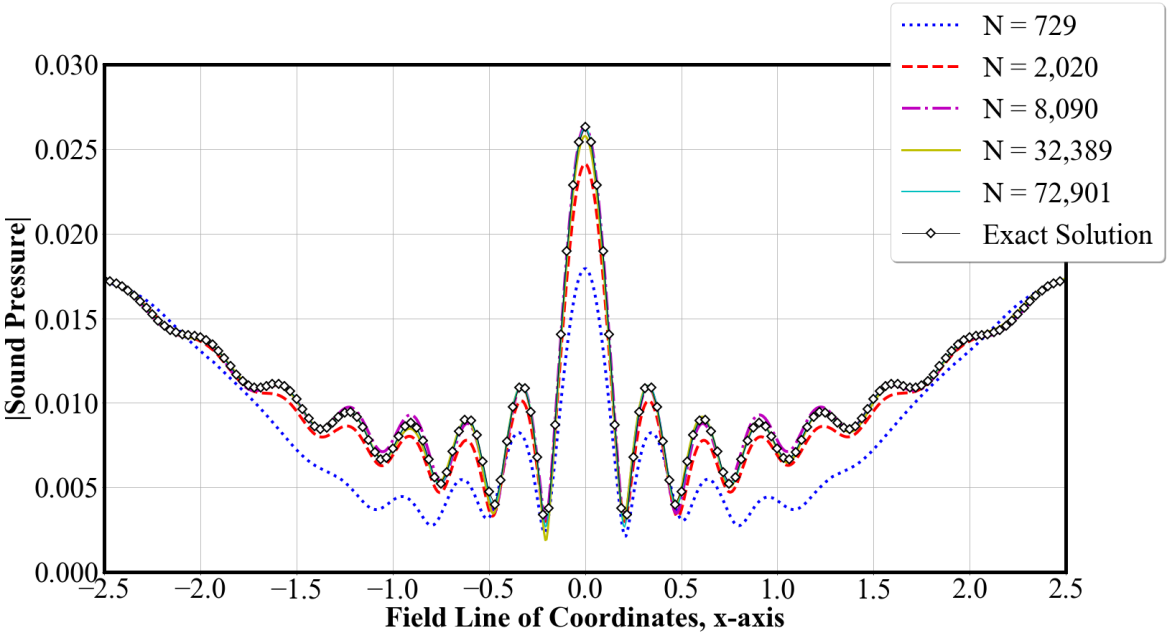

Fig. 78: Frequency-domain solution converted from the time-domain at $\omega = 18\pi$ for rigid body sphere scattering along the field line of coordinates, $-2.5 \leq x \leq 2.5, y = 0, z = -2.5$.

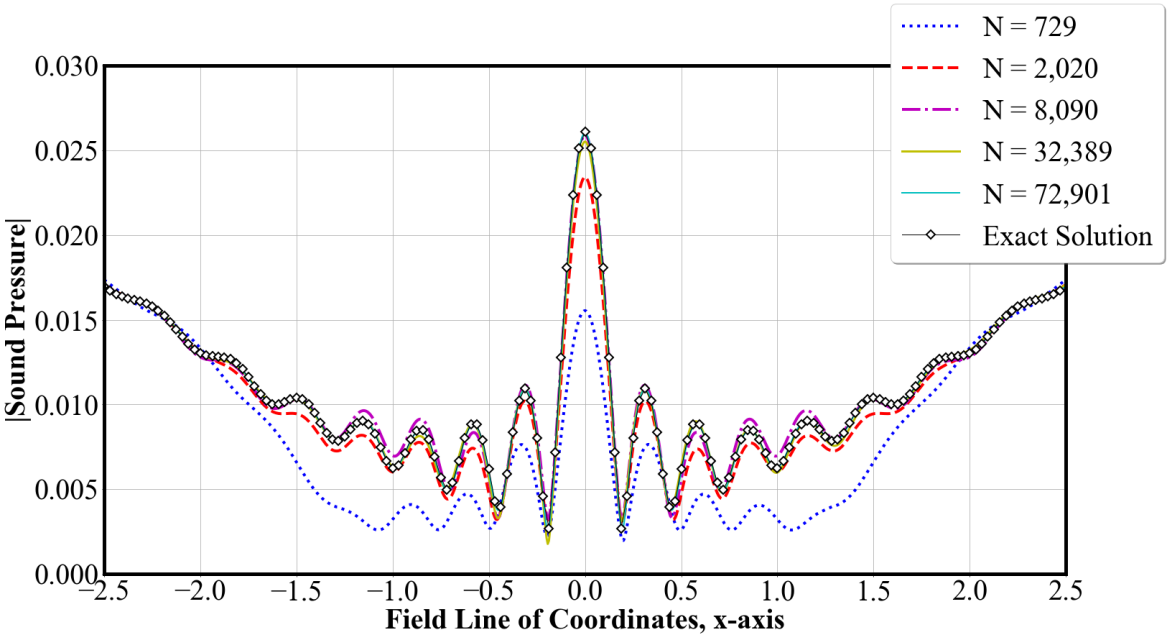

Fig. 79: Frequency-domain solution converted from the time-domain at $\omega = 19\pi$ for rigid body sphere scattering along the field line of coordinates, $-2.5 \leq x \leq 2.5, y = 0, z = -2.5$.

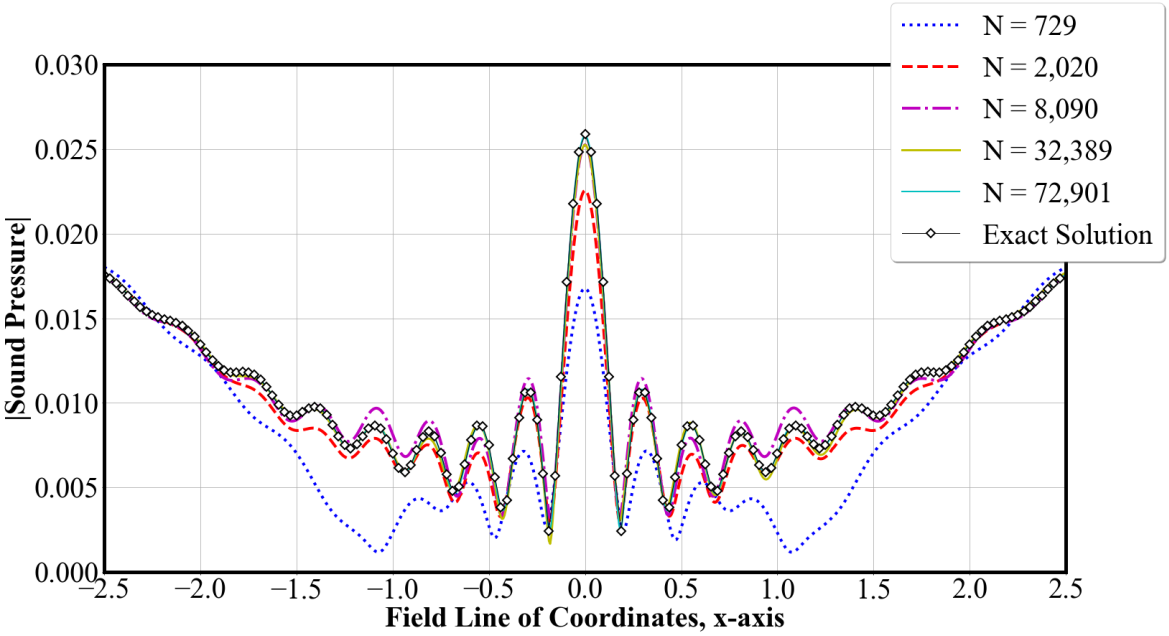

Fig. 80: Frequency-domain solution converted from the time-domain at $\omega = 20\pi$ for rigid body sphere scattering along the field line of coordinates, $-2.5 \leq x \leq 2.5, y = 0, z = -2.5$.

APPENDIX C

AVERAGE CLOCK TIME PER SIMULATION TIME STEP

This appendix illustrates the average clock time for each time step in the simulation graphed versus time step in the simulation for element sizes $N = 1,120$ through $N = 7,000$ using two, four, eight, *etc.* CPU cores. Figures 26 through 29 in Chapter 4 include results of using one core but as the discretization becomes more refined and more processing power is used, it is increasingly difficult to differentiate between larger core counts. Figures 81 through 84 therefore provides a better visualization of the larger core counts shown Figures 25 through 29 by excluding data from one CPU.

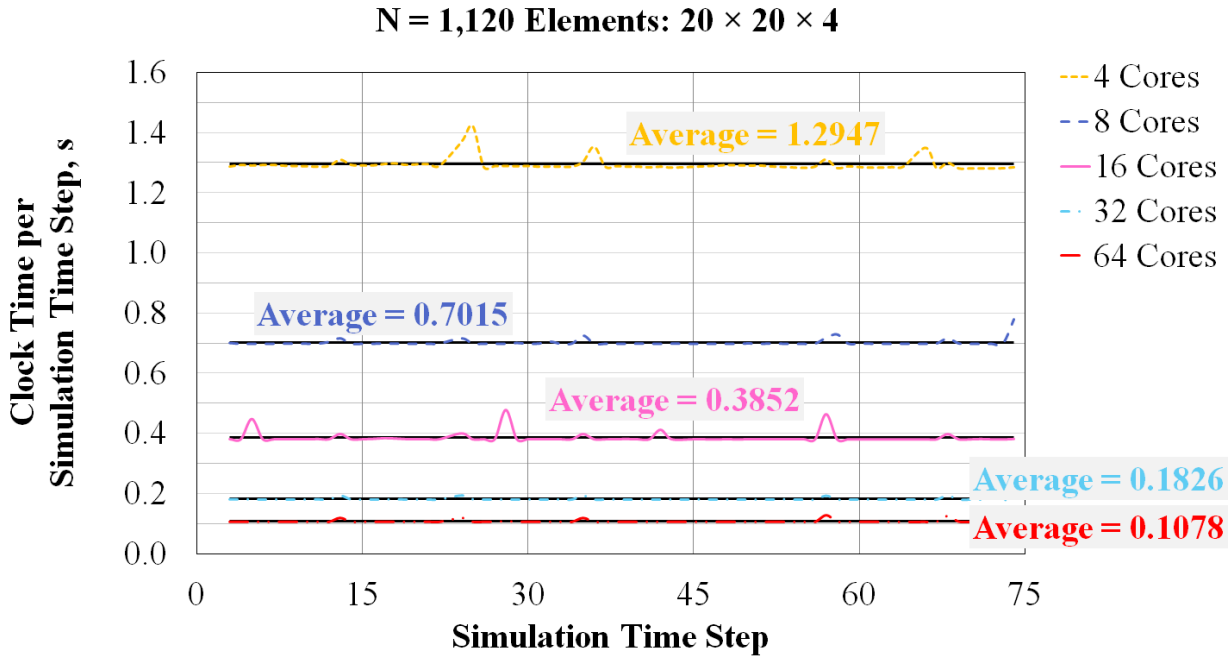

Fig. 81: Average clock time for $N = 1,120$ elements using one exclusive node with four, eight, sixteen, and thirty-two cores and using two exclusive nodes with sixty-four cores.

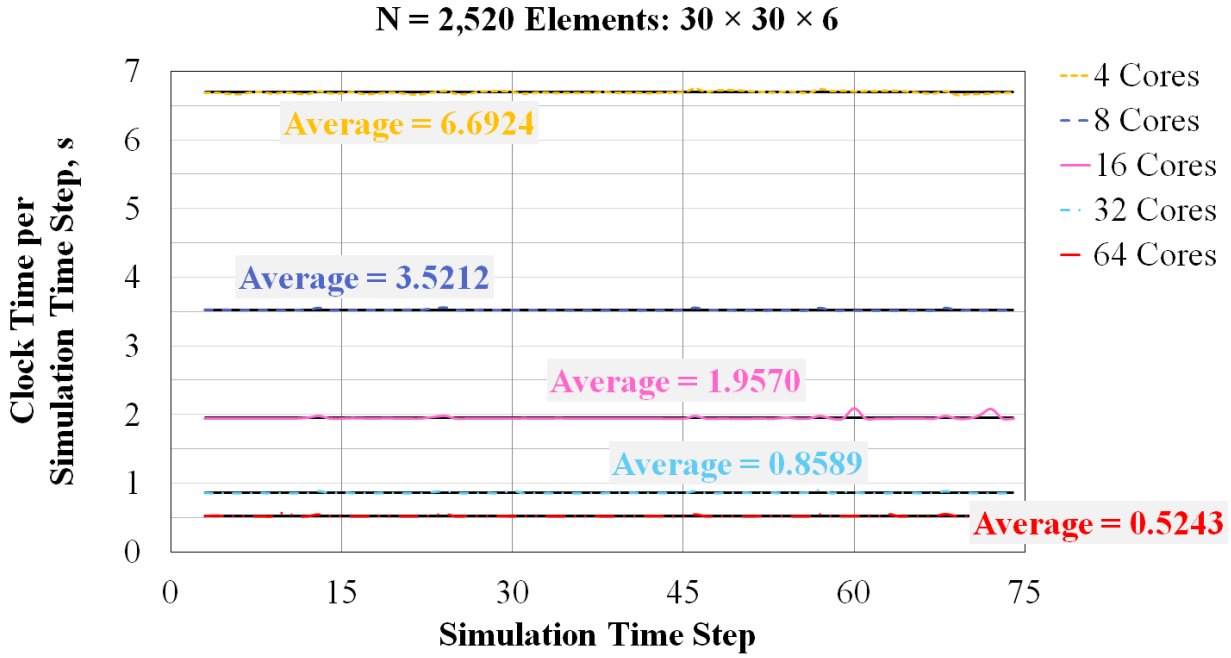

Fig. 82: Average clock time for $N = 2,520$ elements using one exclusive node with four, eight, sixteen, and thirty-two cores and using two exclusive nodes with sixty-four cores.

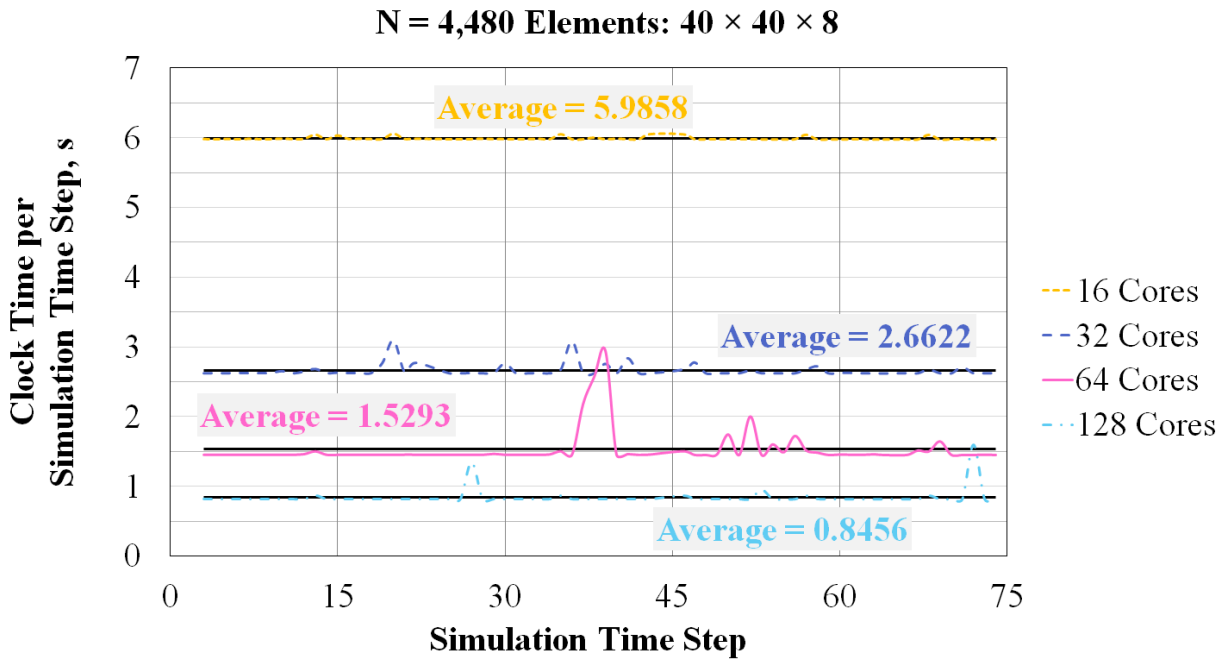

Fig. 83: Average clock time for $N = 4,480$ elements using one exclusive node with sixteen and thirty-two cores, using two exclusive nodes with sixty-four cores, and using four exclusive nodes with 128 cores.

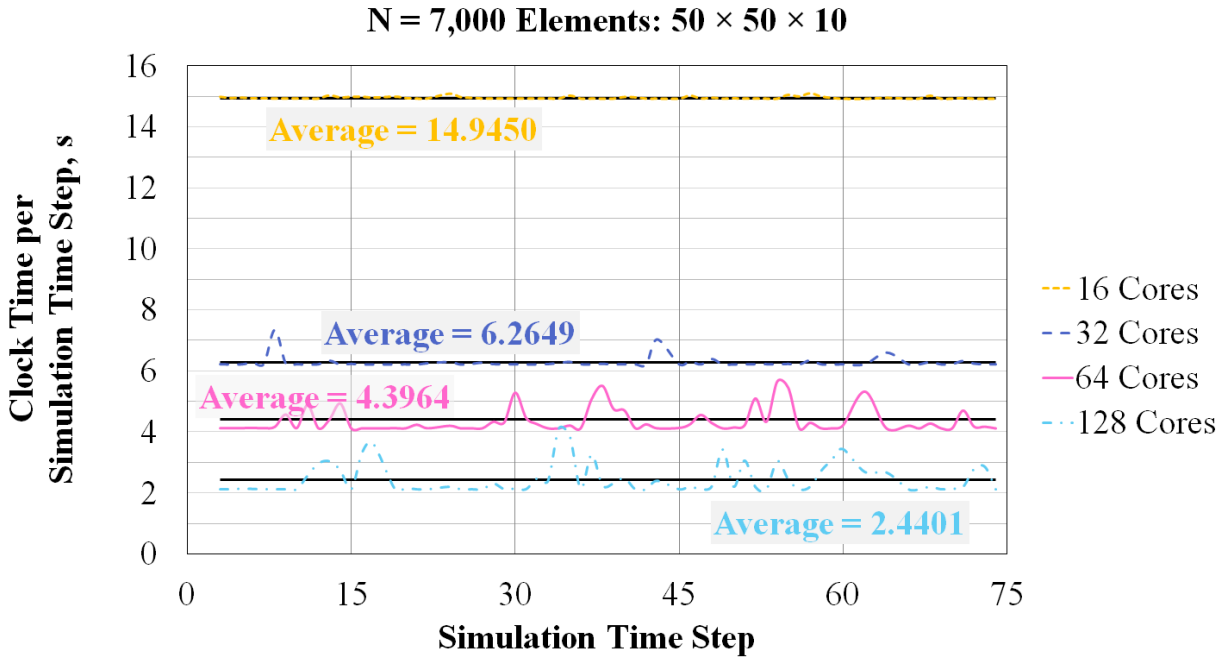

Fig. 84: Average clock time for $N = 7,000$ elements using one exclusive node with sixteen and thirty-two cores, using two exclusive nodes with sixty-four cores, and using four exclusive nodes with 128 cores

APPENDIX D

MATRIX POWER ITERATION METHOD

In this appendix, the methodology for solving a polynomial eigenvalue problem using a matrix power iteration method is discussed.

Seeking solutions of the form (106)

$$\boldsymbol{w^n} = \lambda^n \boldsymbol{e}_0$$

to the corresponding homogeneous system (105)

$$\boldsymbol{A_0 w^n} = \boldsymbol{q_0^n} - \boldsymbol{A_1 w^{n-1}} - \boldsymbol{A_2 w^{n-2}} - ... - \boldsymbol{A_K w^{n-K}} - ... - \boldsymbol{A_J w^{n-J}}$$

yields the polynomial eigenvalue problem given by (107) in Chapter 6:

$$\left[\boldsymbol{A_0}\lambda^J + \boldsymbol{A_1}\lambda^{J-1} + \boldsymbol{A_2}\lambda^{J-2} + \cdots + \boldsymbol{A_{J-1}}\lambda + \boldsymbol{A_J}\right] \boldsymbol{e}_0 = 0$$

where $\boldsymbol{e}_j = \lambda^j \boldsymbol{e}_0 = \lambda \boldsymbol{e}_{j-1}$ for all $j = 1, \ldots, J$, *i.e.*,

$$\boldsymbol{A_0}\lambda \boldsymbol{e}_{J-1} + \boldsymbol{A_1 e}_{J-1} + \boldsymbol{A_2 e}_{J-2} + \cdots + \boldsymbol{A_{J-1} e}_1 + \boldsymbol{A_J e}_0 = 0. \tag{111}$$

Equation (111) is then cast into a generalized eigenvalue problem:

$$\lambda \begin{bmatrix} \boldsymbol{A_0} & 0 & 0 & \cdots & 0 & 0 \\ 0 & \boldsymbol{I} & 0 & \cdots & 0 & 0 \\ 0 & 0 & \boldsymbol{I} & \cdots & 0 & 0 \\ \vdots & \vdots & & \ddots & & \vdots \\ 0 & 0 & 0 & \cdots & \boldsymbol{I} & 0 \\ 0 & 0 & 0 & \cdots & 0 & \boldsymbol{I} \end{bmatrix} \begin{bmatrix} \boldsymbol{e_{J-1}} \\ \boldsymbol{e_{J-2}} \\ \boldsymbol{e_{J-3}} \\ \vdots \\ \boldsymbol{e_1} \\ \boldsymbol{e_0} \end{bmatrix} = \begin{bmatrix} -\boldsymbol{A_1} & -\boldsymbol{A_2} & \cdots & -\boldsymbol{A_{J-2}} & -\boldsymbol{A_{J-1}} & -\boldsymbol{A_J} \\ \boldsymbol{I} & 0 & \cdots & 0 & 0 & 0 \\ 0 & \boldsymbol{I} & \cdots & 0 & 0 & 0 \\ \vdots & & \ddots & & \vdots & \vdots \\ 0 & 0 & \cdots & \boldsymbol{I} & 0 & 0 \\ 0 & 0 & \cdots & 0 & \boldsymbol{I} & 0 \end{bmatrix} \begin{bmatrix} \boldsymbol{e_{J-1}} \\ \boldsymbol{e_{J-2}} \\ \vdots \\ \boldsymbol{e_2} \\ \boldsymbol{e_1} \\ \boldsymbol{e_0} \end{bmatrix}.$$

Simplifying gives:

$$\lambda \begin{bmatrix} \boldsymbol{e_{J-1}} \\ \boldsymbol{e_{J-2}} \\ \boldsymbol{e_{J-3}} \\ \vdots \\ \boldsymbol{e_1} \\ \boldsymbol{e_0} \end{bmatrix} = \begin{bmatrix} \boldsymbol{A_0} & 0 & 0 & \cdots & 0 & 0 \\ 0 & \boldsymbol{I} & 0 & \cdots & 0 & 0 \\ 0 & 0 & \boldsymbol{I} & \cdots & 0 & 0 \\ \vdots & \vdots & & \ddots & & \vdots \\ 0 & 0 & 0 & \cdots & \boldsymbol{I} & 0 \\ 0 & 0 & 0 & \cdots & 0 & \boldsymbol{I} \end{bmatrix}^{-1} \begin{bmatrix} -\boldsymbol{A_1} & -\boldsymbol{A_2} & \cdots & -\boldsymbol{A_{J-2}} & -\boldsymbol{A_{J-1}} & -\boldsymbol{A_J} \\ \boldsymbol{I} & 0 & \cdots & 0 & 0 & 0 \\ 0 & \boldsymbol{I} & \cdots & 0 & 0 & 0 \\ \vdots & & \ddots & & \vdots & \vdots \\ 0 & 0 & \cdots & \boldsymbol{I} & 0 & 0 \\ 0 & 0 & \cdots & 0 & \boldsymbol{I} & 0 \end{bmatrix} \begin{bmatrix} \boldsymbol{e_{J-1}} \\ \boldsymbol{e_{J-2}} \\ \vdots \\ \boldsymbol{e_2} \\ \boldsymbol{e_1} \\ \boldsymbol{e_0} \end{bmatrix}$$

and

$$\lambda \begin{bmatrix} \boldsymbol{e_{J-1}} \\ \boldsymbol{e_{J-2}} \\ \boldsymbol{e_{J-3}} \\ \vdots \\ \boldsymbol{e_1} \\ \boldsymbol{e_0} \end{bmatrix} = \begin{bmatrix} -\boldsymbol{A_0}^{-1}\boldsymbol{A_1} & -\boldsymbol{A_0}^{-1}\boldsymbol{A_2} & \cdots & -\boldsymbol{A_0}^{-1}\boldsymbol{A_{J-2}} & -\boldsymbol{A_0}^{-1}\boldsymbol{A_{J-1}} & -\boldsymbol{A_0}^{-1}\boldsymbol{A_J} \\ \boldsymbol{I} & 0 & \cdots & 0 & 0 & 0 \\ 0 & \boldsymbol{I} & \cdots & 0 & 0 & 0 \\ \vdots & & \ddots & & \vdots & \vdots \\ 0 & 0 & \cdots & \boldsymbol{I} & 0 & 0 \\ 0 & 0 & \cdots & 0 & \boldsymbol{I} & 0 \end{bmatrix} \begin{bmatrix} \boldsymbol{e_{J-1}} \\ \boldsymbol{e_{J-2}} \\ \vdots \\ \boldsymbol{e_2} \\ \boldsymbol{e_1} \\ \boldsymbol{e_0} \end{bmatrix},$$

which can then be written as

$$\boldsymbol{A}\boldsymbol{e} = \lambda \boldsymbol{e} \tag{112}$$

such that

$$\boldsymbol{A} = \begin{bmatrix} -\boldsymbol{A_0}^{-1}\boldsymbol{A_1} & -\boldsymbol{A_0}^{-1}\boldsymbol{A_2} & \cdots & -\boldsymbol{A_0}^{-1}\boldsymbol{A_{J-2}} & -\boldsymbol{A_0}^{-1}\boldsymbol{A_{J-1}} & -\boldsymbol{A_0}^{-1}\boldsymbol{A_J} \\ \boldsymbol{I} & 0 & \cdots & 0 & 0 & 0 \\ 0 & \boldsymbol{I} & \cdots & 0 & 0 & 0 \\ \vdots & & \ddots & & \vdots & \vdots \\ 0 & 0 & \cdots & \boldsymbol{I} & 0 & 0 \\ 0 & 0 & \cdots & 0 & \boldsymbol{I} & 0 \end{bmatrix}$$

and

$$\boldsymbol{e} = \left[\boldsymbol{e_{J-1}}\boldsymbol{e_{J-2}}\cdots\boldsymbol{e_2}\boldsymbol{e_1}\boldsymbol{e_0}\right]^T.$$

The matrix power iteration method is then used to find the largest eigenvalue of (112). The method proceeds as follows:

Step 1) Define an arbitrary unit vector to be $\boldsymbol{\xi}^{(0)}$.

Step 2) For $k = 1, 2, \ldots,$ calculate

$$\boldsymbol{e}^{(k)} = \boldsymbol{A}\boldsymbol{\xi}^{(k-1)}, \boldsymbol{q}^{(k)} = \frac{\boldsymbol{e}^{(k)}}{||\boldsymbol{e}^{(k)}||_2}, \text{ and } \lambda^{(k)} = \left[\boldsymbol{\xi}^{(k)}\right]^T \boldsymbol{A}\boldsymbol{\xi}^{(k)} = \left[\boldsymbol{\xi}^{(k)}\right]^T \boldsymbol{e}^{(k+1)}.$$

Step 3) Calculate the difference between consecutive eigenvalues, $|\lambda^{(k)} - \lambda^{(k-1)}|$.

Step 4) Repeat until the iterative scheme has converged to the largest eigenvalue, $|\lambda|_{\max}$, *i.e.*, when $|\lambda^{(k)} - \lambda^{(k-1)}|/|\lambda^{(k)}| < \delta$ for a given tolerance δ.

Herein, the following limitations are set for the tolerance δ in order to ensure that the matrix power iteration method returns a converged solution within a reasonable amount of iterations: if iterations $< 5,000$ then $\delta = 10^{-9}$ and if iterations $\geq 5,000$ then the solution is considered non-convergent.

APPENDIX E

CASES USED TO MODEL SINGLE FREQUENCY IMPEDANCE

For the *Extended Helmholtz Resonator Model* and the *Three-Parameter Model*, the liner boundary conditions are modeled using numerical data from [59]. In [59], eighteen different resistance and reactance curves are proposed for varying combinations of $Z(\omega)$ and ν within the range $0 \leq \omega\Delta t \leq \pi/5$, where $Z(\omega)$ is the impedance and ν is a constant defined such that the resonator cavity depth is proportional to a multiple of time-step: $2L/c = \nu\Delta t$ for depth L and speed of sound c. All eighteen cases are illustrated in this appendix and the resistance and reactance curves each intersect at the non-dimensional frequency $\omega_0\Delta t = \pi/10$. Cases 1 through 18 are used for the *Extended Helmholtz Resonator Model* analysis. Cases 1, 4, 7, 10, 13, and 16 are used for the *Three-Parameter Model* analysis. In each figure, the values for $Z(\omega)$ and ν are listed.

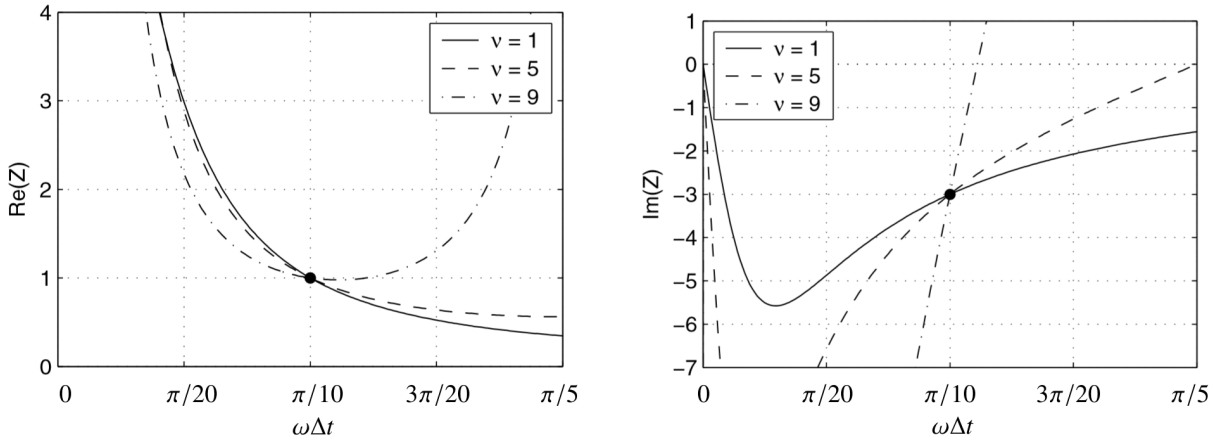

Fig. 85: Resistance and reactance curves for Cases 1, 2, 3. Impedance is $Z(\omega_0 \Delta t) = 1 - 3i$.

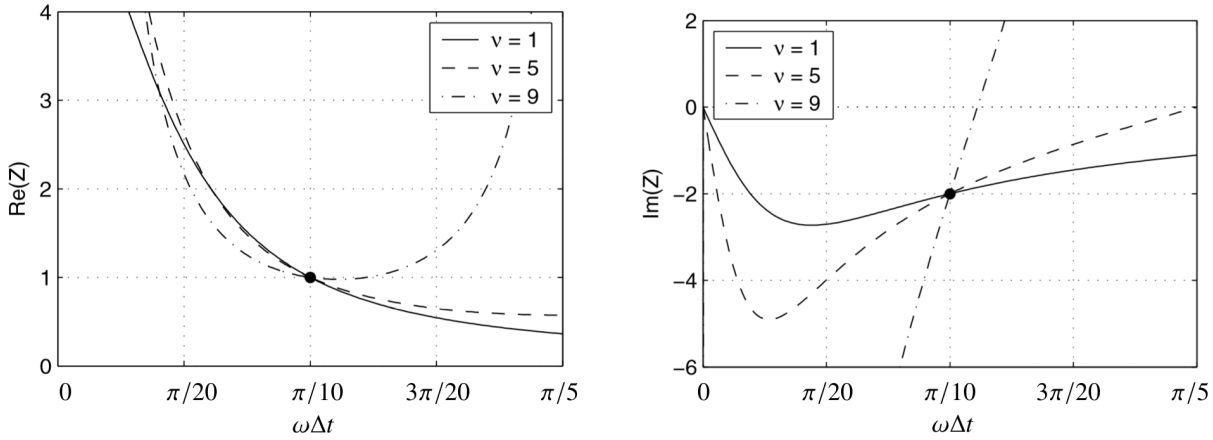

Fig. 86: Resistance and reactance curves for Cases 4, 5, 6. Impedance is $Z(\omega_0 \Delta t) = 1 - 2i$.

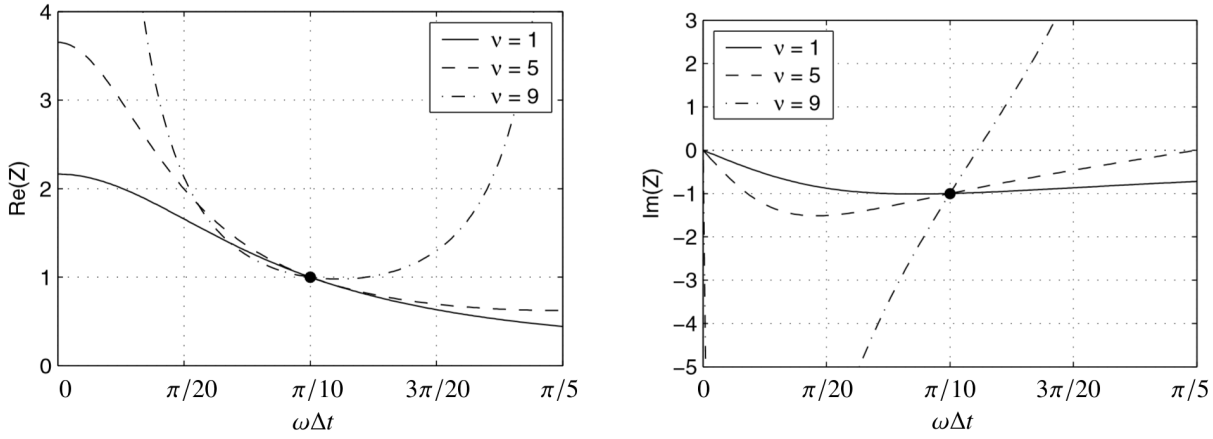

Fig. 87: Resistance and reactance curves for Cases 7, 8, 9. Impedance is $Z(\omega_0 \Delta t) = 1 - i$.

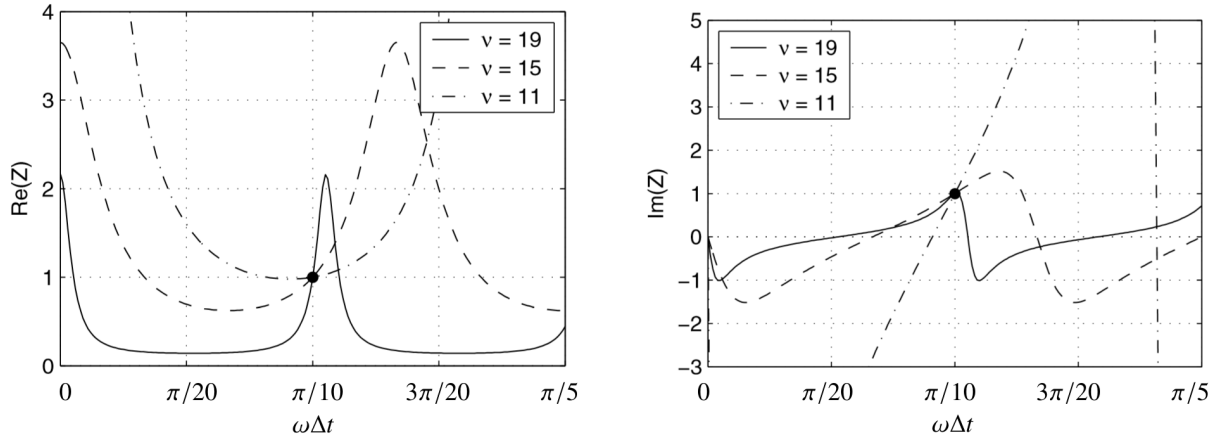

Fig. 88: Resistance and reactance curves for Cases 10, 11, 12. Impedance is $Z(\omega_0\Delta t) = 1+i$.

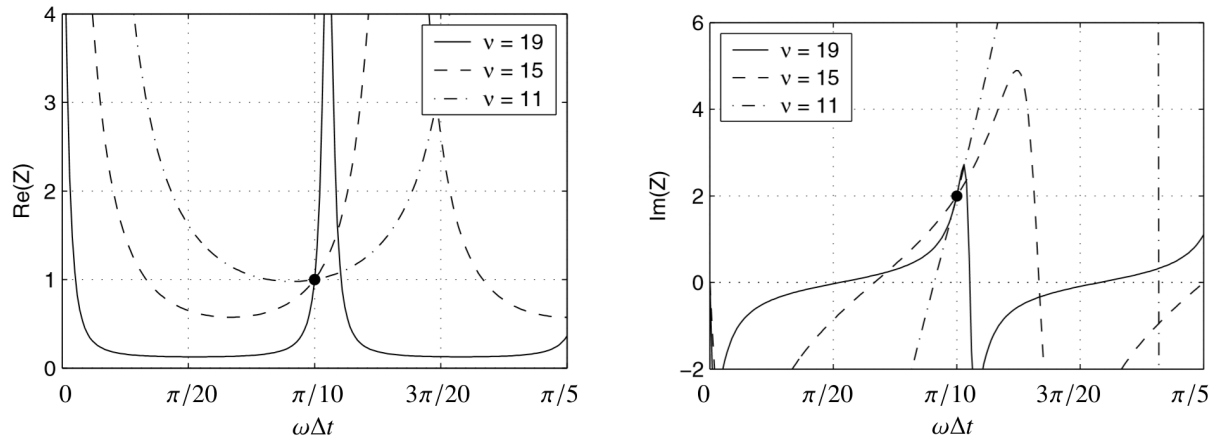

Fig. 89: Resistance and reactance curves for Cases 13, 14, 15. Impedance is $Z(\omega_0\Delta t) = 1+2i$.

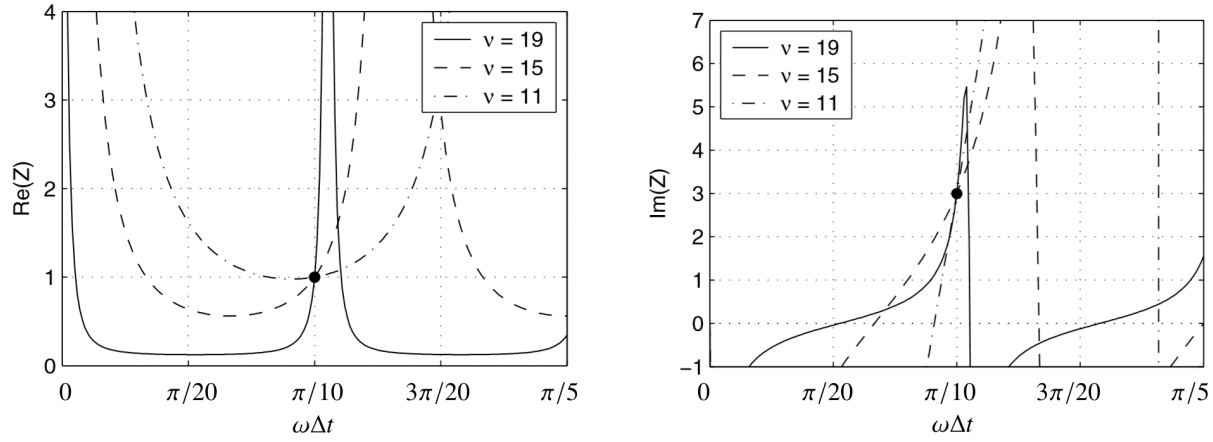

Fig. 90: Resistance and reactance curves for Cases 16, 17, 18. Impedance is $Z(\omega_0\Delta t) = 1+3i$.

APPENDIX F

CASES USED TO MODEL BROADBAND IMPEDANCE

For the *Broadband Impedance Model*, the liner boundary condition is modeled using experimental data. Two different acoustic liners were tested, and impedance values measured along a wide range of frequencies. Using the measured data, twenty-five different models were generated using least squares regression to obtain values for the constants which define the frequency-domain surface impedance (84). All twenty-five cases are illustrated in this appendix. Cases 1-3, 6-8, 20-25 illustrate the CT57 acoustic liner and Cases 4-5, 9-19 illustrate the GE05 acoustic liner. In each figure, the experimental data is graphed using solid circles and the numerical model is graphed with a dotted line.

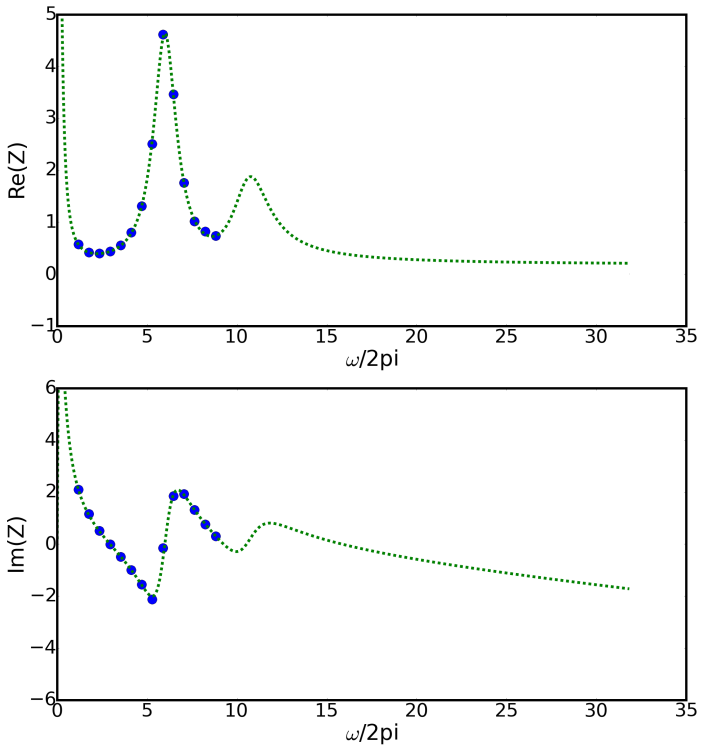

Fig. 91: Resistance and reactance curves for Broadband Case 1.

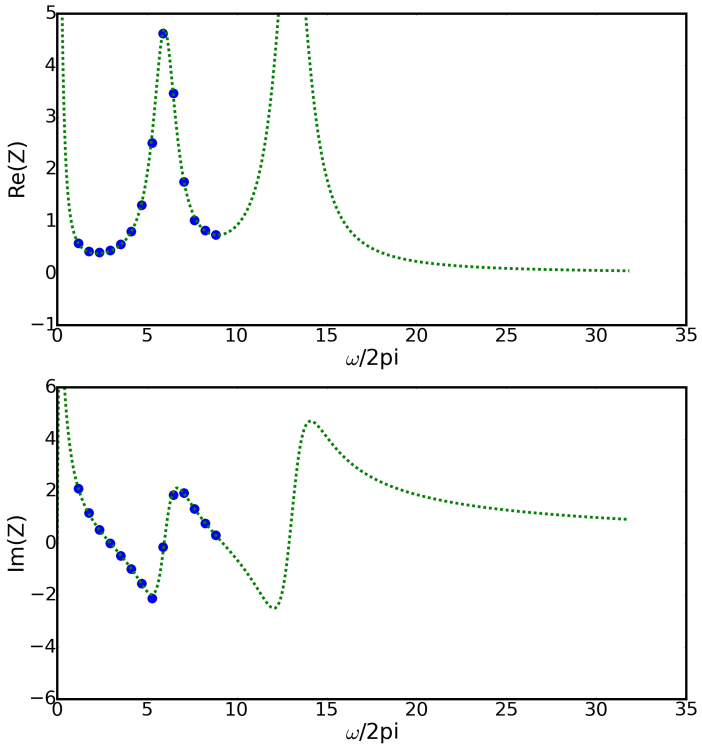

Fig. 92: Resistance and reactance curves for Broadband Case 2.

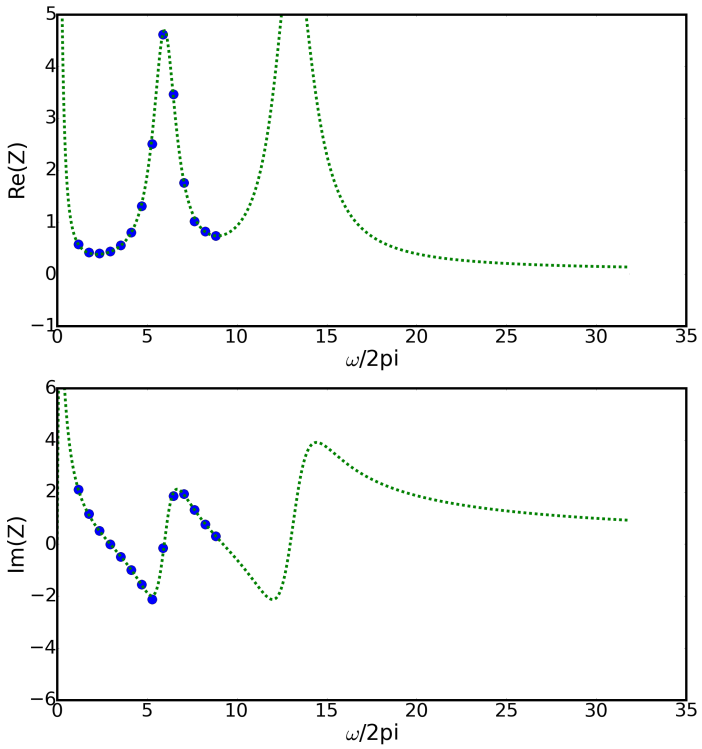

Fig. 93: Resistance and reactance curves for Broadband Case 3.

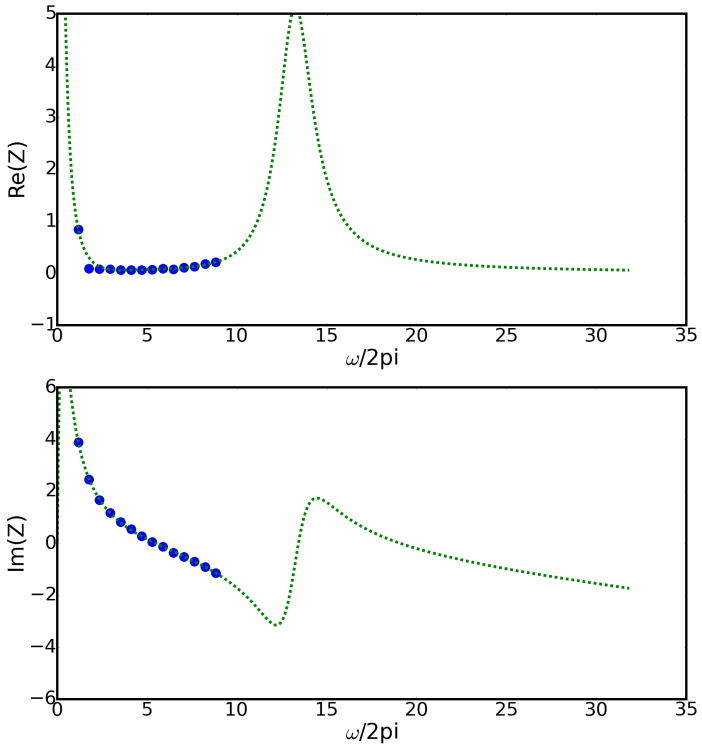

Fig. 94: Resistance and reactance curves for Broadband Case 4.

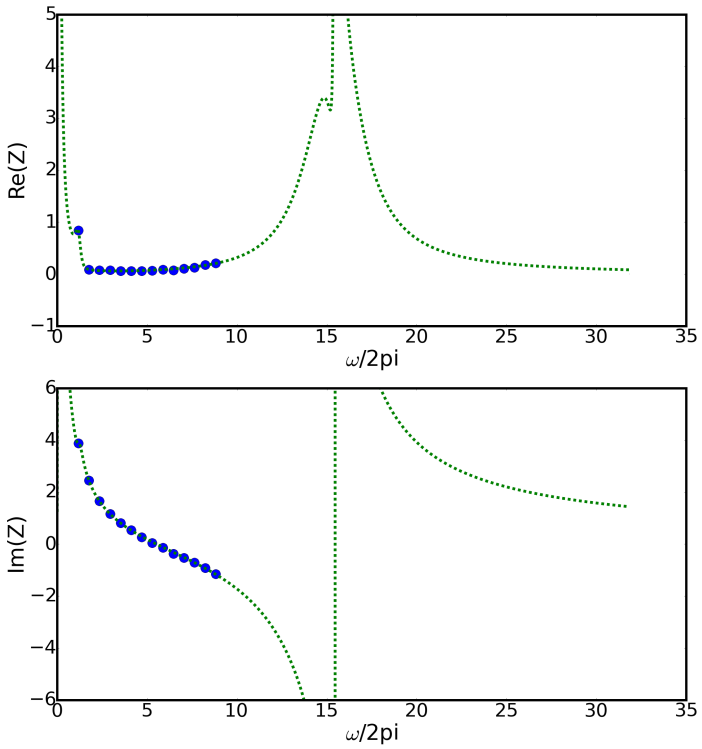

Fig. 95: Resistance and reactance curves for Broadband Case 5.

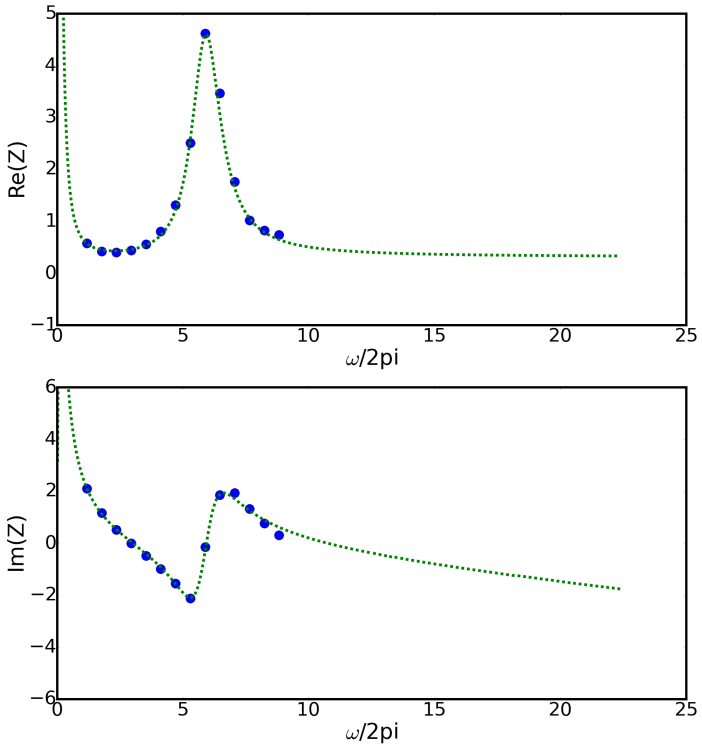

Fig. 96: Resistance and reactance curves for Broadband Case 6.

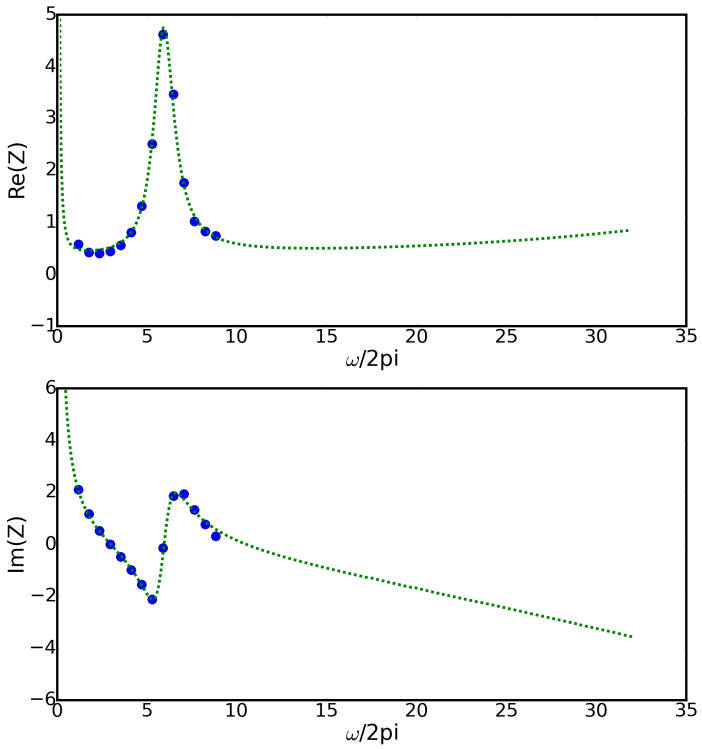

Fig. 97: Resistance and reactance curves for Broadband Case 7.

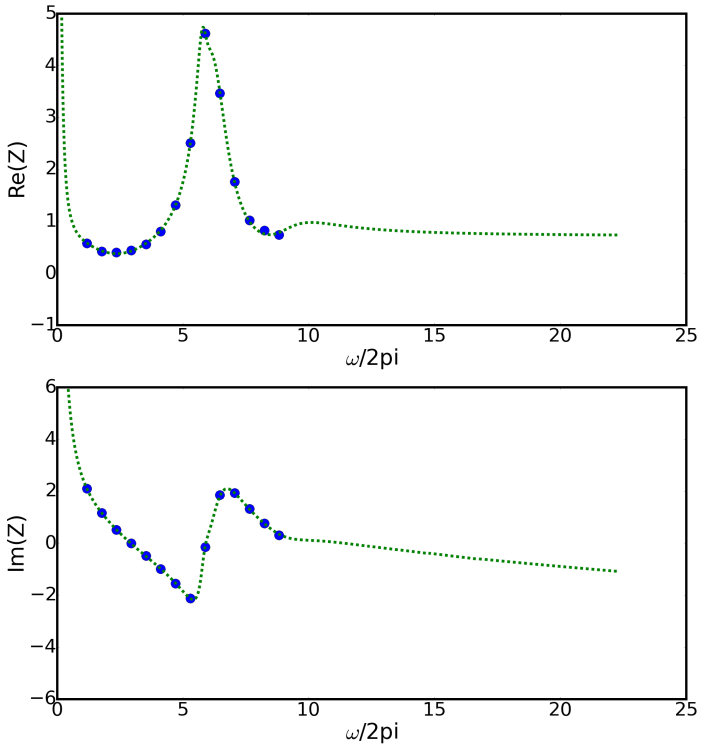

Fig. 98: Resistance and reactance curves for Broadband Case 8.

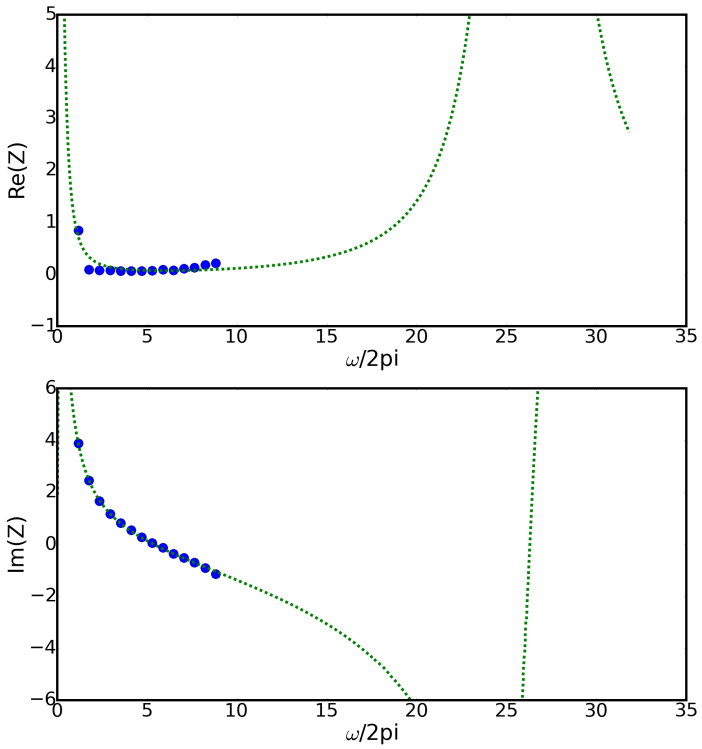

Fig. 99: Resistance and reactance curves for Broadband Case 9.

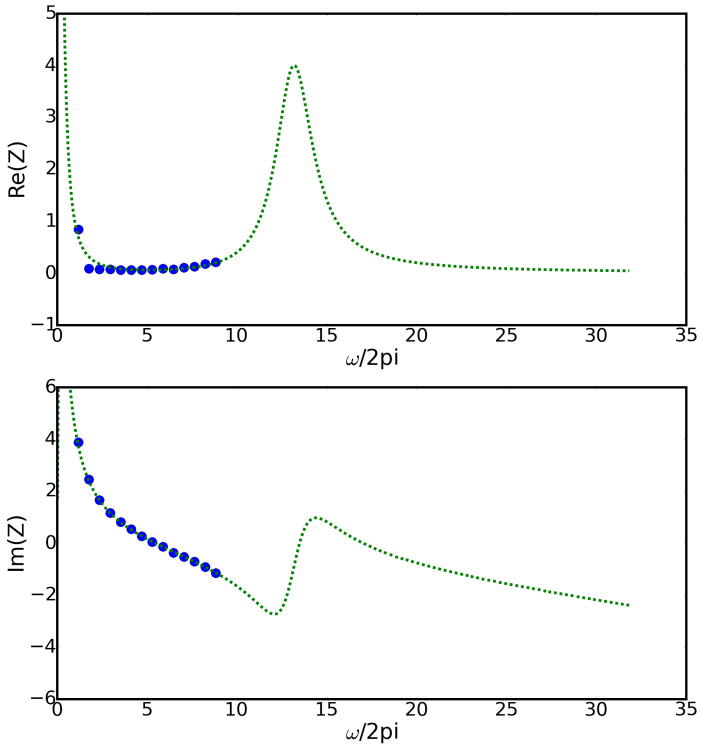

Fig. 100: Resistance and reactance curves for Broadband Case 10.

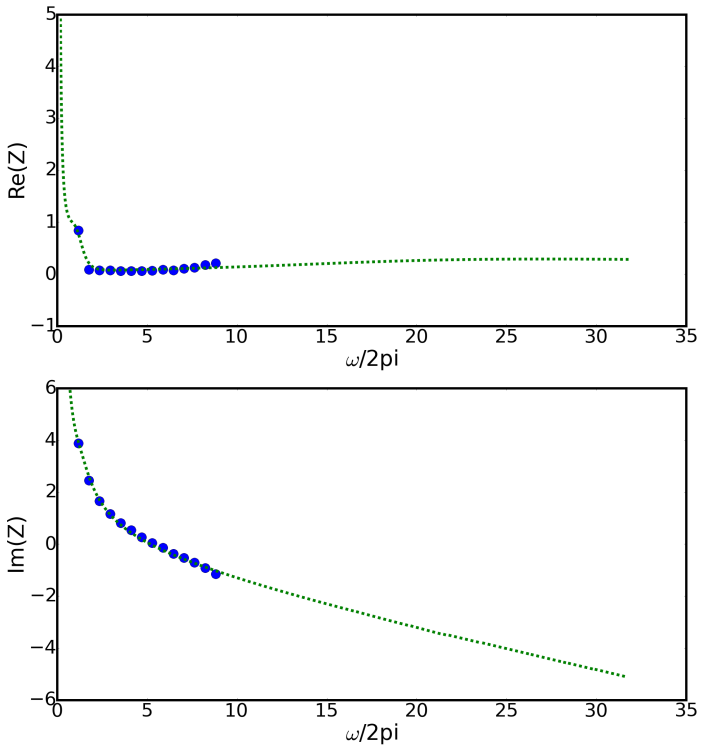

Fig. 101: Resistance and reactance curves for Broadband Case 11.

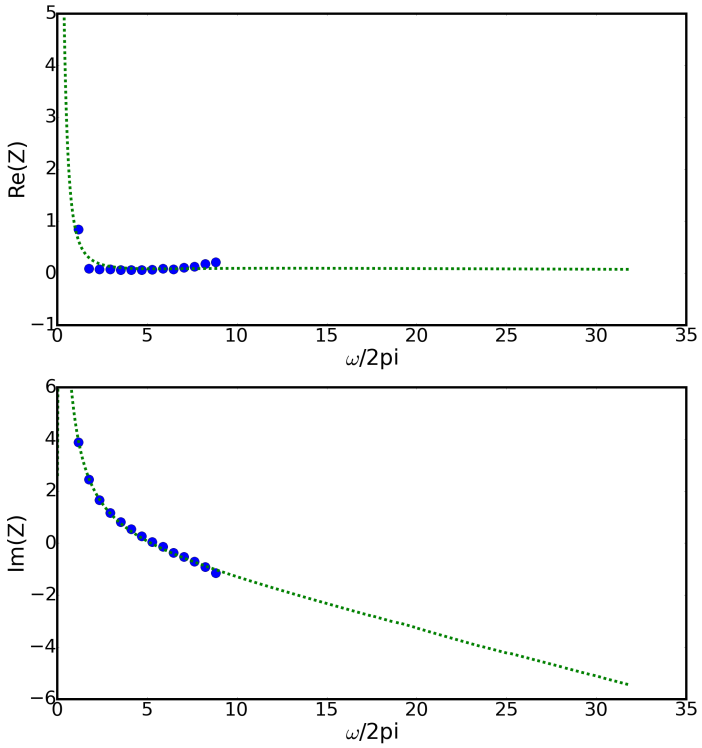

Fig. 102: Resistance and reactance curves for Broadband Case 12.

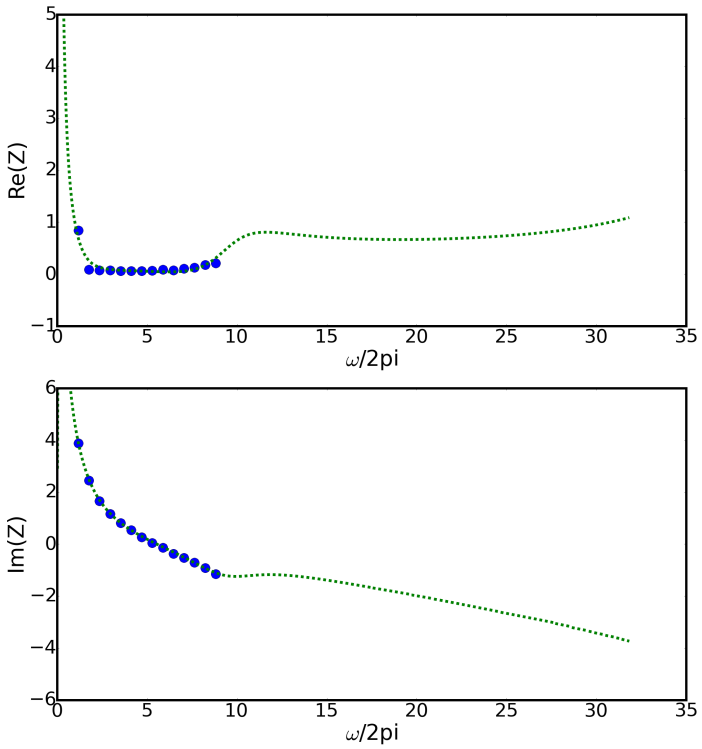

Fig. 103: Resistance and reactance curves for Broadband Case 13.

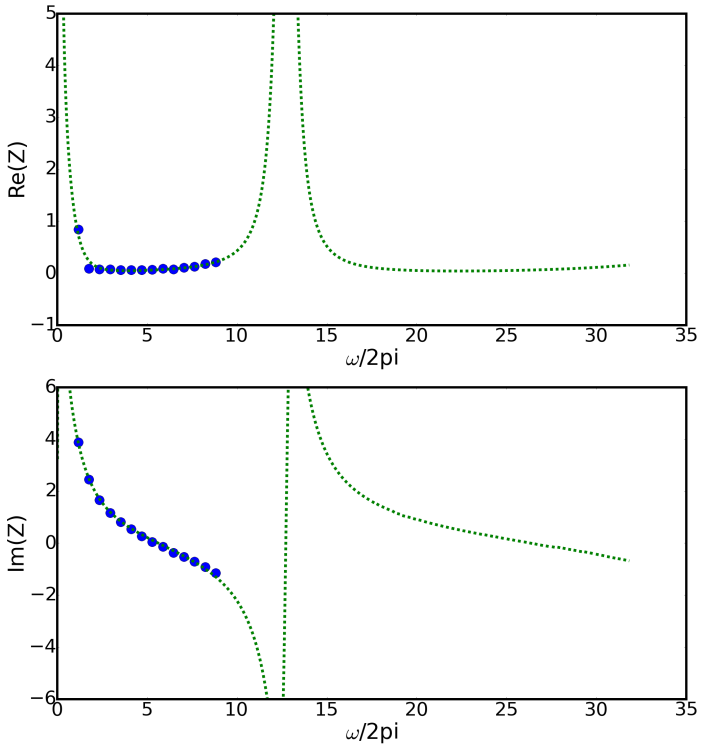

Fig. 104: Resistance and reactance curves for Broadband Case 14.

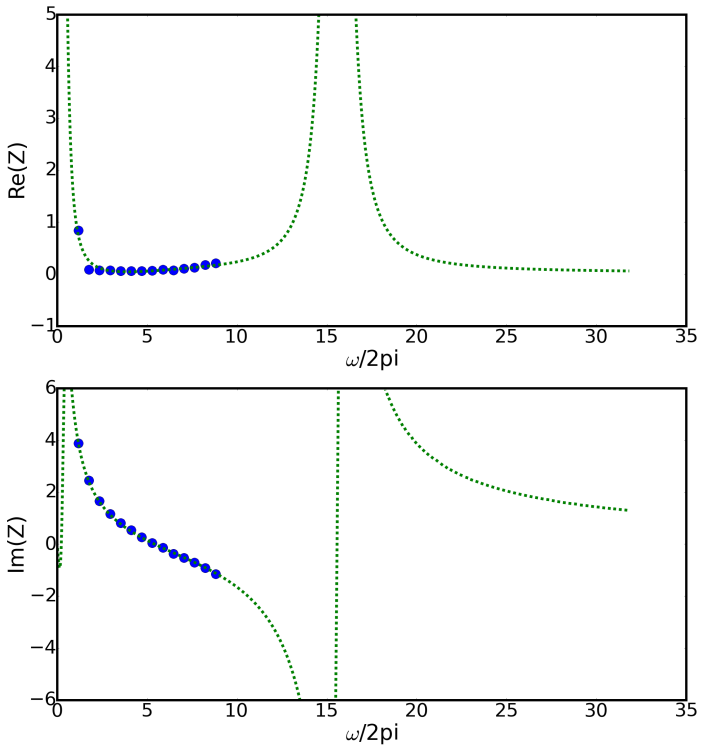

Fig. 105: Resistance and reactance curves for Broadband Case 15.

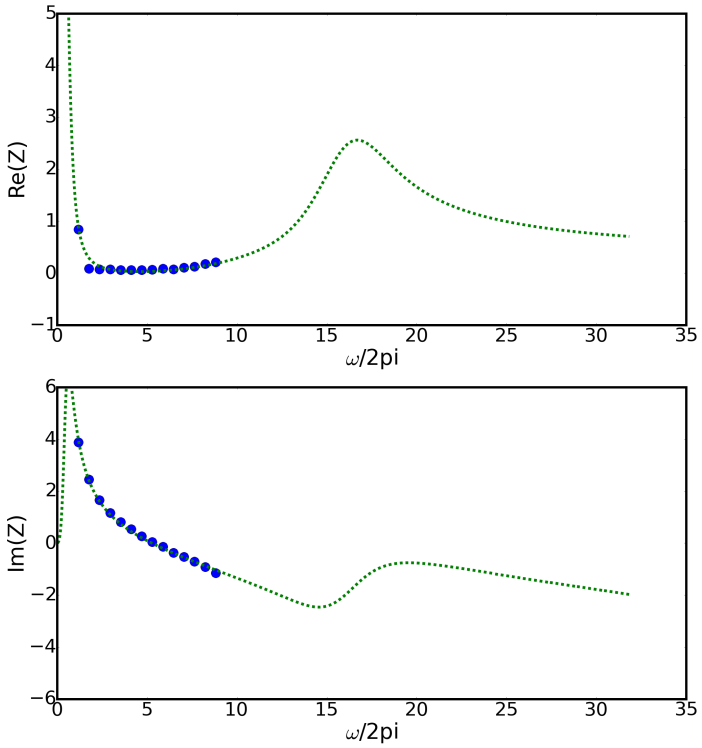

Fig. 106: Resistance and reactance curves for Broadband Case 16.

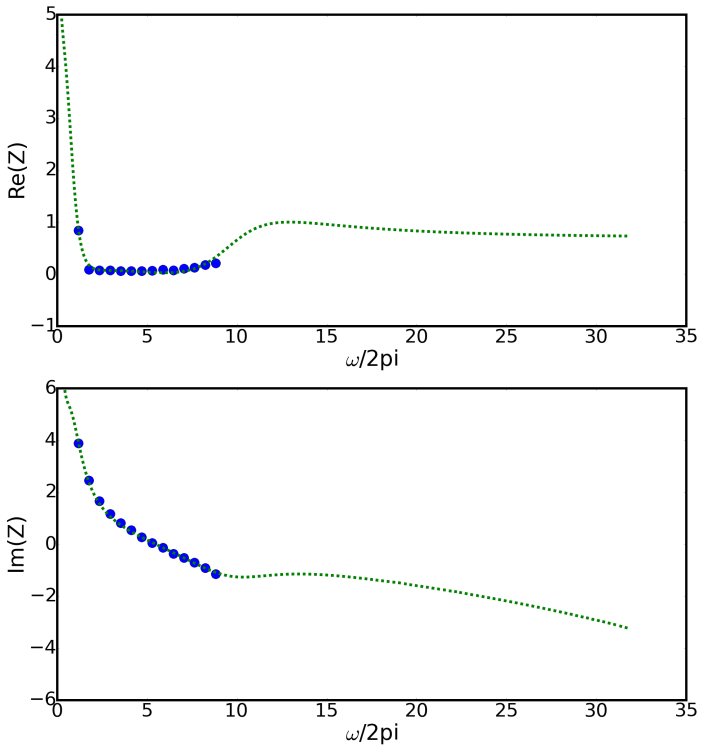

Fig. 107: Resistance and reactance curves for Broadband Case 17.

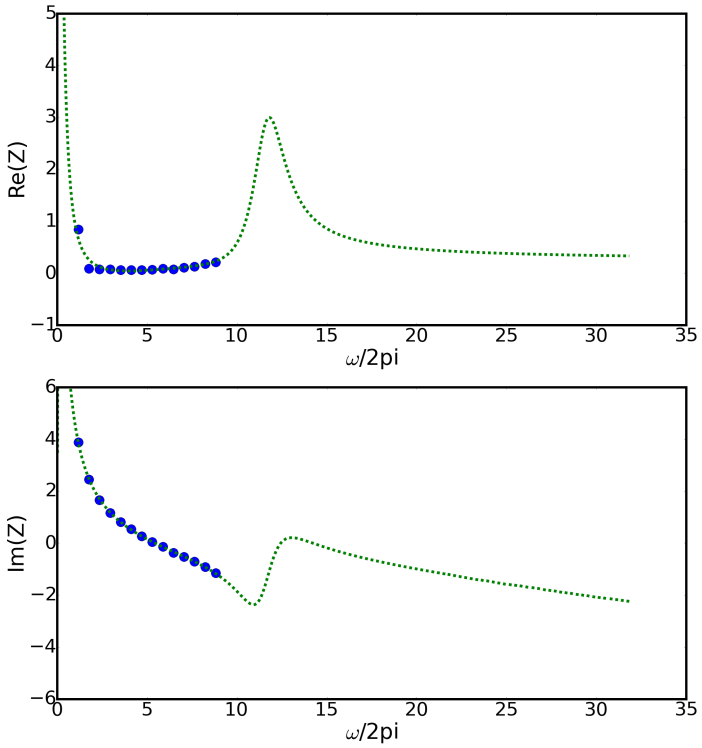

Fig. 108: Resistance and reactance curves for Broadband Case 18.

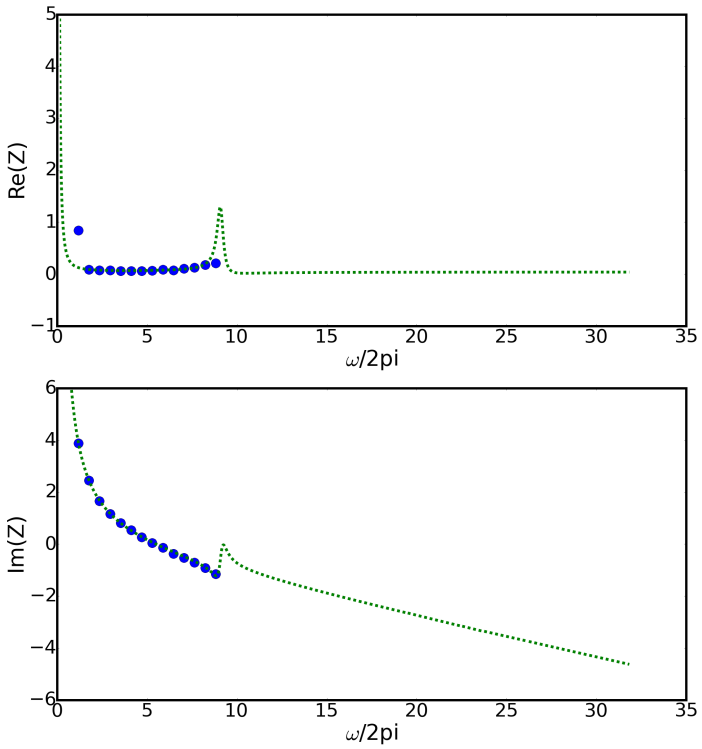

Fig. 109: Resistance and reactance curves for Broadband Case 19.

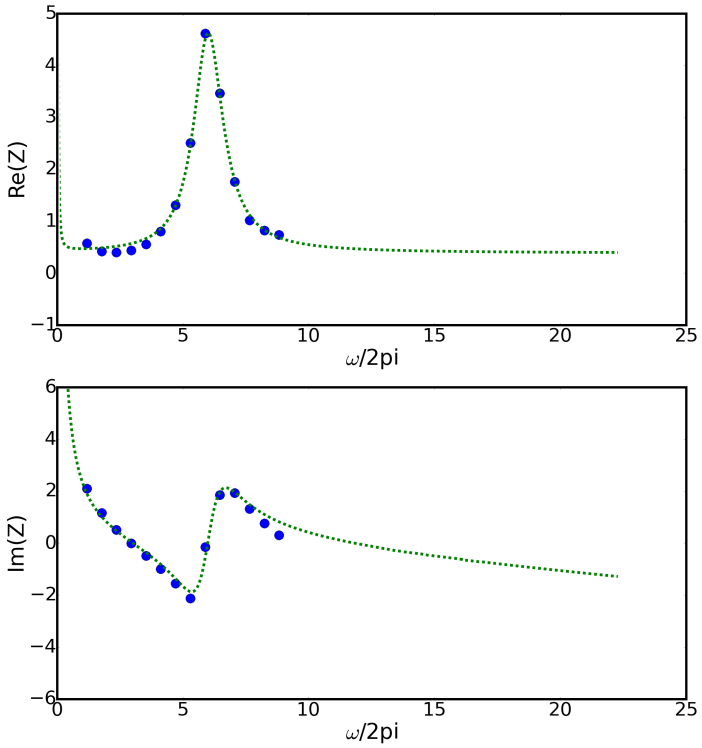

Fig. 110: Resistance and reactance curves for Broadband Case 20.

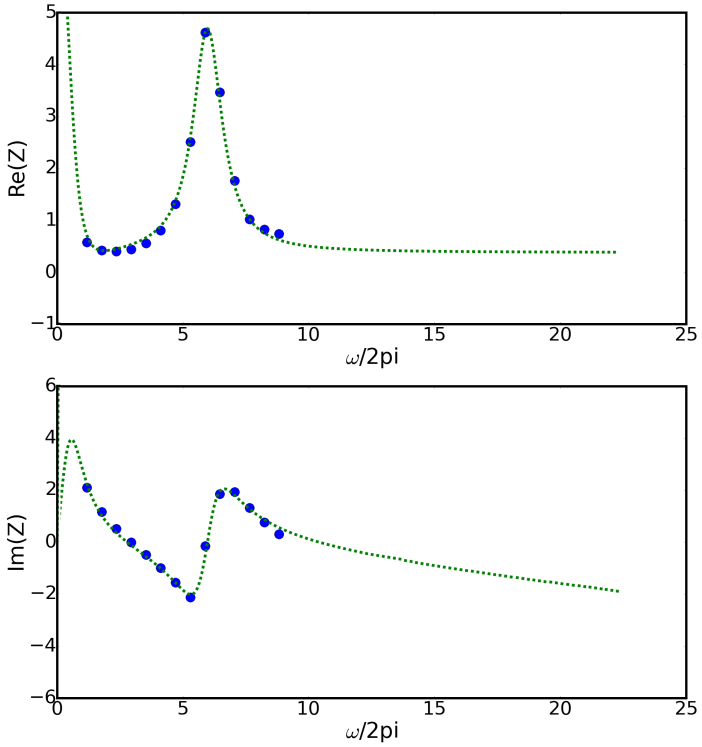

Fig. 111: Resistance and reactance curves for Broadband Case 21.

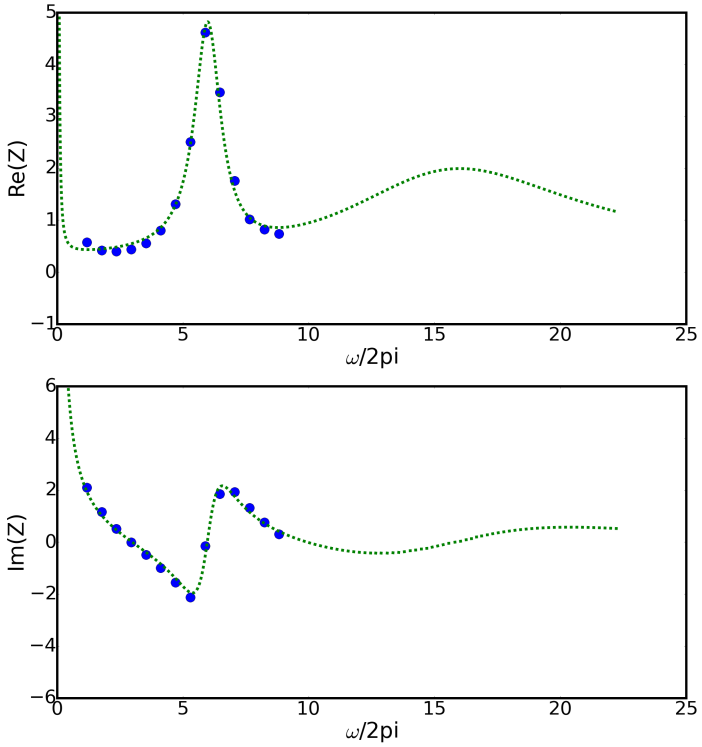

Fig. 112: Resistance and reactance curves for Broadband Case 22.

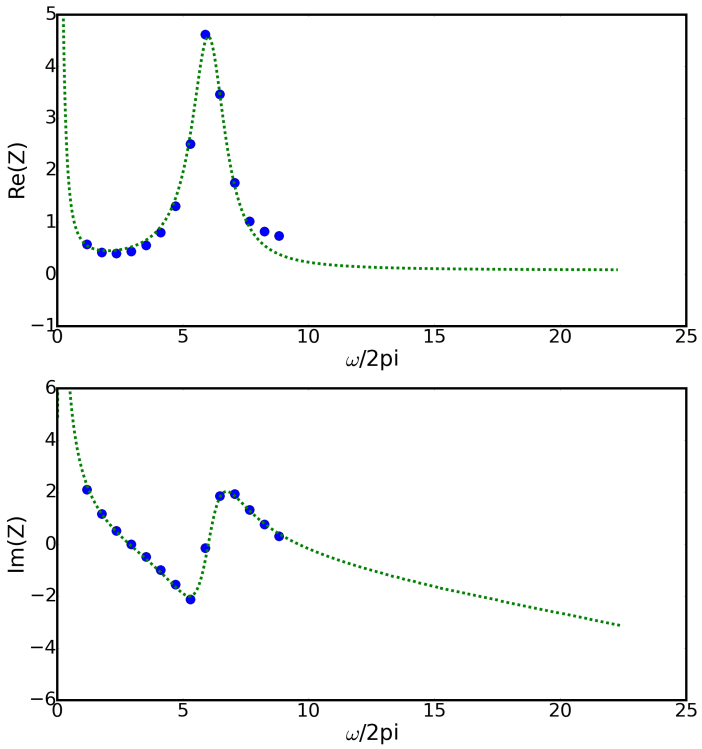

Fig. 113: Resistance and reactance curves for Broadband Case 23.

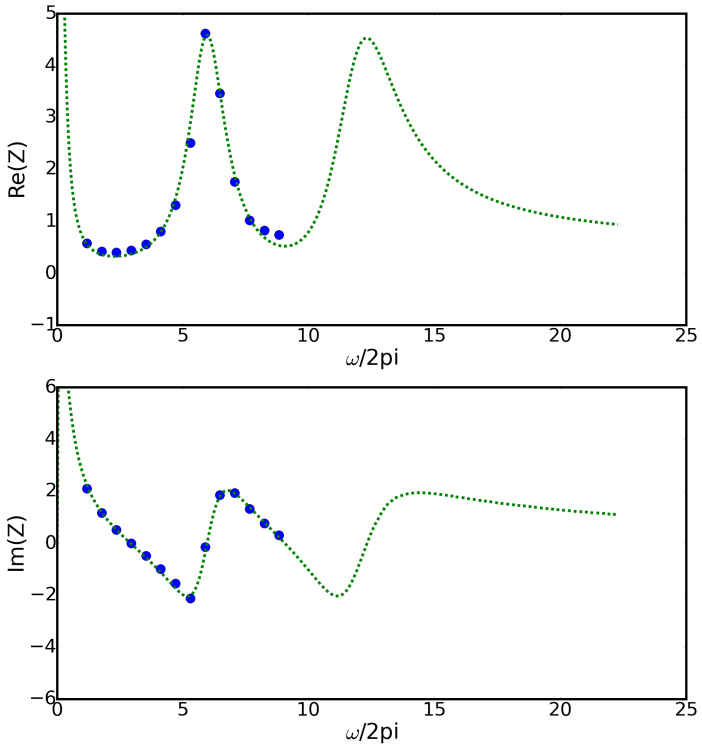

Fig. 114: Resistance and reactance curves for Broadband Case 24.

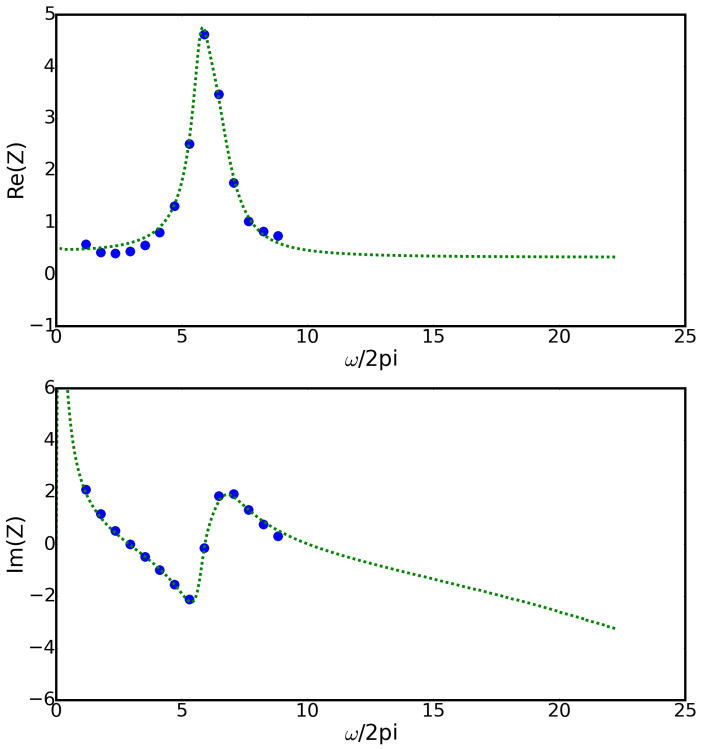

Fig. 115: Resistance and reactance curves for Broadband Case 25.

VITA

Michelle E. Rodio
Department of Computational and Applied Mathematics
Old Dominion University
Norfolk, VA 23529

Education

Old Dominion University, M. S. Computational Mathematics, December 2015, GPA 3.97
Embry-Riddle Aeronautical University, M. S. Mechanical Engineering, May 2012, GPA 4.00
Embry-Riddle Aeronautical University, B. S. Aerospace Engineering, May 2010, GPA 3.23

Journal Publications

F. Q. Hu, M. E. Pizzo, D. M. Nark, On the Use of Prandtl-Glauert-Lorentz Transformation for Acoustic Scattering by Rigid Bodies with a Uniform Flow, The Journal of Sound and Vibration 443, 198-211 (2019).

F. Q. Hu, M. E. Pizzo, D. M. Nark, On a Time Domain Boundary Integral Equation Formulation for Acoustic Scattering by Rigid Bodies in Uniform Mean Flow, The Journal of the Acoustical Society of America 142, 3624 (2017).

Conference Publications

M. E. Rodio, F. Q. Hu, D. M. Nark, Investigating the Numerical Stability of a Time-Domain Boundary Integral Equation with Impedance Boundary Condition for Simulating Sound Absorption of Lined Bodies, 25th AIAA/CEAS Conference, (AIAA 2019-2416).

M. E. Pizzo, F. Q. Hu, D. M. Nark, Simulation of Sound Absorption by Scattering Bodies Treated with Acoustic Liners Using a Time-Domain Boundary Element Method, 24th AIAA/CEAS Conference, (AIAA 2018-3456).

Typeset using LaTeX.